

Sira Ltd, *registered address* South Hill, Chislehurst, Kent, BR7 5EH, UK
Telephone +44 (0) 181 467 2636, Facsimile +44 (0) 181 467 6515
Registered in England No 150576

Sira Ltd is an independent organisation, incorporated in 1918, which operates internationally providing laboratory and engineering services for research, development, evaluation and applications of scientific and industrial instrumentation and control equipment

The Electro-optics Division undertakes research, development, design applications and consultancy with multi-disciplinary teams of engineers and scientists. The Division also supplies contracting services to national and international procurement agencies and engineered equipment on a commercial basis for specialist applications

Issue 1

Authorised



M A Cutter

Technology & Development Manager

Date

29 September 1997

**Final Report on
Radiation Effects in 2-D IR Sensors**

(Report on Call-off order C01 of Work Order WO2 of the
Frame Contract

'Radiation Effects on Sensors and Complex Devices
(ESTEC Contract no 11755/95/NL/NB)

Sira Reference A/9920/00/C104/GRH/001

Copyright © Sira Ltd 1997

The contents of this document are subject
to the terms and conditions of Sira Ltd
available free on request

EUROPEAN SPACE AGENCY
 CONTRACT REPORT

ESA/ESTEC Contract No. 11755/95/NL/NB-WO2-CO1

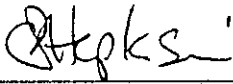
The work described in this report was done under ESA contract
 Responsibility for the contents resides in the author or organization that prepared it

Title

RADIATION EFFECTS IN 2-D IR SENSORS

Summary

This report reviews the published literature on radiation effects in IR detector arrays and summarises the returns from a survey of users having unpublished experimental data. The results of a test programme involving proton and alpha particle irradiation of Mercury Cadmium Telluride arrays from GEC Marconi Infrared Ltd (UK) are also presented

	Name and Function	Date	Signature
Prepared by	G R Hopkinson, Project Manager	3/10/97	
Approved by	M A Cutter, Technology & Development Manager	3/10/97	

Document type	Nb WBS	Keywords Radiation, Infrared, detector arrays
---------------	--------	--

Contents

Section	Page
1 INTRODUCTION	1-1
1.1 Background and Scope	1-1
1.2 Terminology	1-2
1 2 1 Radiation effects	1-2
1 2 2 Infrared detectors	1-4
1 2 2 Device Physics	1-5
1.3 Types of IR detector arrays (overview)	1-7
1.4 Types of IR Detector (further details)	1-12
1 4 1 HgCdTe detectors	1-12
1 4 2 InSb	1-18
1 4 3 Multi-quantum Well (MQW) and Superlattice (SL) Structures for the LWIR	1-20
1 4 4 Schottky Barrier Arrays	1-29
1 4 5 Heterojunction Internal Photoemission (HIP) Devices	1-30
1 4 6 InGaAs Arrays	1-33
1 4 7 Lead salt detectors	1-33
1 4 8 Extrinsic (Si X and Ge X) Detectors	1-34
1 4 9 High Tc Superconductor Detectors	1-39
1 4 10 Uncooled thermal detector arrays	1-39
1 4 11 Multiplexers	1-40
1.5 Summary of space projects using IR detector arrays	1-44
2 BASIC MECHANISMS	2-1
2.1 Transient effects	2-2
2 1 1 Transient Effects in Imaging Detectors	2-2
2.2 Ionization damage	2-8
2 2 1 Ionization Effects on MOS Devices	2-8
2 2 2 Dose enhancement	2-10
2 2 3 Process dependence	2-10
2 2 4 Post irradiation effects (PIE) or time dependent effects	2-11
2 2 5 Effects at low temperatures	2-11
2 2 6 Materials other than SiO ₂	2-13
2.3 Displacement damage	2-13
2.4 Summary	2-20
3 BASIC RADIATION EFFECTS ON BULK MCT	3-1
3 1 Introduction	3-1
3 2 Changes in Carrier Concentration (PC Devices)	3-3
3 3 Type Conversion	3-5
3 4 Changes in Spectral Response	3-6

4	BASIC BULK EFFECTS ON OTHER DETECTOR MATERIALS	4-1
4 1	InSb	4-1
4 2	GaAs and its Alloys	4-3
4 2 1	GaAs Alloys	4-4
4 3	Silicon	4-7
4 4	High T_c Superconductors	4-7
4 5	References	4-7
5	PERMANENT IONIZATION-INDUCED EFFECTS ON MCT FOCAL PLANE ARRAYS	5-1
5 1	Introduction	5-1
5 2	Passivation Technologies	5-1
5 2 1	MCT MIS Arrays	5-3
5 2 2	MCT Photodiode Arrays	5-3
5 3	Dark Current Generation in Photodiode and MIS Devices	5-4
5 3 1	Dark Current Mechanisms in MCT PV Photodiode arrays	5-4
5 3 2	Results for G-MIRL MWIR and LWIR Diodes	5-18
5 3 3	Dark Current Mechanisms in MCT MIS Devices	5-22
5 4	Flatband Voltage Shifts	5-25
5 5	Annealing of Radiation Damage	5-30
6	RADIATION EFFECTS IN INSB AND PTSI ARRAYS	6-1
6 1	InSb arrays	6-1
6 2	PtSi Arrays	6-3
7	RADIATION EFFECTS ON Si:X DETECTORS	7-1
7 1	Extrinsic Si X Detectors	7-1
7 1 1	Monolithic Si X Arrays	7-5
7 2	IBC Detectors	7-8
7 2 1	Ionization Effects	7-8
7 2 2	Effects due to Protons, Neutrons and Cosmic rays	7-9
8	RADIATION EFFECTS IN SILICON READOUT CIRCUITS	8-1
8 1	Introduction	8-1
8 2	Silicon CCD readouts	8-1
8 3	GaAs CCDs and MOSFETS	8-2
8 4	Effects in CMOS circuits	8-4
8 4 1	Previous Sira results on GMIRL CMOS Multiplexers	8-5

9	EXPERIMENTAL RETURNS	9-1
9 1	MMS Survey	9-1
9 1 1	IKS, Phobos, MOP	9-2
9 1 2	The DISR Experiment	9-2
9 1 3	The Isocam Experiment	9-3
9 1 4	The CIRS Experiment	9-4
9 1 5	The MIR Experiment for Spot 4	9-5
9 1 6	The Omega Experiment	9-6
9 1 7	The Seviri Experiment	9-6
9 2	Sira Findings	9-13
9 2 1	InSb Arrays for SIRTf	9-13
9 2 2	Results from SRON (Groningen) on the ISO SWS Experiment	9-15
9 2 3	ATSR	9-15
10	EXPERIMENTAL DETAILS OF RADIATION AND TEST SET-UP	10-1
10 1	Test objects	10-1
10 1 1	256 x 4 Array	10-4
10 1 2	128 x 128 Array	10-6
10 2	test circuits and equipment	10-7
10 2 1	Cooling Arrangements	10-7
10 2 2	Camera Unit	10-7
10 2 3	Programmable Timing Generator	10-11
10 2 4	Power Distribution Unit	10-12
10 2 5	Analogue Signal Processing Unit	10-12
10 2 6	AT Computer and Framegrabber	10-12
10 2 7	Test Software	10-12
10 2 8	Modifications made for the present contract	10-14
10 3	irradiations	10-14
10 3 1	Alpha Particle Irradiations	10-14
10 3 2	Proton Irradiations of the 128 x 128 Array	10-16
10 4	test measurements	10-18
10 4 1	Functionality	10-18
10 4 2	Measurements of Image Data	10-18
10 4 3	Threshold Voltages	10-18
10 4 4	Pixel Uniformity Versus dig Voltage	10-18
10 4 6	Temperature Measurement	10-18
10 4 7	Power Consumption	10-19
10 4 8	Pixel Response Uniformity	10-19
10 4 9	Linearity	10-19
10 4 10	Transient Signals	10-20
11	RESULTS OF THE EXPERIMENTAL TEST PROGRAMME	11-1
11 1	Signal Calibration	11-1
11 2	Transient Events	11-1
11 2.1	Quasi Transient Proton Event	11-7
11 3	Displacement Damage	11-8
11 4	Total Ionizing Dose Effects (TIDE) on the 128 x 128 LWIR Array	11-12
11 4 1	Threshold Voltage Shifts	11-12
11 4 2	Linearity and Responsivity of the 128 x 128 array	11-16

12 DISCUSSION AND IMPACT ANALYSIS

12-1

12 1	Permanent effects in detector materials	12-1
12 1 1	MCT	12-1
12 1 2	InSb	12-2
12 1 3	GaAs/InGaAs QWIP Detectors	12-3
12 1 4	Extrinsic Silicon	12-3
12 1 5	Other Detector Materials	12-3
12 2	Permanent effects in Si readout circuits	12-3
12 3	Transient effects	12-3
12 4	Radiation testing of IR detector arrays	12-4
12 5	HARDNESS Assurance	12-6
12 6	Suggestions for Further Work	12-7

EXECUTIVE SUMMARY

A study of space radiation effects in infrared imaging sensors has been performed within the frame of contract 11755/95/NL/NB. The work involved both a literature survey of published (and unpublished) data and an experimental investigation of radiation effects in commercially available arrays.

A wide variety of detector technologies have been developed for the short wave (SWIR), medium wave (MWIR) and long wave infrared (LWIR). It would be impossible to discuss potential radiation effects without a good understanding of the devices available, and these are discussed in some detail in chapter 1. The principal photon detector materials available are

- mercury cadmium telluride (SWIR, MWIR, LWIR)
- InSb (visible to MWIR)
- InGaAs (SWIR)
- GaAs/GaAlAs quantum well detectors (LWIR)
- PtSi (MWIR)
- extrinsic silicon, including blocked impurity band detectors (LWIR)

There are also a variety of thermal detectors, such as pyroelectric and microbolometer arrays and superconducting detectors are starting to be developed. Also lead chalcogenide arrays are showing a renewed promise as photon detectors for the MWIR.

The choice of detectors for a particular application will depend on parameters such as spectral response, sensitivity, calibration requirements and, most importantly, availability in the desired pixel format. There is little scope for choosing on the basis of radiation performance – and relatively little relevant radiation effects data on which to make such a choice.

Mercury Cadmium Telluride (MCT) has traditionally been one of the most useful IR detector materials and the alloy composition can be adjusted to give cut-off wavelengths from the SWIR to the LWIR. Consequently most of the available radiation effects data relates to MCT. In this material the passivation is important. The bandgap is small (0.1 eV for 10 μm cut-off) and a small amount of surface band bending can easily change the surface conditions (for example causing inversion or surface leakage). Effects can be expected to be most severe for longer wavelength diodes. An important effect is the change in resistance of PV MCT photodiodes, but fortunately it appears that the damage anneals and that effects are not usually large for low dose rate environments. The importance of the effects will however depend on the passivation technology used, the type of readout circuit (and its susceptibility to changes in diode resistance) and on the performance stability required. Imaging applications will tend to be more tolerant of response and non-uniformity changes than radiometric instruments – though frequent calibration against blackbody sources can be used to compensate for radiation-induced changes in the latter case.

For low background applications such as space astronomy, special readout circuits are needed since the commonly used direct injection circuit gives poor performance at low detector currents. For low background and long wavelength uses, the MCT performance is specially limited by leakage currents due to tunnelling effects. Radiation-induced trap assisted tunnelling can then be expected to be important. For other applications it appears that

displacement damage induced defects are not important – and this is borne out by the experimental results of this study (see below)

MCT devices compete with InSb in the MWIR (though InSb requires lower operational temperatures) Results from the US SIRTf and WIRE programmes (discussed in section 9) indicate that InSb is susceptible to bulk damage-induced dark current spikes This is likely to be due to the fact that InSb has intrinsically fewer crystal defects than MCT, so that displacement damage effects are more noticeable

At longer wavelengths, GaAs/AlGaAs quantum well detectors offer advantages because of their relative ease of manufacture and good uniformity However most IR detector developments are driven by military requirements and the defence market is naturally conservative - hence changes in detector availability are slow At the present time, the promise of GaAs/AlGaAs arrays has not been realised at an industrial level However, based on the small amount of data that has been published and experience with GaAs devices in general, it can be expected that these detectors will be relatively radiation resistant

Effects in extrinsic silicon detectors for LWIR space astronomy have been well known since IRAS The detectors are susceptible to transient events and changes in responsivity (due to quasi-permanent charge trapping) after a particle hit The development of blocked impurity band (BIB) detectors has improved performance considerably and such detectors have been used on the ISO SWS instrument and will be used on the US SIRTf and WIRE missions One of the interesting findings of this study has been that BIB detectors are not as radiation tolerant as had previously been thought – leakage currents can be caused by proton damage, perhaps due to ‘punch-through’ of the intrinsic blocking layer (whose purpose is to block the impurity band conduction) This illustrates the general point that it is dangerous to make radiation effects predictions from a limited set of test data and in particular to extrapolate performance in a proton environment from Cobalt60 total dose data

Virtually no information is available on effects in InGaAs, PtSi and lead chalcogenide detectors

Though many detector materials appear to be useful for low dose environments, effects in the readout integrated circuit (ROIC) are also important The most popular technology for the ROIC is CMOS The concerns for radiation performance will be similar to those for any CMOS device and centre on the behaviour of thick field oxide isolations and immunity from latch-up It would appear, in fact, that the improvement in latch-up immunity with decreasing temperature will render this effect unimportant for low temperature use with IR detectors – however there is no report of this in the open literature

In principle, it is possible (by choice of oxide technology and isolation structures) to harden against radiation effects in CMOS readout circuits and many US manufacturers claim to have done this However, for a particular application and detector format, the device used will depend on commercial availability and practicalities may force the use of unhardened circuits Radiation effects should then be closely monitored

As in all areas of radiation effects research, the effects observed depend very much on the device designs and technologies used so it is difficult to make generalised statements Deciding on test strategies is also difficult, particularly as measurements on IR detectors

require specialised test equipment (even more so than for visible imagers such as CCDs). Though general investigations (such as reported here) have a place, the cost of devices and test equipment is likely to prevent the attainment of a comprehensive database. On the other hand, the experimental groups which have access to representative detectors and test facilities (that is the instrument developers) will have little time or experience to investigate effects fully – and there is also the pressure to prove that the instrument works rather than to seek out potential problems. This is to some extent borne out by the unpublished experimental returns gathered by Sira and MMS during the survey of work package C101. Although the irradiations and testing have been undoubtedly competently performed and useful results obtained to verify the performance of the arrays in flight, the level of analysis and interpretation is not high and the usefulness of the data for other projects is hard to determine. The solution perhaps lies in a partnership between instrument developers and radiation effects experts and the Agency may wish to consider how best to develop this in future. Certainly there are many areas where little is known. InGaAs, quantum well and InSb devices have been little studied (even at a general fundamental level). Also many effects will depend on the precise combination of detector material, detector passivation, readout architecture and readout circuit technology.

Following the literature survey, work package C102 was devoted to the development of a plan for radiation testing of IR sensor arrays. The low yield, high development cost and low market for IR detectors tends to result in high procurement cost compared with visible detectors such as CCDs. A solution is to try to obtain lower performance engineering grade arrays as bare devices not mounted in a dewar. However many manufacturers will not supply bare devices but prefer to market camera systems. Also there are issues of documentation (and the level of information needed to drive the detector) and test equipment availability.

After a survey of manufacturers, it was determined that bare devices could be obtained from GMIRL, UK in engineering grade at relatively low cost and that these could be used with existing test equipment at Sira. Accordingly a test plan was evolved based on purchasing one 256x4 staggered linear array with 6.4 μm cut-off MCT photodiodes and one 128x128 10.1 μm cut-off MCT array. Both these devices use a CMOS direct injection readout.

Though total dose effects on multiplexers are important, the influence of CMOS process on radiation tolerance has been well studied. Also total dose effects in GMIRL photodiodes have been investigated in a previous Sira study. Hence it was decided to concentrate on particle-induced transient and displacement damage effects for which there was little information available in the open literature.

An important outcome of the experimental programme (work package C103) was the development of test methods for IR arrays in general and, in particular, a test set-up for performing biased irradiations at 80 K whilst on the 10 MeV proton beam line at Harwell.

It was known from the preceding Sira study and from indications in the literature that displacement damage effects are not as pronounced in MCT as in silicon detectors which have a relatively intrinsically defect-free lattice structure. This is borne out by the experimental work discussed in section 11, since no significant displacement damage effects were seen. Turning to transient effects, it is expected from the theory of Klein (section 2.1) that the energy used up in creating an electron-hole pair is ~ 0.1 eV for LWIR and MWIR MCT, corresponding to $\sim 1 \times 10^5$ electrons per 10 MeV proton hit (assuming a 9 μm thick detector). A previous Sira study placed an upper limit of 2×10^5 electrons per 10 MeV proton and in this

work the sensitivity of the off-chip electronics was improved so that events of 1×10^5 electrons per 10 MeV proton (conforming with the above prediction) were detected - though because of the short stare time used (forced by the detector dark current at 77 K), the number of events observed was small. 5.48 MeV alpha particle tests in the laboratory also gave low count rates but there is good confidence that the maximum event size was $\sim 5 \times 10^3$ electrons. This is about a factor 3 lower than what would be expected from the ionizing energy loss in MCT and may be due to recombination effects in the dense tracks produced by the alpha particles. Differences in event rates were seen between the proton beam (normal incidence) and the wider range of incidence angles obtained with the alpha source.

Tests were also made of the responsivity changes of the LWIR diodes as a result of the total ionising dose received during the 22.4 krad of 10 MeV proton irradiation and during a 29 day unbiased 6 krad alpha particle irradiation at room temperature. The results indicated pixel-to-pixel changes at the 5% level due to the irradiation for the proton irradiation and 1% or less for the alpha irradiation. This suggests that changes in pixel response, though important, are not likely to be a major problem for low dose space environments.

Also observed were changes in threshold voltage for the CMOS readout circuit. The change in effective direct injection voltage is particularly important as it causes changes in fixed pattern non-uniformity and absolute response. A shift of -2.6 mV/krad was found, corresponding to a 4.3% change in average responsivity/krad. Effects in displayed images were noticed after a total dose of only 30 rad. These effects are however consistent with previous Sira findings.

The implications for using similar MCT arrays in future ESA missions are that particular attention should be given to in-flight calibration (in any case likely to be necessary because of fluctuations in the array operating temperature) and to in-flight adjustment of bias voltages (particularly the direct injection gate voltage). However there appear to be no serious drawbacks even for long wavelength (10 μm cut-off) arrays.

1 INTRODUCTION

1.1 BACKGROUND AND SCOPE

The present work is in response to call-off order CO01 of work order W02 of ESA frame contract 11755/95/NL/NB, entitled "Radiation Effects in Sensors and Complex Devices" Frame contract management was provided by MMS, Velizy CO01 is concerned with a study of the potential radiation hazards involved in using 2-D infrared focal plane arrays in a space environment. The technical development of such sensors is advancing at a steady pace and devices are now being proposed for several ESA missions. For example the HRTIR (High Resolution Thermal Infra Red), HRIS (High Resolution, Imaging Spectrometer) and PRISM (Processes Research by an Imaging Space Mission) instruments are being (or have been) proposed to use large 1-D and 2-D arrays of HgCdTe detectors (in the range 1 to 13 μm). However, there is very little information on radiation effects on IR detectors available in the open literature. This is partly because 2-D IR sensors have mainly been developed for military uses and test information is often classified. Partly because the high costs involved in procuring state-of-the-art arrays has discouraged extensive testing.

The Earth's natural radiation environment consists of electrons, protons and heavy ions which are either trapped by the Earth's magnetic field or are in direct transit from the Sun or from other sources in the galaxy. These particles can cause direct effects on the detector and can also produce secondary radiation in the form of x-rays, gamma rays, neutrons and heavy ions by interaction with spacecraft materials, though the fluxes of these secondaries are comparatively small. It is assumed that the reader is familiar with the basic details of the radiation environment. Details can be found in a number of good reviews [1,2,3,4,5,6,7,8,9]. It is expected that most ESA missions will be of 10 years or less and will involve fairly well shielded detectors operating either in low Earth orbits, highly eccentric orbits or geostationary orbit. For these situations the total dose is expected to be less than 20 krad(Si) and to arise predominantly from trapped or solar flare protons. This report is not primarily concerned with nuclear weapons effects, which arise from high fluences (and flux rates) of x-rays, gamma rays and neutrons, although in some cases the available test data is more relevant to performance in a weapons (or weapons-enhanced) environment rather than the natural space environment.

IR sensors can be used in space systems either for viewing objects against the Earth background, or against the background of deep-space. In the former class are Earth resource or environment monitoring instruments and military surveillance systems. In the latter are strategic defence sensors (designed to monitor intercontinental missiles during the high altitude parts of their trajectories) and IR astronomy payloads (such as the focal planes for ESA's ISO, and NASA's SIRTf). Broadly speaking, Earth viewing IR sensors tend to be sensitive to wavelengths from 1 μm up to 14 μm (below 1 μm intrinsic silicon detectors can be used, and these are not considered in this report). On the other hand, space-viewing sensors can be sensitive up to $\sim 26 \mu\text{m}$ (for strategic defence) and up to about 100 μm , for astronomy. Note that the hazards involved in operating in a given radiation environment may depend on the type of application. For example a detector array operated at low temperatures for use in low background deep space observations may be less tolerant to the radiation environment than when used at higher temperature for high background Earth-pointed imaging.

Interface Trap

At the interface between two dissimilar media, wave functions in any periodic solids must be disturbed. At the interface between silicon and an oxide film thermally grown upon it, the opportunities for unique quantum states are numerous due to the presence of lattice mismatch, non-stoichiometric conditions and impurities, especially hydrogen. These states can act as traps. The density of interface traps, D_{it} , is expressed in $\text{cm}^{-2} \text{eV}^{-1}$.

Latch-up

The onset of a self-sustaining conduction mechanism in a junction structure with four regions such as p-n-p-n in series and closely spaced. The mechanism is otherwise known as being of the SCR or thyristor type. Latch-up can be triggered in certain complementary MOS (CMOS) integrated circuit designs and also in many junction-isolated bipolar integrated circuits by a pulse of radiation of dose rate greater than about 10^6 rad s^{-1} or a strike by an energetic cosmic ray ion. If the current supply to a chip is not limited then latch-up can result in device burn-out and a permanent failure, otherwise circuit operation can be restored by a simple power off-on cycle.

Linear Energy Transfer (LET)

The amount of energy deposited by an incident particle per unit of track length expressed in units of eV/mg cm^2 . Heavier ions have higher LETs than do lighter ions of the same energy. A similar parameter is the 'stopping power' expressed for example in $\text{keV}/\mu\text{m}$.

Threshold Voltage (V_T)

In MOS devices, the gate voltage at which the source-drain current reaches a specified value, commonly 10 microamps.

Threshold Voltage Shift (ΔV_T)

One of the most important parameters in the analysis of radiation-induced degradation of MOS and CMOS devices. The difference in V_T values before and after irradiation or other treatment.

1.2.2 Infrared detectors

Responsivity

The current out of a detector per incident photon power, normally measured in A/W .

Noise equivalent power

The signal irradiant power (in a specified spectral band) incident on the detector, which results in a photon signal level equal to the electronic noise level. So the NEP is the irradiant power (in Watts) divided by the signal to noise ratio (SNR).

D (dee-star)*

The inverse of NEP, normalized with respect to detector area (A) and bandwidth (Δf)

$$D^* = \frac{(A \Delta f)^{1/2}}{\text{NEP}}$$

This is an important figure of merit for single element detectors, but is not so meaningful for detector arrays since Δf is not always well defined. For an array Δf is usually taken as $1/2 t_i$, where t_i is the integration (or stare) time. Usually D^* is measured in $\text{cmHz}^{1/2}/\text{W}$ or 'Jones'

Note that it is necessary to define the following conditions

- magnitude and temperature distribution of the flux source
- detector field of view
- background temperature
- chopping frequency (or other measure of bandwidth)
- wavelength (or wavelength range) at which the measurement applies

R₀A (zero bias resistance - area product)

The slope of the current-voltage curve for a PV diode at zero bias times the area of the detector, unit $\Omega \text{ cm}^2$

BLIP (background limited infrared performance)

Operating mode for which the IR background limits the noise performance of the detector. This is the theoretical best performance that can be obtained

Fill factor

The percentage of detector array area that responds to optical signal

NEI (noise equivalent irradiance)

The signal flux that gives a signal to noise ratio of one (the same as NEP but using photon flux rather than Watts)

NEDT (noise equivalent differential temperature)

The minimum resolvable temperature difference (in a scene) between two adjacent pixels in an array

1.2.2 Device Physics*Carriers*

When electrons are excited across the band-gap, both they and the resulting holes are mobile and will move if an electric field is applied. In inorganic oxides and

semiconductors, electrons and holes are the main 'carriers' of current. Ions usually contribute only to a very minor extent.

In n-type semiconductors, electrons are in the majority and holes in the minority (and vice versa in p-type semiconductors). Radiation or forward junction bias can produce 'excess minority carriers'.

Band-gap

In perfectly crystalline inorganic insulators and semiconductors, there are well-defined regions of the energy states diagram which are 'forbidden'. In these regions, there are no quantum energy states which can accommodate electrons or holes. The lowest of these is often referred to as the band-gap. The lower edge is defined by electron potential energy ' E_V ' (the top edge of the valence band), the upper edge is defined by ' E_C ' (the bottom edge of the lowest conduction band).

The band-gap energy ' E_g ' is equal to $E_C - E_V$. Conduction in any inorganic solid involves the excitation of electrons from energy levels below ' E_V ' to levels above ' E_C ' and subsequent motion of the electron or the resulting hole. The bands have a continuous overlap of quantum states which allow this. Very similar conditions occur even in non-crystalline but continuous networks such as the Si-O-Si-O network of an oxide thermally grown on silicon. Defects and impurities (eg. caused by radiation damage) can give rise to energy states ' E_i ' within the band-gap.

Intrinsic semiconductor

One which is essentially pure and free from impurities. In the intrinsic photo-absorption process, photons with energy greater than the bandgap result in electronic transitions from the valence to the conduction band (generating both holes and electrons).

Extrinsic semiconductor

One which is doped with impurities. In the extrinsic photo-absorption process, photons with energy greater than the ionization level of the impurity are absorbed and result in the generation of one free carrier and an ionized impurity site.

Band-Bending

A uniform electric field in a material is associated with a linear variation of potential with distance. If, however, the material responds to the applied potential by producing a space charge the field will not be uniform and the potential-versus-distance plot will be curved. This often occurs near the surface of a semiconductor (as in a MOS device) and is called 'band-bending'. The condition of zero band-bending is called the 'flat band' condition.

Flat-Band Voltage (V_{FB})

In MOS devices, an important parameter which indicates the amount of charge in an oxide. Gate voltage at which no surface band-bending is present. V_{FB} shifts under irradiation.

Heterostructure

A structure that is made up of multiple epitaxial layers of different composition

QWIP

Quantum well infrared photodiode Usually fabricated from layers of GaAs and GaAlAs by molecular beam epitaxy (MBE)

SLS

Strained layer superlattices (SLSs) are a class of semiconductor materials in which the lattice mismatch between adjacent, alternating layers is accommodated by the presence of built-in layer strain This strain, along with quantum size effects, leads to the unique properties of SLS's the ability to independently vary the energy gap, lattice constant and transport properties

SOS

Silicon-on-sapphire (SOS) is single-crystal silicon grown on a sapphire substrate

SOI

Silicon-on-insulator (SOI) devices have a layer of insulating material, usually silicon dioxide, silicon nitride, or silicon oxynitride, separating a silicon substrate from the silicon within which active devices are fabricated SOS is a subclass of SOI

1.3 TYPES OF IR DETECTOR ARRAYS (OVERVIEW)

There have been several recent reviews of the various types of IR detector array ([10],[11],[12],[13],[14],[15],[16],[17]) There are two basic types of IR detector

- Thermal detectors measure the total amount of energy which is absorbed, regardless of its wavelength Examples are bolometers and pyroelectric detectors (both types can be made as arrays)
- Photon detectors respond only to those photons with an energy greater (and wavelength shorter) than a cut-off wavelength, characteristic of the semiconductor material The detector response is proportional to the rate of absorption of these photons, and does not depend on their energy (as long as it is above the cut-off)

Figure 1 3-1 (taken from the review by Pickel [18]) shows some of the main detector materials and their ranges of operation The parameter D^* is the responsivity to noise ratio, normalised to the detector area, measured in $\text{cm}^2\text{Hz}^{1/2}/\text{W}$ (see also section 1 3) The figure also shows the atmospheric transmission as a function of wavelength and the conventional designations for the wavelength bands Because atmospheric constituents such as H_2O and CO_2 cause significant absorption of radiation, particularly at $2.5\mu\text{m}$, $6\mu\text{m}$ and longwards of $13\mu\text{m}$, the infrared region of the spectrum has historically been divided into short wave IR (SWIR) $1-2.5\mu\text{m}$, medium wave IR (MWIR) $3-5\mu\text{m}$ and long wave IR (LWIR) $8-13\mu\text{m}$ wavebands were useful imaging

can be performed. The very long wave (VLWIR) band is not suitable for use within the atmosphere but, since the advent of space-based IR astronomy, there has been a growing interest in detectors with a response out to $\sim 100\mu\text{m}$

There are other reasons for dividing the spectrum into wavelength regions. Firstly there are technological differences between the detectors used for the different wavebands and secondly there are differences in the characteristics of scenes and targets to be imaged, for instance as the wavelength is increased the proportion of scattered sunlight contributing to the detector irradiance diminishes and the contribution from thermal emission increases as typically does the photon flux. On the other hand the photon contrast (the change in the photon flux for unit temperature change in the image) decreases. This report will cover detectors for the whole of the IR region but with special emphasis on MWIR and LWIR arrays. The various detector types will be discussed in some detail later in this section. In the following we give a brief overview.

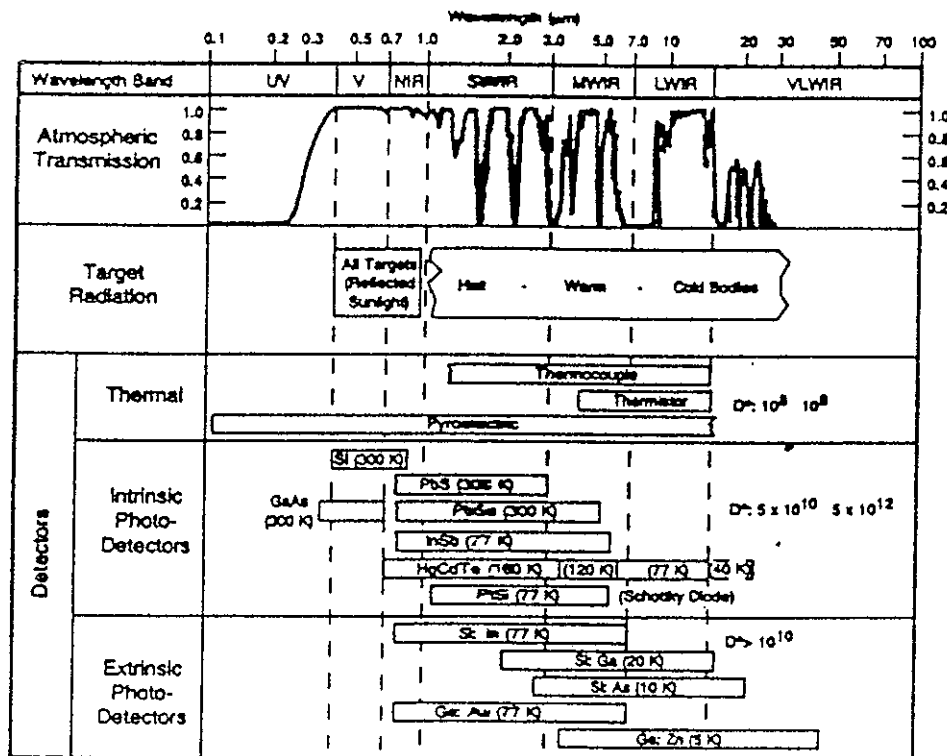


Figure 1 3-1 The main detector materials and their ranges of operation (after Pickel [8])

Thermal detectors are not commonly used in space instrumentation, because of their low responsivity. However they do have advantages in near-room temperature operation and broad spectral response. Examples of applications are Earth sensors, startrackers and scientific instruments (such as ESA's proposed Geostationary Earth Radiation Budget, GERB, instrument)

There are a large number of semiconductor materials which have band gaps (E_g) narrow enough for IR photon detection. Since

$$\lambda_{\text{cutoff}} = 1.24/E_g \quad \text{with } \lambda \text{ in } \mu\text{m} \text{ and } E_g \text{ in eV} \quad (1-1)$$

materials with bandgaps in the range 1.24 eV to 0.00124 are suitable for detecting photons with wavelengths in the range 1 to 100 μm . Below is a list of some of the main candidates

- Mercury Cadmium Telluride (HgCdTe)
- other ternary alloys (e.g. InAsSb, HgZnTe, HgMnTe)
- Indium Antimonide (InSb) for MWIR detectors
- Lead Salts (PbS, PbSe, PbSe/PbTe, PbSnSe, etc.)
- InGaAs/InP for SWIR detectors
- Schottky barrier arrays from platinum silicide (PtSi), and other silicides
- Heterojunction internal photoemission (HIP) devices
- Extrinsic silicon (Si X), including blocked impurity band detectors
- III-V (e.g. GaAs/AlGaAs) quantum well (QWIP) and superlattice (SL) structures
- II-VI superlattices
- High- T_c superconductor infrared detectors

HgCdTe is a particularly useful detector material since its alloy composition can be turned so as to give a cut-off anywhere in the wavelength region of interest, however in the MWIR, InSb has perhaps a more mature manufacturing technology. Most of the work on radiation effects on IR materials has been carried out on HgCdTe. Silicon, although not a useful IR detector material in its own right (cut off wavelength = 1.1 μm), deserves a special mention since silicon is used in Schottky barrier (e.g. Platinum Silicide) detectors and in extrinsic Si X detectors for the far infrared. In addition the manufacturing technologies are well established for silicon, and in particular for metal oxide silicon (MOS) and complementary metal oxide silicon (CMOS) devices. Thus MOS, CMOS or silicon on insulator (SOI) technologies are usually used as readout multiplexers for hybrid detector arrays (GaAs is also used in some cases). The readout integrated circuit (sometimes abbreviated to ROIC) is usually bonded directly to the material of the detector array (so as to form a hybrid device). Since the IR detector is often cooled to cryogenic temperatures (so as to reduce dark current) the readout circuit is also cooled. This has to be borne in mind when considering the radiation effects.

Photon detector materials can be used in four different types of structure, as shown in figure 1.3-2 [14]

- photoconductive (PC) mode detectors, where the absorbed photons cause a change in conductivity. When a constant bias is placed across the detector, the modulation in the current through the semiconductor is proportional to the change in irradiance

- photovoltaic (PV) mode detectors, where the absorbed photons create a change in voltage at a potential barrier (either produced by a p-n junction or induced by electric fields with a metal-insulator-silicon structure)
- photoemissive detectors, such as silicide Schottky barrier devices. In these photons are absorbed in the silicide electrode and a small fraction of the excited carriers are emitted over the Schottky barrier into the semiconductor. The charge generated at the electrode is then transferred to a readout structure.

PC mode intrinsic detectors usually have a low resistance and high bias currents so that buffer amplifiers are needed to couple them to readout circuits. This means that power consumption and fill factor are improved for PV detectors. Quantum well detectors are an exception. These are photoconductive but have a high impedance like photovoltaics (because thermal generation of carriers in the barriers between wells is negligible[19]).

Also, PC detectors are unique in that they can exhibit gain (i.e. more than one electron can be moved around the detection circuit for each absorbed photon). The gain is given by the ratio of the mean carrier lifetime to the transit time of the higher mobility free carriers across the detector - the free carriers can be thought of as traversing the detector (and the external circuit) several times before recombining.

PC detectors are equilibrium devices and do not have a depletion region. They show both generation and recombination noise and so have a factor $\sqrt{2}$ higher noise than PV detectors (which show only generation noise).

Extrinsic silicon detectors can be operated either as high impedance photoconductors or as impurity band conduction (IBC) devices. Unlike intrinsics, ordinary extrinsic semiconductors have only one type of mobile charge carrier. IBC detectors are unique in having some properties in common with conventional extrinsics (like photoexcitation from impurity levels in the bandgap), but IBC detectors can collect both types of carriers (those in the continuum and those in the 'hopping' impurity band). Thus, in some ways, they behave like a photovoltaic (for example they show reduced recombination noise). More details of these detectors are given in the next section.

It is common to have the readout circuit fabricated using silicon (or sometimes GaAs) technology. This allows ease of fabrication and separate optimisation of the detector and readout circuits. However it does involve hybridisation, with electrical connections between the two circuits via indium (or solder) bumps (flip chip circuits) or else via metal feedthroughs. Monolithic detectors can also be produced, usually with a CID (charge injection device) or CCD (charge-coupled device) structure. Figure 1.3-3 [15] illustrates the possibilities.

There are a number of different designs for readout electronics. Amongst these are

- CCD readouts
- MOSFET switch readouts (including CMOS circuits)
- CID readouts
- CIM (charge imaging matrix) readouts

Ways of transferring charge from the detector to the readout circuit include

- direct injection
- buffered direct injection
- gate modulation

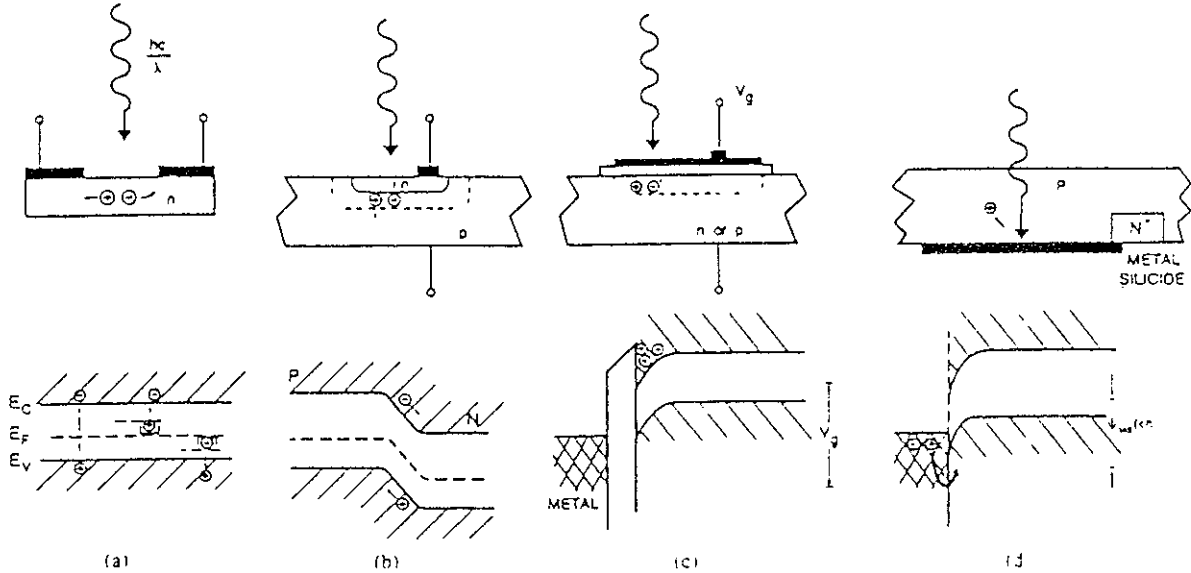


Figure 1 3-2 - Common IR detector structures [14] and their related energy band diagrams
a) photoconductive, b) photovoltaic, C) metal-insulator-semiconductor (MIS), d) Schottky barrier

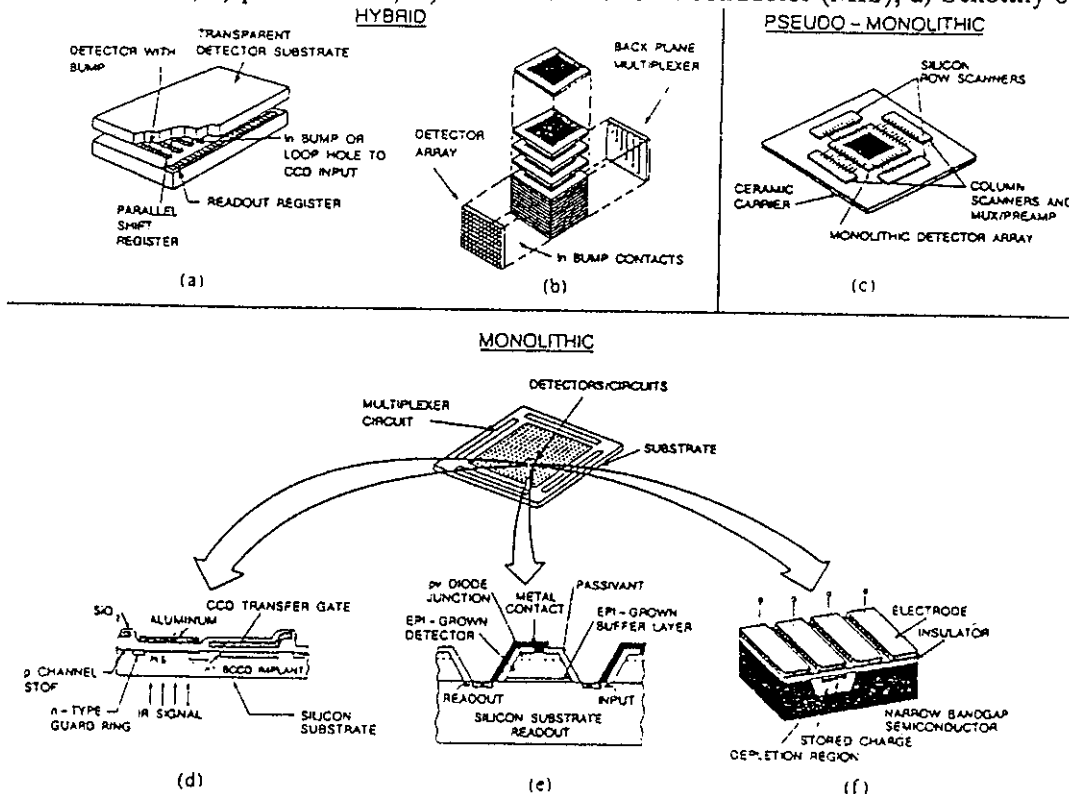


Figure 1 3-1 - IR detector readout architectures (from [15])
a) direct hybrid, b) indirect hybrid, c) monolithic, d) z-plane technology, e) loophole (G-MIRL) and VIMIS 'vertically integrated MIS' (Texas Instruments) technology

1.4 TYPES OF IR DETECTOR (FURTHER DETAILS)

In this section we give an introduction to the various detector types to be considered in this report

1.4.1 HgCdTe detectors

Mercury cadmium telluride ($\text{Hg}_{1-x}\text{Cd}_x\text{Te}$) is an intrinsic semiconductor alloy with a direct band gap. By adjusting the alloy composition, the cut-off wavelength can be selected to lie anywhere in the range 2 to 25 μm and the band gap (E_g) is given by [20]

$$E_g \text{ (eV)} = -0.302 + 1.93x + 5.35 \times 10^{-4} T (1-2x) - 0.810x^2 + 0.832x^3 \quad (1-2)$$

For the 8-12 μm region x needs to be ~ 0.21 . Note that in (1-2) E_g increases with T (in fact in this equation dE_g/dT is a constant, which overestimates the gradient at low T and underestimates it at high T [21]). Thus, the cut-off wavelength can be increased by reducing the operating temperature. *This also has the effect of increasing the R_0A product (R_0 = zero bias resistance, A = detector area)*

MCT can be used in photoconductive, photovoltaic (photodiode) and photocapacitor modes but, as mentioned above, PC mode detectors have a low resistance and high bias currents so that impedance buffer amplifiers are needed to couple them to readout structures. This means that power consumption and fill factor are improved for PV detectors. PC arrays are not likely to be used in a space application and will not be considered in detail in this report.

Since MCT is a direct band gap semiconductor the absorption coefficient of IR radiation is high (10^3 - 10^4 cm^{-1}) and only a thin active layer ($\sim 10 \mu\text{m}$) is needed. Issues related to the manufacturability of HgCdTe arrays have been reviewed by Tennant et al [22]. MCT is normally grown on lattice matched substrates of CdTe and CdZnTe, however there are many problems associated with growing this material, particularly if large arrays are required at low cost. Recently considerable success has been achieved in growing on alternative substrates. For example, Rockwell have used sapphire for SWIR and MWIR arrays [23], [24] (sapphire is transparent out to 5.5 μm) and also GaAs [25]. More recently, silicon with a GaAs buffer layer has been used [21], [26], [27]. The latter offers the possibility of growing the detector material on the same substrate as the readout circuitry. Another possibility is to grow both the MCT and the Si multiplexer on a common sapphire interconnection substrate [28].

MCT detectors can be fabricated as arrays of photodiodes or MIS capacitors and can be either front or back illuminated. MIS architectures typically require better quality HgCdTe. In the back illuminated case the detector electrodes are often bump bonded to connections on the silicon multiplexer via indium columns to form a hybrid detector. As an alternative, GEC-Marconi Infrared Limited (G-MIRL) have developed a 'loop-hole' technology for front illuminated photodiodes [29]. With the ability to grow MCT on Si, RSRE (now DRA, Malvern) and STC have reported a process for fabricating long linear arrays by coupling MCT photodiodes to BICMOS silicon readout circuitry [10].

There are several related alloys which could also be used as IR detectors. PbSnTe is a similar material to CdHgTe but has a higher dielectric constant (hence slower response) and a higher thermal expansion coefficient. It is therefore no longer a popular material. Among the small

gap II-VI semiconductors Cd, Zn, Mn and Mg can be introduced into HgTe and HgSe. Of these HgZnTe (MZT) appears to be the most useful [30]. This material has the advantage of being more stable than MCT and having a higher carrier mobility. Also tunneling currents are likely to be reduced (c.f. chapter 5).

1.4.1.1 Photodiode (photovoltaic) arrays

The basic properties of MCT p-n junction photodiode arrays have been reviewed by Reine, Sood and Tredwell [31]. Infrared radiation of wavelength shorter than the cut-off wavelength is absorbed by the photodiode and produces electron-hole pairs. If the absorption occurs in the depletion region the e-h pairs are immediately separated by the strong electric field, if in the undepleted bulk then charge migrates by diffusion until collected in the depletion region (although some e-h recombination will take place along the way). The resulting photocurrent can be integrated on the self capacitance of the junction or on a separate capacitor, depending on the circuit arrangement employed. Figure 1.4-2 shows the simplest form of injection circuit which transfers charge directly via an injection gate (an MOS transistor). Either way the charge has to be injected into the readout circuit and the injection efficiency (η) is an important parameter which depends on the dynamic resistance of the diode.

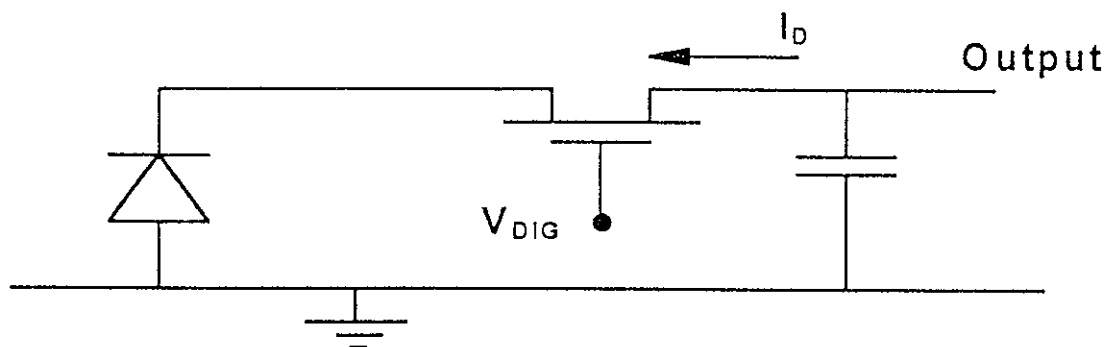


Figure 1.4-2 Direct injection circuit

$$\eta = \frac{g_m R_D}{1 + g_m R_D} \quad (1-3)$$

where R_D is the input impedance of the injection circuit

Thus the slope resistance of the diode must be high for good injection efficiency. Unfortunately a high resistance is hard to achieve for LWIR diodes or high temperatures, or for low photocurrent. Hence several alternatives to the simple direct injection circuit have been proposed [32]. Two of these [28], [33] use a feedback amplifier to increase the effective resistance of the diode.

Particularly in the LWIR, where photon fluxes are high and scene contrasts low, readout schemes which use charge skimming or charge partitioning are often used [34] to match the IR signal to the relatively low charge capacity of readout circuits (particularly for CCDs). However all these modifications (feedback amplifiers, partitioning gates etc) take up real-estate on the multiplexer and they are not easy to implement with 2-D arrays.

The effect of radiation on the readout circuit is an important issue and will be addressed in chapter 8

Note that the diode resistance is increased for negative reverse bias (see, for example, [35] although in this state the current and 1/f noise are increased also. Therefore there is an optimum reverse bias, usually of order 50mV. Reducing the temperature also increases the diode resistance

In 1980 Reine et al [27] commented that

'A wide variety of techniques has been used to form p-n junctions in Hg_{1-x}Cd_xTe. Both n-on-p and p-on-n junctions have been formed, and type conversion has involved introduction of foreign atom impurities, controlled deviations from stoichiometry, and occasionally combinations of both. Junction formation techniques have included ion implantation of donors and acceptors, high energy proton bombardment, diffusion of donors and acceptors, in-diffusion and out-diffusion of mercury, creation of p-type surface layers on n-type material by intense pulsed laser radiation, and in situ cosputtering of donors and acceptors in sputtered Hg_{1-x}Cd_xTe layers

The most technologically significant of these techniques for high performance infrared detectors appear to be ion implantation and Hg in-diffusion'

These comments would still seem to be valid today. At that time the best diodes (those with high RoA products) were reported for boron-implanted n-on-p diodes (isolated regions of n doping in a p-doped matrix). This is partly because implanting n-type layers in p-type MCT is more convenient than implanting p-type layers on n-type because damage annealing is less critical. Recently however several manufacturers (eg Rockwell [36], Loral [37] and SBRC [23] have reported p-on-n diodes and according to Balingall [10], p-on-n structures now tend to give the best long wavelength diodes (see also Tennant et al [21]). It will be seen in section 5.3 that tunneling currents tend to limit the performance of LWIR diodes (particularly for low background applications with an operating temperature below 77K). In this case there are advantages in keeping dopant levels down, which is more easily achievable with diffusion rather than ion implantation techniques [38].

In the 'loop-hole' technology developed by G-MIRL [25] it is interesting to note that the ion beam milling process, which is used to form the loop-holes (or via holes) through the centre of the diodes, itself causes the conversion from p- to n-type so as to form a lateral collection diode. The mechanism appears to be (see [39] and references therein) that interstitial Hg atoms are created and these diffuse rapidly until captured by a Hg vacancy in the lattice creating a region of filled vacancies which is n-type due to residual donor impurities at about the 10^{15} cm^{-3} level.

Another important issue is the surface passivation of the diodes. A high quality insulating passivation is necessary for control of the surface potential and of the surface dark current and to seal the MCT material both electrically and chemically. It also acts as an antireflection coating in front illuminated devices. ZnS is the most commonly used material (anodic oxide causes an inversion layer on a p-type material and it cannot be used for junction devices). Other possibilities are SiO₂ and anodic sulphide or fluoride and also wider band gap MCT (to form a heterostructure). These are discussed in more detail (along with references) in chapter 5.

Figure 1 4-3 charts some of the developments in MCT diode technology (from a US perspective, [40]) Figure 1 4-4 shows the structure of a typical MBE grown heterostructure device [41]

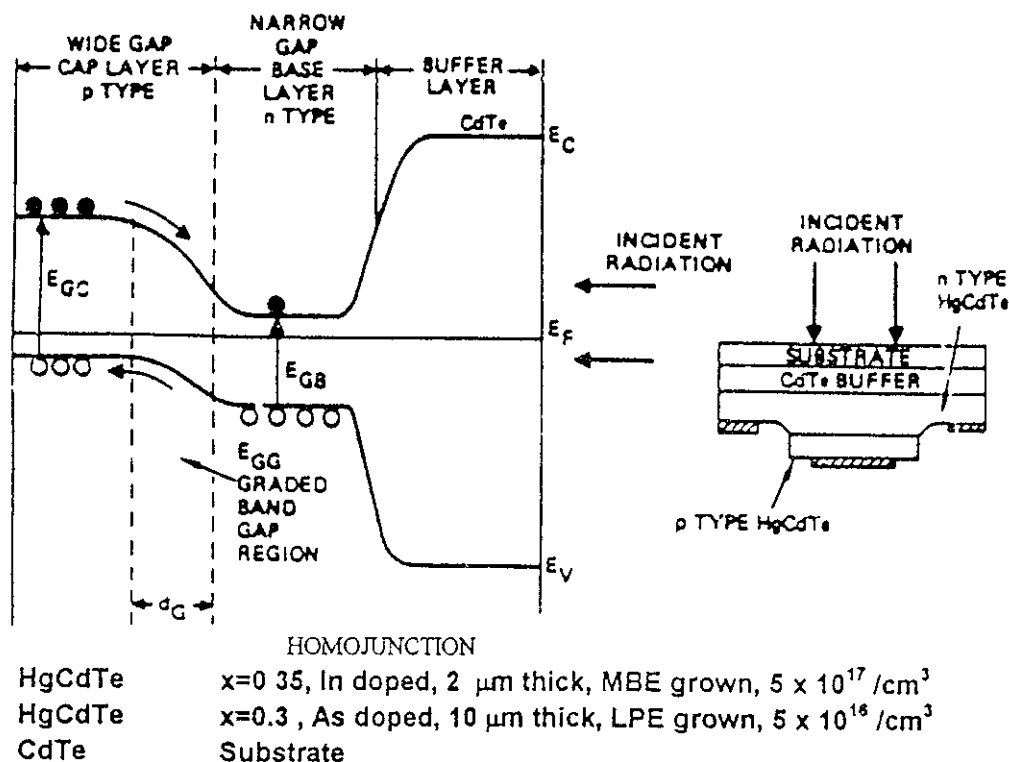


Figure 1 4-4 - structure of a typical MBE grown heterostructure device [41]

Below we list some of the major manufacturers of large MCT arrays together with device details

GEC-Marconi Infrared Ltd (G-MIRL), UK

Though formerly using both CCD and CMOS readout circuits, GMIRL now entirely use CMOS multiplexers. These are described in reference [42]. 128 x 128 and 288 x 384 pixel MWIR and LWIR arrays are available commercially, as is a staggered linear array configured as either 512 x 2 or 256 x 4. While the 246 x 4 and 288 x 384 arrays operate in a staring (or 'snapshot') mode, the 128 x 128 arrays are not staring, i.e. all the pixels are not integrating at the same time (instead the array is scanned line by line). TDI (time delay and integrate) arrays are also under development as are the 1024 x 70 pixel SWIR arrays for ESA's HRIS programme (also baselined for the SWIR channel of ESA's PRISM instrument).

The p-n diodes are normally formed by LPE (liquid phase epitaxy) growth and ion-beam milling. Hybridisation to the CMOS multiplexer is via 'loophole' technology and direct injection. ZnS passivation is used, this also acts as an antireflection coating as the devices are front illuminated. Other technologies (e.g. using doped MOVPE, metalorganic vapour phase epitaxy, heterostructures) are being developed in collaboration with DRA (Malvern).

Also under development are arrays coupled to a microlens plate [43]. The 'immersion' technology allows the sensitive volume to be reduced by up to two orders of magnitude, with benefits in reduced dark current and higher diode resistance. Hence the devices can be

operated at a higher temperature than would be possible with non-immersed diodes Baker et al [44] have recently reported work on heterostructure devices, fabricated using MOVPE growth, also aimed at producing detectors with higher operating temperatures

LETI-LIR/Sofradir (France)

The Laboratoire Infrarouge (LIR) of CEA-LETI have developed a photovoltaic diode technology based on planar ion-implanted n-on-p homojunctions [45], [46] The arrays are passivated with ZnS and bump bonded to CCD or CMOS multiplexers (direct injection readout) The process has been industrialised by Sofradir and several linear (e.g. 288 x 4, TDI) and staring arrays (e.g. 128 x 128) are commercially available both for the 3-5 and 7-10 μm wavebands (256 x 256 is being developed) Sofradir (with support from LETI-LIR) has demonstrated butted linear arrays with $\sim 12.5 \mu\text{m}$ cut-off wavelength [47] and this technology has been baselined for the LWIR arrays on ESA's PRISM instrument LETI-LIR have also developed the 10 x 1 array (200 μm x 200 μm pixels) for the Composite InfraRed Spectrometer (CIRS) instrument on the Cassini probe [48] and a 256 x 256 element 3-5 μm array with a CMOS readout circuit [49]

HgZnTe (MZT) arrays are also being developed [26] This is a potentially useful material because of its better thermal stability and lower tunneling currents than HgCdTe

AEG Infrared Modules, AIM (Germany)

The AEG process [50] uses back-illuminated n on p-type 8-10 μm diodes indium bump-bonded to a CCD or silicon multiplexer Linear arrays up to 288 x 4 (TDI) and area arrays up to 256 x 256 have been reported [51]

Rockwell (USA)

- * 256x256 pixel [20] and 1024 x 1024 pixel [52] SWIR (2.5 μm) and 640 x 480 MWIR arrays [19] using MCT diodes on sapphire substrates (PACE-1) indium bump bonded to silicon CMOS direct inject multiplexers have been reported The 256 x 256 NICMOS3 SWIR arrays are planned to be installed in the Hubble Space Telescope
- * LWIR arrays produced on GaAs (PACE-2) and GaAs/Si (PACE-3) substrates [21] Diodes can be n-on-p or p-on-n-type Passivation is normally with ZnS (overcoated with SiO₂) CdTe passivation has also been reported Some LWIR arrays have a buffered direct inject readout but with an electronically scanned architecture (ESBDI) rather than a conventional staring architecture [53] 640x480 hybrid arrays are under development [54] Recently MBE growth of p-on-n diodes on GaAs structures to form heterostructures with a wide band gap CdHgTe cap layer has been reported [32]

Hughes (formerly SBRC)

Santa Barbara Research Centre (SBRC) is part of Hughes Aircraft and use arrays indium bump bonded to Hughes multiplexers in many of their arrays Hughes have developed a cryo-CMOS process (ARCMOS) for their multiplexers which is of the bond and etch-back silicon on insulator (BESOI) type

A recent review of photovoltaic diode technology has been given by Tung et al [55] LWIR arrays are being developed for production in large quantities for the AAWS-M shoulder

launched 'Advanced Antitank Weapon System' [56] These arrays are 64x64 128x128 and 256x256 arrays are also being developed for the PET project (for a ground based interceptor - GBI) Another program is the development of 960x4 (TDI) arrays for the US Army's Light Helicopter (LH) [57] These use p-on-n heterojunction diodes and readouts with feedback enhanced direct injection circuits The diode arrays and silicon multiplexers are each mounted to a common sapphire interconnect board to form an indirect hybrid 512 x 512 and 640 x 480 MWIR arrays have been reported [44]

Hughes Research laboratories have also reported the development of MBE heterostructure detectors [37] HgZnTe (MZT) is also being developed [58],[59] and arrays with a cut-off wavelength of 17 μm at $T \sim 65\text{K}$ have been reported (the detectors are fabricated from LPE layers on lattice matched CdZnTe substrates)

Norton et al [60] have discussed 128 x 128 and 256 x 256 MWIR arrays available in a Peltier cooled package

Lockheed Martin (formerly Loral) IR Imaging Systems, (USA)

Loral [36] have reported 60-180 element linear PC arrays (capacity 600 units/month) and 128 to 256 element linear, and 64x64 or 128x128 area PV arrays Heterostructure detectors are being developed [33]

Other US Manufacturers

There are several other US companies (eg Amber Engineering, Westinghouse, Honeywell [61] who are believed to be working on the development of PV MCT arrays, but little information is available at present Martin Marietta Laboratories (Syracuse, NY) [62] have reported a front-illuminated 256 element staggered linear array which is beam-lead connected to a buffered direct injection multiplexer The cut-off wavelength was 10.8 μm and the diodes are passivated with CdTe and AR coated with ZnS

Japanese Manufacturers

Both Fujitsu [63] and NEC [64] have recently described 256x256 LWIR MCT arrays

1.4.1.2 Metal Insulator Semiconductor (MIS) arrays

MIS (or photocapacitor) arrays are usually produced as an integral part of charge transfer arrays, eg charge coupled devices (CCDs) or charge injection devices (CIDs) The active element is an MIS capacitor, similar to the gate electrode of an insulated gate field effect transistor A depletion region (potential well) is created under the gate dielectric by applying a voltage to the gate In this form the array is a monolithic device with the CCD (or other charge transfer array) also fabricated in HgCdTe Much of the development of these arrays has been done by Texas Instruments (USA) [65], although Koch et al (SBRC) [66] have also reported a monolithic CdHgTe array The basic physics of monolithic MIS CCD detectors has been reviewed by Kinch [67] and Kinch et al [68], while Baker [69] has reviewed MIS arrays with CCD and CID readout In a CCD the signal charge is progressively clocked through the array to a single output amplifier. In a CID the charge is injected into the substrate (charge recombines) and the change in detector capacitance is sensed In addition MIS capacitors can be used in a charge integration mode [70] in which the capacitor is biased into deep depletion

(forming a potential well) and is then floated. Charge integrated in the potential well then changes the potential on the gate which is sensed by an external circuit. A similar operation is employed by the charge imaging matrix (CIM) developed by Texas Instruments [71],[11]. This was developed for high signal applications (high background MWIR or LWIR) where CCDs do not have adequate full well capacity and because of limitations in the readout speed of CIDs. In a CIM the MIS well is biased into deep depletion as before. On conclusion of the integration the MIS well is biased into accumulation forcing the collected minority carriers under a transfer gate and into an adjacent diode structure (there is one CdHgTe p-n diode for each MIS capacitor). This diode is floated and the charge changes the diode bias, x-y addressing of the CIM is performed by silicon circuits. InSb CID arrays have been reported which also use external silicon addressing circuits (eg [72]) - in that case, wire bonded. Recently Texas Instruments has developed a manufacturing approach called VIMIS (vertically integrated MIS) where the MIS detectors are mounted directly on a silicon readout chip as in the G-MIRL loophole technology (i.e. with adhesive bonding to the silicon multiplexer and etched via hole connection to the MIS capacitor, [12]). 960x4 arrays have been demonstrated and 64x64 arrays have been developed for the Advanced Antitank Weapons System (AAWS-M) [45]. 128 x 128 pixel VIMIS arrays have also been produced [12].

Recently Texas instruments [73] have announced a monolithic 128 x 28 TDI CCD. This is an n-channel device made from ion-implanted p-type HgCdTe and has a four phase overlapping gate CCD for readout. ZnS is used for passivation and electrode isolation.

1.4.2 InSb

InSb is an intrinsic, direct band gap, semiconductor with a band gap of 0.24eV at 77K corresponding to a cut-off wavelength of 5.2 μ m. Like MCT, InSb can be fabricated into photoconductive, photodiode and photocapacitor detectors and, again, for arrays the excessive power consumption of PC detectors has pushed the exclusive development of PV photodiode and MIS devices. In general the technological problems of processing InSb are less severe than for MCT and the technology is mature, so that in the medium waveband there are sometimes advantages in choosing InSb over MCT, though a lower operating temperature is usually needed for InSb compared with MCT.

Photodiode arrays are usually fabricated on n-type InSb with a p-type layer formed on top (either by diffusion or implantation). Masking and etching are then used to delineate a 'mesa' structure onto which a metal contact is placed. Large hybrid arrays are formed by indium bump bonding between the metal contact and a Si multiplexer (usually a switched FET array). The n-type InSb is generally thinned and back-illuminated. InSb MIS detectors can be used in charge injection devices (CIDs) again using Si scanner circuits. Passivation layers (and the insulator layer in a MIS device) are generally formed from silicon oxide (SiO₂) similar to thermal SiO₂ films grown on Si substrates [74].

Below is a brief list of the current manufacturing status of InSb arrays (as published in the open literature)

Cincinnati Electronics (USA, owned by GEC, UK)

PV photodiode arrays with p-on-n mesa structure [75]. 128x128 arrays bump bonded to a Si switched FET array (with possibility of extension to 256x256) have been reported [76]. Most arrays use the photodiode in a capacitive discharge mode (CDM) [77] in which the reverse

biased diode acts as the integrator. After reverse biasing then diode it is the electrically isolated (floated). This sets a known charge on the junction capacitance which is neutralised by photogenerated charge as the integration proceeds. The multiplexer then sequentially connects each detector element to a common video line. The remaining charge is shared between the video line and detector capacitances and the change in voltage is measured. The CDM mode is used in the 128x128 arrays and 64x1 arrays used for the AVIRIS (airborne visible/infrared imaging spectrometer). Recent development of 256x1 arrays for the CRAF/Cassini Visible Infrared Mapping Spectrometer (VIMS) will use arrays with a buffered direct inject operational amplifier which interfaces each diode to an external integration capacitor (both the MOSFET and the capacitor are part of the multiplexer unit cell) [78]. The feedback acts so as to keep the photodiode at zero bias, thus reducing dark current.

A 256 x 256 array for ground-based astronomy has been described by Blessinger et al [79]. This device has a polysilicon capacitance (additional to the diode junction capacitance) in order to improve full well capacity and linearity. The FET switches of the multiplexer are fabricated using Orbit Semiconductor's 1.2 μm p-well double polysilicon, double metal process. Another 256 x 256 device, developed for SIRTf uses the Valley Oakes Semiconductor designed random-access multiplexer, made using the TRW radiation-hard 1.2 μm CMOS process (for operation at ~ 10 K) [80]. The multiplexer has a source follower per detector (SFD) design.

Amber Engineering (USA)

Have produced a 128x128 photodiode array (actually made up of 4 64x64 arrays) and a 256x256 array (with parallel outputs) was reported in 1991, [81]. The photodiodes have an implanted mesa structure [82] and are bump bonded to a Si CMOS switch multiplexer. The signal charge is directly injected onto a capacitor via a common base current mode unity gain amplifier. More recently, Massie et al [83] have discussed several array designs, including 512 x 512 and 480 x 640 pixel arrays with direct injection readout and a 256 x 256 pixel device with a more sophisticated injection circuit (auto-zeroed capacitive feedback transimpedance amplifier, CTIA).

Hughes SBRC

The 58x62 backside illuminated hybrid InSb array has been in much use by ground based IR astronomers (eg [84]), Again it is fabricated on n-type InSb (donor concentration in the range $1\text{-}2 \times 10^{15} \text{ cm}^{-3}$) with p-type regions formed by ion implantation ($1 \times 10^{18} \text{ cm}^{-3}$). A gate is fabricated on the junction side to control the surface potential and reduce the dark current. The readout is an NMOS structure consisting of row and column address decoders, source follower and reset switch unit cells and an output section. There is a non destructive readout capability since the diode does not have to be reset before readout.

Commercially available 256 x 256 arrays have also been reported [85] and a 1024 x 1024 array has been developed for the Aladdin project (NOAO) [86]. The infrared array camera (IRAC) instrument on NASA's SIRTf is planned to use a 256 x 256 array with a multiplexer (Hughes, Carlsbad) that can operate at ~ 10 K. This is needed because the focal plane needs to be at low temperature so as to accommodate far-IR detectors. Both the SIRTf and the 1024 x 1024 arrays use a gateless front-side passivation for the InSb photodiodes. This has implications for radiation behaviour since previous testing of the gated version [87] indicated that cycling of the gate voltage (which controls the surface potential in the earlier, photox passivated arrays) was necessary to partially-anneal-out proton-induced dark current spikes.

SBRC also have 128 x 128 and 256 x 256 arrays sensitive over the whole range from visible to MWIR (0.5 to 5.4 μm)

GE (USA)

128x128 CID arrays have been reported [88] with 256x256 being feasible. The InSb MIS array is front illuminated through a semi transparent gate. As usual for a CID there are two MIS capacitors for each picture element, one connected to a column line and the other to a row line. This allows for x-y addressing (in this case via silicon shift registers connected via wire bonding). The InSb can be grown by liquid phase epitaxy (LPE) which is claimed to give lower dark current (which is predominantly generated in the depletion region).

Northrop (USA)

Northrop have also reported front illuminated 128x128 CID arrays with a reduced number of mask levels needed in manufacture and without using semi transparent electrodes [89] the pixel size is 30x30 μm^2 . Scanning of the CID is via CMOS ICS. It is not clear whether the arrays are actually manufactured at Northrop.

Westinghouse

Have reported a 128x128 InSb array bump bonded to a silicon processor [90]

In Europe

The Société Anonime de Télécommunications (SAT) manufactures a 32x32 CID with wire bonding to Si scanners [91]. This will be used for the MWIR detector in the ISOCAM instrument on the Infrared Space Observatory (ISO) with operation at 4.2K.

In the past, 2x32 staggered array detectors and 32x32 CIDs were available from AEG (Germany) and AEG have manufactured 128x1 InSb detectors with Si CCD readout multiplexers. At present AEG only market single element InSb detectors.

Other InSb arrays

Kepten et al (in Israel) [92] have described an approach for producing monolithic detectors using photodiodes and MIS field effect transistors.

1.4.3 Multi-quantum Well (MQW) and Superlattice (SL) Structures for the LWIR

These are multilayer structures in which two components alternate in very thin films. In compositional superlattices, the two components may be different semiconductors or a semiconductor alternating with a semimetal. Doping lattices, usually referred to as nipi structures, have periodic variations of the doping type in the same host semiconductor. In a superlattice the periodicity imposed by the layer structure changes the band structure and creates additional sub-bands. These are of particular interest for LWIR IR detection because the optical transition energy between sub-bands can be controlled by varying the layer thicknesses.

HgTe-CdTe superlattices have been investigated by several groups (eg [93], [94]) As well as being able to tune the optical band gap the effective masses can be controlled and this can reduce tunneling currents (see section 5) A potential problem arises from the very high diffusion constants for Hg, Cd and Te which tend to result in instabilities

The design of III-V quantum well structures has been reviewed by Osbourn [95], Benedict [96], Andrews [15] and a particularly exhaustive review has been given by Levine [97] Figure 1 4-6 shows the room temperature band gaps that can be obtained with III-V alloy systems It is readily apparent that only the InAsSb system has wavelength cut-offs in the 8-12 μ m range at room temperature Unfortunately, the maximum InAsSb wavelength cut-off is only about 9 μ m at the low operating temperatures (\sim 77K) required for adequate long-wavelength detector performance Thus long-wavelength absorption is not possible via valence-band-to-conduction-band transitions in any of these III-V alloy systems

However the altered crystal potentials in MQW and SL heterostructures lead to new energy band structures which depend on layer thicknesses, layer strains and the bulk properties of the individual layers Several general mechanisms for obtaining long-wavelength band-to-band absorption in MQW and SL structures have been established and these are illustrated schematically in figure 2 4-7 The full lines represent the quantum well potentials, the broken lines represent the resulting MQW or SL energy levels and the arrows represent the lowest-energy band-to-band transitions for these structures

Though appreciable investment is required in systems for MBE growth of these multilayer structures (up to \sim 50 layers) there is considerable scope, by tuning of alloy compositions and layer thicknesses, to achieve improved detector performance Hence these devices may come to dominate the market for LWIR detectors in the future, especially as they offer the possibility of improved material quality, higher uniformity low cost and larger wafer size compared with CdTe (3" compared with 1" for CdTe [15])

The AlGaAs/GaAs detector has been the most studied and this seems to have particular advantages over HgCdTe for $>12\ \mu$ m applications (where HgCdTe diodes tend to be limited by trap-assisted tunnelling [98])

We briefly discuss several of the alloy systems below

InAsSb/InSb

InAsSb/InSb strained layer superlattices (SLSs) exhibit a strain shifted type II band offset as in figure 1 4-7 (b) and absorption is by valence to conduction band transitions This system can be used as a direct replacement for PV or PC devices A schematic of a PV detector is shown in figure 1 4-8 Unfortunately though the InSb substrate technology is mature, that for InAsSb is not Also there is an additional disadvantage in the need to grow InAsSb/InSb SLS structures on (intermediate) graded InAsSb buffer layers which are in tension owing to the larger lattice constant of the InSb substrate Buffer layers in tension are often subject to microcracking, and these defects are unacceptable for detector array applications Though this difficulty may be overcome as development progresses

At the low temperatures required for detector operation it is expected that tunneling across the layer potential barriers will be the main cause of dark current This tunneling contribution is a strong function of the barrier heights, widths and bulk effective masses of the materials, with thin barrier layers and small bulk effective masses leading to greater tunneling In addition the

tunnelling process can be aided by impurity or radiation-induced levels in the barrier layers. Surface passivation is also important, though processes are not yet optimised [99]

AlGaAs/GaAs

In this system a layer of narrow band gap GaAs is deposited on the wider band gap AlGaAs, followed by another layer of GaAs and so on, to form a series of 'potential wells'. As more layers are added the band structure of the semiconductor is perturbed into a series of narrow sub-bands. This structure uses transitions between these sub-bands as in figure 1.4-2 c). In practice as many as 50 layers are grown by molecular beam epitaxy (MBE). An important difference compared with valence-band-to-conduction-band systems (eg InAsSb/InSb) is the need to have electrons occupying the ground state levels of the conduction band quantum wells, ie the AlGaAs/GaAs structures must be doped n-type. The absorption strength clearly depends on the number of electrons in the ground state and the number of unoccupied excited states. The absorption process is analogous to the extrinsic absorption process for neutral (frozen-out) impurities in a doped semiconductor and conventional photovoltaic detectors are not available with this approach, hence only photoconductive detectors can be made. However the photoconductive gain is ~ 1 and the power dissipation need not be excessive. Figure 1.4-9 shows a schematic diagram of a typical structure.

This system can make use of the mature technology (growth, processing and passivation) for making VLSI devices in GaAs (eg as developed at AT and T for GaAs memories) and there are good possibilities for achieving large format, low cost, devices with high uniformity, indeed 128x128 devices have been reported by AT and T [100] and Rockwell [101], Jerusalem College of Technology [102] and Martin Marietta [103], Lockheed Martin [104] and JPL [105] have reported 256 x 256 arrays. These arrays were produced by bump bonding the AlGaAs/GaAs detector array to a Si CMOS multiplexer (of similar design to those used for MCT and InSb arrays). In fact, since the quantum well detectors have a high impedance, they are very easy to couple to most types of silicon readout circuit (with injection efficiencies approaching 90%).

Recently, AT&T have stopped all work on QWIP devices and most of Barry Levine's team have moved to NASA/JPL. JPL have also contracted Quantum Epitaxial Designs (Bethlehem PA) to develop 2 space qualified 128 x 128 focal plane array modules [106]. The JPL group have demonstrated the use of a random reflector array to improve the light coupling (for both 9 μm and 15 μm cut-off arrays). However at long wavelengths the feature sizes need to be large and this is difficult for small pixels.

The group at Thomson-CSF (central research Laboratory) [107] have also produced good quality QWIP arrays (eg 32x32 for an ESA contract). They claim to have an operating temperature at least as high as the JPL group (about 70 K for 9 μm cut-off) but with a conventional 2-D grating structure for optical coupling.

An important advantage of the QWIP device is that although its spectral response is narrow (half width about 1 μm), multispectral imaging can be achieved by stacking two or more detectors (each with its own electrical contact).

It should be noted that though the AlGaAs/GaAs technology is the most well developed of any used for QW or SLS structures, these detectors are not yet fully competitive with MCT in terms of detectivity (at a given temperature). In fact there are fundamental limitations to their performance (based on the extrinsic-like majority carrier characteristics) as discussed by Kinch

and Yariv [108] The situation is somewhat reminiscent of the usefulness of PtSi detectors (section 3.4) in the SWIR and MWIR wavebands because of their producibility and uniformity set against their low quantum efficiency (~1%) However there is scope for increasing the quantum efficiency of MQW devices and, as Andrews and Miller [109] have pointed out, the comments of Kinch and Yariv are more applicable to the comparison of PC detectors rather than PV (which is more favourable to MQWs)

Note that, as with Schottky barrier detectors, the GaAs/AlGaAs MQW detectors allow full monolithic integration of sensor, readout and processing circuitry (in this case in GaAs), though this approach does not seem to have been actively followed - perhaps because MQW arrays are easy to couple to Si readouts The comparison of AlGaAs/GaAs and MCT detectors has also been discussed by DeWames et al [110] and Rogalski [111]

Dark current mechanisms are illustrated in Figure 1.4-10 [96] Sequential tunneling of ground state carriers along the field direction is the main contribution to dark current generation at low temperature (<30 K) [112], [113], [114], [115] The dark current can be reduced by increasing the barrier width to ~500Å [116] or by using a blocking layer At medium temperatures thermally assisted tunneling (thermal excitation plus tunneling through the tip of the barrier into the continuum energy levels) is important At temperatures > 55 K (for 9 µm cut-off devices) the dark current is mainly due to thermionic emission The JPL group have reduced this by using *bound-to-quasibound* QWIPS, where the energy barrier for thermionic emission is about 6 meV less than the photoionization energy (resulting in a factor 3 reduction in dark current) Dark current in the thermionic regime has recently been discussed by Liu [117]

In QWIP devices the quantum efficiency is affected by the doping of the barriers If the doping is reduced (so as to increase the operating temperature) then QE suffers Quantum efficiency can be ~10% in some devices

Figure 1.4-10 [116] shows a comparison of D^* values for MCT and AlGaAs/GaAs QW detectors (Si As IBC detector is also shown) At temperatures below 40K the QW device has superior performance compared with MCT, and further improvements may be expected

InSb/GaSb

This was the first III-V system which was shown to have extended wavelength cut-off values due to a type II offset The system does not provide useful absorption coefficients at long wavelengths and is not suitable for long-wavelength detector applications

InAs/InGaSb SLS

The InAs/InGaSb SLS system has been recently proposed as a new III-V candidate for long-wavelength detectors This system differs from the InAs/GaSb SL system in that the use of mismatched InGaSb alloys causes these structures to be SLSs The theoretical studies predict that strain shifts in thin-layered structures with InGaSb layers are sufficient to obtain both good absorption and 12µm wavelength cut-offs An additional advantage is that such structures can be closely lattice-matched to GaSb substrates, so that graded buffer layers are not needed No experimental work has yet been reported on this system A drawback to this approach is the rapid dependence of the wavelength cut-off on layer thickness The sensitive dependence is undesirable for detector array applications since even monolayer 'errors' or monolayer fluctuations from the desired SL layer thicknesses will shift or broaden the absorption edge by large amounts This approach also employs materials with immature growth technology

SiGe/Si

Recently it has been suggested [118], [119], [120] that MBE grown $\text{Si}_{1-x}\text{Ge}_x/\text{Si}$ superlattice MQW structures can be produced which have the ability to detect normally incident light. These are expected to have an absorption comparable to that in AlGaAs/GaAs and to be compatible with Si readout technology (so allowing easier matching of expansion coefficient and allowing for monolithic devices). However present detector designs give D^* values an order of magnitude less than comparable GaAs/InGaAs MQW detectors, mainly due to the larger doping density required for achieving appreciable quantum efficiency [107]. According to Kearney [121], it is easier to define p-type rather than n-type structures in Si.

Although a substantial effort has been put into large format SiGe/Si arrays at JPL, this work has now been stopped (in favour of other detector types). DRA(Malvern) in the UK is one group that is however pursuing basic research [122].

Nipi Superlattices

Nipis are doping superlattices which can exhibit absorption at energies below the band gap of the corresponding bulk material from which the nipi is formed via an effective type II potential as illustrated in figure 2.4-7 a). Nipis also exhibit band gaps and other properties which are 'turnable' or variable as the biasing or illumination conditions are changed. In theory, the most favourable materials in which to fabricate long-wavelength Nipi detectors are likely to be InSb and InAs since these offer sufficiently low intrinsic band gaps and effective masses that LWIR Nipi structures can be fabricated with practical values of absorption coefficient. The constraint on absorption coefficient implies high doping concentrations ($\sim 10^{19} \text{ cm}^{-3}$) [123], with relatively short superlattice periods ($< 20 \text{ nm}$). These requirements are not feasible for II-VI compounds because of their high diffusion coefficients.

According to Maserjian [109], the advantages of the InSb approach include the use of InSb substrates and the relatively simple growth of doped InSb epilayers. Disadvantages in general include the need for both non-standard device structures and difficult selective ohmic contacts to the alternating p- and n-layers, so that existing processing techniques for InSb infrared detectors may not be sufficient. Selective contacting to thick stacks of n- and p-layers is non-trivial for large-gap materials and should become even more difficult for array structures in lower-gap materials. In addition, the variability of the nipi absorption strength and band gap with illumination may cause problems in detector applications.

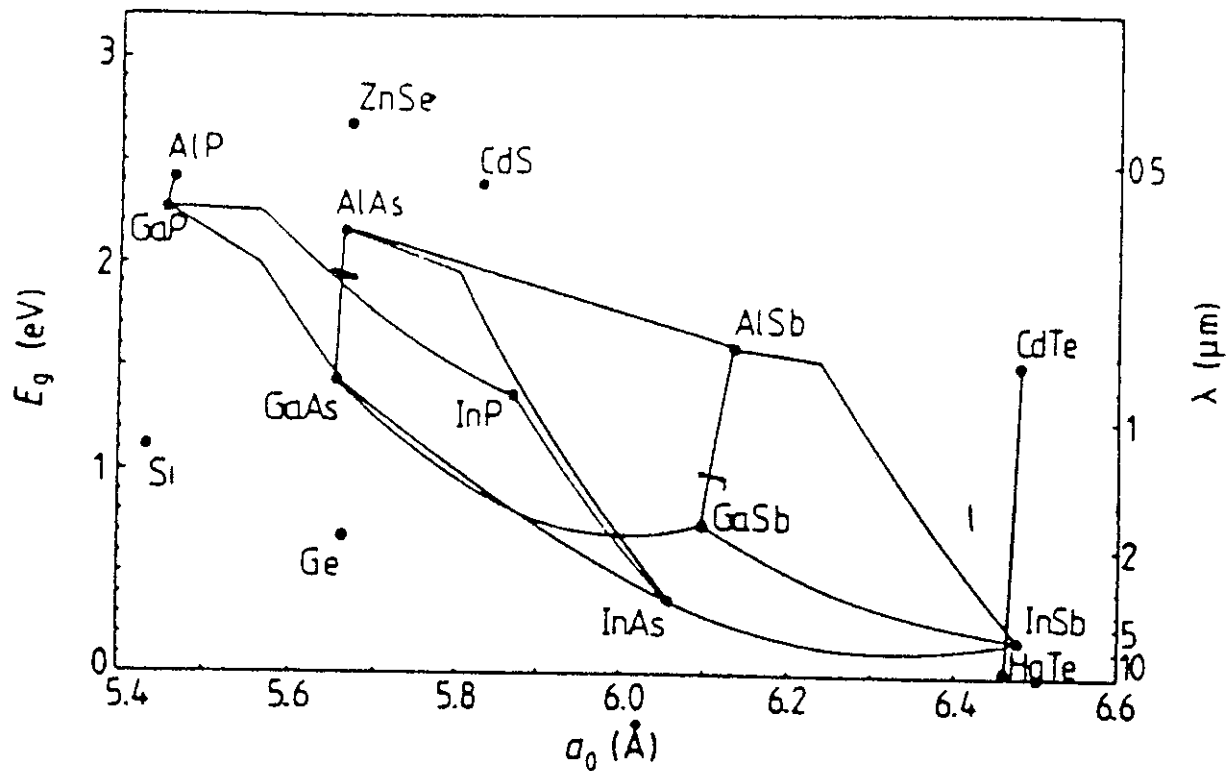


Figure 1.4-6

Room temperature band gaps of the important III-V compounds and alloys as a function of the lattice constants. Some other materials used in photodetectors are also shown. The solid lines are for the alloys of the endpoints, breaks (tick marks) on the curves indicate transitions from direct to indirect band gaps. Individual data points for alloys are not shown, the lines are best fits to the available data.

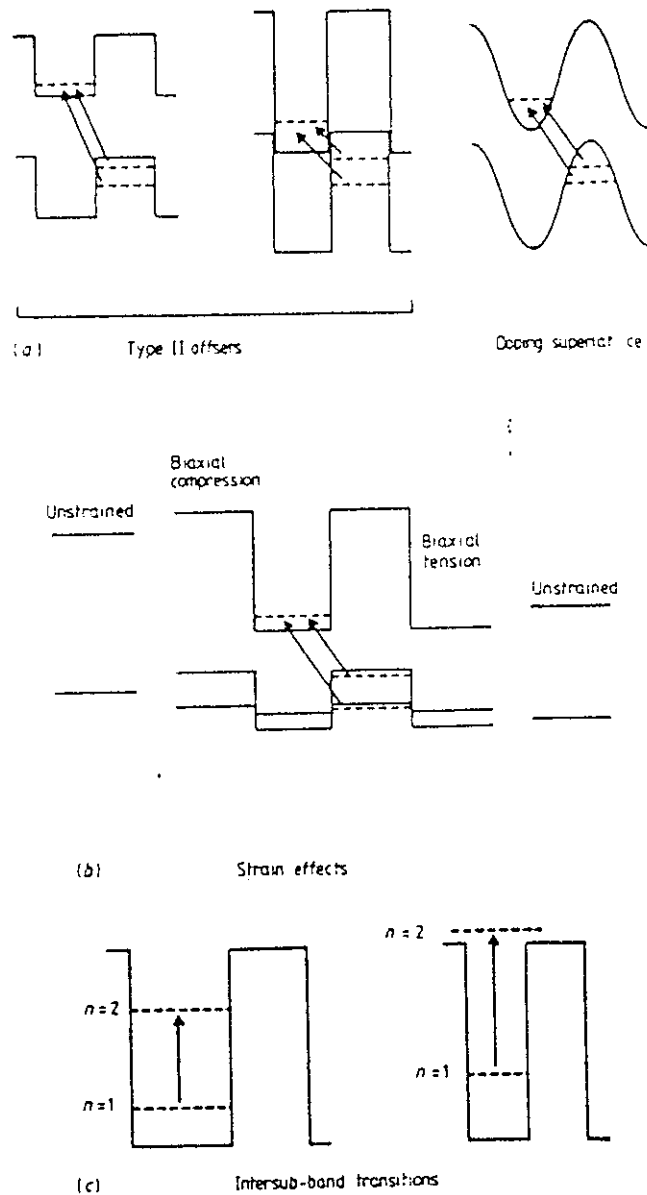


Figure 1.4-7

Schematic diagrams of the mechanisms for obtaining long-wavelength III-V band-to-band absorption discussed in the text. The full lines represent the quantum well potentials and barriers (i.e. the bulk conduction band minima and valence band maxima of the layer materials), the broken lines represent the resulting energy levels and the arrows represent band-to-band optical transitions between the quantum well energy levels. (a) Type II band offsets which can produce band-to-band transition energies less than the bulk band gap energies of the layer materials. The doping superlattice obtains an effective type II offset using electrostatic potentials from pin junctions. (b) Use of layer strains in a strained-layer superlattice to reduce the superlattice band gap. The corresponding unstrained quantum well and barrier energies are illustrated at the far left and far right. For type II offset case shown here, the lowering of the conduction band quantum well in the layers under tension and the splitting of the valence band quantum wells in the layers under compression both contribute to the overall reduction of the strained-layer superlattice band gap transitions. (c) Intersub-band transitions between the ground states and excited states of conduction band quantum wells. Quantum size effects determine the transition energies. The case on the left is for transitions between two confined states and the case on the right represents transitions between the confined ground states and extended (above the barrier) excited states.

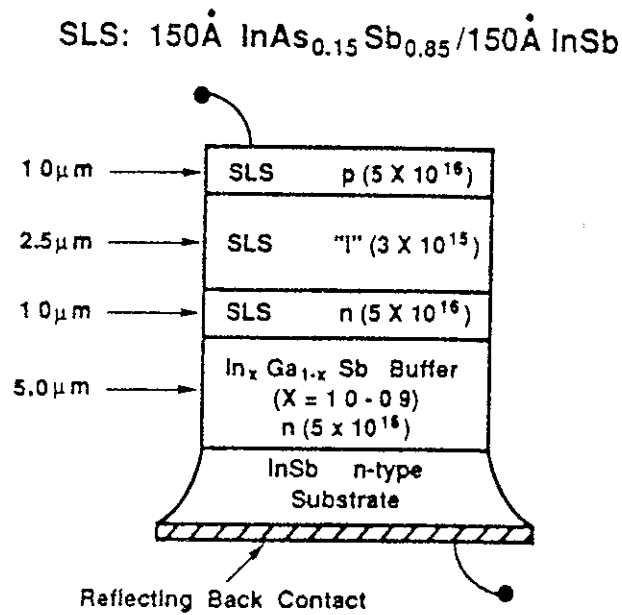


Figure 1.4-8 Schematic of a InAsSb SLS photodiode structure

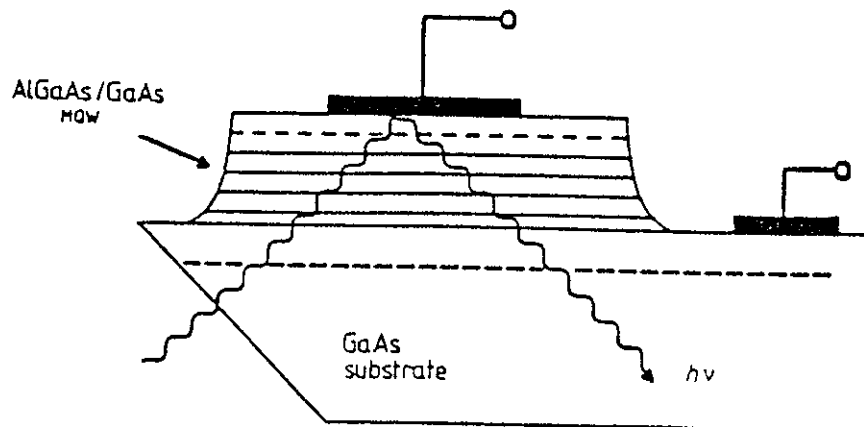


Figure 1.4-9 - Schematic of a GaAs/AlGaAs intersub-band photoconductor structure
Note the 45° cut in the back side to provide photon propagation paths with components along the quantum well layers. This structure can only be used for single elements or linear arrays

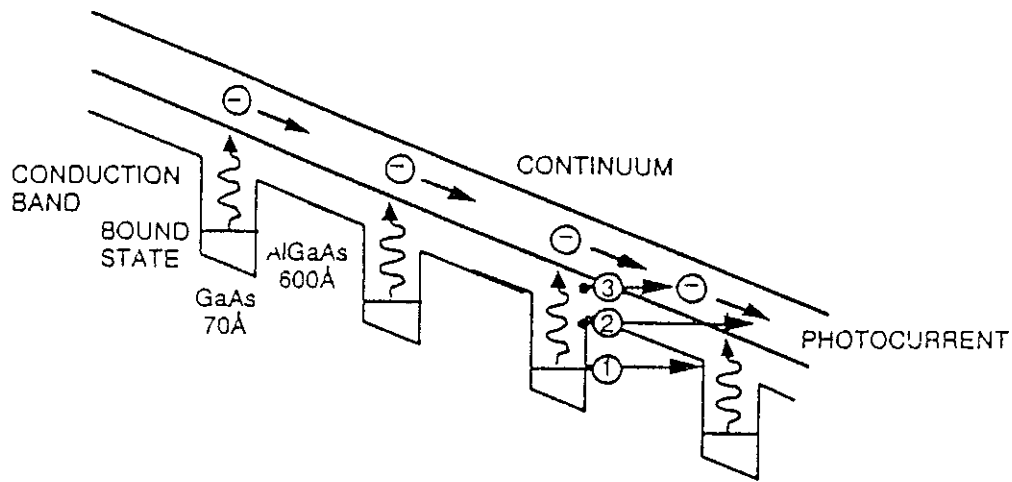


Figure 1.4-10 - Schematic diagram of dark current mechanisms in GaAs/AlGaAs QWIP detectors
 (1) ground state tunneling, (2) thermally assisted tunneling and (3) thermionic emission

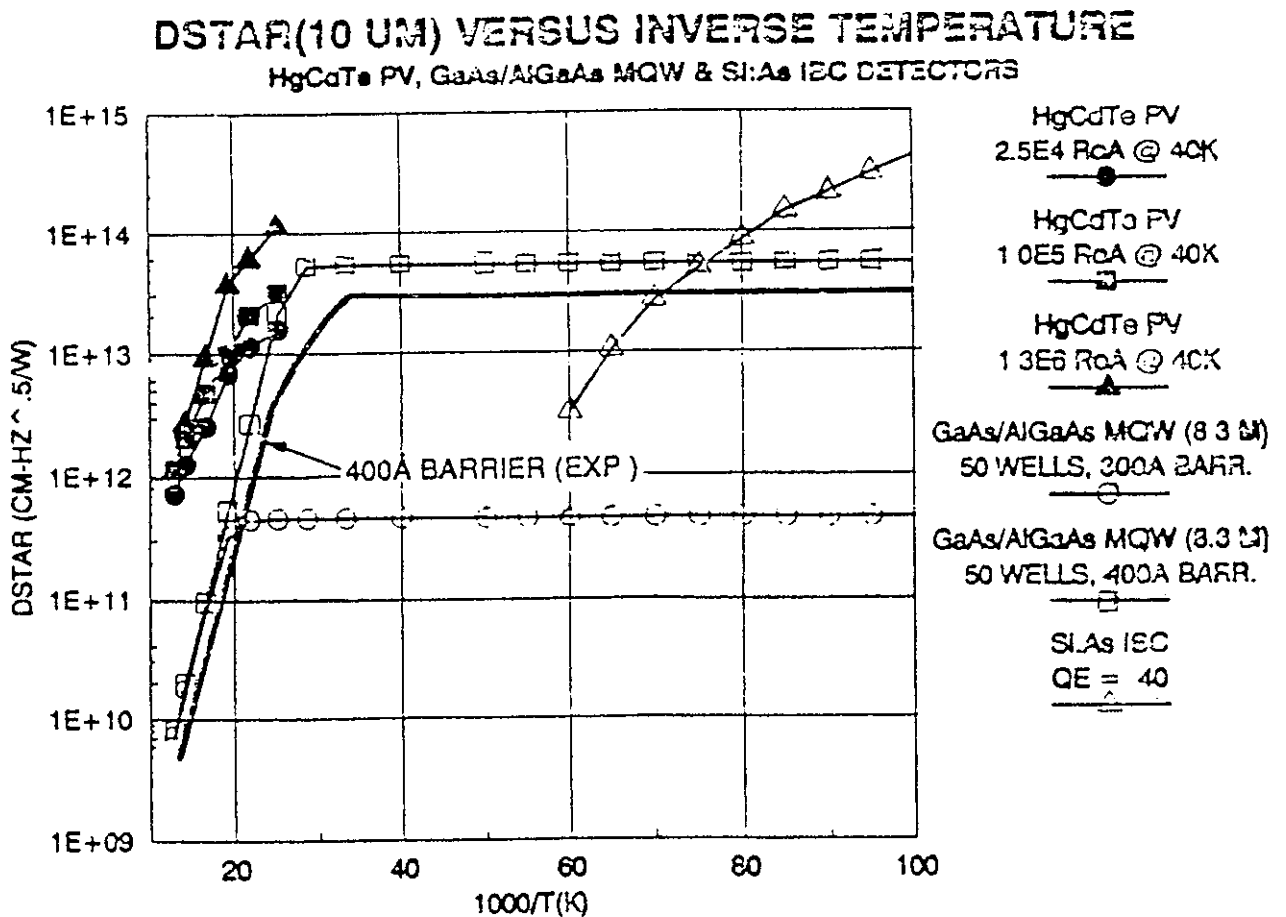


Figure 1.4-11 - Comparison of D^* values for MCT, AlGaAs QW devices and a Si:As IBC detector [116]

1.4.4 Schottky Barrier Arrays

Figure 1 4-11 shows a cross-section through a typical Schottky barrier detector. A Schottky barrier is formed when a silicide metallic conductor comes in contact with a nondegenerately doped silicon semiconductor. The diode effect arises as a result of the difference in Fermi levels (and, hence, electron work functions) of the silicide and silicon, and results in an energy barrier at the interface that produces an asymmetric electronic conduction effect. Infrared radiation with photon energy less than the silicon band gap (1.1 eV) is transmitted through the substrate and is absorbed in the silicide layer which is metallic. The absorption results in excitation of the electron gas in the metal. There is a potential barrier (Schottky barrier) ϕ_{ms} between the silicide layer and the silicon but carriers which have enough momentum can escape into the silicon. These will relax into the substrate majority carrier distribution (this process is fast and is independent of carrier lifetime or diffusion length) and a net charge of opposite sign is left on the silicide electrode. For p type silicon holes are emitted into the substrate and the electrode charge is negative. Since the silicide layer is partly transparent to the IR radiation an oxide layer and reflecting coating are deposited on top so as to increase the quantum efficiency (this sets up an 'optical cavity')

The silicide layer can be deposited very uniformly after the high temperature Si processing. Either monolithic devices or hybrid devices can be made (the latter using indium bump technology). Large arrays are possible at low cost because of the compatibility with conventional silicon processing. Several companies (mainly in the US and Japan) have reported 512 x 512 and 640 x 480 pixel PtSi arrays (see, for example [124] and [125]) and devices can be as large as 1024 x 1024 [126]. In Europe, AEG Infrared Modules (AIM) have discussed a 486 x 640 device [127,128] (indium bump bonded to a CMOS multiplexer).

The response uniformity of is excellent, being typically ~0.1% rms and is superior to that of most visible sensors. The quantum efficiency, however, is low (~1%). For 300K scenes this leads to a D^* reduced by a factor ~6 compared with most higher QE detectors.

The cut-off wavelength (λ_c) is given by

$$\lambda_c = \frac{1.24}{\phi_{ms}} \quad \text{with } \lambda_c \text{ in } \mu\text{m} \text{ and } \phi_{ms} \text{ in eV} \quad (1-4)$$

The value of the barrier height (and hence λ_c) depends primarily on the metal used to form the silicide, though PtSi is the most common silicide used, other materials can be used

Silicide	Emission Coefficient	Cut-off
Pd ₂ Si	0.3 A/W or ev-1	3.5 μm
PtSi	0.5 A/W	5.7-6.0 μm
IrSi	0.16 A/W	7.5-10 μm
PtIrSi	0.075 A/W	9.2 μm

The dark current is given by Richardson's law

$$I = A A^* T^2 \exp[-q \phi_{ms} / kT] \quad (1-5)$$

where A is the diode area
 A^* is the Richardson coefficient (ideally = $32A/cm^2 K^2$ for holes in silicon)
 T is the absolute temperature
 q is the electronic charge

Although PtSi is the most widely used material, IrSi has higher responsivity for wavelengths $>3\mu m$. However, from equation (1-4) we see that as ϕ_{ms} decreases and λ_c increases the dark current also increases. In fact one can write

$$T_{max} = \frac{527}{\lambda_c} \quad (1-6)$$

assuming a maximum allowed dark current density of $= 10^{-7} A/cm^2$

Hence whereas PtSi detectors can be operated at $\sim 77K$, IrSi needs to be operated in the range 40-50K

The cut-off wavelength can also be extended by using molecular beam epitaxy to form a thin p+ layer (or 'doping spike') at the PtSi/silicon interface [129]. The doping spike causes a lowering of the Schottky barrier and detectors with response out to about $12\mu m$. However the quantum efficiency at long wavelengths is very low (less than 1%) and the detectors have to be cooled to $\sim 30K$.

A different kind of silicon homojunction device employing internal photoemission across a barrier has been discussed by workers at NEC [130]. This also offers the prospect of increasing the cut-off wavelength (to $12\mu m$)

1.4.5 Heterojunction Internal Photoemission (HIP) Devices

Recently there has also been interest in heterojunction internal photoemission (HIP) detectors in which the silicide layer is replaced by degenerately doped semiconductor electrode (usually p+ Ge_xSi_{1-x}/Si [131],[132] and arrays up to 400×400 pixels arrays with Ge_xSi_{1-x}/Si heterojunctions have been reported. In these devices the barrier height (and therefore the cut-off wavelength) can be tailored by varying the composition of the Ge_xSi_{1-x}/Si layer and values as high as $25\mu m$ have been achieved. Figure 1 4-12 shows a schematic cross section

The HIP detector offers a higher QE compared with silicon Schottky barriers because a) the states which absorb the IR radiation lie in a narrowband and most photoexcited carriers can cross the barrier - thus leading to a sharp cut-off in wavelength with useful response right out to λ_c , and b) there is less backscattering of photoexcited holes because of the more favourable ratio of effective masses across the heterojunction. HIP detectors can also be fabricated with $In_xGa_{1-x}As/Al_xGa_{1-x}As$ heterojunctions [133]

As with Ge_xSi_{1-x}/Si MQW structures (discussed in para 1 4 3), the possibility of MBE growth of Ge_xSi_{1-x}/Si HIP detectors offers high producibility and uniformity and the prospect of compatibility with monolithic Si readout circuits (both Schottky barrier and HIP devices are compatible with silicon (/GaAs) processing and readout is via conventional CCD or MOS switch arrays)

Park et al [134] have measured the effect of 1 and 8.5 MeV proton irradiations on a $\text{Ge}_x\text{Si}_{1-x}/\text{Si}$ detector. They suggested that the protons produced a reduction in the free carrier density in the SiGe layer and that this caused an increase in the barrier height and in the Richardson constant, A^* . The combined effect being to reduce the dark current. The strain in the SiGe layer did not seem to be affected.

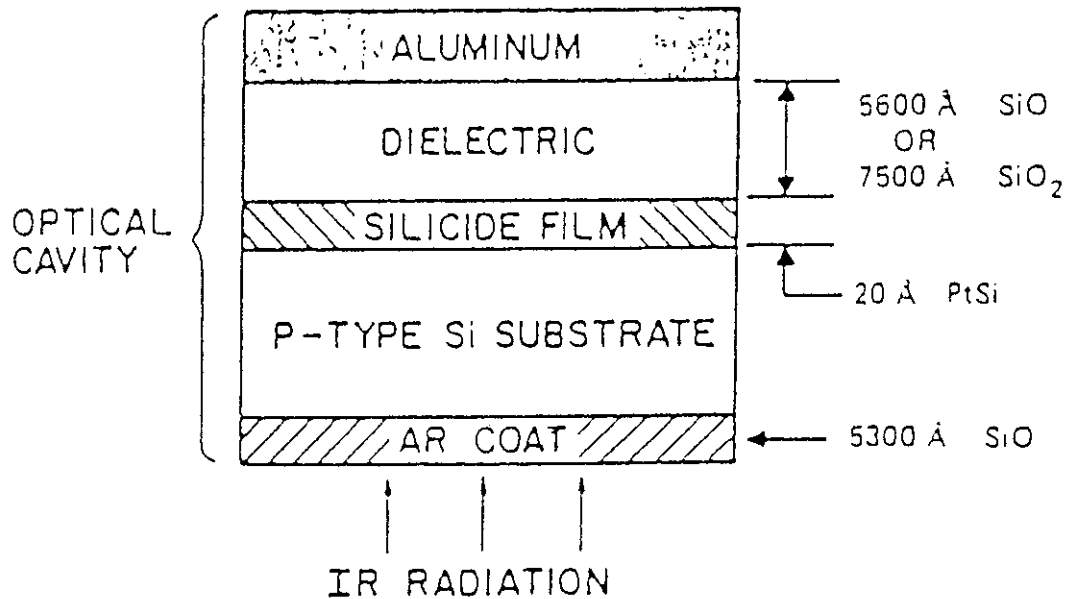


Figure 1.4-11 - Cross-section of a PtSi detector

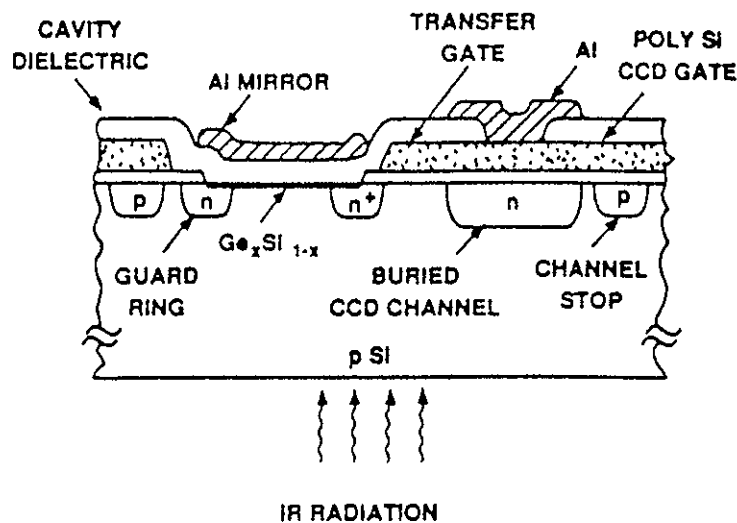


Figure 1.4-12 - Cross section of a single pixel of a GeSi array

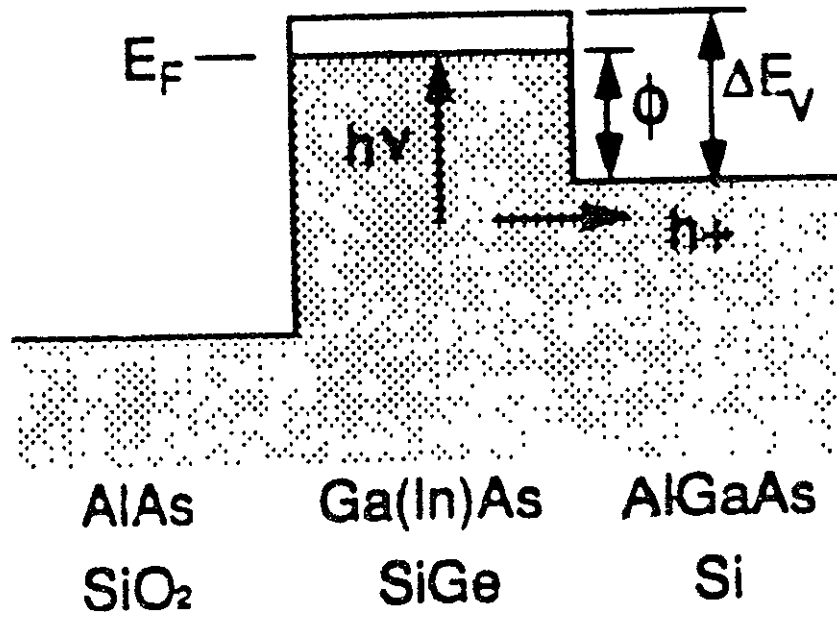


Figure 1.4-13 - Principle of operation of HIP detectors

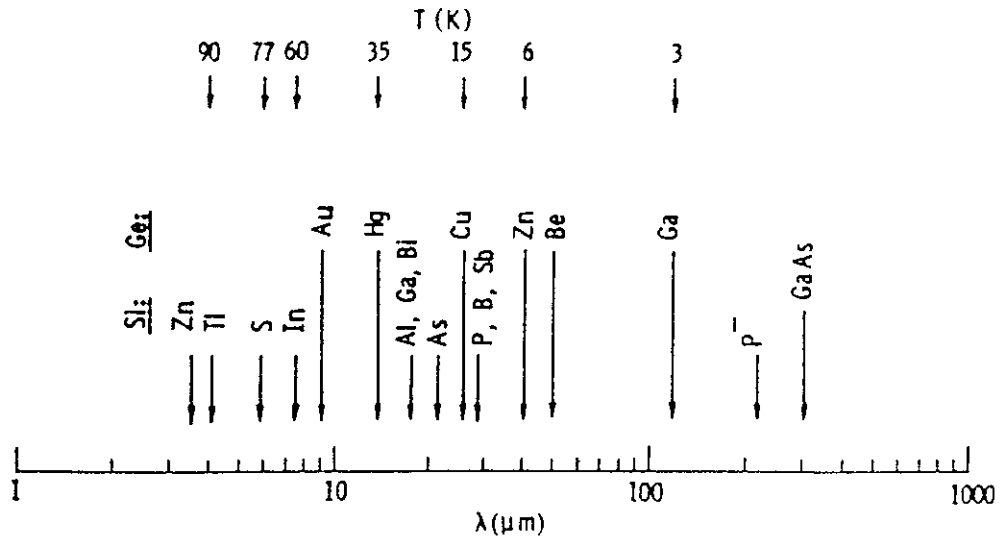


Figure 1.4-14 - Approximate useful upper wavelengths and operating temperatures for extrinsic Si and Ge

1.4.6 InGaAs Arrays

Developed for imaging in the SWIR band, they can operate at near-room temperature. InP is used as a substrate, but for lattice matching the InGaAs composition gives a cut-off at 1.7 μm . However by using a succession of buffer layers a higher cut-off ($\sim 2.5 \mu\text{m}$) can be achieved - though with some difficulty. In the US, arrays are manufactured by Sensors Unlimited (a spin-off from Epitaxx inc). 128 x 128 and 1 x 1024 element lattice matched (i.e. 1.7 μm) arrays are available and the advantages for space instruments (in terms of reduced requirements for detector cooling) have been discussed by Krabach et al [135]. 96 x 25 TDI element arrays from both 1.7 μm and lattice-mismatched material have been discussed by McKee et al [136]. The lattice matched array operated at room temperature and the lattice-mismatched at 220 K. Recently, Sensors Unlimited have announced a 16x16 monolithic array with InP p-i-n/JFET readout [137].

128 element linear arrays are commercially available from Hamamatsu.

In Europe, Thomson TCS (Grenoble) have produced 300x1 arrays for SPOTIV [138], 2x150 arrays for DISR (Huygens probe) and 128x128 arrays [139]. The Thomson arrays are hybridised to a silicon CCD readout.

1.4.7 Lead salt detectors

According to Rogalski [17], because of production and storage problems, HgCdTe photodiodes were in serious competition with IV-VI alloy devices (mainly PbSnTe) from the late 1960s to the mid 1970s. The PbSnTe alloy seemed easier to prepare and appeared more stable. Development of PbSnTe photodiodes was discontinued because the chalcogenides suffered two significant drawbacks. The first was a high dielectric constant that resulted in high diode capacitance and therefore limited frequency response. For scanning systems under development at that time, this was a serious limitation. However, for staring imaging systems under development today using two-dimensional arrays, this is not as significant an issue. The second drawback to IV-VI compounds is their very high thermal coefficients of expansion. This limited their applicability in hybrid configurations with silicon multiplexers. Today, with the ability to grow these materials on alternative substrates such as silicon, this too would not be a fundamental limitation. Moreover, regarding ease of manufacture, homogeneity, and costs, photovoltaic IV-VI arrays on Si substrates offer substantial advantages compared to HgCdTe. The maximum available doping levels because of the onset of tunnelling are more than an order of magnitude higher with IV-VIs than with HgCdTe photodiodes. The research group at the Swiss Federal Institute of Technology continues to pursue this technology and have made significant progress. To overcome thermal mismatch problems between the silicon readout substrate and lead-chalcogenide detector for large arrays, Zogg et al [140] have used an epitaxial stacked CaF_2 - BaF_2 buffer layer of $\approx 200 \text{ nm}$ thickness. They have produced a 'monolithic' 2 x 128 element staggered linear array.

The performance of IV-VI photodiodes are at present inferior to HgCdTe photodiodes, and are still below theoretical limits. However, improvements are possible by optimizing the device fabrication technique. Better results should be obtained using buried p-n junctions with a thin wider-bandgap cap layer (to reduce noise currents) than blocking Pb contacts.

1.4.8 Extrinsic (Si:X and Ge:X) Detectors

Extrinsic detectors rely on the absorption of photons by the freeing of carriers which were originally bound to substitutional impurities in the crystal (Si or Ge). If the impurity states are close to the conduction band then the detector will be sensitive to long wavelength radiation. Since the process creates majority carriers, the devices are usually photo-conductive - ie photodiodes cannot be formed (but see also para 1.4.8.1 below). Figure 1.4-14 shows approximate useful upper wavelengths and operating temperatures for extrinsic Si and Ge. At wavelengths $>13\mu\text{m}$ there are few alternatives to the use of extrinsic materials. A disadvantage is the low temperature required for operation. This is a consequence of the relatively high thermal hole concentration for extrinsic compared with intrinsic semiconductors. A particular feature of extrinsic photoconductors is their high impedance which allows efficient coupling into CCD readout registers in the LWIR even with simple direct injection structures.

Both monolithic and hybrid detectors can be produced. Monolithic devices are typically formed using an epitaxial architecture. The epitaxial layer is of the opposite polarity and is grown on the silicon substrate which is doped with the desired impurity. Majority carriers generated in the substrate are injected into the epitaxial layer where they become minority carriers. A bias voltage, applied across the device is necessary for the injection. A CCD fabricated in the epitaxial layer can act in the normal minority carrier mode for readout. However the high temperatures needed to process the CCD multiplexer tend to have an adverse effect (eg impurity diffusion) on the properties of photoconductor and the most successful devices tend to be manufactured using the planar hybrid structure with the extrinsic silicon slice bump bonded to the multiplexer, both parts may have been processed separately. Note that in this regard extrinsic material has several advantages:

- * the thermal expansion coefficient of photoconductor and multiplexer are matched - allowing for large array dimensions
- * mature Si technology can be used for defect-free wafer production again allowing for large arrays
- * extrinsic photoconductors being indirect band gap devices have a low absorption coefficient and are therefore thick ($\sim 0.5\text{mm}$) but this means they have the mechanical strength to withstand the pressure required to bump bond to the Si mux. The thickness does give increased sensitivity to transient radiation effects however and leads to increased crosstalk between pixels

Monolithic extrinsic arrays have been reviewed by Schroder [141] and a general review of extrinsic arrays has been given by Walter and Dereniak [142]

Most recent work in the open literature has been with arrays developed for IR astronomy applications and table 2-1 gives a list of device types (including blocked impurity band, BIB, detectors to be discussed below). A limited amount of radiation effects data is available as a result of the IRAS, SIRTf and ISO programmes and this is reviewed in section 7. There is little information on extrinsic arrays for military uses. Valvo (Philips) have described a 300×200 Si:In monolithic array [143]. For most applications (including space-based astronomy) BIB detectors are to be preferred (see below), but these have been restricted to Si:As. A 128×192 element Si:Ga array indium bump bonded to a direct voltage readout (DVR) circuit (Thomson-CSF $1.5\mu\text{m}$ process) has been described by Lucas et al [144] at CEA-LETI-LIR. This has been designed for the $8\text{-}14\mu\text{m}$ region and operates at around 10K.

Mission	Detector type	Domain	Range microns	T(K)	Resp. (A/W) or QE (%)	Det. noise e/10 sec	NEP 10 ⁻¹⁷ WHr ^{-1/2}	Array size	
ISO	InSb (CAM)	NIR	2.5 - 5.5	4	30%	1350	3	32 x 32	
	(SWS)		2.4 - 4	4	50%	50	-	1 x 12	
	Si Ga (CAM)	MIR	4 - 17	4	60%	1100	0.2	32 x 32	
			(PHT)	3 - 16	4	40%	600	2	1 x 1
			(PHT)	2.5 - 12	4	40%	600	2	1 x 64
	(SWS)	MIR	4 - 13	4	20%	50	-	1 x 12	
			(PHT)	15 - 29	4	50%	600	2	1 x 1
			(SWS)	12.8 - 28.6	4	20%	50	-	1 x 12
	Ge Be (LWS)	FIR	15 - 25	4	20%	50	-	1 x 2	
			(SWS)	45 - 50	2	14%	300	0.3	1 x 1
			(SWS)	28.6 - 44.1	2	20%	110	-	1 x 12
	Ge Ga (PHT)	FIR	25 - 35	2	20%	110	-	1 x 2	
			(PHT)	44 - 125	2	8%	600	6	1 x 1
			(PHT)	40 - 117	2	9%	600	5	3 x 3
	Str Ge Ga (LWS)	FIR	50 - 110	2	3.7%	100	2	1 x 5	
(PHT)			90 - 204	2	14%	600	3	2 x 2	
(LWS)			110 - 180	2	2.6%	200	2	1 x 4	
SIRTF*	HgCdTe	NIR	1 - 5	60	30% (0.8)	93		256 x 256	
	InSb	NIR	1.8 - 5.3	10	50% (2)	170		256 x 256	
	Si Ga	MIR	4 - 18	7	30% (14)	58		128 x 128	
	Si As (BIBIB)	MIR	4 - 28	4	20-50% (68)	78		128 x 128	
	Si Sb	MIR	14 - 30	5	30% (3.8)	50		128 x 128	
	Ge:Be	FIR	30 - 52	(??)	30-40% (12)	81		2 x 25	
	Ge Ga	FIR	50 - 120	2	20% (39)	75		32 x 32	
	Ge:Ga (BIB)	FIR	50 - 190	2	4% (5)	6000		1 x 20	
	Str Ge:Ga	FIR	120 - 200	1.2	10% (100)	125		1 x 20	
	Bolometer Ge	Submm	200 - 400	0.1			5	1 x 4	
	Bolometer Ge	FIR	400 - 700	0.1			5	1 x 1	
	FIRST*	Ge:Ga	FIR	50 - 120	2				20 x 20
Str Ge:Ga		FIR	120 - 200	2				10 x 10	
Bolometer Ge?		Submm	200 - 850	(0.1-0.3)			20	4 x 4	
Ge:Ga		FIR	80 - 125					7 x 7	
Str Ge:Ga		FIR	130 - 200					7 x 7	
Nb SIS mixer (Solid St. LO Gunn diode)		Submm/mm	900 - 200					2GHz BW	
ESA Contracts FIR/Submm	Si:P (BIB)	MIR	17 - 35	4	50% (24)	40	3	4 x 10 1 x 32	
	Si:P (BIBIB)*	MIR	17 - 35	4	?	40	1	64 x 64	
	Si:P (SSPM)*	MIR	17 - 35	4	(50%?) Gain 5x10 ⁴	?	0.01	64 x 64	
	Ge:Ga (BIB)* SIS*	FIR Submm	40 - 250 250 - ?	2	(20%?)	40	100	32 x 32	

* = Optimum target values not yet achieved

Table 1-1 Characteristics of IR detectors for space astronomy

1 4 8 1 Blocked Impurity Band (BIB) Detectors

As remarked above, the low absorption coefficients of extrinsic silicon detectors necessitate thick active regions which give rise to excessive signals due to interaction with transient particles (in a space environment) and to crosstalk between pixels. In addition PC mode extrinsic detectors are susceptible to changes in sensitivity with changes in temperature and irradiation history (both particles and IR). The blocked impurity band (BIB) or impurity band conduction (IBC) detector overcomes these problems by having a thin active region and by operating in a mode similar to that of photovoltaic detectors. However decreasing the thickness implies that the impurity concentration must increase if quantum efficiency is not to suffer.

When the majority impurity concentration is low, the spacing between atoms is large and there is negligible interaction between impurities. As the concentration is increased and the distance between atoms becomes sufficiently small, carriers can hop from one impurity to another. The probability of hopping is enhanced by compensating impurities, which, by ionizing some of the majority impurities, make empty sites available for carriers to hop into.

For still higher concentrations the ground state electron wave functions overlap (ie there is degeneracy) and the impurity level forms into a band. Conduction then takes place by carriers flowing within this band. For both hopping and impurity band conduction, current flows without the need to excite holes into the valence band. Detector performance is degraded by reducing the ratio of photoconductive/dark current and by increasing device noise.

BIB detectors get around these problems because a thin layer of undoped Si is grown between the heavily doped extrinsic layer and one contact. Under the appropriate bias, this intrinsic layer completely blocks the minority dark current without affecting the photogenerated majority carrier current. A device schematic and energy band diagram for an n-type blocked impurity band detector are shown in figure 1 4-15.

The basic theory of BIB detectors has been reviewed by several authors [145], [146], [147]. In the IR active layer there is a small concentration of acceptors, more than likely boron, which are assumed to be totally compensated and hence all ionized, $N_A^- = N_A$. Thus, before an external bias is applied there must be an equal concentration of ionized donors, $N_D^+ = N_A$. The negative charges associated with the fixed acceptor sites are immobile. But, because of the heavy doping concentration of donors (at least an order of magnitude more than in a conventional extrinsic photodetector), there is a high probability of donor charge hopping (the impurity band effect) from one site to another. Electrons associated with the N_D^0 neutral sites hop to the vacant N_D^+ sites, which can be viewed as 'holes' in the impurity band moving in the opposite direction.

When an external reverse bias is applied to the blocking layer electrode, the N_D^+ charges are swept out through the IR active layer away from the interface with the blocking layer. The blocking layer cannot replenish the N_D^+ charges since the blocking action prevents the hopping carriers from contributing to the current in the absence of a photosignal. The electrons in the conduction band are collected at the transport electrode. Thus, a reverse bias removes all mobile D^+ charges from the IR active layer and leaves behind a depletion region composed of negative space charge.

Thus the BIB detector resembles the photovoltaic detector in its operation. Pairs are created when infrared radiation, with photon energy above the photoionization threshold for the chosen donor impurity, is incident on the detector through the transparent electrode. Those D^+ /electron pairs that are created in the depletion region move in opposite directions in response to its electric field and are collected at the contacts, pairs created in the neutral region recombine. There are also pairs that are produced thermally in the depletion region, or within the diffusion length of the depletion region, that give rise to the dark current and to the associated dark current noise. For large electric fields, electrons accelerating through the depletion region will impact ionize the neutral donors producing internal gain amplification.

We can summarise the basic advantages of BIB arrays over bulk extrinsic detectors as

- * active volume is thin ($\sim 20\mu\text{m}$) therefore reduced sensitivity to transient radiation and crosstalk is reduced
- * mode of operation lends to a stable responsivity (not the case with extrinsic photoconductors)
- * the higher number of recombination centres leads to a faster recovery
- * sensitivity advantage ($\sqrt{2}$ in the background photon noise limit)

Most work on BIB detectors to date has been with Si As and Si Sb and quantum efficiencies $\sim 50\%$ have been achieved. The technology is becoming reasonably mature, so that Si As arrays can almost be thought of as mainstream detectors. Si Ga IBC arrays have been difficult to develop because of the more difficult materials technology involved although Hughes Research laboratories [148] have reported successful growth of Si Ga IBC detectors. In addition the operating temperature of Si Ga arrays is not likely to be high enough to alleviate problems with cryo coolers (as for Si As a 3-stage cooler is still required).

Though 128×128 arrays have been produced for NASA's Space Infrared Telescope Facility (SIRTF) and Wide Field Infrared Explorer (WIRE) programmes (see table 2-1), larger Si As BIB arrays are under development. These arrays are all indium bump bonded to a silicon cryo-CMOS or MOSFET switch array. Rockwell [149] have reported 128×128 Si As and Si Sb arrays and a 256×256 Si As array for high flux applications. Hughes SBRC report that a 320×240 SiAs BIB array is under development [150]. 12×1 Si As arrays made by Rockwell are in use on ESA's ISOPHOT photometer on ISO [151]. Radiation effects in these detectors is reported in chapters 7 and 9. Rockwell have also developed small arrays of Ge Ga BIB detectors and the performance of 6×6 arrays has been discussed by Watson [152].

Devices related to the IBC array are the solid state photomultiplier or SSPM (developed at Rockwell since 1982) and Intrinsic Event Discrimination (IED) devices. The SSPM [153] is a Si As IBC device with a high internal field such that impact ionization can occur in its 'gain region'. The device can be fabricated in linear and area arrays as well as discrete detectors and is sensitive in the range $0.4\text{-}24\mu\text{m}$. Individual photons can be counted (output pulses between 10^4 and 10^5 electrons). The IED concept is useful for operation in a high radiation background since there is an additional readout of the radiation induced signal in a 'c readout' region.

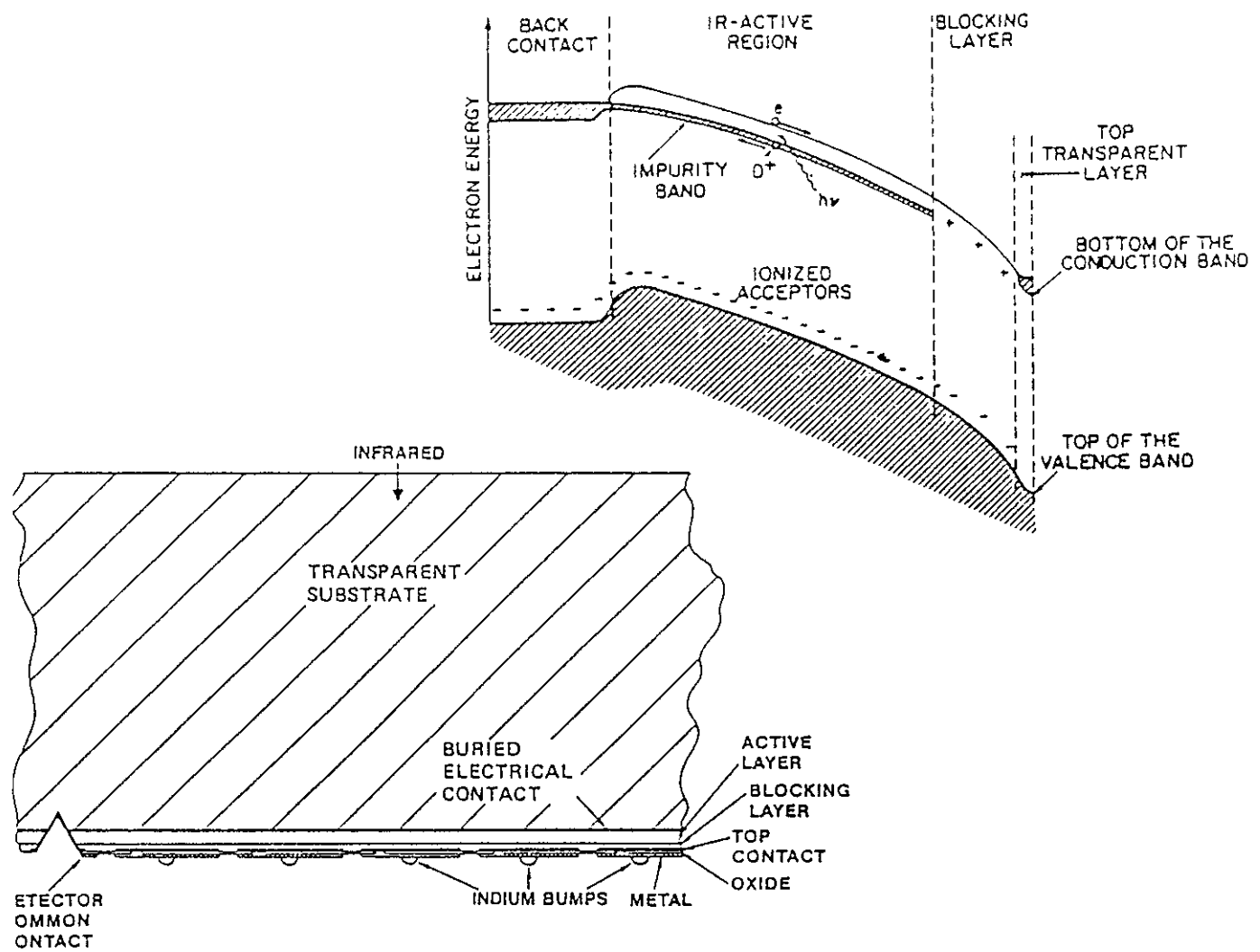


Figure 1.4-15 - Schematic and energy band diagram for an n-type blocked impurity band detector

1.4.9 High T_c Superconductor Detectors

The use of High T_c superconductors (and in particular YBaCuO) as thermal detectors for the IR has been reviewed by Kruse [154]. The type of detector most applicable to IR focal plane arrays is the transition edge microbolometer. A sample is maintained at the transition temperature (around 77K) by a thermal control system, when IR radiation is absorbed there is a change in temperature and a sharp change in resistance is measured. Kruse speculated that large arrays of comparable performance to CMT are possible. Recently, Johnson et al [155] have discussed the performance of YBaCuO microbolometers, each pixel being formed as a meander-line on a Si_3N_4 membrane suspended over an etch pit on a silicon wafer. 64-element linear arrays were fabricated.

Bluzer and Forrester [156] have discussed superconducting quantum detectors with SQUID (superconducting quantum interference device) readout. Also superconducting tunnel devices (STJs) are under development at ESA and other laboratories.

Apart from any effects in the readout circuit, the main mechanism for radiation damage in superconducting microbolometer arrays is likely to be displacement of atoms from the lattice causing shifts in the transition temperature.

1.4.10 Uncooled thermal detector arrays

Over the past few years there have been rapid advances in the availability of uncooled thermal imagers based on microbolometer arrays. The main developments have been in the USA. Honeywell and the technology is now licensed to a large number of other US companies (Lockheed Martin, Loral Infrared and Imaging Systems, SBRC, Amber Engineering and Rockwell). The 1996 and 1997 SPIE IR detector Technology conferences (Proc SPIE volumes 2746 and 3061) have devoted whole sessions to uncooled detector arrays. A common format is 320 x 240 elements. Though these are useful for TV rate imaging in the 8-14 μm band, the sensitivity is low and there are few uses in space applications. An exception is the Geostationary Earth Radiation Budget instrument which is planned to use US microbolometer arrays with a special coating to give a flat spectral response over a wide (1-20 μm) range.

The structure of a typical array is shown in figure 1.4.10-1 (taken from [157]). Each microbolometer is formed by a surface micromachining technique and consists of a 0.5 μm thick bridge of Si_3N_4 supported by two silicon nitride legs. These legs provide thermal isolation from the underlying silicon substrate. A vanadium oxide film (which has a roughly 2% temperature coefficient of resistance) is deposited on the bridge to form the microbolometer resistor. Each microbolometer is connected to an element of a silicon readout integrated circuit (ROIC). The technology used for the ROIC depends on the particular manufacturer but is typically CMOS or BiCMOS. A particular advantage of the microbolometer array is that, unlike pyroelectric detectors (which are also uncooled) the device does not need a mechanical chopper.

A technology which competes with the microbolometer array is the pyroelectric array. This has been developed in the USA by Texas Instruments [158] (who use a barium strontium titanate ceramic, indium bump bonded to a silicon ROIC). Similar devices have been developed in the UK by GEC Marconi Materials Technology who use a solder bump technology to connect to the CMOS readout circuit [159]. IR radiation is first chopped and

then falls on the hybrid. The ferroelectric detector wafer has an array of metallic electrodes deposited on its lower surface to define the detector elements. The chopped radiation produces alternate warming and cooling of the array and this results in alternate positive and negative signals which are subtracted in an image difference processor. This results in twice the signal, but cancels most of spurious fixed pattern noise, since unlike the alternating pyroelectric signals, this noise has a constant polarity.

Pyroelectric arrays have also been developed by Thomson-CSF, who use a pyroelectric polymer deposited on a CCD readout circuit. A 128 x 128 array (TH7441A) is commercially available [160].

The main effects of radiation damage for uncooled bolometer arrays are expected to be in the readout circuit.

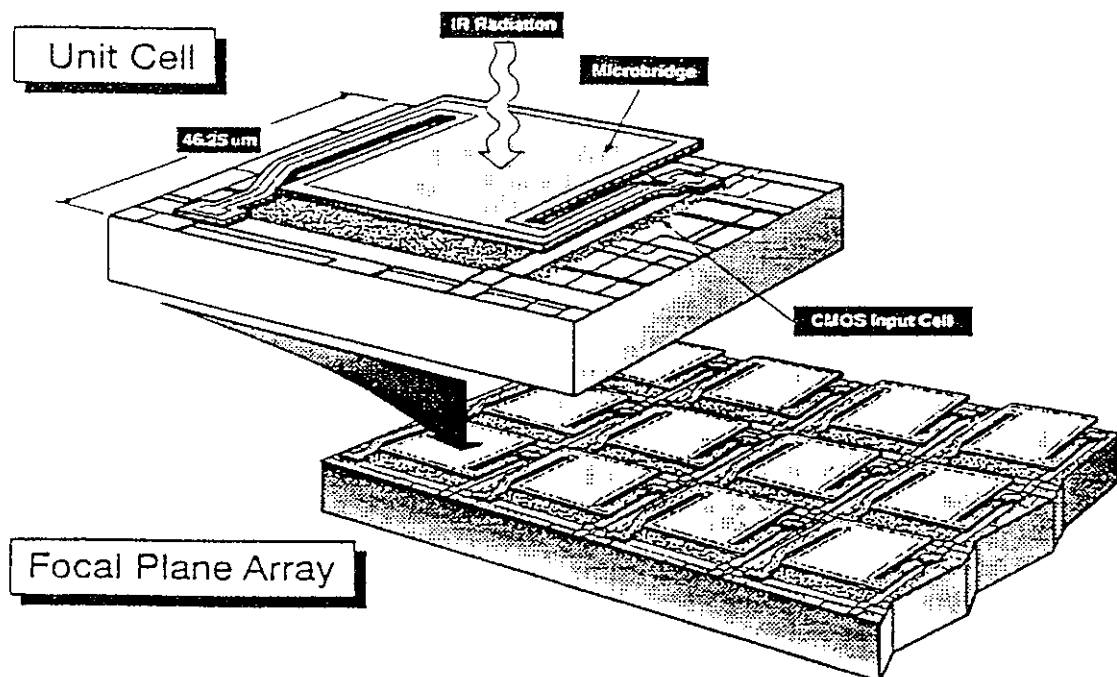


Figure 1.4.10-1 - Structure of a typical microbolometer array [157]

1.4.11 Multiplexers

Readout electronics for infrared detector arrays is normally implemented with silicon circuits hybridised to the detector array. Monolithic detectors are occasionally used (e.g. using, for example, MCT, InSb, PbTe or PbSnTe). For GaAs/GaAlAs QW arrays, GaAs readout circuits can be used but this has not been extensively reported in the literature.

1 4 11 1 Silicon-based circuits

Returning, then, to circuits based on silicon technology, either CCD or CMOS circuits can be used. CCDs architectures are well known and will not be discussed further here - except for the note that surface channel, rather than buried channel devices are usually used for IR detector readouts because of the higher charge handling capacity. CMOS circuits have been reviewed by Fossum and Pain [161] and also by Bluzer and Jensen [162] Kozlowski et al [163] and Kozlowski [164]

The basic detector types are

- source follower per detector (SFD)
- direct injection (DI)
- buffered direct injection (BDI)
- gate modulation input (GMI)
- cascade amplifier per detector (CAD)
- capacitive transimpedance amplifier (CTIA)

These various readout circuits give differing performance in terms of readout noise, power consumption, charge handling, bandwidth, fixed pattern noise, and pixel area. These parameters can therefore be traded-off for a particular application. The circuits are shown schematically in figure 1 4 11-1 and the basic properties are summarised below. Note however that the trade-offs are complex and this can only be an introduction to readout circuit design.

Source follower per detector (SFD)

- simple circuit, so can be used high density arrays
- low power consumption
- high 1/f noise
- high fixed pattern noise (due to threshold voltage nonuniformities)
- disadvantage in that no control of diode bias
- used in US for a wide range of MCT, Si As BIB and InSb arrays

Direct injection (DI)

- simple circuit, so can be used high density arrays
- low power consumption
- injection efficiency low for low resistance LWTR diodes and for low backgrounds
- large integration capacitance implies low voltage sensitivity and increased noise due to downstream circuits
- commonly used for high background (e.g. ground-based) applications

Buffered direct injection (BDI)

- amplifier inserted in the DI circuit to improve injection efficiency, so allowing low background operation - at the expense of a more complex circuit
- good control of detector bias
- power consumption increased due to amplifier
- used mainly in linear arrays where additional circuit size can be easily accommodated. Some 2-D arrays have also used BDI

Gate modulation input (GMI)

- bias voltage developed across a load resistor used to modulate the gate voltage of an output transistor
- large charge to voltage conversion gain leads to high charge detection sensitivity and reduced input-referred noise levels
- hence can have a large integration capacitance (high charge capacity) and still achieve good noise performance
- current gain self-adjusts, depending on background flux - can be used for background suppression
- disadvantage in that pixel-to-pixel current gain variations cause large fixed pattern noise, also variations in linearity

Capacitive transimpedance amplifier (CTIA)

- each pixel has an inverting amplifier with a capacitor in the feedback loop
- complex circuit, so difficult to accommodate with high density arrays
- good control of detector bias (input to amplifier is a virtual ground)
- can have small integration capacitance and very good noise performance
- high power consumption

Cascode amplifier per detector (CAD)

- like the GMI circuit, charge to voltage conversion gain is increased, otherwise properties similar to the SFD circuit
- complex circuit, so difficult to accommodate with high density arrays

1.4.11.2 GaAs - based circuits

Another possibility is to use GaAs circuits. Both CCDs and MOSFET arrays can be made in this material. The advantages are high speed, low temperature operation, radiation hardness and compatibility with GaAs technology detectors (eg GaAs/AlGaAs QW detectors). Due to the lack of stable native oxides on GaAs, buried channel CCDs using Schottky barriers have been developed [165]. There are two types, the capacitive gate CCD and the resistive gate CCD (figure 2.4-19). The former type shows rather poor charge transfer efficiency because of the gaps between electrodes (which give rise to spurious potential pockets which trap charge).

The resistive gate type employs a cermet film and shows higher CTE. For coupling to bandgap engineered detectors (eg GaAs/AlGaAs quantum wells) the recently developed two-dimensional electron gas (2DEG) CCDs have several advantages [166]. These devices use the abrupt heterointerface between the two materials (eg GaAs/AlGaAs or InAlAs/InGaAs/InP) and the consequent conduction band discontinuity to confine electrons.

The advantages are

- high speed operation (as with most GaAs devices, resulting from high mobility)
- charge handling capacity is high (compared with GaAs CCDs) - and can exceed 10^{12} carriers/cm²
- the lattice matched heterointerface has a potentially lower interface trap density than the intrinsically mismatched silicon-silicon dioxide interface as well as improved radiation hardness
- there is the potential for low temperature operation
- GaAs/AlGaAs is the most mature system. The device structure for a two phase, resistive gate 2DEG-CCD delay line is shown in figure 1.4.11-2

Dark current in III-V devices is typically larger than that found in silicon CCDs despite the large energy bandgap of the former. This is because III-V CCDs do not have the benefit of the high gate - SiO₂ dielectric interface barrier height, and thermionic emission over the lower barrier leads to dark current exceeding the band-to-band and heterointerface generation. 2DEG-CCDs have a high electric field at the gate-dielectric interface and this can give rise to even higher dark current (due to thermionic field emission quantum mechanical tunneling into the dielectric conduction band). However this should not be a problem at the low temperatures (77K) needed for IR detector operation.

GaAs MOSFET arrays are being developed for example by Hughes [167]. These have good radiation tolerance (100 Mrad) and can offer nondestructive readout and low power dissipation as well as compatibility with coupling requirements to MCT (via transimpedance amplifiers) or blocked impurity band detectors.

1.5 SUMMARY OF SPACE PROJECTS USING IR DETECTOR ARRAYS

In this section we give a brief list of non-military spaceborne instruments which contain infrared detector arrays (or in some cases 'scientific' instruments which include single element detectors).

Instrument	Institute	Detector
SPOT IV DISR CIRS (Composite Infrared Spectrometer), Casini	LETI-LIR	InGaAs, Thomson CSF InGaAs, Thomson CSF Large area (200 μ m \times 200 μ m PV MCT LWIR diodes)
ISO ISOCAM (Camera & polarimetry) ISOPHOT (Imaging photopolarimeter)	CEN-Saclay MPI für Astronomie	32x32 InSb CID (2.5-5 μ m) 32x32 Si Ga (65-17 μ m) Single pixel Si Ga (3-19 μ m), SiB (9-29 μ m), Ge Ga (37-129) (1x1x1 mm ³) 3x3 Ge Ga (37-129) 2x2 Si Ga (37-129) 64x64 Si Ga (6-12) x (2.5-5 μ m)
SWS (Short wavelength spectrometer)	SRON Groningen	1x12 InSb (2.4-4 μ m) PV 1x12 Si Ga (4-13) PC 1x12 Si As (12-28) IBC 1x12 Ge Be (28-45) PC 1x2 Si Sb (12-25) PC 1x2 Ge Be (25-40) PC
LWS (Long wavelength spectrometer)	QMW College London	Single element Ge Be PC Ge Ga PC (stressed & unstressed)
ATSR	DRAL (UK)	single PC CMT (G-MIRL) single PV InSb (SAT) single Si diodes (Centronics)
COBE (Cosmic badged explorer)	US	Single element InSb Si As IBC Ge Ga
HST 2 nd Generation NICMOS camera	US	256x256 SWIR MCT (Rockwell)
SIRTF IRAC (Infrared array camera)	US	256x256 InSb (PV), CMOS readout 128x128 Si AS IBC, CMOS readout
IRS (Infrared spectrometer)		128x128 Si As IBC, CMOS readout 128x128 Si SB IBC, CMOS readout 4x32 Ge Ga PC, CMOS readout 2x16 Ge Ga PC, stressed CMOS readout

Instrument	Institute	Detector
MIPS (Multiband imaging photometer)		32x32 Ge Ga PC, CMOS readout 2x16 Stressed Ge Gi PC, CMOS readout
AIRS	JPL	Various PV (p-on-n) MCT arrays Cut of wavelengths, 5.6, 8.8, 9.6, 11.9, 13.5, 14.5, 15.6 μm , 300-400 element linear arrays with CMOS readout circuits, 140 and 133 element linear PC arrays for 16.5 and 17.1 μm cut-off bands
ASTER TIR SWIR	Japan	Staggered 5x2 element linear PC MCT arrays, 10.2 and 12.8 μm cut-off 2100 element staggered linear PtSi array
WIRE	US	Si As IBC

REFERENCES

- [1] Radiation Design Handbook, ESA PSS-01-609, Issue 1 (May 1993)
- [2] E J Daly, 'The analysis of space radiation environments for ESA projects', *ESA Journal*, vol 12, pp 229-247 (1988)
- [3] E J Daly, 'The radiation belts', *Radiation Physics and Chemistry*, vol 43(1/2), pp 1-17 (1994)
- [4] W Heinrich, 'Cosmic rays and their interactions with the geomagnetic field and shielding material', *Radiation Physics and Chemistry*, vol 43(1/2), pp 19-34 (1994)
- [5] C Tranquille, 'Solar proton events and their effect on space systems', *Radiation Physics and Chemistry*, vol 43(1/2), pp 35-45 (1994)
- [6] E G Stassinopoulos and J P Raymond, 'The Space Radiation Environment for Electronics', *Proc of the IEEE*, vol 76, pp 1423-1442 (1988)
- [7] J Feynman and S B Gabriel, 'High-energy charged particles in space at one astronomical unit', *IEEE Trans on Nuclear Science*, vol 43(2), pp 344-352 (1996)
- [8] M S Gussenhoven, E G Mullen and D Brautigan, 'Improved understanding of the Earth's radiation belts from the CRRES satellite', *IEEE Trans on Nuclear Science*, vol 43(2), pp 353-368 (1996)

- [9] E J Daly, J Lemaire, D Heynderickx and D J Rodgers, 'Problems with models of the radiation belts', *IEEE Trans on Nuclear Science*, vol 43(2), pp 403-415 (1996)
- [10] A Tebo, 'IR detector technology part II arrays', *Laser focus/Electro-optics*, vol 20(7), pp 68-82 (July 1984)
- [11] G A Walter and E L Dereniak, 'Photodetectors for focal plane arrays Part 1 Extrinsic Silicon', *Laser Focus/Electro-optics*, pp 108-118 (march 1986), 'Part 2 HgCdTe', *Laser Focus Electro-Optics*, pp 86-96 (April 1986)
- [12] C T Elliott, 'Detectors of thermal infrared radiation', in Recent developments in infrared components and subsystems, *Proc SPIE*, vol 915, pp 9-19 (1988)
- [13] R A Ballinghall, 'Review of infrared focal plane arrays' in Infrared technology and applications, *Proc SPIE*, vol 1320, pp 70-87 (1990)
- [14] D A Scribner, M R Kruer and J Killiany, 'Infrared focal plane array technology', *Proc IEEE*, vol 79(1), pp 66-85 (1991)
- [15] P R Norton, 'Infrared image sensors', *Optical Engineering*, vol 30(11), pp 1649-1663 (1991)
- [16] A Rogalski, 'New trends in semiconductor infrared detectors', *Optical Engineering*, vol 33(5), pp 1395-1411 (1994)
- [17] A Rogalski, 'Infrared photon detectors', (SPIE optical Engineering Press, Bellingham, 1995)
- [18] J C Pickel, 'Novel devices and sensors', *Short Course Notes*, IEEE Nuclear and Space Radiation Effects Conference, Snowbird, Utah, July 19, 1993
- [19] S R Andrews, 'Infra-red imaging using quantum well photodetectors', *GEC Journal of Research*, vol 10(3), pp 166-173 (1993)
- [20] G L Hansen, J L Schmit and T N Casselman, 'Energy gap versus alloy composition and temperature in Hg(1-x)Cd(x)Te', *J Appl Phys*, vol 53, pp 7099-7101 (1982)
- [21] J C Brice, 'Direct bandgap of CdHgTe', EMIS Datareview RN = 15630, in Properties of Mercury Cadmium Telluride (IEE INSPEC 1987)
- [22] W E Tennant, C A Cockrum, J B Gilpin, M A Kinch, M B Reine and R P Ruth, 'Key issues in HgCdTe-based focal plane arrays an industry perspective', *J Vac Sci Technol.B*, vol 10(4), pp 1359-1369 (1992)
- [23] L J Koslowski, R B Bailey, S A Cabelli, D E Cooper, I S Gergis, A C Chen, W V McLevige, G L Bostrup, K Vural, W E Tennant and P E Howard, 'High performance 5- μ m 640x480 HgCdTe-on-sapphire focal plane arrays', *Optical Engineering*, vol 33(1), pp 54-63 (1994)

- [24] L J Koslowski, K Vural, D Q Bui, R B Bailey, D E Cooper and D M Stephenson, 'Status and direction of PACE-1 HgCdTe FPAs for astronomy', *Proc SPIE*, vol 1946, pp 148-160 (1993)
- [25] W E Tennant, L J Kozlowski, L O Bubulac, E R Gertner and K Vural, 'Advanced materials techniques for large HgCdTe focal plane arrays', in Advanced infrared detectors and systems, IEEE conference publication No 321, pp 15-19 (1990)
- [26] K R Zanio, 'HgCdTe on Si Hybrid and Monolithic FPAs', in infrared detectors and focal plane arrays, *Proc SPIE*, vol 1308, pp 180-193 (1990)
- [27] S M Johnson, M H Kalisher, W L Ahlgren, J B James and C A Cockrum, 'HgCdTe 128x128 infrared focal plane arrays on alternative substrates of CdZnTe/GaAs/Si', *Appl Phys Lett*, vol 56(10), pp 946-948 (1990)
- [28] F J Kub, C T Yao and J R Waterman, 'Radiation hardened SOS MOSFET technology for infrared focal plane readouts', *IEEE Trans on Nuclear Science*, vol NS-37(6), pp 2020-2025 (1990)
- [29] I M Baker, G J Grimes, C K Ayrd, M D Jenner, J E Parsons, R A Ballingall and C T Elliott, 'Hybrid CdHgTe - Silicon infrared focal plane arrays', in Advanced Infrared Detectors and Systems, IEE Conference Publication No 321, pp 78-87 (1990)
- [30] R Triboulet, M Bourdillot, A Durand and T Nguyen Duy, '(Hg,Zn)Te among the other materials for IR detection', in Future Infrared Detector Materials, *Proc SPIE*, vol 1106, pp 40-46 (1989)
- [31] M B Reine, A K Sood and T J Tredwell, 'Photovoltaic Infrared Detectors', in Semiconductors and Semimetals, vol 18, R K Willardson and A C Beer (eds), pp 201-311 (Academic Press, 1981)
- [32] N Bluzer and A S Jensen, 'Current readout of infrared detectors', *Optical Engineering*, vol 26(3), pp241-248 (1987)
- [33] K Kubo, H Wakayama, N Kajihara, K Awamoto and Y Miyamoto, 'Feedback direct injection current readout for infrared charge coupled devices', in Infrared Technology XV, *Proc SPIE*, vol 1157, pp329-337 (1989)
- [34] W S Chan, 'Detector-charge-coupled device (CCD) interface methods', in Mosaic focal plane methodologies, *Proc SPIE*, vol 244, pp 81-96 (1980)
- [35] R A Ballingall, I D Blenkinsopp, I Baker and J Parsons, 'Two dimensional infrared focal plane arrays utilising a direct inject input scheme', in Infrared technology XII, *Proc SPIE*, vol 685, pp 115-122 (1986)
- [36] J M Arias, J G Pasko, M Zandian, L J Kozlowski and R E Dewames, 'Molecular beam epitaxy HgCdTe infrared photovoltaic detectors', *Optical Engineering*, vol 33(5), pp1422-1428 (1994)

- [37] P Mitra, T R Schimert, F C Case, R Starr, M H Weiler, M Kestigian and M B Reine, 'Meltalorganic chemical vapor deposition of HgCdTe for photodiode applications', *J Electronic Materials*, vol 24(5), pp 661-668 (1995)
- [38] R Wollrab, A Bauer, M Bruder, J Wendler, J Ziegler and H Maier, 'Photovoltaic Hg_{1-x}Cd_xTe detectors for 12 μ m application', in Advanced infrared detectors and systems, IEEE Conference Publication No 321, pp 30-35 (1990)
- [39] C T Elliott, 'Future Infrared Detector Technologies', in Advanced infrared detectors and systems, IEE Conference Publication No 321, pp 61-68 (1990)
- [40] M B Reine, 'Status of LWIR HgCdTe Infrared detector technology', Proc NASA/JPL workshop on innovative long wavelength infrared detectors, Pasadena CA, April 1990, pp 61-77 (1990)
- [41] J N Schulman and O K Wu, 'MBE HgCdTe heterostructure detectors', Proc NASA/JPL workshop on innovative long wavelength infrared detectors, Pasadena CA, April 1990, pp 351-362 (1990)
- [42] I A Baker, G J Grimes, J E Parsons and E S O'Keefe, 'CdHgTe-CMOS hybrid focal plane arrays - a flexible solution for advanced infrared systems,
- [43] I M Baker, D E Charlton, C Arthurs and G Grimes, 'Advanced high performance CdHgTe multiplexed arrays', *Proc ESA Symposium on Photon Detectors for Space Instrumentation*, ESA SP-356, pp 181-165 (1992)
- [44] I M Baker, M P Hastings, L G Hipwood, C L Jones and P Knowles, 'Infra-red detectors for the year 2000' *GEC Review*, vol 10 pp 148-160 (1995)
- [45] G L Destefanis, 'HgCdTe infrared diode arrays', *Semiconductor Science and Technology*, vol 6, pp C88-C92 (1991)
- [46] G Destefanis and J P Chamonal, 'Large improvement in HgCdTe photovoltaic detector performances at LETI', *Journal of Electronic Materials*, vol 22(8), pp1027-1032 (1993)
- [47] R Davencens, A Menardi, L-P Angebault and J-P Chamonal, "Development of a long linear array beyond 12.5 μ m for Earth observation", *Proc SPIE*, vol 2552, pp 853-864 (1995)
- [48] Ph Bouchut, S Guillot, J L Pornin, Ph Rambaud, D Giotta, L Rodriguez and J. Le Pennec, 'HgCdTe photovoltaic linear array for the Cassini infrared spectrometer', *Proc SPIE*, vol 2225, pp360-368 (1994)
- [49] D Marion, J Cluzel, F Mongellaz, P Rambaud and M Ravetto, '256 x 256 (3-5) μ m focal plane array at 77 K operation', *Proc SPIE*, vol 2552, pp 778-784 (1996)
- [50] J Ziegler, M Bruder, J Wendler and H Maier, 'Second generation-FPA's with MCT sensor arrays in hybrid approach', *Proc SPIE*, vol 1735, pp 151-162 (1992)

- [51] AIM Data Sheets, July 1996
- [52] K -W Hodapp, J L Hora, D N B Hall, L L Cowie, M Metger, E Irwin, T Keller, K Vural, L J Kozlowski and W Kleinhans, 'Astronomical characterisation of 1024 x 1024 HgCdTe HAWAII detector arrays', *Proc SPIE*, vol 2475, pp 8-14 (1995)
- [53]
- [54] J Arias, M Zandian, J G Pasko, S H Shin, L O Bubulac, R E DeWames and W E Tennant, 'Molecular-beam epitaxy growth and in-situ arsenic doping of p-on-n HgCdTe heterojunctions', *J Appl Phys*, vol 69(4), pp 2143-2148 (1991)
- [55] T Tung, L V De Armond, R F Herald, P E Herning, M H Kalisher, D A Olson, R F Risser, A P Stevens and S J Tighe, 'State of the art Hg-melt HgCdTe at Santa Barbara Research Center', *Proc SPIE*, vol 1735, pp 109-134 (1992)
- [56] D A Brown, 'Army may shift AAWS development schedule', *Aviation Week and Space Technology*, pp 68-69, (July 8, 1991)
- [57] B Ewing, 'Optical solutions for the army's new light helicopter', *Photonics Spectra*, pp 85-92 (July 1990)
- [58] E A Patten and M H Kalisher, 'HgZnTe-based detectors for LWIR NASA applications', Proc NASA/JPL workshop on innovative long wavelength infrared detectors, Pasadena CA, April 1990, pp 381-397 (1990)
- [59] E A Patten, M H Kalisher, G R Chapman, J M Fulton, C Y Yuang, P R Norton, M Ray and S Sen, 'HgZnTe for very long wavelength infrared applications', *J Vac Sci Technol*, vol B9, pp 1746-1751 (1991)
- [60] P R Norton, M Bailey, I Kasai and P King, 'Thermoelectrically cooled MWIR HgCdTe Image Sensors', *Proc SPIE*, vol 2225, pp 289-292 (1994)
- [61] N N Gurnee and R M Broudy, 'HgCdTe focal plane development concepts', in Solid state imaging arrays, *Proc SPIE*, vol 570, pp 120-126 (1985)
- [62] S C H Wang, G Dudoff, S Jost, J Roussis, J Voelker, M Winn and T Wyman, 'High-performance longwave infrared HgCdTe scanning focal plane arrays for surveillance applications', *Proc SPIE*, vol 1529, pp 335-349 (1994)
- [63] T Kanno, H Wada, M Nagashima, H Wakayoma, K Awamoto, N Kijichawa, Y Ito and M Nakamura, 'A 256x256 element HgCdTe hybrid IRFPA for 8-10 μm band', in Infrared Technology XXI, *Proc, SPIE*, vol 2552, pp 384-291 (1995)
- [64] A Kawahara, A Ajisawa, K Miyamoto, M Kanzaki, T Sasaki, M Tomono, N Oda, T Shima and Y Seihara, 'Hybrid 256x256 LWIR FPA using MBE grown HgCdTe on GaAs' in Infrared Technology XXI, *Proc, SPIE*, vol 2552, pp 411-420 (1995)

- [65] C G Roberts, 'HgCdTe charge transfer device focal planes', in Infrared Detectors, *Proc SPIE*, vol 443, pp 131-143 (1983)
- [66] T L Koch, J H DeLoo, M H Kalisher and J D Philips, 'Monolithic n-channel HgCdTe linear imaging arrays', *IEEE Trans on Electron Devices*, vol ED-32(8), pp 1592-1598 (1985)
- [67] M A Kinch, 'Metal-Insulator-Semiconductor infrared detectors' in Semiconductors and Semimetals, vol 18, R K Willardson and A C Beer (Eds), pp 313-378 (Academic Press, 1981)
- [68] M A Kinch, R A Chapman, A Simmons, D D Buss and S R Borrello, 'HgCdTe Charge-Coupled Device Technology', *Infrared Physics*, vol 20, pp1-20 (1980)
- [69] W D Baker, 'Intrinsic focal plane arrays', in Charge-coupled devices, D F Barbe (Ed), pp 25-26 (Springer-Verlag, 1980)
- [70] J R Waterman, 'Radiation induced interface trap limited storage times in 10 micron cut off wavelength (Hg,Cd)Te MIS capacitors', *IEEE Trans on Nuclear Science*, vol NS-35(6), pp 1313-1318 (1988)
- [71] J P Omaggio, 'Monolithic HgCdTe MIS IR detectors with a floating diode sense mechanism', *IEEE Trans on Electron Devices*, vol ED-33(10), pp 1494-1501 (1986)
- [72] S C H Wang, C -Y Wei, H H Woodbury and M D Gibbons, 'Characteristics and readout of an InSb CID two dimensional scanning TDI array', *IEEE Trans on Electron Devices*, vol ED-32(8), pp 1599-1607 (1985)
- [73] M V Wadsworth, S B Borello, J Dodge, R Gooch, W McCardel, G Nado and M D Shilhanek, 'Monolithic CCD imagers in HgCdTe', *IEEE Trans. on Electron Devices*, vol 43(2), pp 244-250 (1995)
- [74] S C Chen and J R Srour, 'Ionizing radiation effects on indium antimonide MIS devices', *IEEE Trans on Nuclear Science*, vol NS-26(6), pp 4824-4827 (1979)
- [75] J T. Wimmers, R M Davis, C A Niblack and D S Smith, 'Indium antimonide detector technology at Cincinnati Electronics Corporation', in Infrared detectors and arrays, *Proc SPIE*, vol 930, pp 125-138 (1988)
- [76] G C Bailey, C A Niblack and J T Wimmers, 'Recent developments on a 128x128 indium antimonide/FET switch hybrid imager for low-background applications', in Infrared detectors, sensors and focal plane arrays, *Proc SPIE*, vol 686, pp 76-83 (1986)
- [77] C A Niblack, 'Improved performance characteristics for indium antimonide photovoltaic detector arrays using a FET-switched multiplexing technique', in Solid state imaging arrays, *Proc SPIE*, vol 570, pp 127-136 (1985)
- [78] C A Niblack, M Blessinger, J Forsthoefel, C Staller and H Sobel, 'InSb linear multiplexed FPAs for the CRAF/Cassini and infrared mapping spectrometer', in Space Astronomical Telescopes and Instruments, *Proc SPIE*, vol 1494, pp 403-413 (1991)

- [79] M A Blessinger, G W Apgar, J D Biggs, M L Louderback and C A Niblack, 'A 256 x 256 element InSb focal plane array for ground-based astronomy', in Infrared Detectors and Instrumentation, *Proc SPIE*, vol 1946, pp 55-60 (1993)
- [80] J Heynssens and A Fowler, 'Valley Oakes/Cincinnati Electronics 256 x 256 array evaluation', in Infrared Detectors and Instrumentation, *Proc SPIE*, vol 1946, pp 18-24 (1993)
- [81] J D Blackwell, W J Parrish and G T Kincaid, 'High performance InSb 256x256 infrared camera', in Surveillance Technologies, *Proc SPIE*, vol 1479, pp 324-334 (1991)
- [82] J Blackwell, S Botts, A Laband and H Arnold, 'An affordable 128x128 InSb hybrid focal plane array', *Proc SPIE*, (1989)
- [83] M A Massie, J D Vincent, R F Cannata and J Metschuleit, 'Versatile large format focal planes for remote sensing applications', in Infrared Spaceborne Remote Sensing, *Proc SPIE*, vol 2019, pp 353-364 (1993)
- [84] A M Fowler, R G Probst, J P Britt, R R Joyce and F C Gillett, 'Evaluation of an indium antimonide hybrid focal plane array for ground based infrared astronomy', *Optical Engineering*, vol 26(3), pp 232-240 (1987)
- [85] A Hoffman, and D Randall, 'High performance 256 x 256 InSb FPA for astronomy', in Infrared Technology XVII, *Proc SPIE*, vol 1540, pp 297-302 (1991)
- [86] A M Fowler, J B Heynssens, I Gatley, F J Vrba, H D Ables, A Hoffman and J Woolaway, 'ALADDIN, the 1024 x 1024 InSb array test results', *Proc SPIE*, vol 2475, pp 27-33 (1995)
- [87] W J Forrest, H Chen, J D Garnett, S L Solomon and J D Pipher, 'Near infrared arrays for SIRTf, the space infrared telescope facility', in Infrared Detectors and Instrumentation, *Proc SPIE*, vol 1946, pp 18-24 (1993)
- [88] M D Gibbons, S C Wang, S R Jost, V F Meikleham, T H Myers and A F Milton, 'Developments in InSb material and charge injection devices', in Focal plane arrays. technology and applications, *Proc SPIE*, vol 865, pp 52-59 (1987)
- [89] A Bahraman, C-H Chen, J M Geneczko, M H Shelstad, R N Ting and J G Vodicka, 'Current state of the art in InSb infrared staring imaging devices', in Infrared Systems and Components, *Proc SPIE*, vol 750, pp 27-31 (1987)
- [90] P R Beaudet, 'Low light level imaging', presented at the 1990 IEEE Workshop on Advanced Solid-State Imagers, Harriman, New York, May pp 18-20 (1990)
- [91] D Tiphene, F Lacombe and D Rouan, 'Performance measurements on a 32x32 InSb-CID detector array for astronomical applications', in Focal plane arrays. Technology and Applications, *Proc SPIE*, vol 865, pp 122-127 (1987)

- [92] A Kepten, Y Shacham-Diamand and S E Schacham, 'p-channel MIS Double-metal process InSb monolithic unit cell for infra-red imaging', in Infrared Detectors and Focal Plane Arrays II, *Proc SPIE*, vol 1685, pp 305-316 (1992)
- [93] M W Goodwin, M A Kinch and R J Koestner, 'Metal-insulator-semiconductor properties of HgTe-CdTe superlattices', *J Vac Sci Technol*, vol A6(4), pp 2685-2692 (1988)
- [94] K A Harris, T H Myers, R W Yanka, L M Mohnkern and N Otsuka, 'A high quantum efficiency in situ doped mid-wavelength infrared p-on-n homojunction superlattice detector grown by photoassisted molecular-beam epitaxy', *J Vac Sci Technol*, vol B9(3), pp 1752-1758 (1991)
- [95] G C Osbourn, 'Design of III-V quantum well structures for long-wavelength detector applications', *Semicond Sci Technol* vol 5, pp S5-S11 (1990)
- [96] M K Benedict, 'Review of band-gap engineered photodiodes' in Infrared detectors and arrays, *Proc SPIE*, vol 930, pp 87-100 (1988)
- [97] B F Levine, 'Quantum-well infrared detectors', *J Appl Phys*, vol 74(8), pp R1-R81 (1993)
- [98] A Rogalski and K Joswikowski, 'GaAs/AlGaAs quantum well infrared photoconductors versus HgCdTe photodiodes for long-wavelength infrared applications', *Optical Engineering*, vol 33(5), pp 1477-1484 (1994)
- [99] S R Kurtz, L R Dawson, T E Zipperian and R D Whaley Jr, 'High detectivity ($>1 \times 10^{10} \text{cm-Hz/W}$) InAsSb strained-layer superlattice, photovoltaic infrared detector', *IEEE Electron Device Letters*, vol EDL-11(1), pp 54-56 (1990)
- [100] C G Bethea and B F Levine, 'Infrared imaging using a 128 x 128 pixel array of GaAs/Al_xGa_{1-x}As quantum well infrared photodetectors', in Infrared Detectors. State of the Art, *Proc SPIE*, vol 1735, pp 198-203 (1992)
- [101] L J Kozlowski, G M Williams, G J Sullivan, C W Farley, R J Anderson, J Chen, D T Cheung, W E Tennant and R E DeWames, 'LWIR 128x128 GaAs/AlGaAs multiple quantum well hybrid focal plane array', *IEEE Trans on Electron Devices*, vol ED-38(5), pp 1124-1130 (1991)
- [102] S I Borenstein, U Arad, A Afanasyev, I Luybina and A Segal, 'Processing and characterization of a 128x128 GaAs/GaAlAs quantum well infrared detector array', *Proc SPIE*, vol 2554, pp 159-166 (1995)
- [103] W A Beck, T S Faska, J W Little, J Albritton and M Sensiper, 'LWIR imaging performance of 256 x 256 miniband transport multiple quantum well infrared focal plane arrays', *Proc SPIE*, vol 2225, pp 130-138 (1994)

- [104] G Milne and C Gooden, 'Advanced multiple quantum well staring focal plane array status and performance', presented at the 2nd NATO/IRIS Joint Symposium, London 25-28 June 1996
- [105] S D Gunapala, J K Liu, J S Park, M Sundaram, C C Scott, E Hoelter, T-L Lin, S T Massie, P D Baker, R E Muller and G Sarusi, '9-mm cutoff 256x256 GaAs/Al_xGa_{1-x}As quantum well infrared photodetector hand-held camera', *IEEE Trans Electron Devices*, vol 44(1), pp51-57 (1997)
- [106] in *Compound Semiconductor*, July/Aug 1995
- [107] Ph Bois, E Costard, J Y Duboz, J Nagle, E Rosender and B Vinter, 'Optimised multi quantum well infrared detectors', in *Infrared Technology XXI, Proc SPIE*, vol 2552, pp 755-766 (1995)
- [108] M A Kinch and A Yariv, 'Performance limitations of GaAs/AlGaAs infrared superlattices', *Appl Phys Lett*, vol 55(20), pp 2093-2095 (1989)
- [109] S R Andrews and B A Miller, 'Experimental and theoretical studies of the performance of quantum-well infrared detectors', *J Appl Phys*, vol 70(2), pp 993-1003 (1991)
- [110] R E DeWames, J M Arias, L J Koslowski and G M Williams, 'An assessment of HgCdTe and GaAs/GaAlAs technologies for LWIR infrared imagers', in *Infrared Detectors. State of the Art, Proc SPIE*, vol 1735, pp 2-16 (1992)
- [111] A Rogalski, 'GaAs/AlGaAs quantum well infrared photoconductors versus HgCdTe photodiodes for long-wavelength infrared applications', *Proc SPIE*, vol 2225, pp 118-129 (1994)
- [112] E Pelvé, F Beltran, C G Bethea, B F Levine, V O Shen, S J Hsieh and R R Abbott, 'Analysis of the dark current in doped-well multiple quantum well AlGaAs infrared photodetectors', *J Appl Phys*, vol 66(11), pp 5656-5658 (1989)
- [113] B F Levine, C G Bethea, G Hasnain, V O Shen, E Pelvé, R R Abbott and S J Hsieh, 'High sensitivity low dark current 10 μ m GaAs quantum well infrared photodetectors', *Appl Phys Lett*, vol 56(9), 851-853 (1990)
- [114] M Rosenbluth, M O'Loughlin, W Boss, F DeLuccia, H Kanter, B Janousek, E Perry and M Daugherty, 'Long wavelength GaAs quantum well IR detectors low-temperature performance characteristics', in *quantum-well and superlattice Physics III, Proc SPIE*, vol 1283, 82-91 (1990)
- [115] C S Wu, C P Wen, R N Sato and M Hu, 'Low dark current photovoltaic multiquantum well long wavelength infrared detectors', Proc NASA/JPL workshop on innovative long wavelength infrared detectors, Pasadena CA, 1990, 263-274 (1990)

- [116] B K Janousek, M L Rosenbluth, M J O'Loughlin, W L Bloss, F J De Luccia, H Kanter, L E Perry and M J Daugherty, 'Characteristics of AlGaAs/GaAs multiple quantum well infrared detectors', Proc NASA/JPL workshop on innovative long wavelength infrared detectors, Pasadena CA, 243-255 (1990)
- [117] H C Liu, "The Basic Physics of Quantum Well Infrared Detectors", in Long Wavelength Infrared Detectors, ed M Razeghi, ch 1 (Gordon Breach, PA, 1995)
- [118] Y Rajakarunanayake and T C McGill, 'Intersubband absorption in Si_{1-x}Ge_x/Si superlattices for long wavelength infrared detectors', Proc NASA/JPL workshop on innovative long wavelength infrared detectors, Pasadena CA, pp 305-321 (1990)
- [119] R J Hauenstein, R H Miles and M H Young, 'Possibilities for LWIR detectors using MBE-grown Si/Si_{1-x}Ge_x structures', Proc NASA/JPL workshop on innovative long wavelength infrared detectors, Pasadena CA, pp 323-337 (1990)
- [120] R P Gamani Karunasiri, J S Park, K L Wang and S K Chun, 'Infrared hotodetectors with SiGe/Si multiple quantum wells', *Optical Engineering*, vol 33(5), pp 1468-1476 (1994)
- [121] M J Kearney, 'The physics and device applications of epitaxially grown Si and Si_{1-x}Ge_x heterostructures', *GEC J Of Research*, vol 10(3), pp 158-165 (1993)
- [122] D Robbins, R Carline and M Stanaway, 'A novel resonant SiGe/Si quantum well detector for LWIR imaging' presented at the NATO/IRIS conference, London, 25-28 June 1996
- [123] J Maserjian, F J Grunthner and C T Elliott, 'LWIR detector arrays based on nipi superlattices', *Infrared Physics*, vol 30(1), pp 27-32 (1990)
- [124] H Yagi, N Yutani, J Nakanishi, M Kimata, M Nunoshita, T Seto and M Kamei, 'Monolithic Schottky-barrier infrared image sensor with 71% fill factor', *Optical Engineering*, vol 33(5), pp 1454-1451 (1994)
- [125] T S Villani, B J Esposito, T J Petcher, D J Sauer, P A Levine, F V Shallcross, G M Meray and J R Tower, 'Performance of generation III 640 x 480 PtSi array', *Proc SPIE*, vol 2225, pp 2-10 (1994)
- [126] A Akiyama, T Sasaki, T Seto, A Mori, R Ishigaki, S Itoh, N Yutani, M Kimata and N Tubouchi, '1040 x 1040 infrared charge sweep device imager with PtSi Schottky barrier detectors' *Optical Engineering*, vol 33(1), pp 64-71 (1994)
- [127] W Cabanski, R Koch, H Maier, J Wendler and J Ziegler, 'Development of hybrid PtSi focal plane arrays', *Proc SPIE*, vol 2225, pp 323-334 (1994)

- [128] W Cabanski, R Koch, H Maier, J Wendler and J Ziegler, K Hoffmann, K Eberhardt, P Diemel, U Prechtel and K Kapser, 'AEG PtSi modules a summary' *Proc SPIE*, vol 2746, pp 256-267 (1996)
- [129] T L Lin, J S Park, S D Gunapala, E W Jones and H M Del Castillo, 'Doping-spike PtSi Schottky infrared detectors with extended cutoff wavelengths', *IEEE Trans on Electron Devices*, vol 42(7), pp 1216-1219 (1995)
- [130] S Tohyama, N Teranishi, K Konuma, M Nishimura, K Arai and E Oda, 'A new concept silicon homojunction infrared sensor', *IEEE Trans on Electron Devices*, vol 38(5), pp 1136-1140 (1991)
- [131] B Y Tsaor, C K Chen and S A Marino, 'Heterojunction GexSi1-x/Si infrared detectors and focal plane arrays' *Optical Engineering*, vol 33(1), pp 72-78 (1994)
- [132] J S Park, T L Lin, E W Jones, H M Del Castillo, T George and S D Gunapala, 'Long-wavelength stacked Si1-xGex/Si heterojunction internal photoemission infrared detectors, in *Infrared Technology XIX*, *Proc SPIE*, vol 2020, pp 12-21 (1993)
- [133] J Maserjian, 'New heterojunction LWIR detector options', Proc NASA/JPL workshop on innovative long wave infrared detectors, Pasadena CA, April 1990, pp 291-301 (1990)
- [134] J S Park, T L Lin, E W Jones, S D Gunapala, G A Soli and B A Wison, 'Proton irradiation effects on strained Si1-xGex/Si heterostructures', *Applied Physics Letters*, vol 63(25), pp 3497-3499 (1993)
- [135] T N Krabach, C Staller, S Dejewski, T Cunningham, M Herring and E R Fossum, 'InGaAs detectors for miniature infrared instruments', *Proc SPIE*, vol 1874, pp 214-223 (1993)
- [136] R McKee, D Lampe, J Halvis, T Henricks, T Wison, K Linga and M Lange, 'Near room temperature performance of a SWIR InGaAs/Si hybrid 96 element x 25 TDI high performance FPA', *Proc SPIE*, vol 2746, pp 152-161 (1996)
- [137] D-S Kim, S R Forrest, M J Lange, G H Olsen and W Kosonocky, 'A monolithically integrated InGaAs-InP p-i-n/JFET focal plane array', *IEEE Photonics Technology Letters*, vol 8(4), pp 566-568 (1996)
- [138] X Hugon, O Amore, S Cortial, C Lenoble and M Villard, 'Near-room temperature SWIR InGaAs detectors in progress' *Proc SPIE*, vol 2552, pp 738-747 (1995)
- [139] X Hugon, O Amore, S Cortial, C Lenoble and M Villard, 'Near-room operating temperature SWIR InGaAs detectors in progress', *Proc SPIE*, vol 2552, pp 738-747 (1995)
- [140] H Zogg, A Fach, C Maissen, J Masek and S Blunier, 'Photovoltaic lead-chalcogenide on silicon infrared sensor arrays', *Optical Engineering*, vol 35(5), pp 1440-1449 (1994)

- [141] D K Schroder, 'Extrinsic silicon focal plane arrays', in *charge-coupled devices*, D F Barbe (Ed), 57-90, (Springer-Verlag, 1980)
- [142] G A Walter and E L Dereniak, 'Photodetectors for focal plane arrays Part 1 Extrinsic silicon' *Laser Focus/Electro-Optics*, pp 108-118, (March 1986)
- [143] J Von der Ohe, J Siebeneck and U Suckow, 'Thermal imaging using silicon', in *Infrared Technology XIV*, *Proc SPIE*, vol 972, pp 314-319 (1988)
- [144] C Lucas, I Bischoff, G Chamming's, M Ravetto F Rothan, M Vilain, P Galdemard, R Jouan, P-O Lagage and P Masse, 'Development of gallium-doped silicon 128 x 192 element arrays for 8-14 μm observation', *Proc SPIE*, vol 2475, pp 50-55 (1995)
- [145] F Szmulowicz and F L Madarz, 'Blocked impurity band detectors - an analytical model figures of merit', *J Appl Phys*, vol 62(6), pp 2533-2540 (1987)
- [146] B G Martin, 'Theory of injected current behaviour associated with blocked impurity-band-conduction', *Solid-State Electronics*, vol 33(4), pp 427-433 (1990)
- [147] D B Reynolds, D H Seib, S B Stetson, T Herter, N Rowlands and J Schoenwald, 'Blocked impurity band hybrid infrared focal plane arrays for astronomy', *IEEE Trans on Nuclear Science*, vol NS-36(1), pp 857-862 (1989)
- [148] T M Krabach, J E Huffman and D M Watson, 'Extrinsic germanium blocked impurity band detectors', *Proc Third Infrared Detector Workshop*, NASA-Ames Research Centre, February 7-9, 1989, NASA Technical Memorandum 102209, pp 117-123 (October 1989)
- [149] M G Stapelbroek, D H Seib, J E Huffman and R A Florence, 'Large-format blocked-impurity-band focal plane arrays for long wavelength astronomy', *Proc SPIE*, vol 2475, pp 41-48 (1995)
- [150] J Venzon, N Lum, S Freeman and G Domingo, 'High-background, longwave IR focal plane array development using Si As IBC detectors', *Proc SPIE*, vol 2475, pp 34-40 (1995)
- [151] J Wolf, L Wiest, U Grozinger, D Lemke and J Schubert, 'SiAs blocked-impurity-band detectors for ISO's photometer' *Proc SPIE*, vol 2553, pp 482-488 (1995)
- [152] D M Watson, 'Extrinsic germanium blocked-impurity-band detector arrays', *Proc SPIE*, vol 1874, pp 256-265 (1993)
- [153] S Eikenberry, G G Fazio and S Ransom, 'An SSPM-based high speed infrared photometer', *Proc SPIE*, vol 2475, pp 210-220 (1995)
- [154] P W Kruse, 'Physics and applications of high - T_c superconductors for infrared detectors', *Semicond Sci Technol*, vol 5, pp S229-S239 (1990)

- [155] B R Johnson, M C Foote and H A Marsh, 'High performance linear arrays of YBa₂Cu₃O₇ superconducting infrared microbolometers on silicon', *Proc SPIE*, vol 2475, pp 56-61 (1995)
- [156] N Bluzer and M G Forrester, 'Superconducting quantum detectors', *Optical Engineering*, vol 33(3), pp 697-703 (1994)
- [157] C Marshall, N Butler, R Blackwell, R Murphy and T Breen, 'Uncooled infrared sensor with digital focal plane array', *Proc SPIE*, vol 2746, pp 23-31 (1996)
- [158] R Owen, J Belcher, H Beratan and S Frank, 'Producibility advances in hybrid uncooled infrared devices - II', *Proc SPIE*, vol 2746, pp 101-112 (1996)
- [159] R Watton, P N J Dennis, J. P Gillham, P A Manning, M C J Perkins and M A Todd, 'IR bolometer arrays, the route to uncooled, affordable thermal imaging', *Proc SPIE*, vol 2020, pp 379-390 (1993)
- [160] J-L Courtures, R Lemaitre, E Pourquier and G Boucharlat, 'Uncooled infrared monolithic imaging sensor using pyroelectric polymer', *Proc SPIE*, vol 2552, pp 748-754 (1995)
- [161] E R Fossum and B Pain, 'Infrared readout electronics for space science sensors state-of-the-art and future directions', *Proc SPIE*, Vol 2020, pp 262-285 (1993)
- [162] N Bluzer and A S Jensen, 'Current readout of infrared detectors', *Optical Engineering*, Vol 26(3), pp 241-248 (1987)
- [163] L J Kozlowski, W V McLevige, S A Cabelli, A H B Vanderwyck, D E Cooper, E R. Blazejewski, K Vural and W E Tennant, 'Attainment of high sensitivity at elevated operating temperatures with staring hybrid HgCdTe-on-Sapphire focal plane arrays', *Optical Engineering*, Vol 33(3), pp 704-715 (1994)
- [164] L J Kozlowski, 'Low noise capacitive transimpedance amplifier performance vs alternative IR detector interface schemes in submicron CMOS', *Proc SPIE*, Vol 2745, pp 2-11 (1996)
- [165] J-I Song, D V Rossi and E R Fossum, 'GaAs CCD readout for engineered bandgap detectors', in *Infrared detectors and focal plane arrays*, *Proc SPIE*, vol 1308, pp 254-260 (1990)
- [166] E R. Fossum, J-I Song and D V Rossi, 'Two-dimensional electron gas charge-coupled devices (2DEG-CCD's)', *IEEE Trans on Electron Devices*, vol ED-38(5), pp 1182-1192 (1991)
- [167] N A Doudoumopoulos, 'GaAs readout development for IR FPAs', Presented at the 1990 IEEE Workshop on Advanced Solid-State Imagers, Harriman, New York, May 18-20 (1990)

2 BASIC MECHANISMS

In this chapter we review the basic mechanisms of radiation damage in electronic devices and comment on their importance for the detector types discussed in chapter 1. General comparisons between detector materials technologies will also be made.

Because of the dominant use of silicon devices in present day electronics, most of the work on radiation damage centres on the Si/SiO₂ system and basic mechanisms in other materials are not so well understood. Hence this section will be grounded on the fundamentals of radiation effects on MOS devices with extensions to IR materials where appropriate.

The three basic effects which occur when radiation strikes an imaging detector are

- transient effects
- ionization damage, and
- displacement damage

With charged particles, ionization (i.e. generation of electron-hole pairs) occurs all along the particle track by way of Coulomb interactions with outer shell electrons, and with x-rays or gammas it is produced in a small cloud around the initial absorption event (which occurs via the photoelectric effect, pair production or Compton scattering - depending on the material and the photon energy).

In the insulating dielectric layers the generated carriers can become trapped so as to impart a fixed charge to the layer (which produces a shift in flatband voltage). The generation of electron-hole pairs in the gate dielectric or passivation also leads, by a complex process of transport, bond breaking and trapping, to the generation of trapping states at the interface. These interface traps can communicate with the active detector material and cause generation of thermal dark current (i.e. surface leakage) and trapping of minority carriers if they happen to come into contact with the surface (e.g. in a surface channel device or a buried channel CCD near saturation). Trapped charge at the interface can also add a component to the flatband voltage shift. In the bulk of the detector the electron-hole pairs will be transported by drift or diffusion and be readout as transient (i.e. spurious) signal charge.

Thus the ionization produces permanent damage in the insulating layers (known as total ionizing dose, or TID, effects) and transient (prompt) charge production in the detector material. In addition, extrinsic detectors can suffer from changes in responsivity (increases or decreases) as a result of trapping of the ionization-generated charges at the optically active sites. The effects are quasi permanent and can last for long periods (minutes or hours, depending on operating conditions).

The third effect is the displacement of atoms in the bulk of the detector by collision with bombarding particles. This gives rise to defect states part way between the valence and conduction bands and can lead to a variety of effects such as dark current generation, compensation, minority carrier trapping or trap assisted tunneling. Note that energetic photons (such as Co60 gamma rays) can also result in small amounts of displacement damage via the production of high energy Compton electrons which can collide with lattice atoms.

Useful general reviews of radiation effects on IR detectors have been given in two papers by Arne Kalma [1],[2]

2.1 TRANSIENT EFFECTS

2.1.1 Transient Effects in Imaging Detectors

Transient radiation effects are those which occur during the exposure to the radiation, and which decay away on a relatively rapid time scale (usually \ll one second) after the exposure or particle hit ceases. As discussed above they typically result from ionization which produces electron-hole pairs in the semiconductor.

An important response in infrared detectors is produced by exposure to low dose rate but long term ('steady state' or persistent) fluxes of ionizing particles (electrons, protons, gamma rays) as occur in space. The large size of imaging detectors, which is mandated by the required optical absorption depth and the required optical area, means that the ionizing particles travel long distances in the detectors and therefore create significant amounts of spurious charge. In fact, pulses are sometimes large enough to completely mask any optical signal that is present. The number of electron hole pairs produced varies as

$$n_{\text{pairs}} = \frac{E_{\text{deposited}}}{\Delta E} \quad (2-1)$$

where ΔE is the energy needed to create an electron hole pair (or, more correctly, the amount of energy that is given up in the process of generating an electron-hole pair). Klein [3] has given the following semi-empirical formula

$$\Delta E = (14/5) E_g + r(h\nu_R), \text{ where } 0.5 \leq r(h\nu_R) \leq 1.0 \text{ eV} \quad (2-2)$$

In this expression $r(h\nu_R)$ is the energy lost to optical phonons (Raman quanta) and for many materials is in the range 0.5 to 1.0 eV. The remaining energy which is lost ($= 9/5 E_g$) is the residual kinetic energy of carriers which have an energy below the threshold for impact ionization. This ends up as lattice vibrations (i.e. heat). Note that in deriving equation (2-2), Klein made several assumptions, in particular that the bands are parabolic and that electrons and holes behave in the same way. These assumptions may not hold for all semiconductors, however it appears to be approximately correct in many cases. Figure 2.1-1 shows data taken from [3]. The table below lists values of ΔE for several materials of interest for IR sensors and predictions for LWIR and MWIR MCT (bandgap 0.12 and 0.19 eV) assuming (2-2) with $r(h\nu_R) = 0.75$.

Material	Bandgap (eV)	ΔE (eV)
InSb	0.24	1.1
Ge	0.66	2.9
InGaAs	0.73	3.2
Si	1.12	3.6
GaAs	1.42	4.6
MWIR MCT	0.19	1.3*
LWIR MCT	0.12	1.1*

* = predicted from (2-2)

For silicon the energy loss (dE/dx) is such that the charge deposited per micron of particle track is $80/\beta^2$ e-h pairs/ μm [4], where $\beta = v/c$, v = particle velocity. Thus for a minimum ionising particle ($\beta \sim 1$) we have 80 e-h pairs per micron, or typical signals of 2000 electrons for a $25\mu\text{m}$ thick detector. This e-h pair production rate will also hold for extrinsic Si X detectors and Si X BIB arrays. In this connection there has been some discussion as to whether ionising radiation can generate impurity band carriers in BIB detectors as well as the intrinsic carriers. However an upper limit of 10% has been determined [5] for the ratio of impurity band holes to valance band holes in an Si As BIB detector. Hence the carrier generation rate should be approximately as for intrinsic silicon.

In narrow bandgap (~ 0.1 eV) LWIR MCT detectors, we expect the signal generated per unit track length to be a factor ~ 3 greater than in silicon. However there is very little quantitative information available in the literature. A previous study by the author [6] on a 256×4 G-MIRL LWIR MCT array employed a proton flux of $\sim 10^7$ protons/ cm^2/s so that with a stare time of ~ 10 μs and a pixel size of $\sim 30 \mu\text{m} \times 30 \mu\text{m}$, the expected event rate was $\sim 10^3/\text{pixel}/\text{s}$. No transient signals were found. This is probably because the gain of the measurement system was too low (the smallest resolvable signal change being ~ 10 mV or 2×10^5 electrons), but it does indicate that transient effects may not be important for many applications. For 10 MeV protons we expect an energy loss of roughly 15 keV/ μm (from simulations using the TRIM code [7]). For a notional diode depth of 10 μm we then get an expected average signal of $\sim 1 \times 10^5$ electrons per proton. Note that it is possible that some recombination takes place in the HgCdTe. Williams et al [8] have pointed out that the carrier density within the core of a track is likely to be comparable or higher than the doping density and Auger recombination is likely to take place. Further measurements are discussed in chapter 11.

A value of 1737 e-h pairs/ μm has been reported for minimum ionising particles in InSb (bandgap 0.24 eV) [9]. For protons of a few tens of MeV, dE/dx is about 2 keV/ μm , so for a $20 \mu\text{m}$ thick detector we expect signals of $\sim 4 \times 10^4$ electrons. This is in agreement with the SIRTf results given in section 9.2.1.

In calculating the magnitude of transient signals it should be mentioned that the energy deposited (dE/dx) for thin ($\sim 20\mu\text{m}$) slabs of material is slightly less than for a bulk detector. This is because some of the energy goes into long range delta rays (electrons) which can escape from a thin target. Thus the dE/dx for silicon, as calculated from codes such as TRIM [6] would give a value of ~ 100 e-h pairs/ μm for a minimum ionizing particle rather than 80 e-h pairs as given above. The calculation of energy losses in thin detectors has been recently considered by Bischel [10]. These processes are statistical in nature and even for a given fixed track length there will be a distribution of pulse heights (basically the Landau distribution but somewhat broadened).

The variations in the amount of charge deposited in each pixel arise primarily because, in a space environment, there is a large spread in the energy of the incident particles (predominantly protons). However, even in the case of ground based testing with monoenergetic protons, one would expect to observe fluctuations in the amount of charge deposited in a pixel by incident particles. A general theoretical treatment based on the work of Kellerer [11], together with experimental verification has been given by Burke et al [12]. This work treats the case of gamma ray interactions with CCDs, but as the authors point out, the basic principles also apply to charged particle-induced transients. The three basic factors contributing to variations in transient signal size for monoenergetic protons are

- i) A detector in an omnidirectional environment will experience a variety of track lengths. Track length distributions have been given for rectangular parallelepiped geometries by Vickers et al [13] and Bradford [14] (with typographical corrections as given by Ziegler and Landford [15]). Langworthy [16] has discussed the extension to the more realistic case of active volumes with rounded corners. Whatever theory is used, the root mean square variation in track length is comparable with the average value (which, for a convex volume, is given by $4 \times$ the volume divided by the surface area). So within a particular pixel of dimensions $20 \mu\text{m} \times 20 \mu\text{m} \times 20 \mu\text{m}$ we can expect fluctuations in track length of order $10 \mu\text{m}$.
- ii) For those parts of the track which are deep within the active layer of the detector, there will also be lateral spreading (to adjacent pixels) because of charge diffusion.
- iii) There is a spread in the energy lost by an ion (an effect known as energy loss straggling). In addition, some of the energy is carried outside of the sensitive volume by long range secondary electrons. For example, Xapsos [17] estimates that for the case of 100 MeV protons incident on a sensitive volume with an average path length of $\sim 10 \mu\text{m}$, the fluctuations in energy loss will be comparable with the mean energy loss and that 10 % of the energy will be carried away by long range electrons. However these estimates would be difficult to corroborate in laboratory measurements on CCDs because the sensitive volumes are not precisely known and diffusion effects are difficult to model with great accuracy.

In a space environment, the effects of variations in the proton energy and path length are by far the most important.

That models (such as discussed by Pickel and Petroff [18]) used to predict pulse height spectra for IR detectors can give reasonable agreement with in-orbit results was confirmed in an early paper by Holman et al [19].

Pulse height spectra for a MCT detector subjected to Co60 gammas are shown in figures 2 1-2 a) [2] and b) [20]. The latter figure shows the reduced pulse heights obtainable with a thin detector. Figure 2 1-3 [2] shows the relative gamma-induced noise for different IR detector types versus thickness. The three lines reflect the changes in bandgap (and hence e-h creation energy) for the different materials and the thickness (determined by absorption coefficients) for the different technologies are shown. For example superlattice (SL) detectors have thin layers and are relatively hard to transient radiation. Extrinsic detectors are also good (because of the high bandgap) but unless BIB detectors are used the detector thicknesses will be large (conventional extrinsic arrays with $t \sim 500 \mu\text{m}$ are off the scale of the graph). It is often said that the relatively small thickness of BIB and SL detectors makes them hard to radiation, in fact, this hardness only relates to transient radiation. Hardness to total dose depends on the technological processes used for insulating and passivation layers (including in the multiplexer). As it happens, BIB detectors can be made relatively radiation hard to total dose also (there are no insulating layers in the detector itself).

The radiation induced noise in effect reduces the detectivity, D^* , of the sensor and figure 2 1-4 shows relative D^* values.

Finally we note that it is often possible to circumvent the effects of transient radiation by appropriate image processing. In a space application this would probably have to be done on-

board in real time. However there is a large body of work on the subject (particularly for gamma circumvention) and real time processors have been developed (sometimes based on custom designed CCD architectures). Two papers [21], [22] illustrate the use of image processing algorithms to remove transient spikes. The Intrinsic Event Discrimination (IED) detector, based on the BIB device, has also been developed for gamma circumvention (cf section 1.4.6.1).

In summary we can say that, particularly for small bandgap materials and relatively thick detectors, the transient signals from radiation hits can be comparable with those from the imaged scene. Hence unless circumvention software/circuits are efficiently used, high signal to noise observations in low earth orbit are restricted to the quiet periods intervening between passages through the SAA and polar regions. Detailed modelling of pulse height distributions is possible knowing the detector geometry but experimental data for IR detectors in the space environment (or for bombardment by particle beams) is not readily available.

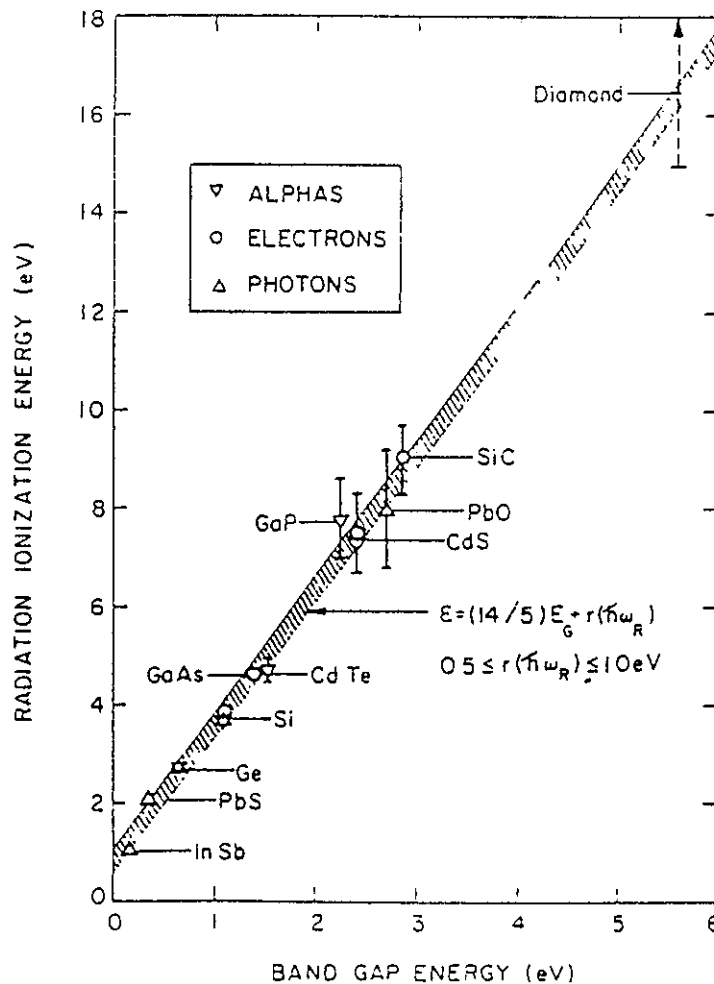


Figure 2.1-1 values of the energy lost per e-h pair created for several semiconductors (after Klein [3])

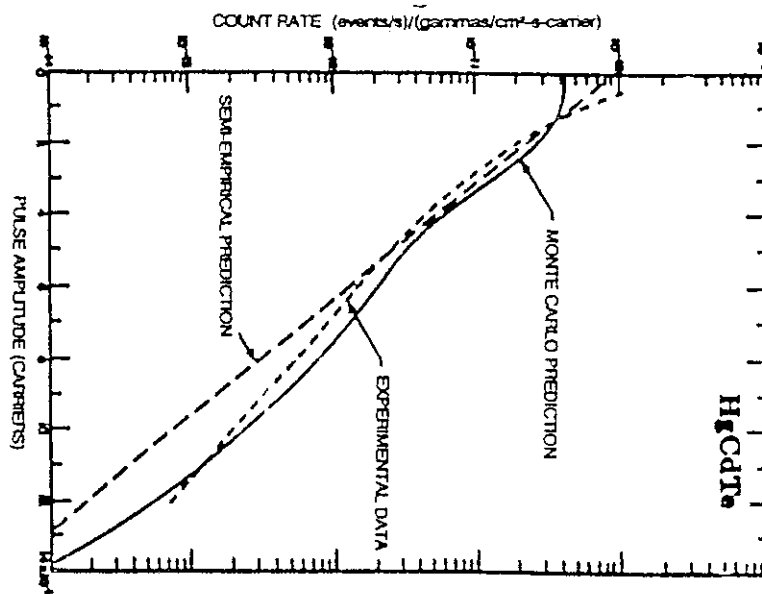


Figure 2 1-2 a) Experimental and predicted Co-60 pulse height spectra for a MCT detector [2]

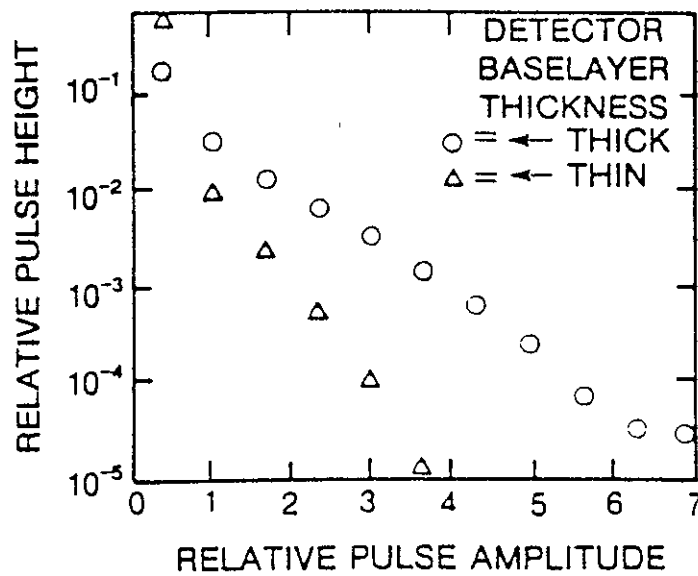


Figure 2 1 2 b) Experimental Co-60 pulse height spectra for thick and thin MCT detectors [19]

2.2 IONIZATION DAMAGE

This section will start with a general consideration of effects in MOS devices and then will briefly consider other materials. Effects on special low temperature oxides (as used in multiplexers for hybrid focal plane arrays) are discussed further in chapter 8.

2.2.1 Ionization Effects on MOS Devices

Many excellent reviews are available on effects in MOS devices, [23], [24], [25], [26], [27]. Ionization damage results in hole trapping in the oxide and the creation of interface traps.

The primary effect of hole trapping in microcircuits is to cause a negative shift in threshold voltage. A positive gate voltage during irradiation produces the largest threshold shift. In n-channel devices which have a positive threshold voltage initially, the radiation-induced shift can cause a normally "off" device to be "on" at zero volts (V_T near zero or V_{TNZ} effect). The positive charge can also invert p-type isolation regions and cause leakage currents between adjacent devices for certain process technologies. As with hole trapping, interface trap generation from ionizing radiation is quite process-dependent. The radiation-induced interface traps act as acceptors in the upper half of the silicon band gap and donors in the lower half. When the surface potential is at the centre of the band gap, the net charge of the interface traps is near zero. The effect of the interface traps is to cause a net negative charge in n-channel MOS transistors (MOSFETs) and a net positive charge in p-channel transistors. Thus, in n-channel MOSFETs the interface traps act to offset the effect of the trapped holes, whereas in p-channel MOSFETs, the effects add. This results in complex failure modes in complementary MOS (CMOS) microcircuits which utilize both n- and p-channel devices.

The fraction of the generated charge that is permanently trapped (F) is very dependent on the actual processing steps performed during the manufacture of the devices, including the oxidation environment, the oxide growth and anneal temperature, post-oxidation thermal cycles, and the metallization process. To date, it has not been possible to predict F even when all process details are known, so F is an experimentally determined parameter for a given process.

The threshold voltage shift has a strong dependence on oxide thickness. Thus thin gate oxides are harder. With process improvements (low F and low interface trap build up) thin radiation hard oxides can be tolerant to several Mrad (at room temperature) and in such cases it is often found that leakage currents in thick field oxides or isolation oxides around the MOSFET are the major source of failure.

The other effect of interface traps is to act as energy levels within the silicon bandgap. Whatever their cause (intrinsic defects, ionization damage or bulk displacement damage) such states can give rise to five basic effects as shown in figure 2 2-1 [24].

- i) generation of e-h pairs
- ii) recombination of e-h pairs
- iii) trapping of carriers
- iv) compensation of donors or acceptors
- and v) tunneling of carriers

A given level can manifest any of the above effects depending on the temperature, carrier concentration and the location in which it resides (e.g. in a depletion region).

i) Generation

This is the thermal generation of electron-hole pairs through a level near midgap. This process can be viewed as the thermal excitation of a bound valence-band electron to the defect centre and the subsequent excitation of that electron to the conduction band, thereby generating a free electron-hole pair. Alternatively, it can be seen as hole emission from the centre followed by electron emission. Only centres with an energy level near midgap make a significant contribution to carrier generation, an exponential decrease in generation rate occurs as the energy level position is moved from midgap. Note that the emission processes only dominate over capture processes (recombination) when the free-carrier concentrations are significantly less than their thermal equilibrium values. Thus, thermal generation of electron-hole pairs through radiation-induced defect centres near midgap is important only in device depletion regions or at a depleted surface. Introduction of such centres is one of the main mechanisms for leakage current increases in devices and, in particular, for surface dark current increases in IR and visible detector arrays.

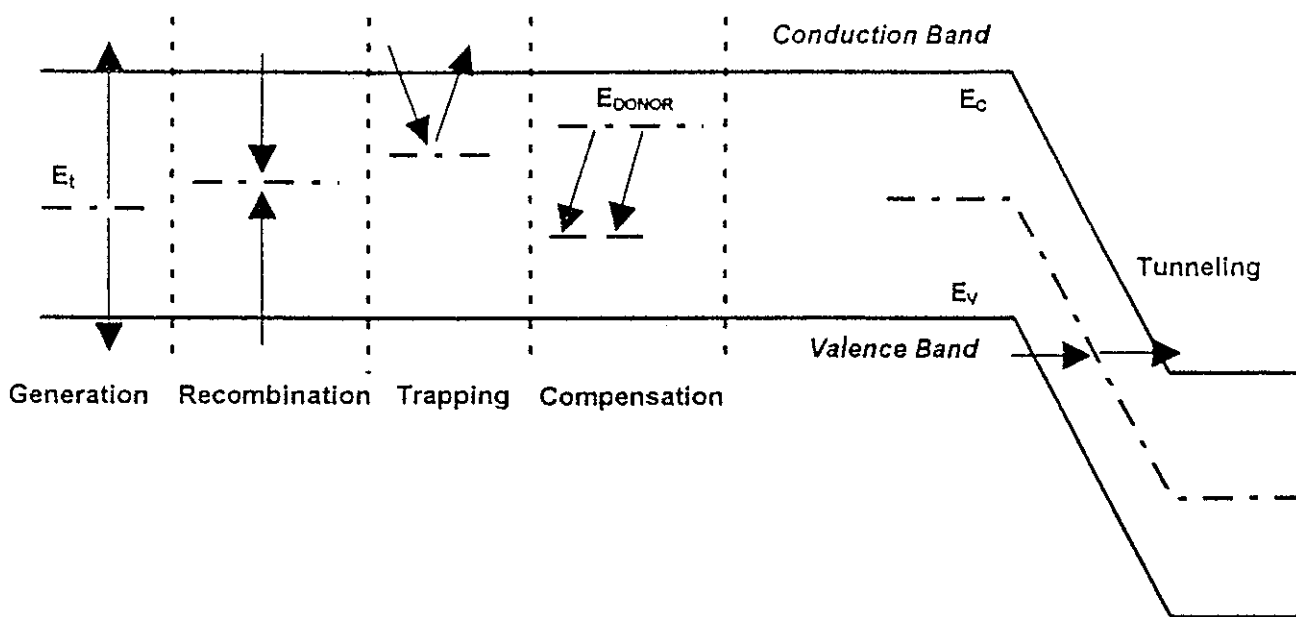


Figure 2 2-1 Illustration of effects due to defect centres in the bandgap of a semiconductor

ii) Recombination

In this process a free carrier of one sign is first captured at the defect centre. This is then followed by capture of a carrier of the opposite sign. Thus recombination removes electron-hole pairs, as opposed to the generation process which creates them. In general, the recombination rate depends on the defect centre density, the free carrier concentration, the electron and hole capture cross-sections, and the energy level position. The mean time a minority carrier spends in its band before recombining is referred to as the recombination lifetime. Radiation-induced recombination centres cause this lifetime to decrease, this is the dominant mechanism for gain degradation in bipolar transistors.

iii) Trapping

Is the temporary trapping of carriers, typically at a shallow level. In this process, a carrier is captured at a defect centre and is later emitted to its band, with no recombination event taking place. In general, trapping of both majority and minority carriers can occur (at separate levels). The presence of radiation-induced traps, will reduce CCD charge transfer efficiency.

iv) *Compensation*

This process is the compensation of donors or acceptors by radiation-induced centres. In the example shown in Figure 2.2-6, some of the free electrons available from the donor level are compensated by deep-lying radiation-induced acceptors. The result is a reduction in the equilibrium majority-carrier concentration. This 'carrier removal' process will cause an alteration in any device or circuit property that depends on carrier concentration. For example, the resistance of the collector in bipolar transistors will increase due to carrier removal, and the compensation effect also alters the sensitivity of extrinsic silicon detectors.

v) *Tunneling*

This process is the tunneling of carriers through a potential barrier by means of defect levels. The defect-assisted (or trap-assisted) tunneling process can cause device currents to increase in certain situations. For example, there may be a defect-assisted tunneling component of the reverse current in a p-n junction diode or MIS capacitor. Trap-assisted tunneling is particularly important for low bandgap materials and can be the dominant source of dark current for detector materials such as MCT at low temperatures (as discussed in section 5).

2.2.2 Dose enhancement

Dose enhancement (sometimes called interface dose enhancement) occurs near the interface of materials with differing atomic numbers that are irradiated with energetic photons (x-rays or gamma rays). The interactions with the target materials produce energetic free electrons. These electrons then lose energy and give rise to secondary electrons of various energies. The range of maximum energy electrons produced in both materials define distances on either side of the interface over which electrons lose energy and reach equilibrium. For distances from the interface that are greater than the maximum electron range, electron equilibrium exists, and no dose enhancement occurs. A dose gradient will occur in the transition zone near the interface. This gradient is due to differences in the electron production and transport properties of the two materials. That is, more electrons enter a given volume than leave it. Dose enhancement effects in an integrated circuit are greatest for x-ray energies ~ 100 keV and for large changes in density across the interface (e.g. Au on Si). They must be taken into account when using, say, a 10 keV x-ray source to simulate the space ionizing radiation environment, but for Co60 testing dose enhancement is of little importance (particularly for photodetectors, where the interfaces do not involve large changes in density).

2.2.3 Process dependence

It has already been stated that ionizing effects on MOS devices depend strongly on the manufacturing processes. The situation is complicated since the fabrication of a device (e.g. a CMOS integrated circuit) may involve as many as 300 separate steps (e.g. process such as cleans, oxidations, implants, diffusions, depositions, photolithographic patterning and etches). The precise details of any of these steps can have an effect on the radiation hardness (either in their own right or by interaction with the other steps in the process flow). To cope with this complexity, guidelines and 'recipes' have been developed by manufacturers over the years, many of which are proprietary.

The process dependence does mean that device response can vary from batch to batch (even wafer to wafer) and certainly from manufacturer to manufacturer. This implies that quality procedures are needed to control the traceability of devices for military and space use, particularly as a vendor can sometimes have a given part manufactured at a number of different fabrication facilities. It is usually the case that radiation tests will be performed by or for the customer as part of the lot acceptance process for each device procurement.

2.2.4 Post irradiation effects (PIE) or time dependent effects

Because of effects such as trapped hole annealing and build up of interface traps many of the changes in device performance can occur after irradiation has ceased - and certainly they will be dependent on the rate at which dose is absorbed. Testing of components therefore has to take into account such effects and procedures such as high temperature baking (e.g. at 100°C) are used to accelerate the annealing.

At the low temperatures encountered when operating IR focal plane arrays, many of the processes occurring in radiation damaged insulators will be slowed down (cf. the following section, 2.2.5) but time dependent effects (and dose rate) can still be important.

2.2.5 Effects at low temperatures

In MOS structures used at temperatures below about 120K the radiation-generated holes are effectively immobile and become trapped near to their point of creation. This tends to produce a large fixed charge in the oxide (or passivation) and large threshold shifts (and also to insert p-type surface regions and cause leakage paths on thick isolation oxides). The holes are not trapped at defect sites in the oxides, as for long-term hole trapping observed at room temperature, but are self-trapped (by interaction of the hole with the lattice to form a polarized state or polaron). Since the trapping sites tend to be intrinsic to the insulator they cannot be eliminated by processing. Thus even an oxide which is hard at room temperature may show a large threshold voltage shift when irradiated at 77K. A recently reported example is the effect on a Harris 1.2µm CMOS process [28] where the current room temperature hardened oxide gave a threshold voltage shift of 93mV for 200 krad(Si) when irradiated at room temperature but a 1.17V shift at 77K. Also at 77K a room temperature soft oxide gave a shift within 10% of the 1.17 Volt value observed for the room temperature hard oxide.

There are, however, a variety of techniques which can be used to produce radiation tolerant devices for low temperature applications, such as IR focal plane arrays, e.g. i) use of ion implantation's to pin the surface potential and prevent inversion, ii) use of devices with high electric fields or very thin oxides which assist electrons to tunnel into the dielectric from the silicon and produce annealing of the trapped holes, iii) use of dual dielectric insulators such as silicon nitride/silicon dioxide (in a MNOS - Metal Nitride Oxide Semiconductor structure) which use a thin oxide layer giving a relatively low trapped charge, the effects of which can be compensated by electron trapping in the nitride layer [29], finally, iv) use of reoxidised nitrated SiO₂ (RNO) as explained by Boesch and Dunn [30]. In this material the trapped hole annealing can be enhanced, particularly if a high electric field (between 2 and 5 MV/cm) can be applied periodically.

Interface state buildup, on the other hand is suppressed at low temperatures [31] because the processes, such as H⁺ diffusion, which lead to their generation take place only at temperatures

above about 120K. Figure 2 2-1 shows a schematic diagram of the interface trap model proposed by Saks et al [30]. There are two processes proposed: the 'LT' process occurs for $T > 120K$ and the 'HT' for $T > 250K$. Thus interface state generation only occurs when the sample is warmed up after irradiation, once produced however they will not be annealed out except at high temperatures ($> 400K$).

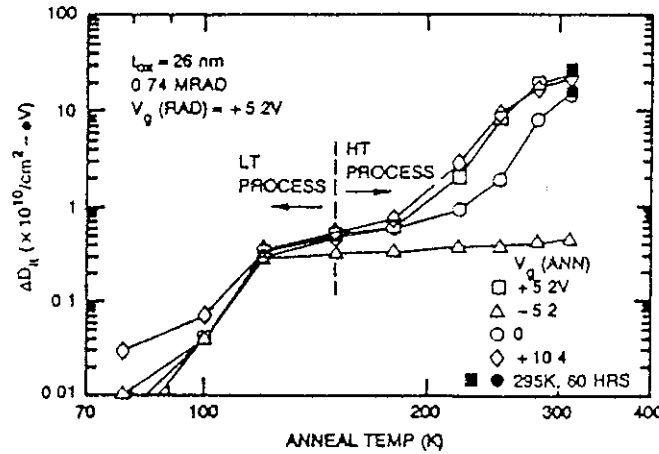


Figure 2 2-1 a) Isochronal annealing data on 4 MOSFETs irradiated at 78K and annealed to 310K with different anneal gate biases V_g (ann). Two distinct D_{it} formation processes are observed - the LT processes at $T \sim 120K$ and the HT process at $T \sim 180K$ [30].

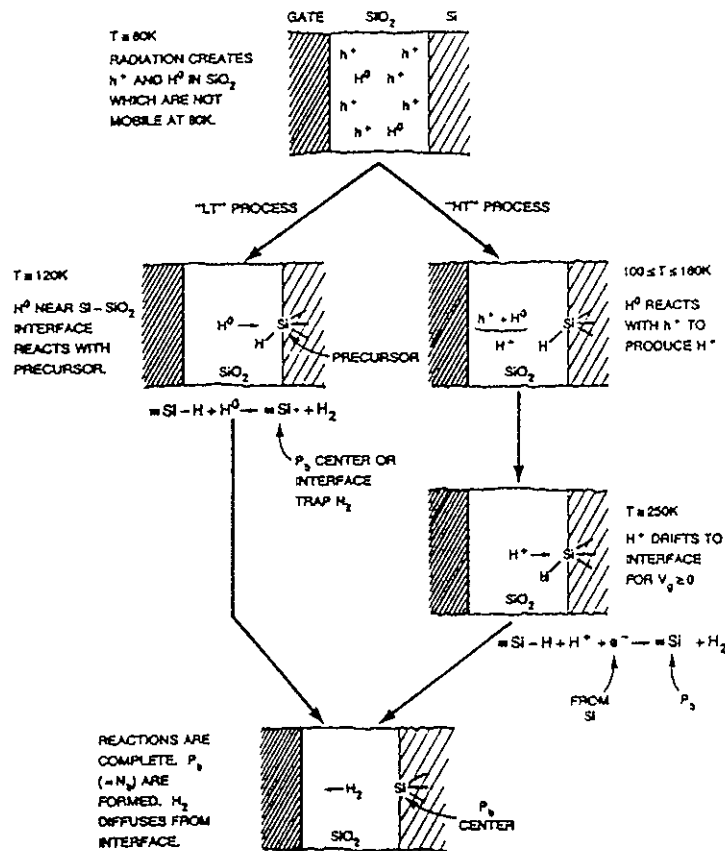


Figure 2 2-1 b) Proposed model of Nit formation by ionizing radiation showing the rate-limiting step of the two N_{it} formation mechanisms. The LT process is limited by H^0 reaction at the interface, while the HT process is limited by H^+ drift through the oxide [30].

2.2.6 Materials other than SiO₂

As noted above, the basic phenomenology of ionization damage in MOS devices is similar for other structures such as HgCdTe MIS devices with ZnS or SiO₂ passivations. In ZnS, for example, the e-h creation energy is 11 eV [32] and 2.3×10^{13} e-h pairs/cm³/rad(Si) are created in the insulator. This can lead to charge trapping and build-up of interface states as before. Important differences are that both electrons and holes have a high enough mobility in ZnS for significant charge transport to occur before trapping and that both electrons and holes can be trapped at the interfaces in HgCdTe devices with anodic oxide (or sulphide)/ZnS passivations (depending on the direction the carriers are swept by the applied electric field). Thus compensation (both e and h trapping together) and recombination (trapped electrons being removed by capturing a hole, or vice versa,) can occur (see for example [33]). In addition, the barrier height between MCT and insulator materials is less than for Si-SiO₂, so that carrier injection into the insulators (from the MCT) takes place more easily [31], and gives enhanced annealing of trapped charge. These effects are discussed further in later sections on individual detectors. Here we emphasise that the basic effects of changes in flatband voltage and surface leakage currents are just as important for IR detectors as for MOS devices. In addition, compensation effects and trap-assisted tunneling can be important. The previous comments on the dependence on device processing are equally relevant for IR focal plane arrays.

Figure 2 2-2 shows an overall view of the relative effects on detectivity (D^*) of total ionizing dose [2]. Although only relative total dose was given in the original publication, it is likely that the origin (100 dose) will be ~ 4 krad giving GaAs devices a tolerance to $\sim 2 \times 10^8$ rad which is reasonable for these devices since they do not employ insulating layers and they have a pinned surface potential. On that scale MCT devices would be hard to $\sim 4 \times 10^5$ rad (it will be seen that a tolerance to roughly 1 Mrad is possible with heterostructure devices). Further comments on individual detector types will be made in the relevant detector section.

2.3 DISPLACEMENT DAMAGE

When particles (electrons, protons, neutrons etc) pass through a semiconductor there is the possibility of collisions with target nuclei. These cause displacement of atoms from their lattice sites and the creation of vacancy - interstitial pairs. These pairs are usually mobile and depending on the material and the temperature migrate through the lattice until a stable defect is formed (by association with other defects, impurities or dopants). These stable defects give rise to states with energy levels within the forbidden bandgap and these can affect device properties by any of the five basic mechanisms discussed in section 2.2.1.3 (i.e. generation, recombination, trapping, compensation and tunneling) depending on the energy level, the temperature and their location within the device.

During the initial collision the incident particles transfer part of their energy and produce primary knock-on atoms (PKAs). The recoil energy spectra, and the directions of the PKAs depend on the type, charge and energy of the incident particles. The PKAs in turn collide with other atoms in the lattice thereby producing additional knock-on atoms and lattice vacancies. The end result is that part of the particle energy goes into production of vacancies and phonons (lattice vibrations). This fraction is termed the non-ionizing energy loss or NIEL. The rest of the energy (of the incident particle and of the knock-on atoms) goes into ionization with no permanent effects. Typically only 0.1% of the total energy loss for an ion goes into non-ionizing collisions.

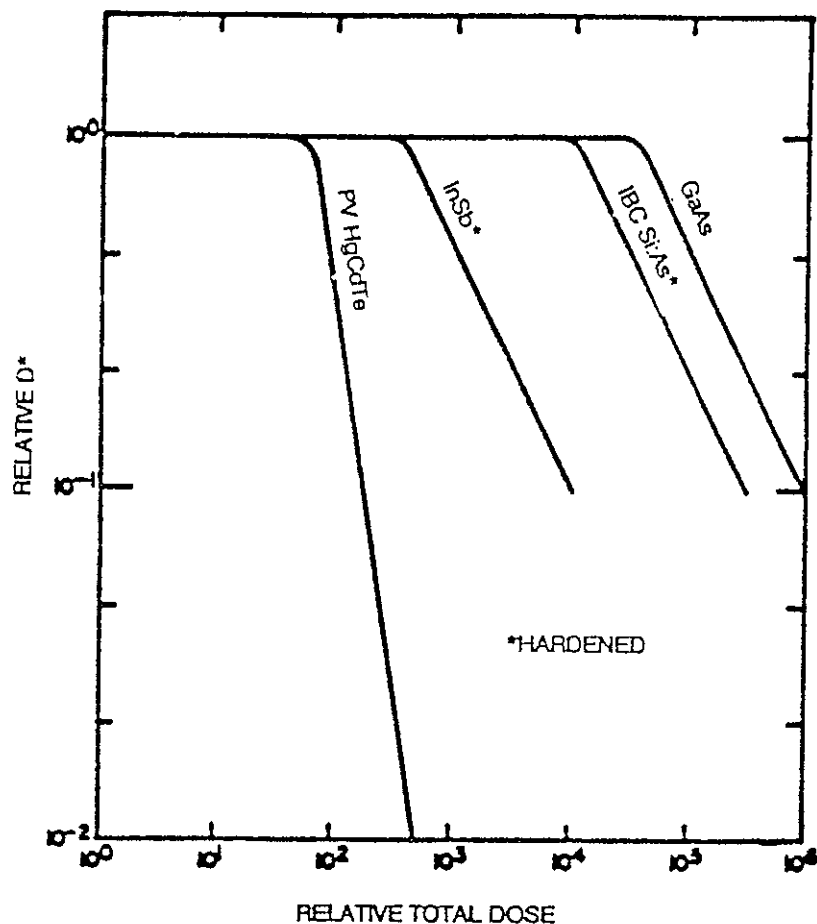


Figure 2 2-2 Overview of D^* versus relative total dose for various IR detector types [2]

The NIEL has been calculated for silicon by Burke [34] for GaAs by Summers et al [35], in Ge by Marshall et al [36], in InGaAs by Walters et al [37] and in the high temperature superconductor $YBa_2Cu_3O_7$ by Summers et al [38], plots of NIEL versus particle energy are given in figure 2 3-1. It is seen that there is a broad similarity in the plots for the different materials. On a microscopic level there are a number of collision processes which can take place depending on the energy. Below a particle energy of about 10 MeV almost all the displacement damage is caused by Rutherford scattering by the outer electrons of the silicon atoms and this gives elastic scattering via Coulombic interactions. At higher energies nuclear elastic collisions start to become important and at energies greater than ~ 10 MeV nuclear inelastic collisions start to occur. These reactions dominate for energies greater than ~ 150 MeV. At the highest energies (above 100 MeV) the incident protons initiate intranuclear cascade processes and the recoil energies can be very high (up to 0.3 MeV for Si and 2 MeV for Ge).

At first glance it might be thought that the wide variety in PKA spectra from different incident particles would result in a corresponding variety of device damage and that models of cascade processes would be needed to correlate the effects. In practice for the materials studied (and probably for most IR detector materials) it turns out that the nature of the displacement damage does not depend on the energy spectrum of the PKAs. Thus the partitioning of the incident particle energy into isolated defects, cascades and subcascades is independent of PKA energy. A higher energy PKA will produce more overall damage but the microscopic nature of the damage is not significantly different. Thus the non ionizing energy loss can be simply written as a sum of terms due to the elastic and inelastic interactions i.e.

At any energy, $S_{Di} = (N_A/A_i) \sum \sigma_j T_j$ (2-2)

where σ_j is the cross section for the j th type of interaction (e.g. Coulomb, nuclear inelastic etc) and T_j is the damage energy of the recoil, i.e. the average PKA recoil energy partitioned so that the energy going into the ionization is removed. S_{Di} is the total energy which goes into damage (i.e. displacements) in $\text{MeV cm}^2/\text{g}$, A_i is the gram atomic weight of a given target atom and N_A is Avagadro's number

The number of lattice displacements is then proportional to S_{Di} , the constant of proportionality depending on the threshold energy for a displacement

Target material	mean displacement threshold
Si	25 eV
InSb	7.7 eV [39]
GaAs	9.2 eV [38]
MCT	6.6 eV for Hg

Note the low threshold energies for the III-V compounds

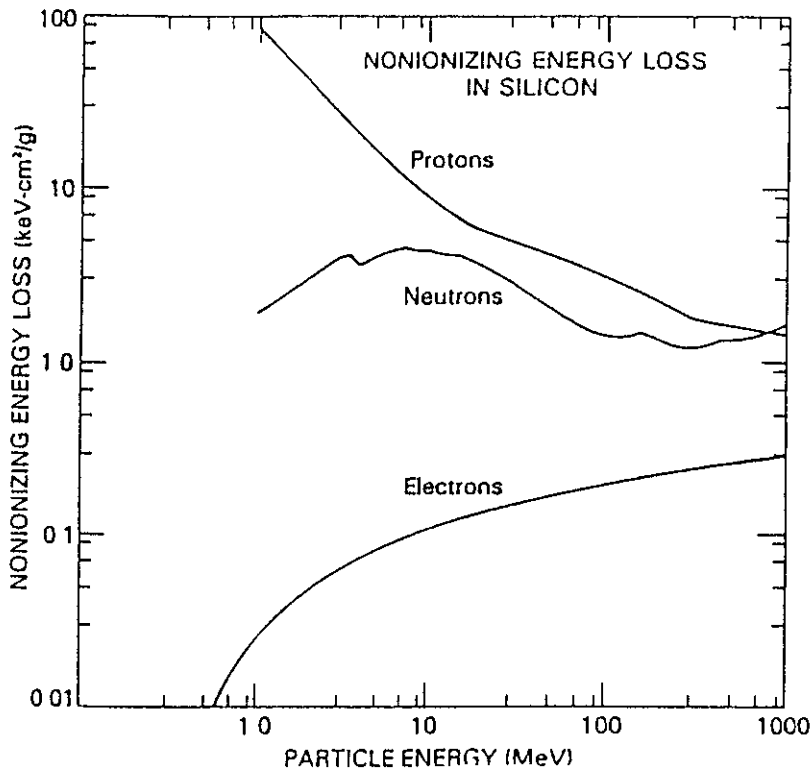


Figure 2.3-1 a) Nonionizing energy loss for Si [33]

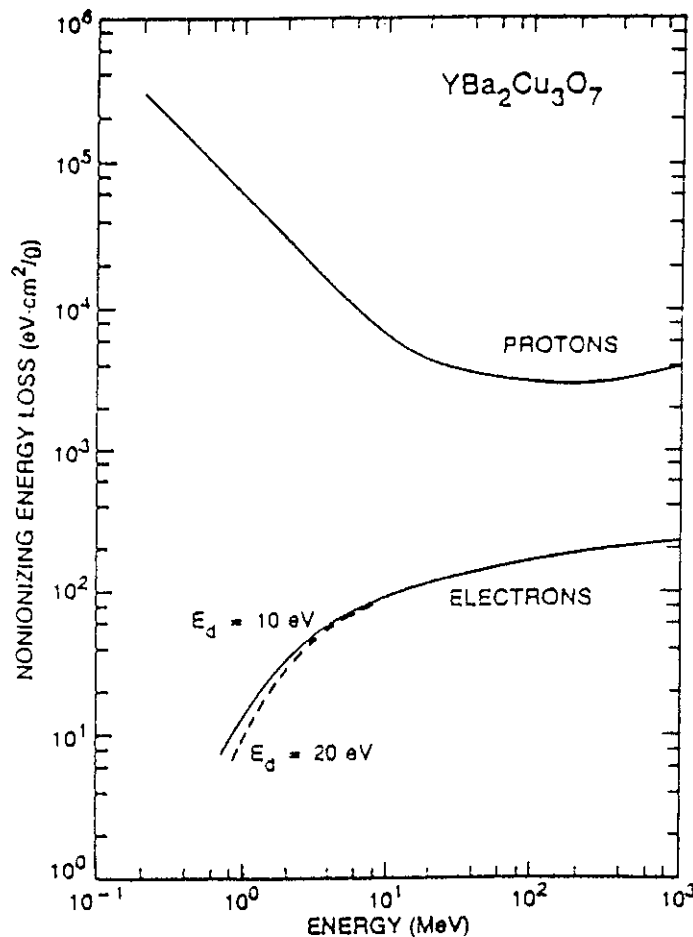


Figure 2 3-1 d) Nonionizing energy loss for $\text{YBa}_2\text{Cu}_3\text{O}_7$ [37]

In the materials studied so far it turns out that the device damage is also proportional to NIEL (as found from dark current and charge transfer efficiency measurements on visible CCDs, transistor gain degradation in Si, Ge and GaAs and shifts in transition temperature T_c for the superconductor) The relationship with NIEL is expected to hold for all detector materials This allows an easy comparison of the effects for different particle energies All that is necessary is a measurement of the constant of proportionality between device damage (if it can be expressed as a single parameter) and NIEL at one energy (or at most a few) and then the damage can be predicted for any environmental energy spectrum.

It is recognised (see for example [40]) that displacement damage is important for sensitive analogue devices such as CCDs However this only applies for small signal applications with the CCD operated in the range -100 to 0°C For CCDs used as multiplexers for IR FPAS we should note

- i) the CCD is used at low temperatures, hence dark current generation by bulk displacement damage states should be negligible (with the exception that virtual phase CCDs have an implant which allows removal of one layer of front face electrodes - and hence improved UV response for a visible imager - however this results in large fields within the device such that proton damage can produce bulk defects where avalanche breakdown can occur leading to large dark current spikes, which are insensitive to temperature)
- ii) In a buried channel CCD proton damage leads to trapping states and a degradation in CTE However below -100°C these traps are essentially 'frozen out' and should not affect performance In any case most CCD multiplexers will be surface channel (to cope with high signal handling) - although this makes them sensitive to ionization damage (interface states)

Figure 2 3-2 shows the types of defects that can occur in an elemental semiconductor [41] In compound semiconductors, such as GaAs or InSb, the variety of intrinsic point defects increases significantly Vacancies on both sublattices and self-interstitials from both components need to be considered, as well as atoms from one sublattice occupying positions in the other sublattice (antisite defects) An important example of the latter is the deep donor EL2 defect in GaAs, which renders unintentionally p-doped material semi-insulating

In semiconductors such as MCT the crystal structure of the active region is disordered by dislocations and point defects and the lattice is by no means perfect Hence displacement damage effects may not be important in PV photodiode or MIS devices until high fluences ($\sim 10^{14}$ p/cm²), which can cause type conversion, are reached (cf section 4)

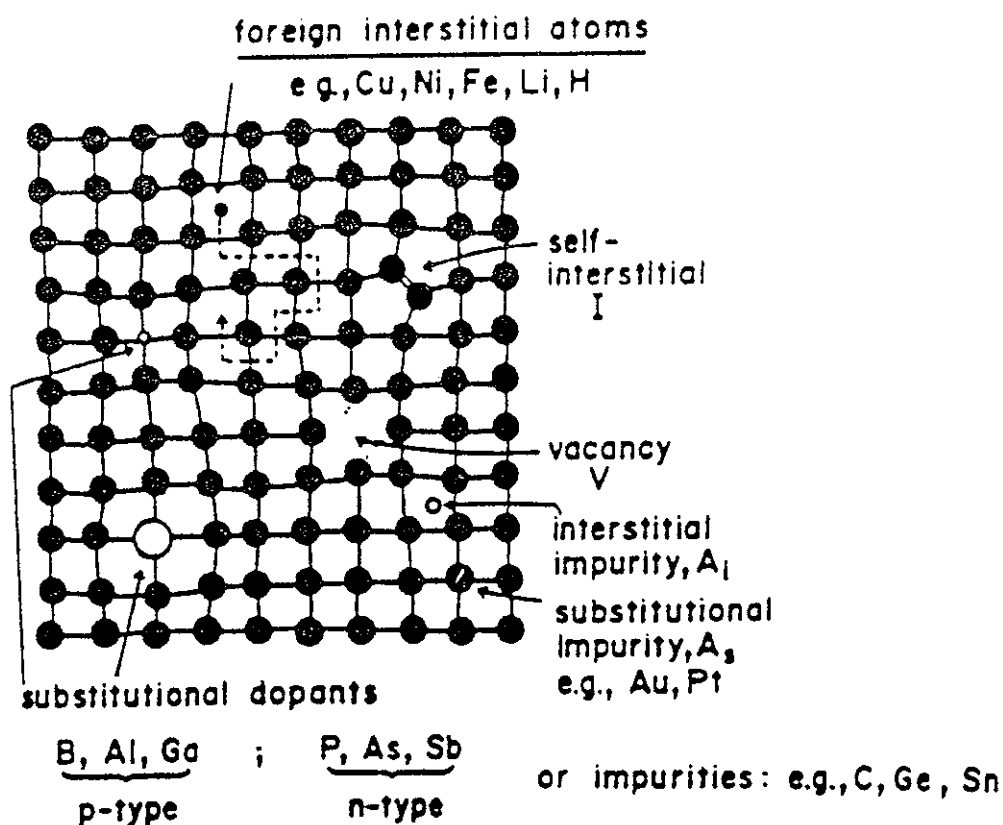


Figure 2 3-2 The types of defects that can occur in an elemental semiconductor [40]

In extrinsic photoconductive detectors we have a different situation since damage starts to be noticeable when the number of radiation-induced defects is comparable with the acceptor concentration [1] The acceptor concentration in extrinsic silicon is generally two or three orders of magnitude less than the carrier concentration in MCT, while the defect introduction rates (by irradiation) are comparable Hence extrinsic detectors are more vulnerable to displacement damage than photoconductive MCT

In extrinsics the radiation-induced recombination sites are of the same type as the initial ones (both are ND^+ sites) We have [1]

$$\frac{R}{R_0} = \frac{1}{1 + [(1/N_A) (dN_A/d\phi)\phi]} \quad (2-3)$$

where $dN_A/d\phi$ is the introduction rate of acceptor centres. Displacement damage at low temperatures is independent of the presence of impurities, so $dN_A/d\phi$ is independent of N_A (It is of the order of 15 to 20 /cm at $\sim 10^\circ\text{K}$ for neutrons). With this in mind, it can be seen from Eq (2-3) that detectors with lower initial N_A will degrade more rapidly. Unfortunately, high responsivity detectors are ones with low N_A , which means that the better detectors will be more vulnerable to radiation.

This situation applies to blocked impurity band (BIB) detectors also. For example the model given by Petroff and Stapelbroek for Si As detectors (with a low signal flux $< 5 \times 10^{13}$ photons/cm²/s and low electric field) has the depletion width (and hence the responsivity) determined by the acceptor concentration in the IR active region

$$R \propto (2\epsilon\epsilon_0 V_B/e N_A + t_B^2)^{1/2} - t_B \quad (2-4)$$

where N_A is the acceptor concentration, t_B the blocking layer thickness and V_B the bias voltage. Thus, again, R is increased for lower acceptor concentrations and improved material processing techniques are being developed. These reduce impurities in the host material and reduce N_A in the active volume of the detector. Recently Clement et al [42] have determined that in Si As IBC detectors after bombardment by Cf-252 neutrons N_A increases by an average of 2 acceptor states per cm³ for each neutron/cm² independent of detector donor concentration. A similar proportionality is expected for the proton environment. Again the best detectors are the least radiation tolerant.

Figure 2 3-3 shows an overall view of detectivity changes with relative neutron fluence [2]. The origin (10° neutrons relative) is likely to be $\sim 10^{10}$ fission neutrons (cm⁻²). The comparative susceptibility to damage is likely to be similar for protons. Note the sensitivity of InSb and Si As IBC compared with PV MCT.

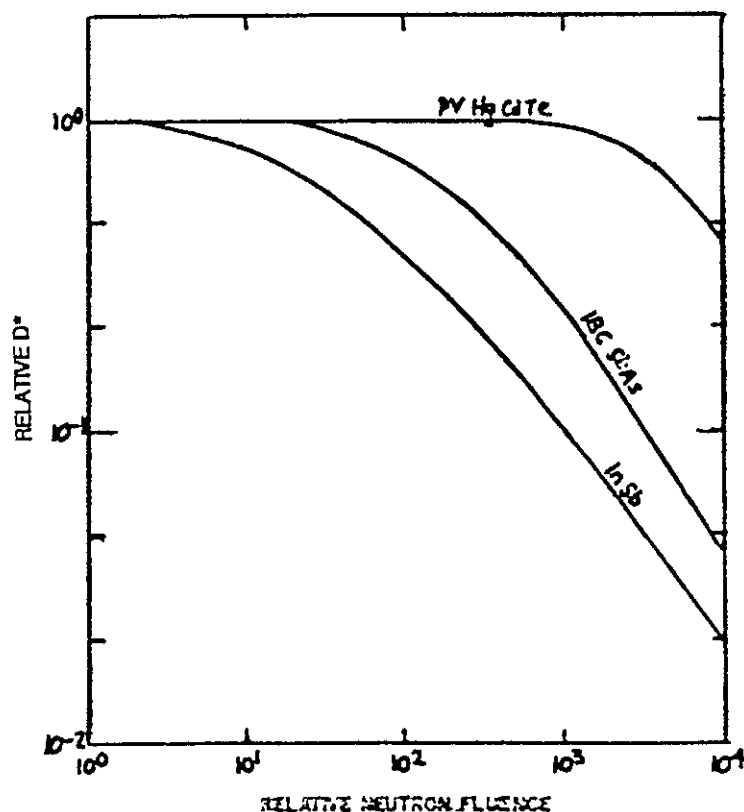


Figure 2 3-3 D^* versus relative Cf-252 neutron fluence for various IR detectors [2]

2.4 SUMMARY

Table 2 4-1 below summaries the radiation effects expected for various IR detectors in the space environment

Table 2 4-1 Importance of radiation damage effects in space

	Transient effects	Ionization damage	Displacement damage	Comments
PV MCT	**	** (unless hardened)		Disordered crystal structure
PV InSb	**	*	* (high fluences)	
Extrinsic	***	*	* (high fluences)	Thick active layer makes transient effects large
IBC (Si As)	*		* (high fluences)	
Si CCDs (IR multiplexers)		** (unless hardened)		Used at low temperatures
(Visible sensors)	*	*	*	Used at high temperatures
GaAs and QW devices		*?		Hard to most types of radiation but may be susceptible to ionization damage as technology improves and responsivity increases

*** = very sensitive, ** = sensitive, * = moderately sensitive, blank = not sensitive

REFERENCES

- [1] A H Kalma, 'Nuclear and space radiation effects in infrared detectors', in Advances in Focal Plane Technology, Proc SPIE, 217, 186-191 (1980)
- [2] A H Kalma, 'Radiation response issues for infrared detectors', Proc NASA/JPL Workshop on innovative long wavelength infrared detectors, Pasadena CA, 24-26 April 1990, 151-157 (1990)
- [3] C A Klein, 'Bandgap dependence and related features of radiation ionization energies in semiconductors' *J Appl Phys*, vol 39(4), pp 2020-2038 (1968)
- [4] E H M Heijne, 'The use of semiconductor imagers in high energy particle physics', in Solid State Imagers and their Applications, Proc SPIE, vol 591, pp 2-11 (1985)
- [5] J T Montroy, R Baron, G C Albright, J Boisvert and L D Flesner, 'Energetic electron-induced impurity ionization in Si As detectors', *IEEE Trans on Nuclear Science*, vol NS-35(6), pp 1307-1312 (1988)
- [6] G R Hopkinson, C J Baddiley, D R P Guy and J E Parsons, 'Total Dose and Proton Testing of a Commercial HgCdTe Array' *IEEE Transactions on Nuclear Science*, vol NS-41(6), pp 1966-1973, (1994)
- [7] J F Ziegler, J P Biersack and U Littmark, The Stopping and Range of Ions in Solids, (Pergamon Press, Oxford, 1985), PC version developed by J P Biersack and J F Ziegler, IBM Research, York-Town, NY, U S A
- [8] G M Williams, A H B Vanderwyck, E R Blazejewski, R P Ginn, C C Li and S J Nelson, 'Gamma radiation response of MWIR and LWIR HgCdTe photodiodes', *IEEE Trans on Nuclear Science*, vol NS-34(6), pp1592-1596 (1987)
- [9] A M Fowler, R. G Probst, J P Britt, R R Joyce and F C Gillett, 'Evaluation of an indium antimonide hybrid focal plan array for ground based infrared astronomy', *Optical Engineering*, vol 26(3), pp 232-240 (1987)
- [10] H Bichsel, 'Energy loss and ionization of fast charged particles in a 20 μ m silicon detector', *Nuclear Instrum and Methods*, vol A235, pp 174-??? (1985)
- [11] A. M Kellerer, 'Analysis of Patterns of Energy Deposition-A Survey of Theoretical Relations in Microdosimetry Theory', in *Proc Second Symp on Microdosimetry Theory*, Ed H G Ebert, pp 107-135 (Commission of the European Communities, Brussels, 1969)
- [12] E A Burke, J J Boyle and H J Huemmler, 'Gamma-induced noise in CCDs', *IEEE Trans. on Nuclear Science*, vol NS-28, pp 4068-4073, (1981)
- [13] V E Vickers, F D Shepherd Jr, and E A Burke, 'Ionizing Radiation Dosimetry and Noise in Small Geometry Devices', *IEEE Trans on Nuclear Science*, vol NS-21, pp 107-112, (1974)
- [14] J N Bradford, 'A Distribution Function for Ion Track Lengths in Rectangular Volumes',

-
- J Appl Phys*, vol 50, pp 3799-3801 (1979)
- [15] J F Ziegler and W A Landford, 'The Effect of Sea Level Cosmic Rays on Electronic Devices', *J Appl Phys*, vol 52, pp 4305-4312 (1981)
- [16] J B Langworthy, 'Depletion Region Geometry Analysis Applied to Single Event Sensitivity', *IEEE Trans on Nuclear Science*, vol NS-36(6), pp 2427-2434, (1989)
- [17] M A Xapsos, E A Burke, P Shapiro and G P Summers, 'Energy Deposition and Ionization Fluctuations Induced by Ions in Small Sites-An Analytical Approach', *Radiation Research*, vol 137, pp 152-161 (1994)
- [18] J C Pickel and M D Petroff, 'Nuclear radiation induced noise in infrared detectors', *IEEE Trans on Nuclear Science*, NS-22(6), 2456-2461 (1975)
- [19] A B Holman, E C Smith and G W Autio, 'Verification of radiation background rates in an IR sensor system', *IEEE Trans on Nuclear Science*, vol NS-23(6), pp 1775-1780 (1976)
- [20] E L Devita, M J Holtzman, R E Mills and D T Walsh, 'Methodology for testing IR detectors in simulated nuclear radiation environments', in Test and evaluation of infrared detectors and arrays, *Proc SPIE*, vol 1108, pp 274-287 (1989)
- [21] M A Parish, 'Development of algorithms for on-focal plane gamma circumvention and time delay integration', in Materials, Devices, Techniques, and Applications for Z-plane Focal Plane Array Technology II, *Proc SPIE*, vol 1339, pp 120-127 (1990)
- [22] K H Norsworthy and J M Michels, 'On-array spike suppression signal processing', *ibid*, pp 99-110 (1990)
- [23] F B McLean, H E Boesch and T R Oldham, 'Charge Generation, Transport and Trapping', in Radiation Effects in MOS Devices and Circuits, Edited by T P Ma and P V Dressendorfer, (Wiley-Interscience, New York, 1989), chap 3
- [24] J Schwank, 'Basic Mechanisms of Radiation Effects in the Natural Space Environment', Short Course Notes, pp II-1-II-109, IEEE Nuclear and Space Radiation Effects Conference, Tucson, A7-, USA, July 1994
- [25] J R Srour and J M McGarrity, 'Radiation Effects on Microelectronics', *Proc IEEE*, vol 76, pp 1443-1469 (1988)
- [26] P S Winokur, "Radiation Induced Interface States", in Radiation Effects in MOS Devices and Circuits, Edited by T P Ma and P V Dressendorfer, (Wiley-Interscience, New York, 1989), chap 4
- [27] D Braunig and F Wulf, 'Atomic Displacement and Total Ionizing Dose Damage in Semiconductors', *Radiation Physics and Chemistry*, vol 43, pp 105-127 (1994)
- [28] D C Pantelakis, D F Hemmenway, N W. Van Vonno and T J Sanders, "Freeze-out characterization of radiation hardened N⁺ polysilicon gate CMOS transistors", *IEEE Trans Nuclear Science*, vol 38, pp 1289-1296 (1991)

- [29] N S Saks and J, M, Modolo, "Radiation effects in N-channel MNOS CCDs at low temperature", *IEEE Trans Nuclear Science*, vol 30, pp 4197-4204 (1983)
- [30] H E Boesch and G J Dunn, "Hole transport in SiO₂ and reoxidised nitrated SiO₂ gate insulators at low temperatures", *IEEE Trans Nuclear Science*, vol 38, pp 1083-1088 (1991)
- [31] N S Saks, R B Klein and D L Griscom, 'Formation of interface traps in MOSFETs during annealing following low temperature irradiation', *IEEE Trans Nuclear Science*, vol 35, pp 1234-1240 (1988)
- [32] M M Moriwaki, J R Srour, L F Lou and J R Waterman, 'Ionizing radiation effects on HgCdTe MIS devices', *IEEE Trans on Nuclear Science*, vol NS-37(6), pp 2034-2041 (1990)
- [33] J R Waterman and R A Schiebel, 'Ionizing radiation effects in N-channel (Hg,Cd)Te MISFETS with anodic sulfide passivation', *IEEE Trans on Nuclear Science*, vol NS-34(6), pp 1597-1601 (1987)
- [34] E A Burke, 'Energy dependence of proton-induced displacement damage in silicon', *IEEE Trans on Nuclear Science*, vol NS-33(6), pp 1276-1281 (1986)
- [35] G P Summers, E A Burke, P Shapiro, S R Messenger and R J Walters, "Damage correlations in semiconductors exposed to gamma electron and proton irradiations" *IEEE Trans on Nuclear Science*, vol NS-40(6), pp 1372-1379 (1993)
- [36] P W Marshall, C J Dale, G P Summers and E A Wolicki, 'Proton, neutron and electron-induced displacement damage in germanium' *IEEE Trans Nuclear Science*, vol 36(6), pp 1882-1888 (1989)
- [37] R J Walters, G J Shaw, G P Summers, E A Burke and S R Messenger, "Radiation effects in Ga_{0.47}In_{0.53}As devices" *IEEE Trans Nuclear Science*, vol 39(6), pp 2257-2264 (1992)
- [38] G P Summers, D B Chrisey, W G Maisch, G H Strauss, E A Burke, M Nastasi and J R Tesmer, 'Electron and proton radiation effects in the high temperature superconductor YBa₂Cu₃O₇', *IEEE Trans on Nuclear Science*, vol NS-36(6), pp 1840-1847 (1989)
- [39] F H Eisen, 'III-V Compound review', *Radiation Effects*, vol 9, pp 235-242 (1971)
- [40] G R Hopkinson, C J Dale, and P W Marshall, 'Proton effects in CCDs', *IEEE Trans Nuclear Science*, NS-43, 2, 614-627, (1996)
- [41] U M Gosele and T Y Tan, 'Point defects in semiconductors', *MRS Bulletin*, pp 42-46, November 1991
- [42] R E Clement, J C Boisvert, R K Bentley and J D Merrian, 'Acceptor state generation in Si As impurity band conduction detectors', *Proc IRIS speciality group on infrared detectors vol II*, pp 9-19 (1989)

3 BASIC RADIATION EFFECTS ON BULK MCT

3.1 INTRODUCTION

As a background to the discussion of effects in mercury cadmium telluride arrays in section 5, this chapter considers basic effects on single element MCT detectors. This section will concentrate on displacement damage in single element detectors, irradiated to high fluences. Ionization damage depends strongly on passivation technology and is more pertinent to the discussion on complete arrays. Since the MCT lattice is disordered (with many dislocations and point defects) the usual argument is that radiation-induced bulk defects will make little difference to array performance at low fluences [1]. This was found to be the case in a previous study on a 256 x 4 MCT array from G-MIRL [2]. It will be seen that fluences $\sim 10^{14}$ p/cm² are needed to cause significant changes in lattice properties - much higher than would normally be encountered in a space environment.

As discussed in section 1.4.1, mercury cadmium telluride is a II-VI compound whose composition is usually expressed in the form Hg_{1-x}Cd_xTe. The band gap of the material can be adjusted by changing the value of x, and consequently also its electrical and optical properties, from that of mercury telluride (semi-metallic) to cadmium telluride (semiconductor - large band gap, 1.605 eV). An extensive literature exists on radiation effects in cadmium telluride, and there is a fair amount on MCT, though much of the work on bulk damage, which concentrates on properties such as carrier concentration, mobility, spectral response and luminescence, was carried out some years ago. Because of its importance in p-n junction formation there is also a large body of work on defects induced by ion implantation (recently reviewed by Destéfani [3]).

MCT is a defect solid where deviations from stoichiometry control both the magnitude of the extrinsic carrier density and the carrier type (n or p). The interpretation of bulk damage data is complex since any of the three constituent atoms (Cd, Hg or Te) can be in an interstitial or vacancy configuration, charge states can be Fermi level dependent and displaced atoms can act as donors or acceptors. Also, significant annealing of defects can occur in the temperature range 10 to 300 K.

Both cadmium and mercury atoms are regarded as donors in the interstitial configuration whereas their respective vacancies act as acceptors (Te antisites, Hg antisites on Te vacancies and Te vacancies act as donors).

After irradiation the produced material is frequently highly compensated due to the large numbers of both n- and p-type electrically active defects. A high degree of compensation is evident by degradation in material parameters eg mobility and lifetime at low temperatures.

In addition, radiation induced bulk defects are different in II-VI compounds from those created in III-IV materials. This is primarily related to the difference in binding energies between the covalent II-VIs, and the mostly ionic III-V semiconductors. In the high-binding-energy covalent materials, defects are localized in the region where ions lose their energy by nuclear collisions. In II-VI compounds, with lower binding energies and where ionic bonds are dominant, the irradiation induces extended defects (probably dislocation loops) rather than point defects. These can propagate to a long range, well beyond the depth at which ions penetrate.

Favre et al [4] have conducted a set of 0.7-2.7 MeV electron irradiations on MCT with different alloy compositions (at 20 K). They concluded that the only electrically active defect was due to Hg interstitials, which act as donors (as mentioned above). They measured a displacement energy for Hg atoms of 16 eV and figure 3-1-1 shows the effective displacement cross-section as a function of cadmium content x . As would be expected, as the Hg content goes down so does the cross-section (note number of defects = $\sigma \times$ fluence). Favre et al also studied the annealing behaviour. They found a first annealing stage at around 70K and another stage at ~ 180 K which was present in $\text{Hg}_{0.3}\text{Cd}_{0.7}\text{Te}$ but not in $\text{Hg}_{0.7}\text{Cd}_{0.3}\text{Te}$. They concluded that the lower the cadmium content (smaller x) the more stable the defects. It also seemed that bombardment by heavy ions (with higher ionization energy loss) gave less stable defects.

According to Petrosky [5] the displacement damage threshold energy (T_d) should depend on the reciprocal of the lattice constant (as discussed in section 2). Since the lattice constant varies less than 3% in going from CdTe to HgTe, T_d should be roughly the same for any MCT alloy and should have a value ~ 6.6 eV.

Petrosky gives the formula

$$\text{maximum no. of defects} = (6 \ln 2 / \pi^2) (T_d / T_d) \quad (3-1)$$

where T_d is the displacement damage energy deposited. As a rough estimate, Petrosky calculates 10^{10} displacements generated from 200 krad of 1 MeV electrons passing through 10 mm of MCT. However only a small fraction of these will survive recombination and result in stable defects.

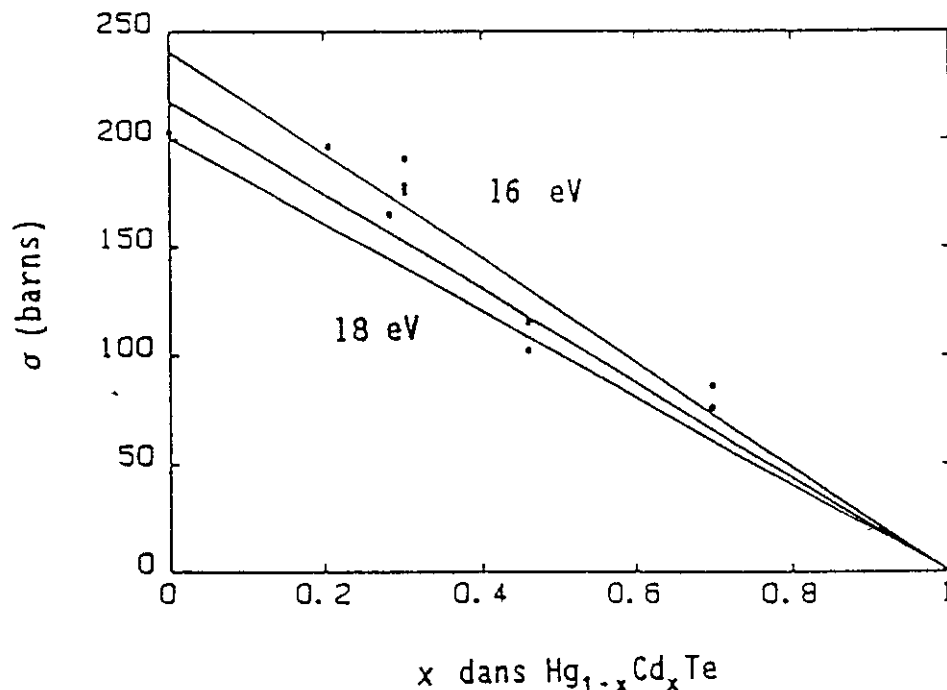


Figure 3-1-1 Effective displacement cross-sections for mercury atoms in MCT (2.5 MeV electron irradiation) [4]

3.2 CHANGES IN CARRIER CONCENTRATION (PC DEVICES)

In intrinsic materials (eg HgCdTe and PbSnTe), *displacement damage causes the introduction of donors* [6]. The defect sites can also act as recombination sites. In photoconductive CdHgTe detectors, which are made from n-type material, irradiation degrades the lifetime as a result of either increased Auger recombination (caused by the added donors) or increased Shockley-Read-Hall recombination at the defects. In either case, the optical responsivity degrades. However, in the HgCdTe detector case, the number of radiation-induced defects must be comparable to the carrier concentration in the material before significant damage can take place, since it is the addition of these carriers that affects the lifetime. The degradation equation for MCT detectors is

$$\frac{R}{R_0} = \frac{\tau}{\tau_0} = \frac{1}{1 + K\tau_0\phi} \quad (3-2)$$

where R is the optical responsivity, τ is the lifetime, K is the degradation coefficient, ϕ is the irradiation fluence, and the subscript "o" denotes the pre-irradiation value.

This can be written [5]

$$\frac{R}{R_0} = \frac{\tau}{\tau_0} = \frac{1}{[1 + (1/n_0)(dn/d\phi)\phi]^x} \quad (3-3)$$

where n_0 is the initial carrier concentration, $dn/d\phi$ is the carrier addition rate, and x is 3 for Auger-limited lifetime or 2 for Shockley-Read-Hall limited lifetime.

A variety of radiation studies have been carried out using MCT bulk samples, typically with high energy electrons. The majority of these studies have used $\text{Hg}_{1-x}\text{Cd}_x\text{Te}$ with $x = 0.2$. For $x = 0.2$, the cut-off wavelength is 14 μm at 80K (for $x = 0.27 - 3$ it is $\sim 5 \mu\text{m}$).

Low Temperature Measurements

A study of lightly compensated material ($\sim 1.5 \times 10^{15}/\text{cm}^3$) used electrons, gammas and neutrons (Mallon et al [7]). The irradiations were carried out at 10 K using 14 MeV neutrons and 2 and 30 MeV electrons. The maximum electron fluence was $3.75 \times 10^{14}/\text{cm}^2$. The samples were sequentially irradiated (and annealed) by the different types of radiation. For all radiations the carrier density (n type samples) increased with increasing dose, the carrier introduction rate increased with energy, whereas the Hall mobility and carrier lifetime decreased with dose. Major annealing stages were observed at 50, 160 and 240K. A fluence of $\sim 4 \times 10^{14}/\text{cm}^2$ at 5 MeV increased the carrier concentration by a factor of 5, a 15 minute anneal at 300K restored this to the pre-irradiation value. Figure 3.2-1 shows how the neutron and electron-induced displacement damage (donor defects) affected the PC device response at 80K (cf the results for InSb in figure ***).

A similar study using 5 MeV electrons, but carried out at 80K, again demonstrated that the carrier density increased with dose (Naber et al [8]), now however the Hall mobility initially increases and then saturates. The samples were n type with $x = 0.2$ and carrier concentrations of $10^{13}-10^{15}/\text{cm}^3$. Similar annealing stages were observed at 140 K and 230 K with virtually complete annealing at 340K. The maximum electron fluence used was $3 \times 10^{16}/\text{cm}^2$, and after this dose the photoconductive signal had decreased by a factor of 10^6 and the spectral response had shifted to shorter wavelengths (higher energy). It was suggested that this effect had

occurred because the radiation had introduced a donor defect with an energy level well above the conduction band minimum, such an observation is possible because of the Burstein-Moss effect in which the degeneracy forbids transitions to the bottom of the conduction band (see section 3.3)

Another experiment (5 MeV electrons, 80K) of highly compensated material ($2 \times 10^{14}/\text{cm}^3$), [9], showed similar effects to the previous studies. However, for a total fluence of $5 \times 10^{14} \text{e}/\text{cm}^2$ no significant degradation in excess carrier lifetime was observed. The photoconductivity response, initially peaking at $15 \mu\text{m}$, had completely vanished at this maximum fluence. After isochronal annealing at 235K, the response was recovered, but peaking at $10.5 \mu\text{m}$. Successive annealing increased this response wavelength, which achieved its pre-irradiation value at 340K. It was suggested that for a photoconductive detector the change of carrier concentration resulting from the irradiation could adversely affect device performance. From the results of this investigation a 10% increase in excess carrier concentration - giving a 20% decrease in photoconductive signal - would occur for an electron dose of $8 \times 10^{15} \text{e}/\text{cm}^2$. From this it seems that contrary to silicon, the carrier concentration is more crucial than the carrier lifetime.

The previous investigations all demonstrated an increase in carrier concentration with increasing radiation dose for n type material. When p type samples were irradiated at 25K with 2.5 MeV electrons to a fluence of $4.7 \times 10^{15} \text{e}/\text{cm}^2$ (Melngailis et al [10]) this effect *changes the type from p to n*. The range of 2.5 MeV electrons in MCT is $\sim 1.2 \text{mm}$, the damage effect was therefore uniform in these 0.33mm samples. The observed effects in the n type samples was an increase in carrier mobility, concentration and conductivity. Annealing stages were observed at 50K and 75K with complete recovery to the p type state after annealing at temperatures $> 220\text{K}$. The suggested mechanism was that the radiation introduces compensating donors into the p type material, and for fluences $> 2 \times 10^{15} \text{e}/\text{cm}^2$ these donors contribute electrons to the conduction band, making the sample n type.

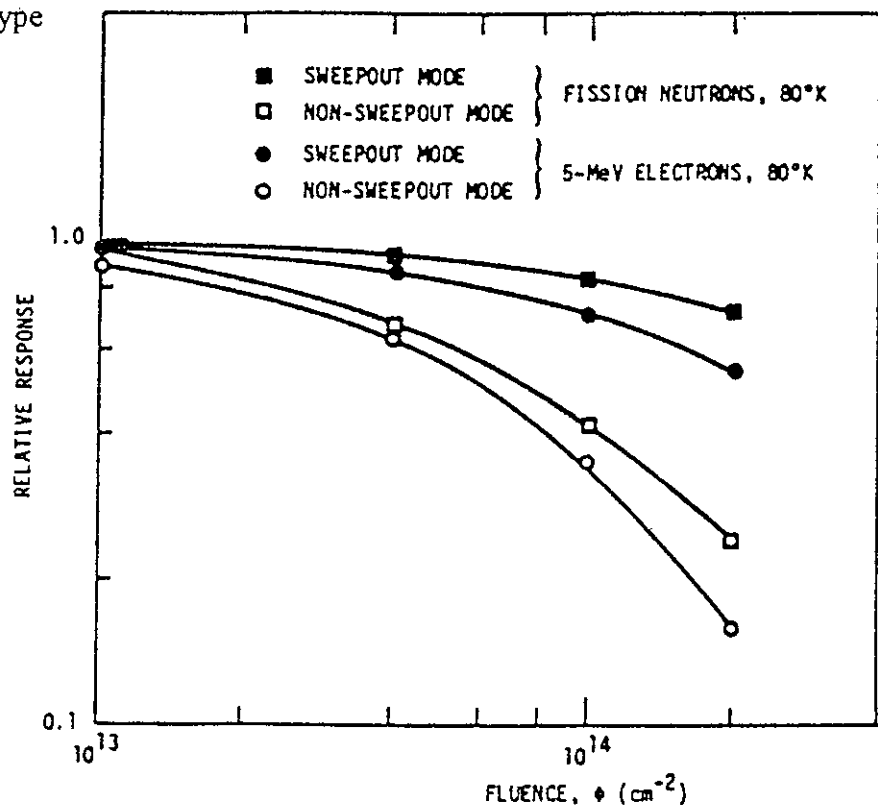


Figure 3.2-1 Relative response of PC MCT detectors versus electron and fission neutron fluence [5]

High Temperature Measurements

The electron irradiation experiments of Voitshovski et al [11] were performed with the MCT samples at a temperature of 300K during irradiation. For high electron fluences up to about $2 \times 10^{18}/\text{cm}^2$, the initially n-type samples showed no significant change in carrier concentration. *The initially p-type samples converted to n-type* at a dose of $5-8 \times 10^{17} \text{ cm}^{-3}$. Unlike the earlier low temperature results, these donor defects introduced at 300K were relatively stable and only annealed in the 360-430K temperature range.

Petrosky [4] quotes results from Morral who used Hall measurements to characterize changes due to 30 MeV electrons of bulk p-type MCT wafers. He found that at $\sim 295 \text{ K}$ p to n-type conversion occurred after $6 \times 10^{15} \text{ e}/\text{cm}^2$. Lowering the temperature reversed the effect. No conversion occurred at low temperatures (below $\sim 240 \text{ K}$), suggesting that a donor level can be created which dominates at high temperatures, but is frozen in at lower temperatures.

The results of all the early electron irradiations have been summarized by Reine et al [12] as shown in Table 3 2-1.

These studies were extended to simple devices by irradiating unpassivated (native oxide only) mesa diodes with 6 MeV electrons (which have enough energy to displace any of the constituent atoms) at 77 K and 193 K ($x = 0.3$) (Domkowski et al [13]). The reverse leakage current I_R and rms noise were measured as a function of dose. At 77K for fluences up to $10^{14} \text{ e}/\text{cm}^2$ (2.8 Mrads) the I_R values were unchanged, however in going from $10^{14} \text{ e}/\text{cm}^2$ to $10^{15} \text{ e}/\text{cm}^2$ the I_R values increased by $\times 100$. Maintaining the sample temperature at 77K after the irradiation ceased resulted in a slight annealing effect, but after 15 minutes at 300 K the I_R value had reduced by $\times 10$. If the irradiation temperature is now changed to 193 K no increase is observed in I_R until a dose of $10^{15} \text{ e}/\text{cm}^2$, thus the device appears to be radiation hard at this higher temperature. However it must be remembered that now the I_R values are larger and possibly masking any small radiation induced changes, also some annealing may be taking place. *After the irradiation a short anneal at 300K removed the observed increase in I_R .* The accompanying radiation induced increase in rms noise could not be fully accounted for by the increased leakage and may have a contribution from surface effects. Note that these bare etched mesa diodes remained useful up to the 2.8 Mrad dose at 77 K (and operation at 193 K extended the radiation tolerance by a further factor 10 at the expense of poorer initial performance).

3.3 TYPE CONVERSION

As mentioned above, Melngailis et al [8] found that p-type samples irradiated at 25 K with 2.5 MeV electrons ($4.7 \times 10^{15} \text{ e}/\text{cm}^2$) changed to n-type. Foyt et al [14] were the first to report type conversion with protons. n-p junction photovoltaic detectors with $x = 0.50, 0.31$ and 0.25 were created using 100 keV and 200 keV protons (with fluences in the range 1.6 to $5 \times 10^{14} \text{ p}/\text{cm}^2$). Since then ion implantation (bombardment by heavy ions) has become a standard technique for type conversion. Early work has been reviewed by Reine et al [10] and the present situation is discussed by Destéfanis [3]. Radiation damage is of major use in junction formation because it leads to the formation of an n+ layer in a very reproducible way, depending very little on implantation conditions or on the initial doping of the crystal. Recently n-p and p-n junctions have been obtained after annealing of implantation defects and activation of implanted impurities (indium or arsenic).

The technique of ion beam milling is an interesting example of type conversion. This process is used for example in the loophole diodes manufactured by G-MIRL (cf section 1.4.1.1). The milling process (to create the central loophole) also produces type conversion, in fact to a depth much greater than the penetration of the ions, by a process of diffusion of Hg interstitials. Ion beam milling has recently been reviewed by Bahir and Finkman [15].

3.4 CHANGES IN SPECTRAL RESPONSE

As noted by Shepherd [16], photovoltaic (PV) devices and photoluminescent (PL) data show that the spectral response of CdHgTe broadens after high electron fluences ($\sim 10^{15}$ - 2.5 MeV e/cm^2) and there is the production of a long wavelength tail. In contrast PC devices show a shift to lower wavelengths. These effects are explained by the types of transitions that occur when IR radiation is absorbed in these devices (figure 3.4-1). This is described in detail in [15]. Basically the electron radiation introduces donor defects and electrons and these fill the lower conduction band of the MCT resulting in a situation of electron degeneracy (overlap of wavefunctions). The onset of degeneracy can occur at donor electron concentrations as low as $10^{13}/\text{cm}^3$ because of the low density of states and effective mass of MCT.

At high defect densities the conduction band no longer has a sharp edge but statistical fluctuations in defect density cause the conduction band energy to vary from point to point in the crystal which leads to a spreading of the conduction band into the forbidden gap (and hence a long wavelength tail in PV devices). This effect is more pronounced at longer wavelengths (lower x) and higher fluences exhibit the *Burstein-Moss effect* which is a shift in response to lower wavelengths. This arises because the radiation-induced donor electrons are allowed to fill the lower conduction band and tail states and transitions can only occur between the valence band and unoccupied states higher in the conduction band (hence the shift to shorter wavelengths). Again the shift is worse for longer wavelength detectors and higher fluences. Although the conduction band tail states are filled for PV detector, the valence band edge is also smeared and there is an equivalent valence band tail in the energy gap.

Note that high fluences (of the order 10^{14} - 10^{15} e/cm^2) are needed to cause appreciable changes in spectral response in all devices - corresponding to several Mrad of total ionizing dose.

PC detectors will also experience an increase in dark current because of the introduction of donor electrons into the conduction band which effectively constitute a free-electron gas. The free electron dark current is not present, however, in PV devices unless the fluence is high enough to cause type conversion (p- to n- type) in which case the device would in any case be destroyed.

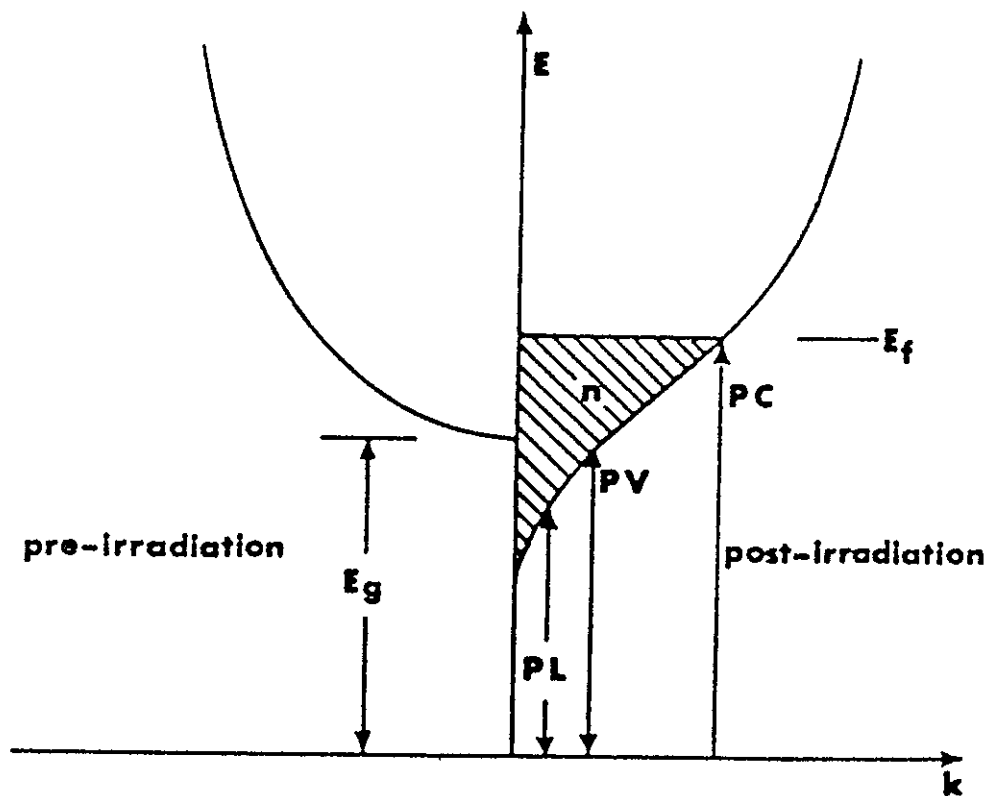


Figure 3 4-1 Schematic representation of the MCT density of states before and after irradiation [15] PL, PV and PC refer to photoluminescent, photovoltaic and photoconductive transitions respectively

Table 3.2-1 Electron Irradiation Experiments in HgCdTe (from [17])

Electron energy (MeV)	Maximum electron fluence (cm ⁻²)	Sample temperature during irradiation (K)	Preirradiation electrical type	Preirradiation carrier concentration ^a (cm ⁻³)	Preirradiation mobility ^a (cm ² /v sec ⁻¹)	Alloy composition	Donor introduction rate ^b (cm ⁻¹)	Reference
2.5	4.7 x 10 ¹⁵	25	p	2.5 x 10 ¹⁶	780	0.22	28	Melngailis et al (1973) [8]
5	5 x 10 ¹⁴	80	p	4 x 10 ¹⁶	300	0.31	-	Mallon et al (1973) [7]
5	4 x 10 ¹⁴	10 80	n	2.6 x 10 ¹⁴	5.8 x 10 ¹⁴	0.188	5.7	Mallon et al (1975) [5]
5	8.5 x 10 ¹⁴	80	n	1.3 x 10 ¹⁵	1.5 x 10 ¹⁵	0.20	16 (10K) 6 (80K)	Leadon and Mallon (1975) Brudnyi et al (1977) and Votsehovshi et al (1979)[9]
2	2 x 10 ¹⁸	300	p	6 x 10 ¹³	322	0.26		
	n	1.7 x 10 ¹⁵	p	2.7 x 10 ¹⁶	117	0.26		
			2.5 x 10 ⁴	9.6 x 10 ¹⁶				
			n	0.24				
			n	1.2 x 10 ¹⁵	1 x 10 ⁵	0.26		
			n	2.6 x 10 ¹⁵	2 x 10 ⁴	0.28		

a Based on 80/K Hall data.

b Measured at the temperature of sample irradiation

- [1] J C Pickel, 'Novel devices and sensors', *Short Course Notes*, IEEE Nuclear and Space Radiation Effects Conference, Snowbird, Utah, July 19, 1993
- [2] G R Hopkinson, C J Baddiley, D R P Guy and J E Parsons, 'Total Dose and Proton Testing of a Commercial HgCdTe Array' *IEEE Transactions on Nuclear Science*, vol NS-41(6), pp 1966-1973, (1994)
- [3] G L Destéfánis, 'Electrical doping of HgCdTe by ion implantation and heat treatment', *J Crystal growth*, vol 86, pp 700-722 (1988)
- [4] J Favre, M Konczykowski and C Blanchard, Défauts d'irradiation dans les alliages $Hg_{1-x}Cd_xTe$, (in French), *Annales de Physique*, vol 14, pp 193-202 (December 1989)
- [5] J C Petrosky, 'Modeling the total dose radiation effects of $Hg_{1-x}Cd_xTe$ photodiodes using numerical device simulators', Defense Nuclear Agency Technical Report DNA-TR-93-50, January 1994
- [6] A H Kalma, 'Nuclear and space radiation effects in infrared detectors', in Advances in Focal Plane Technology, *Proc SPIE*, vol 217, pp 186-191 (1980)
- [7] C E Mallon, B A Green, R E Leadon and J A Naber, 'Radiation effects in $Hg_{1-x}Cd_xTe$ ', *IEEE Trans on Nuclear Science*, NS-22(6), 2283-2288 (1975)
- [8] J A Naber, R E Leadon, H T Harper, B A Green and C E Mallon, Inst Phys Conference Ser No 23, p 325 (1975)
- [9] C E Mallon, J A Naber, J F Colwell and B A Green, 'Effects of electron irradiation on the electrical and optical properties of HgCdTe', *IEEE Trans on Nuclear Science*, vol NS-20(6), pp 214-219 (1973)
- [10] J Melngailis, J L Ryan and T C Harman, 'Electron radiation damage and annealing of $Hg_{1-x}Cd_xTe$ at low temperatures', *J Appl phys*, vol 44(6), pp 2647-2651 (1973)
- [11] A V Voitshovski, V N Broudnyi, Y V Lilenko, M A Kirov and A S Petrov, 'High temperature defects in electron irradiated semiconductors HgCdTe, PbSnTe', *Solid State Communications*, vol 31, pp 105-108 (1979)
- [12] M B Reine, A K Sood and T J Tredwell, 'Photovoltaic Infrared Detectors', in Semiconductors and Semimetals, 18, R K Willardson and A C Beer (eds), pp 201-311 (Academic Press, 1981)
- [13] D W Domkowski, D G Feller, L R Johnson, C I Westmark, C B Norris, C T Fuller and J Bajaj, 'Effects of 6 MeV electron irradiation on the electrical characteristics of LPE $Hg_{0.7}Cd_{0.3}Te$ mesa photodiodes', *IEEE Trans on Nuclear Science*, vol NS-33(6), pp 1471-1473 (1986)
- [14] A G Foyt, T C Harmon and J P Donnelly, 'Type conversion and n-p junction formation in $Hg_{1-x}Cd_xTe$ produced by proton bombardment', *Appl Phys Lett*, vol 18(8), pp 321-323 (1971)

-
- [15] G. Bahır and E. Finkman, 'Ion beam milling effect on electrical properties of $\text{Hg}_{1-x}\text{Cd}_x\text{Te}$ ', *J Vac Sci Technol*, vol. A7(2), pp. 348-353 (1989)
- [16] F. D. Shepherd, 'Radiation effects on the spectral response of HgCdTe ', *IEEE Trans on Nuclear Science*, vol. NS-21(6), pp. 34-39 (1974)

4 BASIC BULK EFFECTS ON OTHER DETECTOR MATERIALS

As in section 3 (on MCT), this section concentrates on effects in bulk material or simple devices such as photodiodes or solar cells. Most of the available literature is on InSb, GaAs and GaAs alloys.

4.1 InSb

InSb is a III-V semiconductor. Its behaviour is dominated by three electron trapping states: one just below the conduction band and the others being mid-gap states at approximately 100 meV and 150 meV above the valence band. The electron trapping effectively immobilizes photoexcited electrons and the dominant photo-effects are due to holes. As in MCT the interpretation of displacement damage data is complicated by the fact that there is more than 1 lattice (2 sublattices in this case). The average displacement energy for In and Sb is 7.7 eV [1]. There is little information available on basic radiation effects, but some electron irradiation studies, particularly by Russian workers show similarities in displacement effects between InSb and MCT.

In most of the reported materials studies, both n and p type InSb has been irradiated with MeV electrons and the electrical properties, eg conductivity, Hall coefficient, measured. Some confusion exists over the details concerning the comparison of data from room temperature and low temperature irradiation. Irradiation at 80K gives opposite results to that at 300K, in the former the hole concentration increases with dose and eventually n type material is converted to p type, whereas at 300K p type is converted to n.

Irradiation with 4.5, 15 and 25 MeV electrons [2] at 300K converted p to n as did a 77K irradiation if followed by a 300K anneal. It was proposed that at low temperature both donor and acceptor defects were produced, but at 300K the donor defect predominates. The relative production rates of both types of defect are dose rate dependent (Vitovskii et al [3]) for 7 MeV electron irradiation to fluences of 10^{18} e/cm². At high dose rates additional complexes are generated compared to the low temperature case. For these n type samples total annealing was observed at 300K. In an extension of this study (Vitovskii et al [4]) 50 MeV electrons, again at very high fluences $\sim 10^{16}$ - 10^{17} e/cm², were used to irradiate n and p type material at 300K, conversion to n type (for the p type) was confirmed. Annealing at 100-200°C returned all samples to the pre-irradiation condition. In this early work the donor, acceptor nature of the defects were investigated and energy levels identified.

After further 25 MeV electron irradiations it was concluded that oxygen was involved in a complex defect exhibiting donor properties (Zaitov et al [5]). Changes in the acceptor level were independent of impurity concentration. From this study it was concluded that a vacancy on the antimony sublattice (V_{Sb}) was also involved in donor formation. This model was also suggested from an attempt to convert n to p type at 300K using 4-8 MeV electrons, this in contrast to the opposite effect reported earlier (Skipetrov et al [6]). These authors proposed that indium sublattice defects act as acceptors whereas antimony sublattice defects act as donors. For irradiation at 300K the indium defect concentration rises at a faster rate because indium has a lower displacement threshold. The dominant acceptor level in all these studies is at $E_c - 0.05$ eV.

Type conversion should therefore be possible using other types of radiation if the process is based on atomic displacement. Proton irradiation at 17.5 MeV to doses of 10^{12} - 10^{15} /cm² of both n and p type material produced n type conversion, while still producing the acceptor level at $E_c - 0.05$ eV (Zaitov et al [7]). The damage could be annealed at 300°C. The same defect distribution was observed in the irradiated samples as on the original n type ones, and those which had previously been electron irradiated. The possibility of the existence of a large disordered region has not been resolved.

The basic displacement mechanism is similar for all compound materials. Both donor and acceptor defects are possible and therefore type conversion can be achieved. The relative production rates of each defect type may well be impurity and temperature dependent. However it is probably not relevant to apply that data to the space irradiation environment because many, if not all, of the total fluences used are in excess of those expected in orbit.

The first use of type conversion to produce diodes was described by Foyt et al [8]. In an experiment analogous to that carried out for MCT, p type InSb was irradiated with 100 keV protons to a dose of 10^{14} p/cm². This converted localised (by masking) regions of p type materials (5×10^{15} /cm³) to n type (5×10^{13} /cm³). The diodes produced were successfully used as infrared detectors.

The effects of displacement damage on the performance of InSb infrared detectors has been studied using fast neutrons (Wilsey et al [9]). Both photoconductive and photovoltaic mesa structures were used and irradiated with 14 MeV neutrons to fluences of 5×10^{12} n/cm². The photovoltaic detector is a minority carrier device, whereas the photoconductive devices use majority carriers. The former device should therefore be more displacement damage sensitive as this process affects minority carrier lifetime, mobility and diffusion length and indeed the photovoltaic devices were found to be more radiation sensitive. With increasing neutron dose the signal to noise ratio decreased whereas that of the photoconductive devices remained relatively unchanged. Figure 4.1-1 shows the effect of the neutron fluence on relative signal. Note that in comparison with figure 5.2-1 for MCT the InSb damage starts to occur at a lower fluence (see also figure 3.3-2).

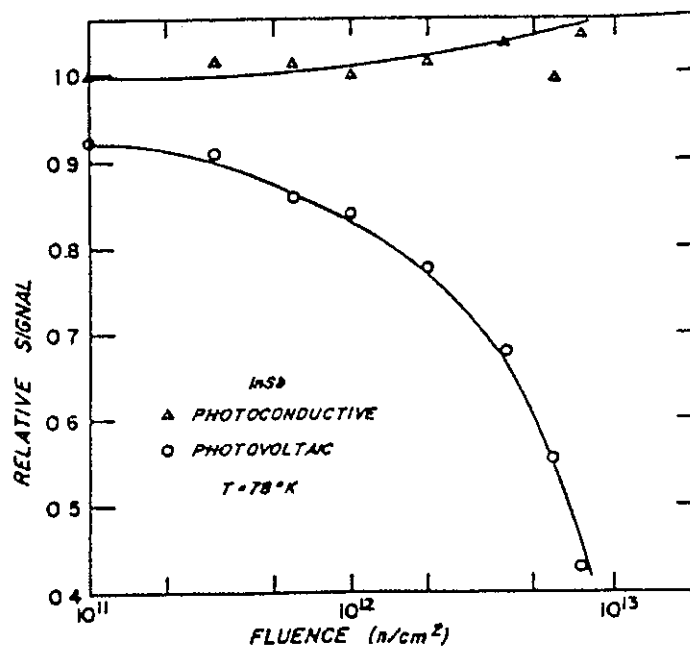


Figure 4.1-1 Comparison of relative signal versus 14 MeV neutron fluence for InSb PC and PV detectors [9]

Room temperature 2.5 MeV electron irradiation of injection photodiodes resulted in a decrease in hole mobility after a dose of 10^{14} e⁻cm⁻², this fluence was not sufficient to achieve type conversion (Kurmasher et al, [10]). Analysis of their results led these authors to conclude that interstitial atoms of both types act as shallow donors, whereas Sb vacancies are shallow acceptors and In vacancies are deep donors, these conclusions are in some conflict with those of previous studies

4.2 GaAs and its Alloys

GaAs is another III-V semiconductor similar in structure to InSb. The main interest for IR detectors is in GaAs readouts, GaAlAs/GaAs quantum well devices and InGaAs SWIR detectors. It has been extensively studied due to its importance in communications devices. Barnes and Greenwell [11] have recently summarized the literature available on GaAs and InGaAs devices as part of their exhaustive review on photonic modulators.

GaAs devices have no equivalent of an oxide layer and so permanent degradation due to ionization effects does not occur until a total dose of 10 Mrad or higher. As an example, Witmer et al [12] found little change in performance for GaAs/AlGaAs and InGaAs/AlInGaAs heterojunction bipolar transistors until a total dose (cobalt60) of ~ 80 Mrad.

Hence we expect the main radiation effects to be due to the creation of defect centres by displacement damage. However, despite the large amount of work performed on GaAs and related compounds, the identification of defect centres is not clear-cut. A good summary of early work has been given by Pons and Bougoin [13]. They suggest that most defects are due to the creation of vacancy/interstitial pairs in the As sublattice and that vacancy/interstitial pairs in the Ga sublattice recombine soon after irradiation. The resulting defects are electron traps (for example the well known EL2 defect, which is associated with the As antisite). This view is repeated in several more recent publications - for example Bourgoïn et al [14], Ziebro et al [15] and Shaw et al [16]. However Khanna et al [17,18] have recently found evidence for defects related to the gallium vacancy. They suggest that the EL2 defect is not seen in MBE GaAs (a material important for modern devices such as QWIPs). Instead they saw defect complexes which anneal at 450°C (the EL2 anneals at 820°C). In n-type (silicon doped) GaAs these complexes probably involve the divacancy ($V_{As} + V_{Ga}$) and the silicon dopant atom transferred from the gallium site (Si_{Ga}) to the arsenic site (Si_{As}). The annealing results in the release of As and an increase in the number of gallium vacancies. These vacancies can be replaced by another atom, for example to form an As antisite. In p-type (zinc doped) GaAs the complexes formed by irradiation may involve zinc dopant atoms and arsenic vacancies [17].

The correlation of damage with NIEL has been discussed by Summers et al [19,20] and Xapsos et al [21]. Khanna et al [17] discuss this work and have performed a detailed investigation of the correlation of damage (as measured by a photoluminescence technique) with NIEL - for protons, electrons, neutrons and cobalt60 gammas. Discrepancies were seen for cobalt60, probably because the Compton electrons produced do not have enough energy to form complexes. The defects produced by protons and neutrons also differ as do effects in n-type compared with p-type GaAs. In a study on proton irradiated GaAs LEDs, Barry et al [22] found good agreement with the proton NIEL except for energies above 150 MeV. Again this may be due to differences in the defects (possibly damage clusters) created.

The conclusion is that defect identifications are tentative at this time and also that care must be exercised in extrapolating damage data from one particle type to another.

Lehmann et al [23] have discussed the energy threshold for displacement damage (T_d). Previously, several authors had provided data consistent with $T_d = 25$ eV by studies of device resistivity, carrier mobility or carrier concentration. Other papers dealing with lifetime measurements or developed transient spectroscopy (DLTS) give values of 9-10 eV. Reference [12] suggests values of 15.5 eV for n-type, $\langle 100 \rangle$ GaAs and 9 eV for the $\langle 111 \rangle$ orientation. That there is an angle dependence is a result of the presence of two sublattices (as for InSb also). For electron irradiated n-GaAs they found fine majority carrier trap levels in every case.

4.2.1 GaAs Alloys

Basic work on proton-induced defects in AlGaAs-GaAs solar cells was reviewed by Li et al [24]. A more recent study has been performed by Shaw et al [16], who observed an increase in the leakage current of $\text{In}_{0.53}\text{Ga}_{0.47}\text{As}$ diodes irradiated with 1 MeV electrons. This was attributed to defects produced by displacements in the As sublattice (but see the comments above about defect identifications). The damage annealed in timescales ~ 1 day at 300 K, but with a logarithmic dependence on time, suggestive of a range in activation energies (and hence a degree of local disorder in the lattice). The results also indicated that the annealing behaviour in InGaAs may depend on particle flux and temperature. Note that if the material is not lattice matched to the substrate (InP), then dislocation loops can be formed at the interface. This may lead to additional radiation effects.

Degradation in InGaAs photodiodes by fast neutrons has been discussed by Ohyama et al [25] and the effect of high ($>10^{14}/\text{cm}^2$) electron fluence on InGaAs solar cells by Walters et al [26] - who also give theoretical NIEL curves for protons and neutrons, assuming displacement energies of 6.7 eV for In, 10.0 eV for Ga and 8.8 eV for As (figure 4.1-2). Effects in InGaAs/GaAs/AlGaAs quantum well laser diodes have been studied by Evans et al [27].

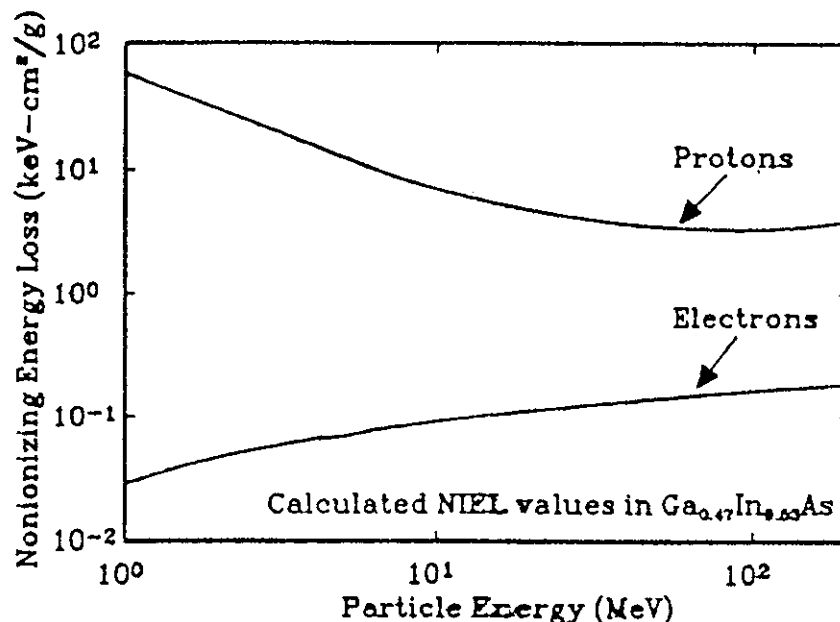


Figure 4.1-2 Theoretical NIEL curves for $\text{In}_{0.53}\text{Ga}_{0.47}\text{As}$ (from [26])

As discussed in section 1.4.3, the fabrication of multilayer structures gives rise to band-offsets. According to Bourgoin et al [13] the characteristics of a defect are only perturbed by the potential step produced by the band offset if the distance of the defect from the heterostructure interface is less than the spatial extent of the defect wavefunction. Thus deep levels whose wavefunctions are localised within one or two interatomic distances are not perturbed by the presence of an interface provided that they do not lie at the interface itself. This means that a defect energy level, E_T , and its capture cross-section, remain linked to the original band structure of the material which composes the heterostructure. Consequently when the structure is a superlattice, i.e. a periodic heterostructure in which the original bands of the materials which compose the well and barriers are replaced by minibands, the energetical location of the defect level within the superlattice gap becomes (see figure 4.1-3)

$$E_w = E_T + \delta$$

or

$$E_b = E_T - \Delta + \delta$$

for a defect located in a well or in a barrier, respectively

In principle, then, in superlattices the new defect characteristics can be deduced once the superlattice band structure is known and the problem of defect characterisation and identification is the same as for bulk materials. Bourgoin et al [13] have illustrated this for the EL2 and DX centre defects. However the knowledge and understanding of the defects is still at an early stage.

The fact that, for defects located away from the interfaces, defect levels remain unchanged even when the band structure of the heterostructure is changed (into a series of minibands) implies that defect levels can act as probes to determine band offsets and structure [28].

Barnes et al [29] have reported on gamma and neutron irradiation of GaP/GaAsP strained layer superlattices. They found that the majority carrier removal rate for neutron irradiation was less in the SLS samples (figure 4.1-3) and that gamma irradiation to $\sim 10^8$ rad doses produced oscillations in the doping profile, possibly due to the creation of composition-dependent point-like defects (figure 4.1-4).

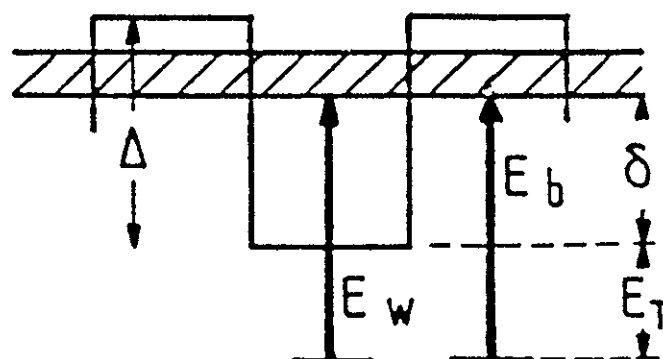


Figure 4.1-3 Electron emission (E_w and E_b) into the miniband from a defect level located in the barrier (b) or the well (w) of a superlattice [14]

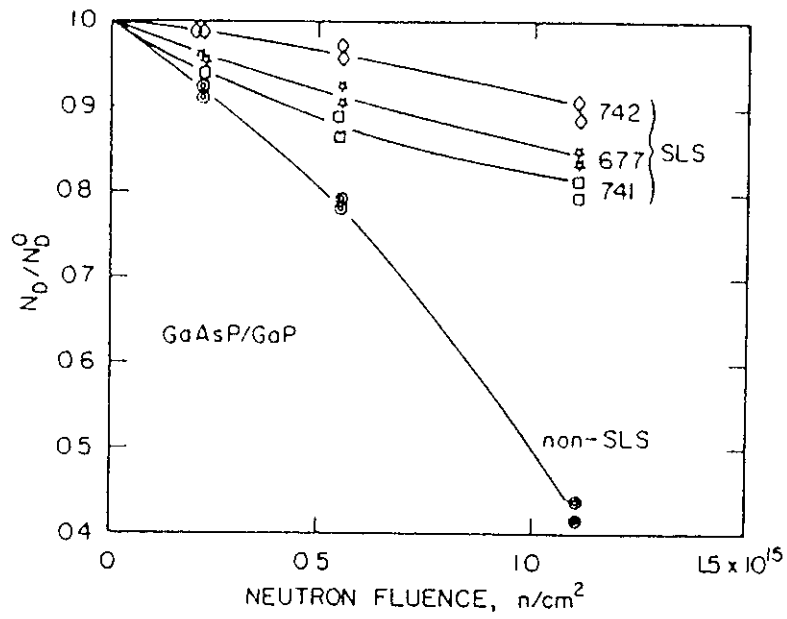


Figure 4.1-4 Normalized carrier removal for neutron irradiation of a GaP/GaAsP superlattice [29]

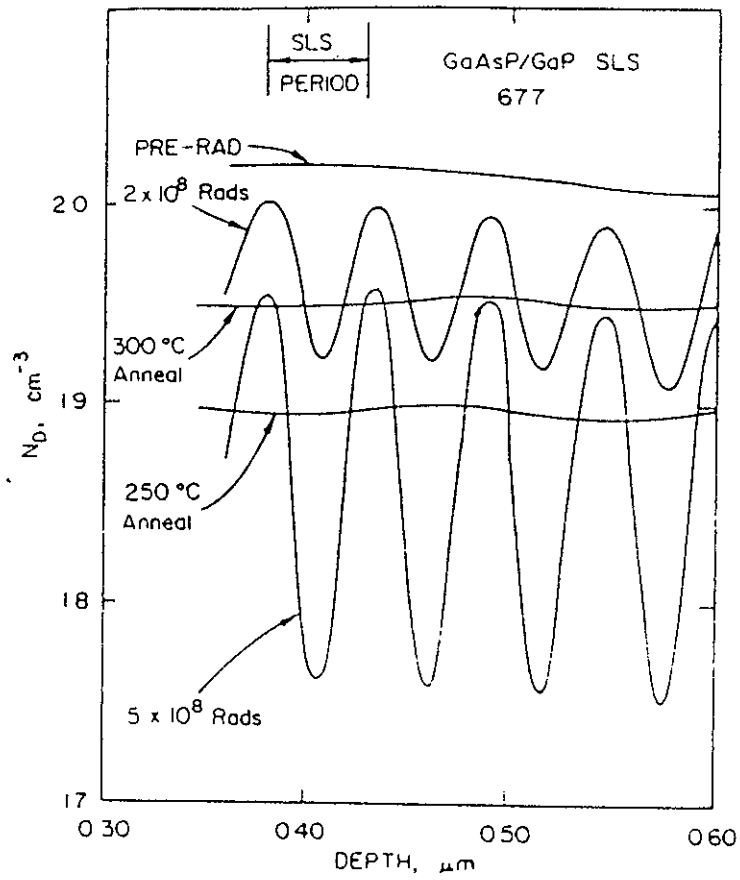


Figure 4.1-4 Gamma-induced modifications in donor doping profile in a GaP/GaAsP superlattice [29]

Recently Khanna et al [30] have performed proton and alpha particle irradiations of discrete GaAs/AlGaAs quantum well infrared photodiodes (QWIPs) They found that performance was only affected only for high fluences The suggested mechanism is that the displacement damage leads to carrier removal and degradation in carrier mobility and lifetime The main effect is to remove electrons from the quantum wells Since the dark current depends exponentially on the carrier density this is affected more than the responsivity (which depends linearly on the carrier density) Also the effect of defects in the barriers tends to increase the effective barrier height [31] and this leads to a further decrease in dark current For 10 MeV proton irradiation, Khanna et al found significant changes (a factor 2 decrease in responsivity and a five-fold decrease in dark current) only for the highest fluence used (10^{14} p/cm²) This is very encouraging for the use of quantum well detectors in space applications

4.3 SILICON

Silicon is important as the material for multiplexers and support electronics, Si X detectors and internal photoemission (Schottky barrier and HIP) devices Displacement damage can introduce a number of stable defects into the Si bandgap [32] gives a reasonably up to date list) As discussed in section 3 3 permanent bulk displacement damage is not likely to be important for Si multiplexers since the operating temperature is low Likewise ionization effects will, in most cases, dominate for Si support electronics In extrinsic Si X detectors (discussed in section 7) it is the trapping of ionization induced charge that is important for the loss in responsivity of these detectors

4.4 HIGH T_C SUPERCONDUCTORS

As discussed in section 2.4, high T_c superconductors can be used as IR detectors Displacement damage will cause shifts in the transition temperature as discussed by Summers et al [33] and recently by Lombardo et al [34] and Weaver et al, [35]

4.5 REFERENCES

-
- [1] F H Eisen, 'III-V Compound review', *Radiation Effects*, vol 9, pp 235-242 (1971)
 - [2] F A Zaitov and A Ya Polyakov, *Sov Phys. Semiconductors*, vol 12(9), p 1055, (1978)
 - [3] N A Vitovskii, T V Mashovets and O V Oganessian, *Sov Phys Semiconductors*, vol 12, p 1277 (1978)
 - [4] N A Vitovskii, T V Mashovets, O V Oganessian and N K L Pambukhchyan, *Sov Phys Semiconductors*, vol 13(6), p 664, (1979)
 - [5] F A Zaitov, O V Gorshkova, A Polyakov, M I Kevorkov, A N Popkov and M D Khlystovskaya, *Izv Akad Nauk, SSSR Neorg Mat*, vol 18, p 8, (1982)
 - [6] E P Skipetrov, U V Dmitriev, F A Zaitov, G I Kotsov and E A Ladygin, *Sov Phys. Semiconductors*, vol 20(10), p 1120, (1986)

-
- [7] F A Zaitov, O V Gorshkova, V N Ovanesov and A Ya Polyakov, *Sov Phys Semiconductors*, vol 14(2), p 234, (1980)
- [8] A G Foyt, W T Lindley and J P Donnelly, 'n-p junction photodetectors in InSb fabricated by proton bombardment', *Appl Phys Lett*, vol 16(9), pp 335-337 (1979)
- [9] N D Wilsey, C S Guenzer, B Moinar and W J Moore, 'A comparison of fast neutron irradiation effects in photoconductive and photovoltaic InSb infrared detectors', *IEEE Trans on Nuclear Science*, vol NS-27(6), pp 2448-2445, (1975)
- [10] S D Kurmasher, O P Dem'yanchuk and I I Chalaya, *Sov Phys Semiconductors*, vol 20(5), p 585, (1986)
- [11] C Barnes and R Greenwell, 'Radiation effects in photonic modulator structures', *Proc SPIE*, vol 2482, pp 48-98 (1995)
- [12] S B Witmer, S D Mittleman, D Lehy, F Ren, T R Fullowan, R F Kopf, C R Abernathy, S J Pearton, D A Humphrey, R K Montgomery, P R Smith, J P Kreskovsky and H L Grubin, "The effects of ionizing radiation on GaAs/AlGaAs and InGaAs/AlInAs heterojunction bipolar transistors", *Materials Science and Eng*, vol B20, pp 280-291 (1993)
- [13] D Pons and J C Bougoin, "Irradiation-induced defects in GaAs", *J Phys C Solid State Phys*, vol 18, pp3839-3871 (1985)
- [14] J G Bourgoïn, S L Feng and H J von Bardeleben, 'Deep levels in III-V compounds, heterostructures and superlattices', in Physical concepts of materials for novel optoelectronic device applications, *Proc SPIE*, vol 1361, pp 184-194 (1990)
- [15] B Ziebro, J W Hemsley and D C Look, "Defect models in electron-irradiated n-type GaAs", *J Appl. Phys*, vol 72(1), pp 78-81 (1992)
- [16] G J Shaw, R. J Walters, S R Messenger and G P Summers, 'Time dependence of radiation-induced generation currents in irradiated InGaAs photodiodes', *J Appl Phys*, vol 74(3), pp 1629-1635 (1993)
- [17] S M Khanna, A Jorio, C Carlone, M Parenteau, A Houdayer and J W Gerdes Jr, "Nuclear displacement damage prediction in gallium arsenide through low temperature photoluminescence measurements", *IEEE Trans Nuclear Science*, vol 43(6) pp 2601-2608 (1996)
- [18] S M Khanna, A Houdayer, A Jorio, C Carlone, M Parenteau and J W Gerdes Jr, "Particle dependence of the gallium vacancy production in irradiated n-type gallium arsenide", *IEEE Trans Nuclear Science*, vol 42(6) pp 2095-2103 (1995)
- [19] G P Summers, E A Burke, M A Xapsos, C J Dale, P W Marshall and E L Petersen, 'Displacement damage in GaAs structures', *IEEE Trans on Nuclear Science*, vol NS-35(6), pp 1221-1226 (1988)

- [20] G P Summers, E A Burke, P Shapiro, S R Messenger and R J Walters, "Damage correlations in semiconductors exposed to gamma electron and proton irradiations" *IEEE Trans on Nuclear Science*, vol NS-40(6), pp 1372-1379 (1993)
- [21] M A Xapsos, G P Summers C C Blatchley, C W Colerico, E A Burke, S R Messenger and P Shapiro, "Co60 gamma ray and electron displacement damage studies of semiconductors", *IEEE Trans on Nuclear Science*, vol NS-41(6), pp 1945-1949 (1994)
- [22] A L Barry, A J Houdayer, P F Hinrichsen, W G Letourneau and J Vincent, "The energy dependence of lifetime damage constants in GaAs LEDs for 1-500 MeV protons, *IEEE Trans Nuclear Science*, vol 4, pp, (1994)
- [23] B Lehmann, M Brière, D Braunig and A L Barry, 'Displacement threshold energy in GaAs determined by electrical and optical investigations', *Proc ESA Electronics Components Conference*, ESTEC, Noordwijk, The Netherlands, 12-16 November 1990, ESA SP-313 (March 1991)
- [24] S S Li, W -L Wang, P -W Lai, R Y Loo, G S Kamath and R C Knechtli, 'Deep level defects, recombination mechanisms and their correlation to the performance of low-energy proton-irradiated AlGaAs-GaAs solar cells', *IEEE Trans on Electron Devices*, vol ED-27(4), pp 857-864 (1980)
- [25] H Ohyama, J Vanhellefont, Y Takami, K Hayama, T Kudou, T Hakata, S Kohiki and H Sunaga, "Degradation and recovery of In_{0.53}Ga_{0.47}As photodiodes by 1-MeV fast neutrons", *IEEE Trans Nuclear Science*, vol 43(6), pp 3019-3026 (1996)
- [26] R J Walters, G J Shaw, G P Summers, E A Burke and S R Messenger, "Radiation effects in Ga_{0.47}In_{0.53}As devices" *IEEE Trans Nuclear Science*, vol 39(6), pp 2257-2264 (1992)
- [27] B D Evans, H E Hager and B W Hughlock, "5.5 MeV proton irradiation of a strained quantum well laser diode and a multiple quantum-well broad-band LED", *IEEE Trans Nuclear Science*, vol 40(6), pp, (1993)
- [28] S L Feng, J C Bourgoin, A Mauger, D Stiévenard, E Barbier, J P Hirtz and A Chomette, 'Point defects in GaAsGa_{1-x}Al_xAs superlattices', *Phys Rev B*, vol 39(18), pp 13252-13263 (1989)
- [29] C E Barnes, G A Samara, R M Biefeld, T E Zipperian and G C Osbourn, 'Radiation effects in strained layer superlattice (SLS) structures', *Proc 13th International Conference on defects in semiconductors*, Coronado CA, August 12-17, 1984, The Metallurgical Society of AIME, pp 471-477 (1985)
- [30] S M Khanna, H C Liu, P H Wilson, L Li and M Buchanan, "High energy proton and alpha radiation effects on GaAs/AlGaAs quantum well infrared photodetectors", *IEEE Trans Nuclear Science*, vol 43(6), pp 3012-3018 (1996)

-
- [31] H Chaabane and J C Bougoin, "Irradiation effect on electron transport through GaAlAs barriers", *Appl Phys Lett*, vol 64(8), pp 1006-1008 (1994)
- [32] W Fengmei and Z Xiangqin, 'Structure of electron-induced defects in silicon', in *Properties of Silicon*, emis data reviews no 4 (IEE, INSPEC, 1988)
- [33] G P Summers, D B Chrisey, W G Maisch, G H Strauss, E A Burke, M Nastasi and J R Tesmer, 'Electron and proton radiation effects in the high temperature superconductor $\text{YBa}_2\text{Cu}_3\text{O}_7$ ', *IEEE Trans on Nuclear Science*, vol NS-36(6), pp 1840-1847 (1989)
- [34] L Lombardo, A Kapitulnik, A Leon and R Dammann, 'Alteration in the superconducting properties of $\text{Bi}_2\text{Sr}_2\text{CaCu}_2\text{O}_8$ crystals due to proton irradiation', *IEEE Trans on Nuclear Science* vol NS-38(6), pp (1991)
- [35] B D Weaver, E Jackson, J M Pond, H Newman, G P Summers, D B Chrisey, J S Hurwitz and E A Burke, 'Radiation effects in devices made from high temperature superconductors', *IEEE Trans on Nuclear Science* vol NS-38(6),pp (1991)

5 PERMANENT IONIZATION-INDUCED EFFECTS ON MCT FOCAL PLANE ARRAYS

5.1 INTRODUCTION

In this section we discuss permanent ionization damage in MCT devices and also consider the related material MZT (mercury zinc telluride). MCT arrays are probably the most suitable type for many space-based, relatively high background, applications. Hence this section is one of the most important effects sections in this study. Transient effects and bulk damage were considered in section 2 and bulk damage again in section 3. Ionization damage is important for MCT arrays because of threshold shifts in passivation layers and increases in surface and trap-assisted tunneling currents. Kalma [1] has summarized the general effects on PV MCT arrays as shown in figure 5.1-1, where relative D^* and R_0A product are plotted against relative total dose. In that review Kalma states that

- damage mechanisms are not fully understood and any of several can dominate in a given situation
- standard hardening approaches have not been effective and hardness has not been repeatable, with variations of hardness often observed in the same array

Also it will be seen that annealing effects are important for the low dose rate space environment.

In principle, it seems that with techniques such as MBE growth of heterostructure junctions and attention to passivation technologies and stresses induced during bump-bonding, large area MCT devices can be manufactured in producible quantities with total dose tolerances as high as 1 Mrad. However the tolerance of any particular array, chosen (for example) for its availability or suitability for a given application, may not be as high.

This section will consider the parameters most likely to affect radiation response and will review the published literature on array performance. Since the technology used to passivate the detector surface plays an important part in the tolerance to ionization effects, this will be considered first.

5.2 PASSIVATION TECHNOLOGIES

Passivation of MCT detectors is needed in order to chemically seal the surface and prevent contamination or out diffusion of Hg and also to control the surface potential and reduce the number of surface traps (caused for example by dangling bonds and Hg vacancies).

In the absence of surface states, the energy bands of a semiconductor are flat up to the surface (provided there are no external fields). When surface states are introduced, they may charge the surface either positively or negatively, in order to maintain equilibrium, depending on the relative position of their energy level with respect to the Fermi level. The energy bands at the surface bend, by an amount described by Φ_s , the surface potential and a space-charge layer is formed near the surface.

In $\text{Hg}_{1-x}\text{Cd}_x\text{Te}$ with x in the range 0.2 to 0.3 the bandgap at 77K varies between 0.1 and 0.25 eV. Hence, the surface potential band bending is often of the order of the band gap energy and can easily accumulate, deplete, or invert the surface significantly, thus drastically affecting device performance.

As well as having suitable electrical properties (surface recombination velocity, fixed charge density, dielectric constant etc) the passivating layer needs good adherence and mechanical properties. MCT surface passivation is complex because of the compound nature of the semiconductor, the difference in the chemical properties of the constituents, and also due to the tendency of electrically active defects to form in the interface region during the passivating process. In addition, due to the extreme temperature sensitivity of bare HgCdTe surface, passivation treatments and deposition processes are limited to near room temperature. Because of these features an ideal passivation treatment has not been agreed upon. An excellent review has been given by Nemirovsky and Bahir [2]. Passivations can be divided into three groups

- deposited dielectrics (ZnS , SiO_2 and SiN_x),
- native layers (anodic, plasma and photochemical oxides, anodic and chemical sulphides, and anodic fluorides), and
- heterostructures formed by MBE growth of CdTe or wide band gap MCT

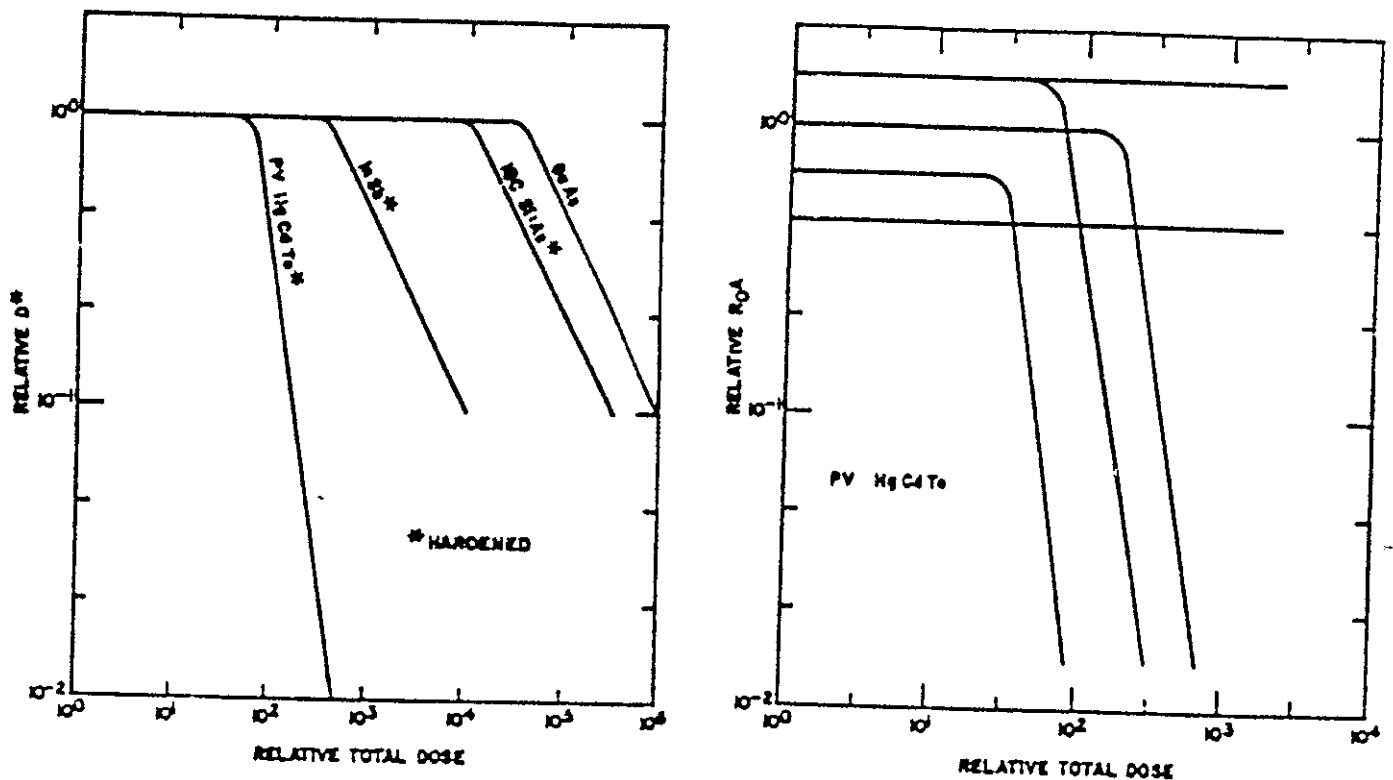


Figure 5.1-1 Relative D^* and R_{0A} for PV MCT devices

In a radiation environment the flatband voltage can change either because of fixed charge build up in the insulator or because of charging of interface traps. This can lead to band bending and changes in surface state (inversion or accumulation). Changes in leakage currents can arise simply from increases in the number of dark current generating states at the surface (increases in surface recombination velocity), because of the creation of new interface states at which trap assisted tunneling can occur, or because the changes in surface state lead to the creation of additional junctions (and associated high field regions). It will be seen in the next section that trap assisted tunneling is particularly important for MCT devices (and the more so the longer the wavelength cut-off and the higher the internal fields). Tunneling is also associated with increased 1/f noise. Charge trapping characteristics of passivation layers are

<u>Passivation</u>	<u>Carriers trapped</u>
ZnS	electrons and holes
SiO ₂	holes
SiN ₃	electrons

5.2.1 MCT MIS Arrays

The most common passivation is the native oxide because of its good interface properties. But since this can only be formed in a thin film it is combined with a deposited layer of ZnS which has a high dielectric strength (and can be used for large area passivations). In a multilevel system (eg a CCD) the ZnS forms the insulator between electrode layers. Unfortunately the native oxide starts to degrade above 65°C [3]. Though the anodic oxide/ZnS system is extensively used, for example by Texas Instruments for CCD, CID, CIM and VIMIS arrays (cf section 1.4.1.2) the thermal stability at 100°C is poor and this is a major drawback for vacuum packaging [4]. Also, anodic oxides incorporate a large fixed positive charge. Other options are to use anodic sulphide/ZnS or to incorporate fluoride ions into the anodic oxide [5], [6]. Anodic sulphides and fluorides are stable at high temperatures and can be tuned to give a flatband condition.

5.2.2 MCT Photodiode Arrays

Anodic oxide, which is commonly used as a passivant on n-type MCT, cannot be used on p-type since it forms a strong inversion layer on p-type material and tends to form a conducting channel between devices. Hence anodic sulphide is often used [7]. Coatings of SiO₂ and ZnS can also be used but they do not chemically react with the surface, thus interface properties are very sensitive to process parameters and may degrade with time. As noted by Nemirovsky and Bahir [2]

'since tunneling (either in the field-induced junction between the inverted surface and bulk material, or between the accumulated surface and junction) is such an important current mechanism in narrow-band-gap HgCdTe photodiodes, it is extremely important to control the surface potential of HgCdTe photodiodes. The smallest dark currents are obtained when the surface adjacent to the junction is in a flat-band condition'

With anodic sulphide (and possibly fluoride) passivation it is possible to approach the flatband condition. With heterostructures it is possible to physically separate the low bandgap active layer from the surface wider gap layer in which high electric fields can be more easily

accommodated. The interface must have a low density of interface states (after irradiation also). As with SiO₂ layers in MOS devices, any of the process parameters (surface preparation, temperature profiles etc) can have a strong effect on radiation tolerance and the exact details of the fabrication process need to be controlled. It is important to note that good starting MCT material is also necessary and growth of better MCT materials and the issue of surface passivation are closely linked [3].

Note that the loop-hole diodes used by GEC-Marconi Infrared Ltd (UK) are something of a special case as regards passivation, since these are lateral collection diodes formed by the ion beam mulling process. The top (backside surface) is coated with ZnS to give an antireflection coating but the junction region near the base contact with the silicon multiplexer is basically passivated by the glue layer. There will be a thin (~50Å) native oxide layer but not enough to give significant inversion at the surface of the n-region.

5.3 DARK CURRENT GENERATION IN PHOTODIODE AND MIS DEVICES

The leakage current in MCT PV diode and MIS arrays can arise from several mechanisms. It is possible to separate these by looking at its dependence on temperature and bias voltage (as well as by using localised irradiation sources such as laser or electron beams). However studies on photodiodes [8], [9] and MIS devices [10] all agree that leakage, both before and after irradiation, is predominantly generated at the device surface and hence ionization rather than bulk displacement damage is the key radiation effect. In this section we look at generation mechanisms in detail. It is convenient to treat diode arrays and MIS devices separately although, ultimately, it is expected that the mechanisms for radiation damage are similar.

Note that as well as giving spurious signal and limiting storage time in the array, the leakage current also has an effect on the dynamic differential (slope) resistance of the diode as a function of reverse bias and is related to the R₀A product.

Since leakage current will be reduced for small area detectors (provided that electric fields are not high at the surface) there is some merit in using microlens arrays in front of the IR detector so as to concentrate the IR illumination onto a smaller area. This technology has been developed, for example, by G-MIRL (UK) [11].

5.3.1 Dark Current Mechanisms in MCT PV Photodiode arrays

Generation mechanisms in photodiodes have been reviewed by Reine et al [12] and more recently by Nemirovsky et al [13] and De Wames et al [14], [15] and can be listed as follows:

- Intrinsic mechanisms
 - * Diffusion current (thermally generated current)
 - n-side
 - p-side
 - * Direct band-to-band (interband) tunneling current (Zener tunneling)

- Defect-mediated mechanisms
 - * Generation-recombination (g-r) current
 - * Trap-assisted tunneling current

Defects can be in the bulk or, as is predominantly the case, at the surface (in which case we can lump the two as a surface leakage current)

5.3.1.1 Diffusion Current

This arises from the random thermal generation and recombination of electron-hole pairs within a minority carrier diffusion length on each side of the depletion layer. In a n-on-p diode the diffusion current is essentially determined by the current from the neutral p-type substrate (the n region is thin). This is fortunate since the n region usually has a graded composition and is difficult to model, though as pointed out by Schacham and Finkman [16], the contribution from the graded n-region can be significant. Similarly in a p-on-n diode the p-region will give a small contribution, though the modeling is somewhat more exact since the p-material does not become degenerate until high doping concentrations are reached [16].

In a n-on-p diode, the dominant p-side term is

$$I_d = eA \frac{n_i^2}{N_A} \frac{kT}{e} \frac{\mu_n}{\tau_n} \frac{1}{2} [\exp(eV/kT) - 1] \quad 5-1$$

where I_d is the diffusion current, V is the bias voltage, N_A is the equilibrium doping level of the substrate, n_i is the bulk intrinsic carrier concentration, A is the junction area, μ_n and τ_n are the minority carrier (electron) mobility and lifetime, respectively.

The dynamic resistance of the diode $R_d = (dI/dV)^{-1}$ is then given by

$$R_d A = \frac{N_A}{en_i^2} \frac{kT}{e} \frac{\tau_n}{\mu_n} \frac{1}{2} \exp(eV/kT) \quad 5-2$$

For a thin p-layer such that the diffusion length \ll the thickness (d) we have

$$R_d A = \frac{kT}{e^2} \frac{N_A}{n_i^2} \frac{\tau_n}{d} \quad 5-3$$

Thus the dominant temperature dependence on the slope resistance at zero bias (R_0) is due to n_i^2 and a logarithmic plot of $R_0 A$ against $1/T$ gives a straight line of slope $-E_g$ (though the temperature dependence of μ_n and τ_n will also have an effect). The diffusion current decreases with temperature decrease. In most good quality diodes the diffusion component dominates for temperatures above about 60 or 70K (pre-irradiation). Note that $R_d A$ increases with reverse bias. Hence operating with a slight negative bias of ~ 50 mV improves the coupling to output circuits.

5.3.1.2 Direct Band-to-band (DBTB) Tunneling

This mechanism dominates at high reverse biases and at low temperatures. These conditions are relevant for low-background applications such as strategic defence and space astronomy, but not for Earth observation. We give a brief discussion here and, for more details, refer the reader to Nemirovsky et al [13] and Adar et al [17] and references therein. As its name implies, this leakage current arises from direct energy-conserving tunneling across the bandgap as shown in figure 5.3.1a)

According to Nimirovsky et al [13], the dynamic resistance is given by

$$(R_{\text{dbtb}}A)^{-1} = \frac{e^2}{2\pi\hbar} \frac{E_g kT}{p^2} T(E_{\text{max}}/2) \quad 5-4$$

where $p = 1.35 \times 10^{-28}$ [Jm] is the matrix element, $E_{\text{max}} = -eV + E_f - E_v$ (E_f and E_v are the Fermi energy and the valence band energy). T is the tunneling probability which is exponentially related to the bandgap and strongly varies with the electric field. With this mechanism, the temperature dependence is fairly weak but the dark current increases (and R decreases) as the temperature is lowered and this sets a limit of $\sim 40\text{K}$ for the useful operation of many MCT devices (as T decreases, the bandgap decreases also - making tunneling more probable). However by lowering the doping this source can be almost eliminated at zero bias and in practice (for MIS devices also) trap-assisted tunneling is usually a more important mechanism

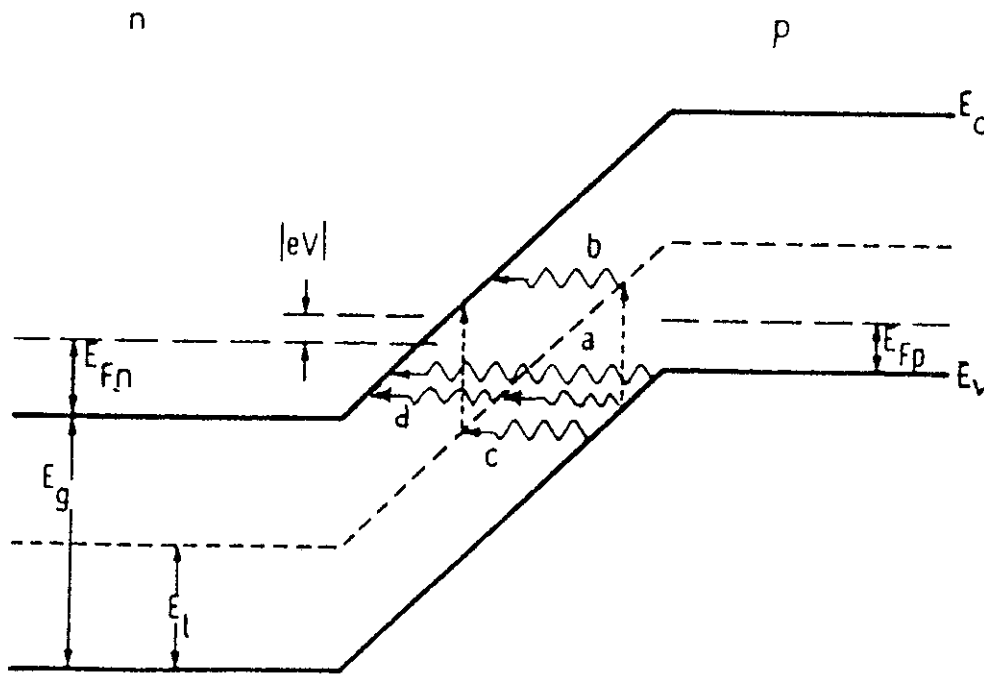


Figure 5.3-1 Energy diagram for an n^+ -on-p junction with a small reverse bias applied, showing a direct energy conserving tunneling transition a) and three trap-assisted tunneling transitions b), c) and d). The trap level energy is E_t . The n-side conduction band is degenerate, the p-side valence band is non-degenerate [12].

5.3.1.3 Generation-Recombination (g-r) Current

This has been described by Reine et al [12]. As discussed in section 2.2.1, impurities or defects which give rise to energy levels within the bandgap (and exist at a depleted surface or within the depletion region) act as a source of junction current. For mid gap states (which tend to dominate the dark current) with emission time constant τ_e , we have for the depletion region

$$(R_0A)_{gr} = \frac{e n_i W}{V \tau_e} \quad 5-5$$

where W is the depth of the depletion region and V is the applied bias. Thus R_0A is proportional to n_i (rather than n_i^2 as for diffusion current) and dominates the current at intermediate temperatures (cf figure 5.3-2). Current which arises from fast surface states I_s is also proportional to n_i and can be written

$$I_s = e n_i S A \quad 5-6$$

where S is the surface recombination velocity. In good quality diodes (low concentrations of defects and good passivation), g-r components can be almost negligible before irradiation [14].

Increased g-r noise can be caused by excessive strain, due for example to the force exerted during hybridisation [18]. It is possible that stress effects can also affect radiation hardness in that the build-up of interface states and electric fields at the surface may be influenced. Note that due to the narrower bandgap and reduced microhardness, the effects are likely to be worst for LWIR detectors.

5.3.1.4 Trap Assisted Tunneling

Together with changes in fast interface state density this is the dominant mechanism for radiation-induced dark current increases in MCT devices. As for DBTB tunneling there has been a large amount of discussion on mechanisms and modeling of trap-assisted tunneling (cf [13] and references therein). Figure 5.3-1 shows the paths by which tunneling can occur. The details of the modeling will depend on the energy level of the trap, the doping level and the nature of the junction (eg graded or abrupt) there will also be differences for MIS devices. Regardless of whether or not there is a thermally assisted (excitation) step (as in 5.3-1 b and c), there will be a tunneling step (or steps) with probability given by [13]

$$T \propto \exp \frac{-8\pi (2m_e^*)^{1/2} (E_g - E_t)^{3/2}}{3 e h E} \quad 5-7$$

where E is the electric field and m_e^* is the effective electron mass.

This is for tunneling across a triangular barrier. In fact the expression is largely unchanged with the shape of the barrier (only numerical constants are affected). For example a similar expression has been quoted for a parabolic boundary [19].

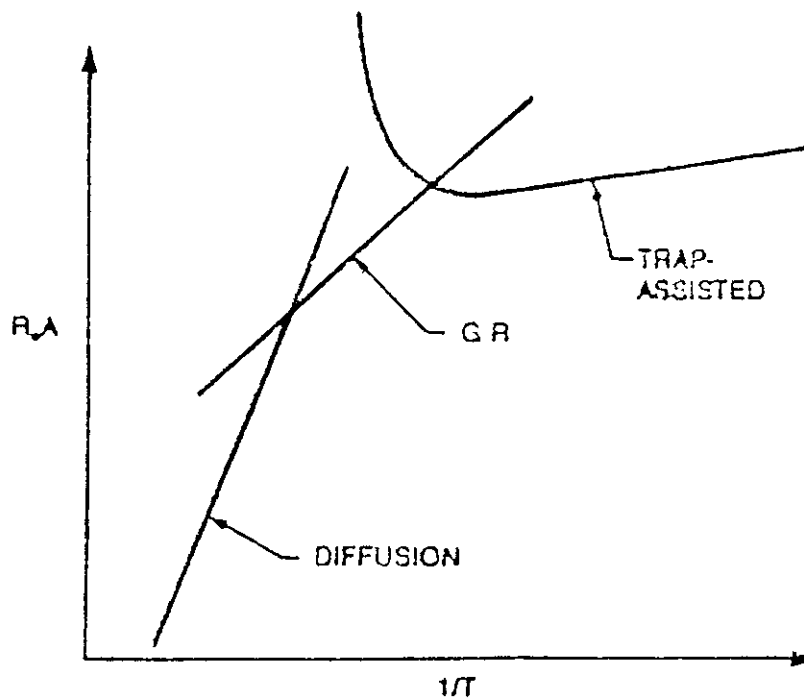


Figure 5.3-2 Temperature behaviour of dark current mechanisms in MCT photodiodes

Equation (5-7) shows that the tunneling current is exponentially related to the effective mass and the electric field. It is usually assumed that $m_c^* = 0.07 E_g$. Hence the effective mass is small for low bandgap materials (eg LWIR MCT) and tunneling is increased (Note E_g depends on temperature). The effects are also worse for high electric fields. We thus have the following dependences

Trap assisted tunneling is greatly increased for

- * narrow bandgap (eg LWIR MCT)
- * high electric fields (eg at junction edges and corners)

As a general rule the electric field (and the tunneling current) is reduced with low doping. This tends to favour diffused rather than ion implanted junctions. The tunneling current will also be proportional to the number of traps. Since these are located close to the depletion region (in the 'bulk' of the device) this number will not be greatly affected by ionization. A larger effect is caused by the exponential dependence on electric field. The field is related to the charge density in the surface layers which is in turn related to ionization damage. As Sarusi et al [8] have pointed out, the electric field is given by

$$E \propto (Q_a + Q_i) \quad (5-8)$$

where Q_a is the charge contributed by the applied voltage and Q_i is the charge due to radiation induced traps and interface states

or

$$E = K_1(1 + K_2D) \quad (5-9)$$

where K_1 and K_2 are constants and D is the dose

$$\text{Hence we have } I_u = \text{const exp}(-K_3/(1 + K_2D)) \quad (5-10)$$

This expression has been verified by Sarusi et al [8] and also by De Wames et al [9] who give a more explicit equation

$$I_u = \text{const exp} \left[- \frac{U_0}{(V_{bi} + V)^{1/2} (1+aD)} \right] \quad (5-11)$$

$$\text{where } U_0 = \frac{\pi(m^*)^{1/2}}{2e} E_g^{3/2} \frac{W_1}{2}$$

$$\text{and } W_1 = \frac{2\epsilon_s}{e} \frac{N_A + N_D}{N_A N_D}^{1/2}$$

This expression was obtained for Co60 γ ray irradiation of planar passivated ion implanted diodes. It follows from simple expressions for the maximum field in an abrupt junction [20] N_A and N_D are acceptor and donor concentrations and V_{bi} the built in voltage. W_1 is related to the depletion layer thickness (W)

$$W_1 = W/(V_{bi} + V)^{1/2} \quad (5-12)$$

For different assumptions (eg a graded junction) the dependence on voltage would be different (cf [20])

Equations (5-9) and (5-10) imply that at low dose the leakage current is proportional to $\exp(\alpha \text{ dose})$ and at high dose to $\exp(-\beta/\text{dose})$ as illustrated in figures 5.3-3 [9] and 5.3-4 [8]. Note that figure 5.3-3 does not give an absolute scale for dose. An assumption is that this is measured in rad so that significant changes in R_0A are occurring for these diodes (which are planar ZnS passivated, homojunctions) at ~ 10 krad. For the devices reported by Sarusi et al [9] the changes occur at slightly higher dose - but note that at 100 krad there are significant changes for the zero bias condition. In both these works it was confirmed that surface damage was responsible (by studies with localised laser and UV irradiations, which gave rise to similar damage).

Measurements by DeWames et al [14] at Rockwell indicate that for good quality photodiodes operated at intermediate reverse bias voltages and $T \sim 77K$ the temperature behaviour of the dark current is $\exp(\gamma T)$, hence $R_D \propto \exp(-\gamma T)$ (in contrast to DBTB tunneling which increases as T decreases). In un-irradiated diodes at 77K the impedance close to zero bias is dominated by diffusion and as the temperature is lowered this impedance increases very fast as $\exp E_g/kT$ but soon becomes limited by the trap-assisted tunneling current ($\propto \exp(-\gamma T)$) which increases with decreasing temperature but less rapidly than $\exp E_g/kT$. Because of the slow temperature dependence of R_D in this regime, DeWames et al termed the trap-assisted tunneling contribution the ohmic current (a weak dependence of temperature is always a characteristic of tunneling mechanisms).

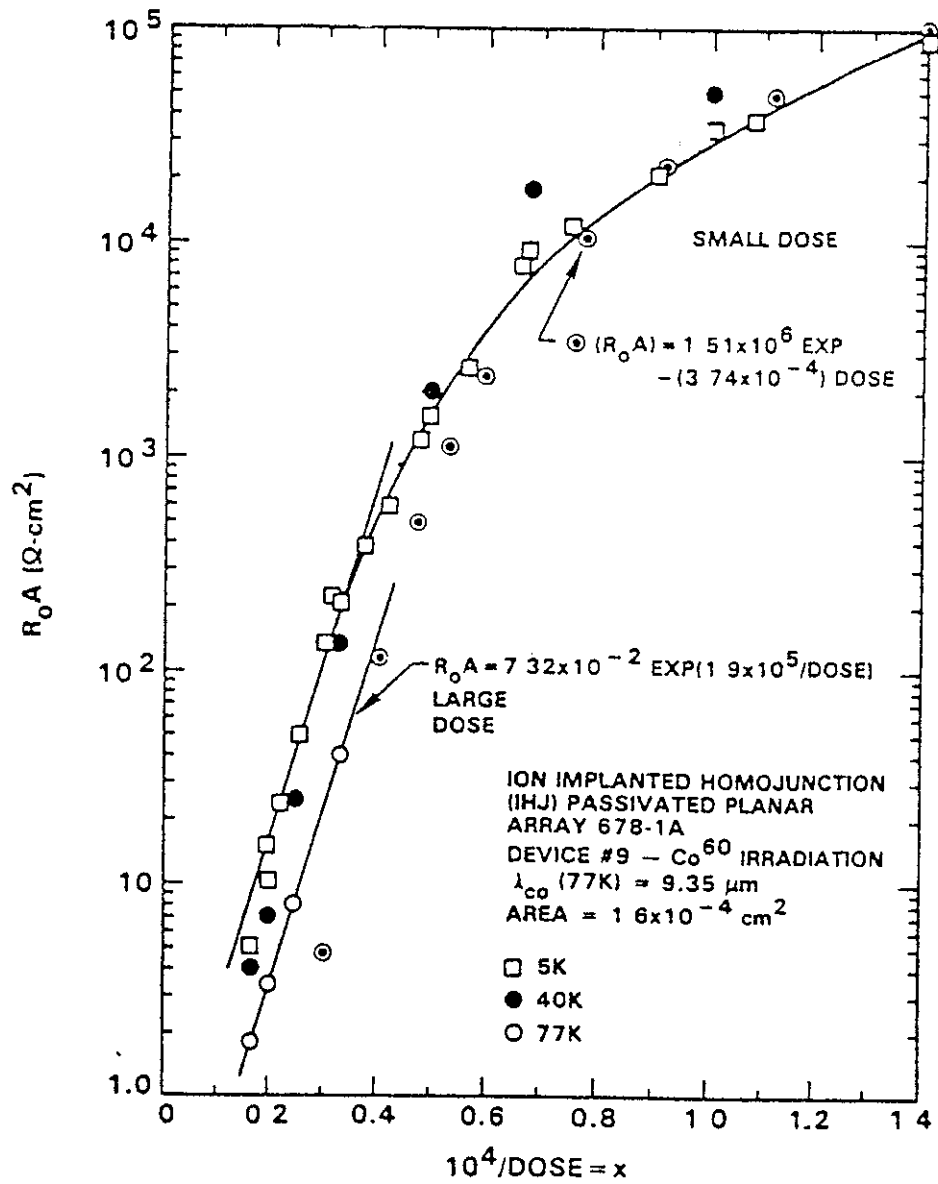


Figure 5.3-3 Dose dependence of R_{0A} for LWIR ion implanted diodes irradiated with Co^{60} [9]

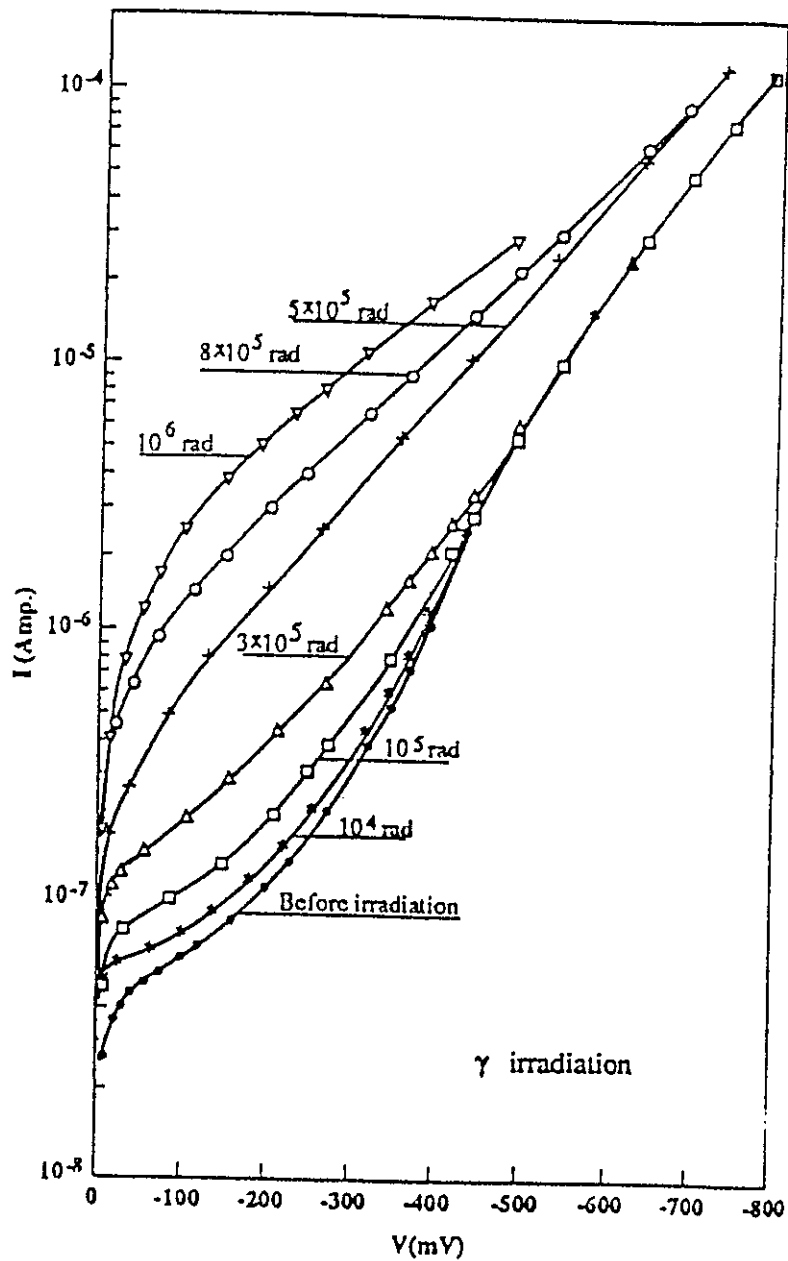


Figure 5.3-4 Dose dependence of reverse diode current for LWIR ($\chi=0.23$) ion implanted diodes [8]

This temperature dependence has been difficult to explain with most theories, which have taken the most effective trap level, E_t , as being mid gap ($E_g/2$). However, Nemirovsky et al [21] have shown that the $\exp(-\gamma T)$ dependence can be obtained by assuming a trap level at $E_t = E_f$ which is populated by thermal emission (after which follows tunneling), see also [22]

From the above considerations we expect the radiation-induced trap assisted current to be mainly a surface related phenomenon arising from changes in the electric field distribution. As well as changes in the magnitude of the field, radiation-induced charge in the passivation can lead to accumulation or inversion conditions and changes in field geometry (introduction of field induced junctions) and this is discussed further in the next section, in connection with studies using gated diodes

Because of the exponential dependence, it is important that focal plane arrays are uniformly processed since small deviations in field geometry (caused for example by non-uniform doping) can lead to large changes in current density. The pixel with the smallest bandgap, highest electric field and largest trap density will contribute a disproportionate amount of tunnel current. O'Brien and Flesner [23] have given an example (figure 5 3-5) of localised soft spots in photodiode leakage currents, arising from charge build up in the ZnS layer (scanning e-beam irradiation). In that case a doubling of the dark current from 25 to 52nA was observed in the diode after 15 krad(Si)

The model proposed by DeWames et al [9] assumes that it is the field at the main p-n junction that is being modified. Sarusi et al [8] assume that ionization damage-induced traps at the ZnS/MCT interface are negatively charged and produce an upward band bending giving rise to a strong inversion (p^+) layer on top of the n^+ ion implanted region of the diode as shown in figure 5 3-6. There is now a p^+/n^+ junction across which tunneling can occur. Either way there is the same functional dependence on dose. The exact form of the model must necessarily depend on the architecture of a particular device. Certainly there is a link with band bending at the surface - which should be avoided if possible (keeping the flatband condition is best). Hence there is also a link with threshold voltage shift (cf section 5 4) and there may also be a link to $1/f$ noise in the diodes (probably associated with slow surface states [9,10]). Band bending at the surface can also produce large changes in quantum efficiency because the change in field geometry alters carrier collection efficiency. Sarusi et al [8] found a decrease in QE by a factor 3 after 0.5 Mrad, due to the p^+ surface layer.

On the other hand Williams et al [24] have found that large changes in R_0A can be caused without significant changes in surface condition as noted below in table 5 3-1 (ZnS passivated $10\mu\text{m}$ diodes)

These data point towards a mechanism involving interface state build up and surface g-r current, although at the low temperature used (40K) thermal currents should be significantly reduced. It cannot be ruled out, however, that small changes in interface charge are causing the required increase in tunnel current. The authors state the mechanisms have yet to be determined.

Having established that trap-assisted tunneling is a major source of performance degradation, particularly for LWIR diodes (where the bandgap is small) and at low temperatures (where thermal diffusion and/or g-r currents are reduced), the next question is how the effects can be reduced. Firstly, proper passivation (eg with anodic sulphide or fluoride or epitaxial CdTe) to reduce interface trap production could be employed. Use of heterojunction structures not only help to maintain the flatband condition but also place the wider bandgap material (with eg $x=0.3$) near the surface where the fields will be highest - thus reducing the tunnel current.

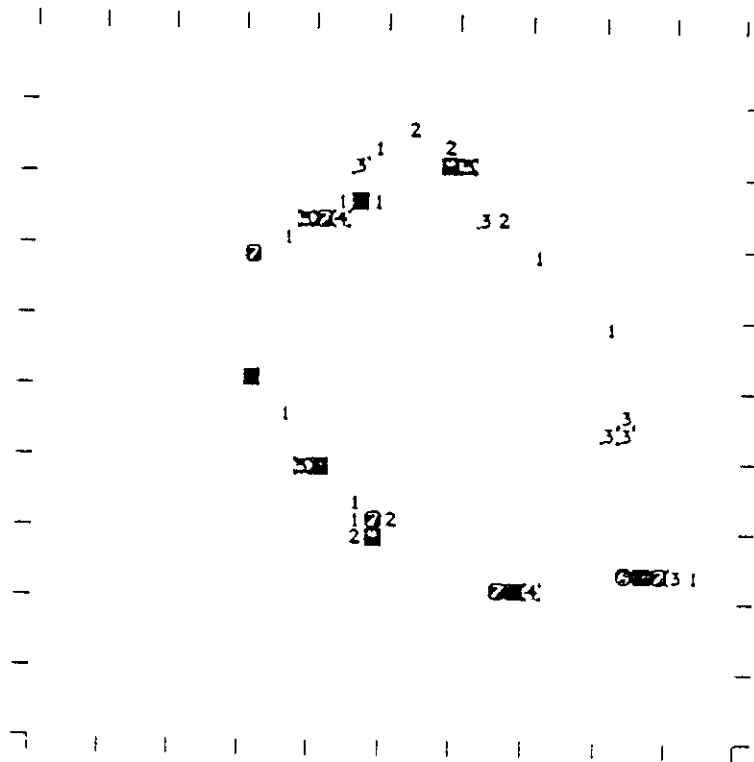


Figure 5.3-5 Localised 'soft spots' in the leakage current of a n-on-p ion implanted MCT diode ($0.5\mu\text{m}$ ZnS passivation) [23]. $T=40\text{K}$, $\lambda_c=10\mu\text{m}$

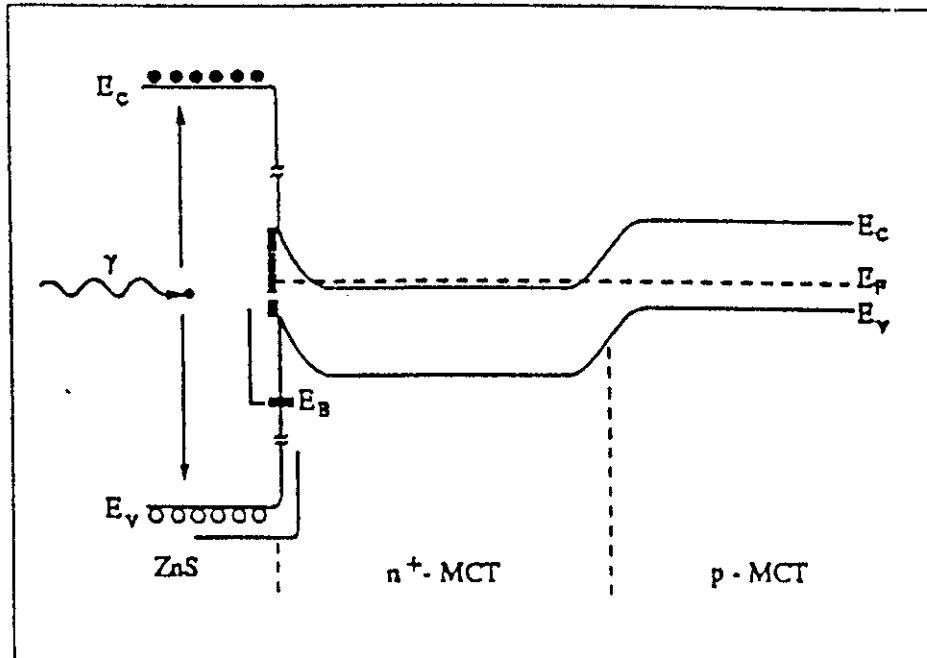


Figure 5.3-6 Schematic illustration of γ -induced band bending as proposed by Sarusi et al [8]

After Accumulation Device	Pre-irradiation R_0 Product ($x-cm^2$)			R ₀ A Product After Accumulated Dose			R ₀ A Product After 105K Anneal		R ₀ A Product Additional Total Dose	
	1.0krad	4.9krad	13.4krad	18.8krad	8 1 x 10 ³	5 9 x 10 ²	12.2krad	8 5 x 10 ¹	5 9 x 10 ²	12.2krad
1	4.3 x 10 ⁴	7 7 x 10 ⁴	1 4 x 10 ⁵	1 4 x 10 ³	8 1 x 10 ³	5 9 x 10 ²	8 5 x 10 ¹	8 5 x 10 ¹	5 9 x 10 ²	12.2krad
2	8 4 x 10 ⁴	8.5 x 10 ⁴	3 5 x 10 ⁴	2.5 x 10 ³	1.2 x 10 ⁴	2.3 x 10 ³	1 1 x 10 ²	1 1 x 10 ²	2.3 x 10 ³	12.2krad
3	5 2 x 10 ³	5.3 x 10 ³		3 1 x 10 ³	3 5 x 10 ³		5 0 x 10 ²	5 0 x 10 ²		
4	8 8 x 10 ⁴	7 8 x 10 ⁴		3 5 x 10 ³	1 7 x 10 ⁴		2 5 x 10 ²	2 5 x 10 ²		
5	1.2 x 10 ⁵			7 4 x 10 ³	3 4 x 10 ⁴		4 0 x 10 ²	4 0 x 10 ²		
6	8.2 x 10 ³			5 0 x 10 ²	1 7 x 10 ³		3 5 x 10 ¹	3 5 x 10 ¹		

All doses are in units of rad(H₂O).

Table 5.3-1
Degradation of LWIR Detector R₀A Product at 40K as a Function of Total Absorbed Dose [24]

Recently Vydyonath et al [25] have reported LWIR photodiodes tolerant to at least 0.85 Mrad using this architecture (figure 5.3-7). The wide bandgap layer will also reduce g-r leakage currents (proportional to $\exp(-E_g/2kT)$, and E_g is increased) - as pointed out by Yoshida et al [26]. There is a drawback in that a potential barrier can be created in the band (valence or conduction depending on the doping p-on-n or n-on-p). This tends to impede the flow of minority carriers and results in a loss in quantum efficiency. Yoshida et al got round this by removing the wide bandgap N region in their n-on-p structure as shown in figure 5.3-8. As discussed in section 1.4, several manufacturers are working on heterostructure devices.

The heterostructure arrays currently being developed by Hughes (cf section 1.4) for AAWS-M and other programmes, have been reported to be tolerant to ~1 Mrad levels, with only a few percent change in R_0A (private communication, 1991).

As noted in section 5.3.1.3, it is also likely that reducing stress in the array by optimisation of hybridisation and metal contacts is useful in reducing g-r and tunneling currents.

Blanks et al [22] have pointed out that new low temperature growth techniques such as MBE or MOCVD may not have the advantage of allowing the x -value to homogenise by way of Hg diffusion through the lattice, especially in heterostructures and superlattices for which Hg diffusion must be minimised to maintain sharp interfaces. Hence local variations in bandgap (and hence tunnel current) may be produced.

An interesting possibility is to use mercury zinc telluride as a detector material since for a given bandgap, E_g , the electron effective mass, m^* , is predicted to be less [27] and so tunneling will be reduced. Several groups are now working on MZT devices.

5.3.1.5 Studies with Gate Controlled Diodes

As discussed in section 5.3.1.4, changes in the flatband voltage can produce accumulation or depletion at the surface and this will affect both the g-r recombination current (because of changes in the effective generating area) and the tunneling current (because of changes in field distribution). Both these currents are sometimes lumped together as a 'surface leakage current'. The situation is illustrated in figure 5.3-9 (Reine et al [12]).

In the absence of oxide charge (figure 5.3-9a) an annular area A_s of the surface defined by the junction perimeter and the junction depletion layer width W_b will lie within the depletion layer. Fast interface traps in this depleted region of the surface will generate carriers (g-r current). When sufficient positive fixed charge is present, the p side can become inverted and an n-type surface channel can form as shown in figure 5.3-9b). The space-charge region will become larger, and additional current can be collected by this field induced junction. The channel length L_c will depend on the bias voltage applied to the junction, on the surface conductivity, and on the amount of current flowing across the field induced junction. The generation current due to Shockley-Read centres in the surface channel is given by

$$I_s = \frac{1}{2} e n_i A_s W_b / \sqrt{(\tau_{n0} \tau_{p0})} \quad (5-13)$$

where W_c is the channel width and A_s is the channel area

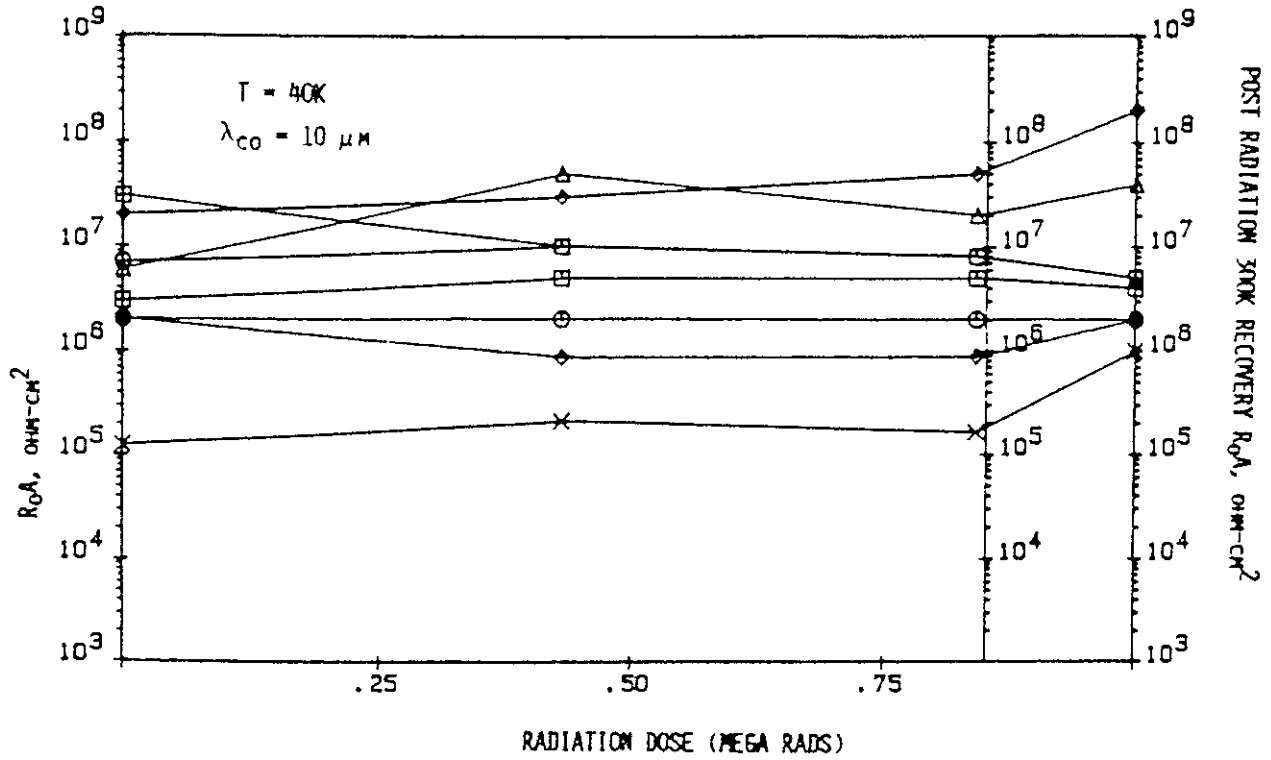


Figure 5.3-7 R_{0A} performances at 40K versus total dose for MCT heterostructure photodiode arrays [25]

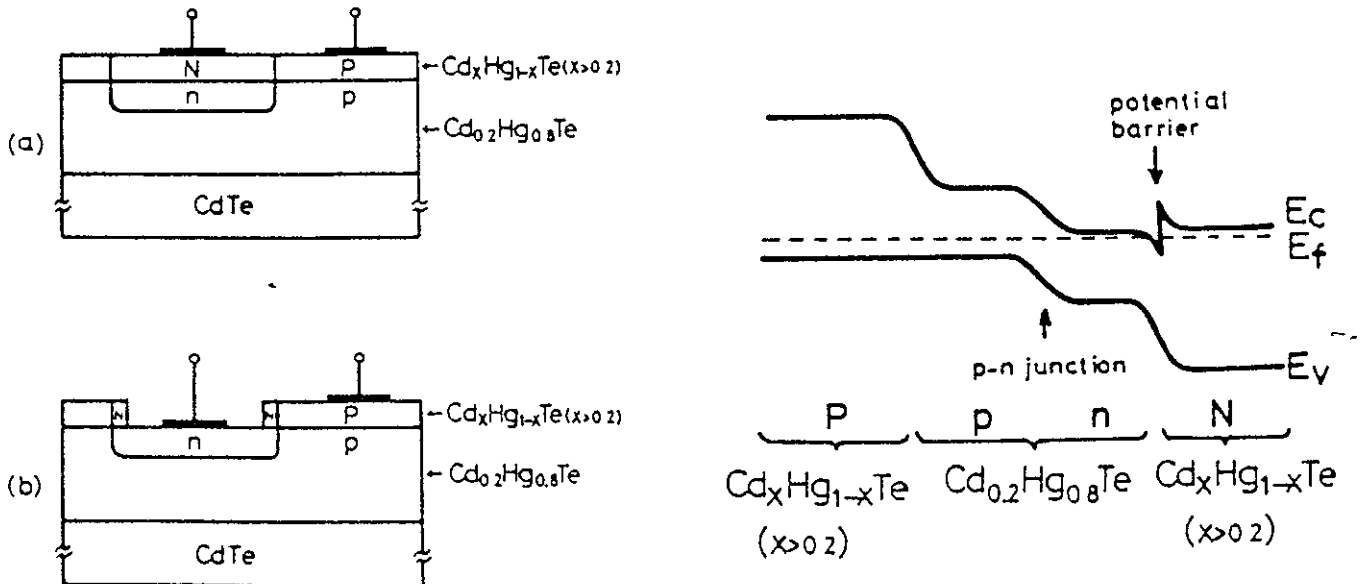


Figure 5.3-8 Cross sections of MCT photodiode heterostructures and the energy band diagram for structure a) [26]

When negative fixed charge is present, the p side becomes accumulated and, as shown in figure 5.3-9c), a narrow field induced junction can occur at the surface, offering a region in which tunneling can occur. A larger amount of negative fixed charge can invert the n side (figure 5.3-9d) and form a p-type surface channel. In figure 5.3-9c), the depletion layer is narrowed by surface charge. The fixed charge strongly accumulates the lightly doped p side of the junction at the surface, pinching off the depletion layer. Since the electric field across the junction is given by $(V + V_{bi})/W$, where V_{bi} is the built-in voltage and W the depletion layer width, tunneling or even surface breakdown can occur at low or even at zero applied voltage. In figure 5.3-9d) the fixed charge inverts the heavily doped n side of the junction. Because of the high carrier concentration, the depletion layer between the inversion charge and the heavily doped region is very narrow and the electric field across the depletion layer correspondingly large. Again, tunneling or breakdown can occur at comparatively low junction voltages.

In order to investigate surface-related current mechanisms, an insulated gate electrode (sometimes termed a field plate) is often fabricated around the junction perimeter in order to externally control the surface potential. Figure 5.3-10 shows the qualitative behaviour of the various surface-related current mechanisms as functions of applied gate voltage V_G for a gate-controlled n-on-p junction.

The use of insulated field plates to externally vary the surface potential in the vicinity of a p-n junction is a standard technique for localizing and identifying surface leakage current mechanisms. Unfortunately however the method can only be conveniently used on large area test structures. This is because the field plate needs to stop at the edge of the junction - but the position of the junction moves with changes in applied bias and it is not normally possible to use the technique in small geometry production devices (as in photodiode arrays). Many MIS devices do however have a guard ring around the MIS gate to prevent positive oxide charge resulting in an inversion layer at the surface and prematurely filling the potential well as the device is pushed into deep depletion [19] and the voltage of this can be varied so as to investigate surface properties (cf the next section and references therein).

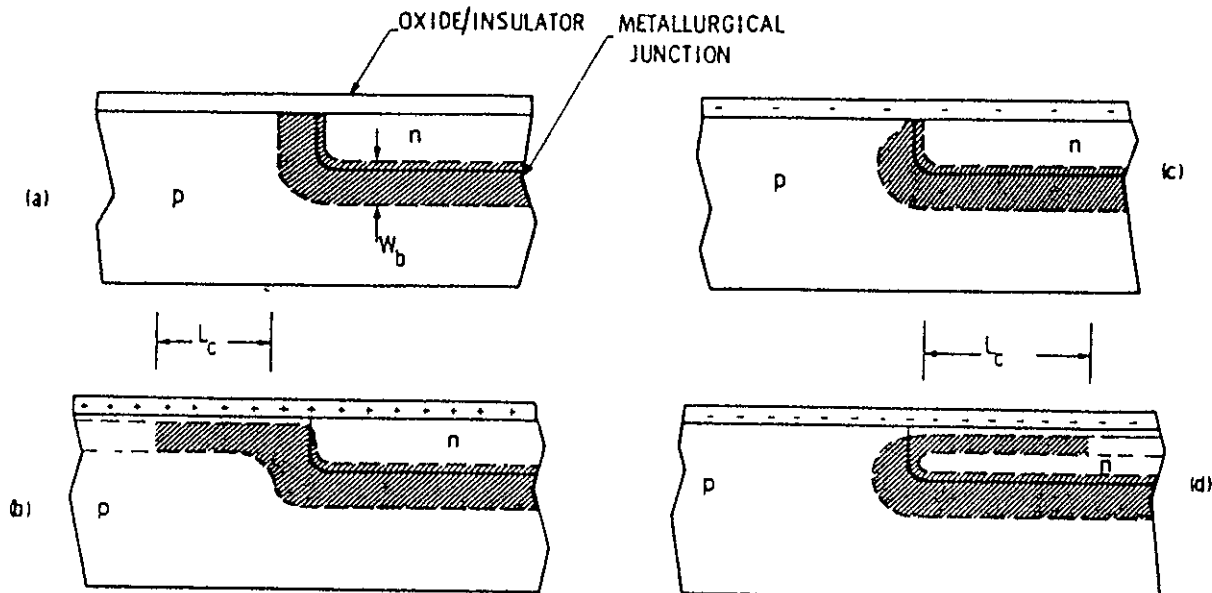


Figure 5.3-9 Effect of fixed oxide/insulator charge on the effective junction depletion layer:
 (a) flat-band condition, (b) positive fixed charge causes inversion of the p side and formation of a n-type surface channel, (c) negative fixed charge causes accumulation of the p side and a narrow field induced junction at the surface, (d) larger amount of negative fixed charge causes inversion of the n side and formation of a p-type surface channel [12]

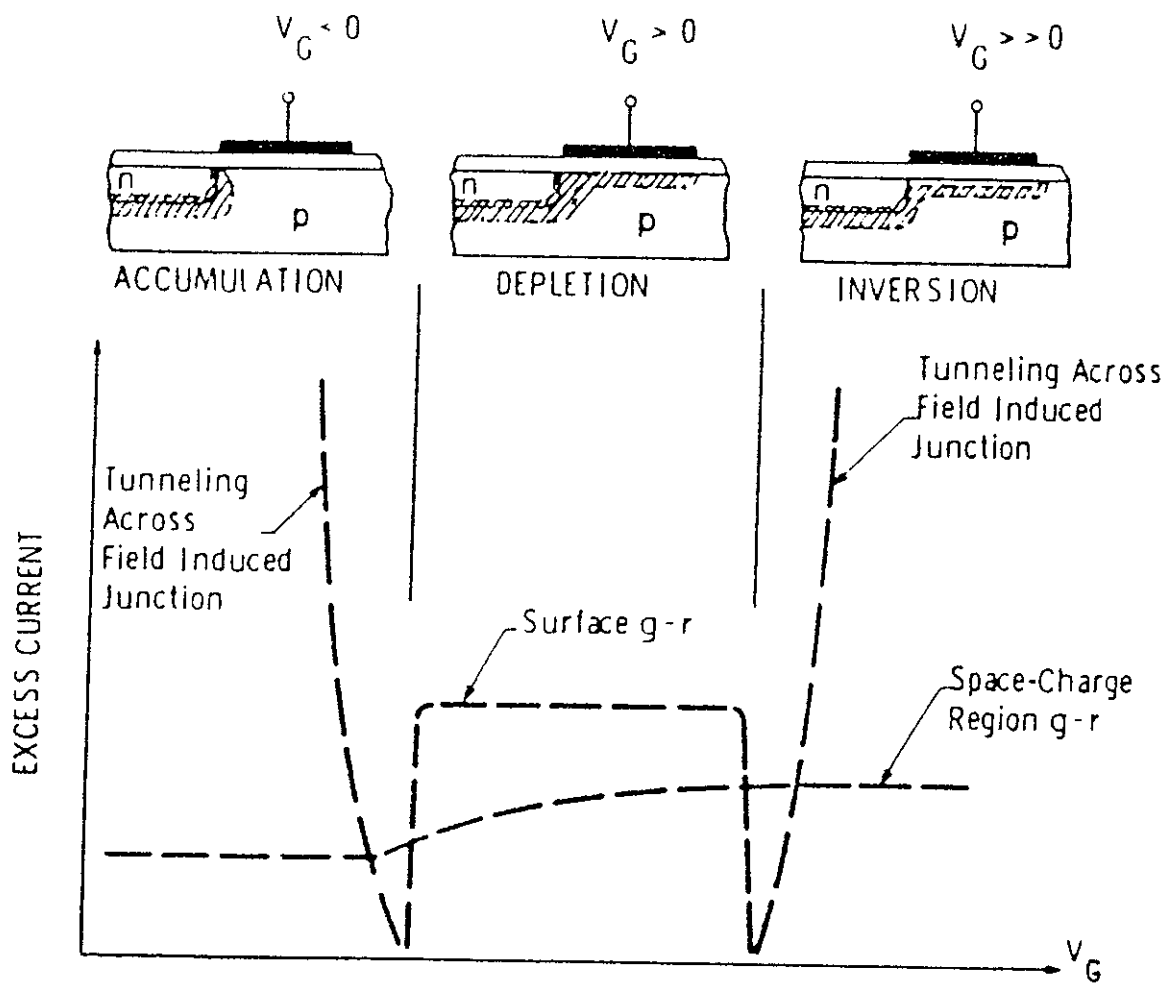


Figure 5.3-10 Qualitative behaviour of the various excess (leakage) current mechanisms in a narrow-bandgap gate-controlled photodiode, shown as functions of gate voltage V_G . The actual current versus gate voltage curve observed would be the sum of the currents from the various mechanisms

5.3.2 Results for G-MIRL MWIR and LWIR Diodes

A study on 20x1 photodiode test structures has been performed by Hopkinson et al [28]. Figures 5.3-1 and 5.3-2 show how the reverse bias IV and slope resistance for a typical longwave (8-10 μ m) diode change with cobalt-60 dose. Figure 5.3-3 shows the spread in the data for all the diodes in the same 20x1 structure (these results were for an unbiased structure but the results were similar in the biased case). The diode slope resistance decreases with increasing dose but it can be seen from figure 5.3-3 that there was significant annealing even with overnight storage at 85 K and that recovery was complete with warm up to room temperature. For each hour of storage at 85 K there was an increase in slope resistance of approximately 1%. Similar annealing effects have previously been seen in HgCdTe photodiodes by several authors ([10], [11], [12]).

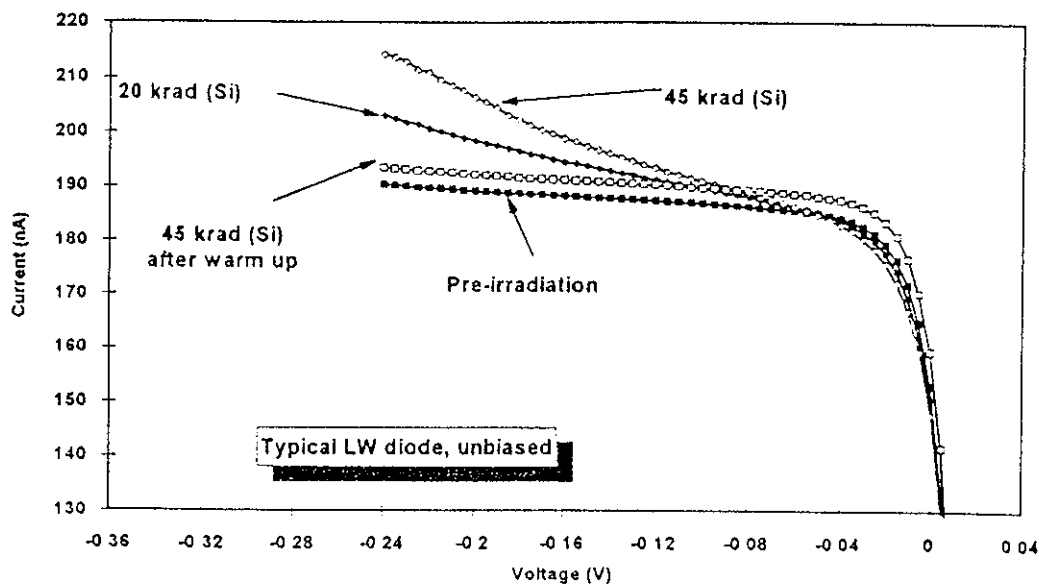


Fig. 5.3-11 IV curves for a typical G-MIRL LWIR loop-hole diode, unbiased during irradiation. 25°C blackbody source.

Results for a second irradiation carried out 3 months afterwards are also shown in figure 5.3-3. This irradiation was carried out at a slightly higher dose rate (4.7 rather than 3.3 krad/hr), without overnight annealing and with only short (~1 hour) interruptions for measurements after 10 and 20 krad. It can be seen that the decrease in resistance is not linear with dose. This suggests that a mechanism involving trap-assisted tunneling is involved. There were no significant changes in diode responsivity, indicating that the depletion region geometry does not change with ionizing dose.

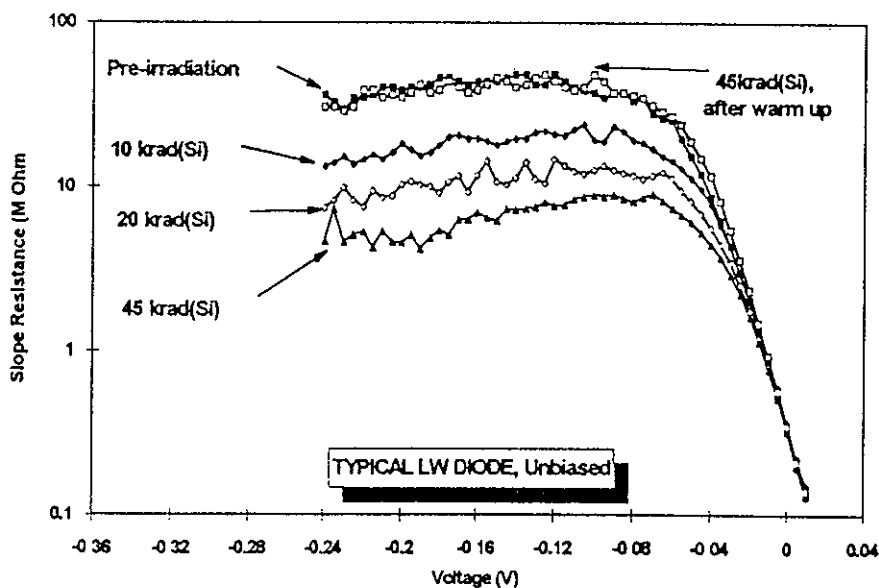


Fig. 5.3-12 Slope resistance curves for a typical G-MIRL LWIR loop-hole diode, unbiased during irradiation. 25°C blackbody source.

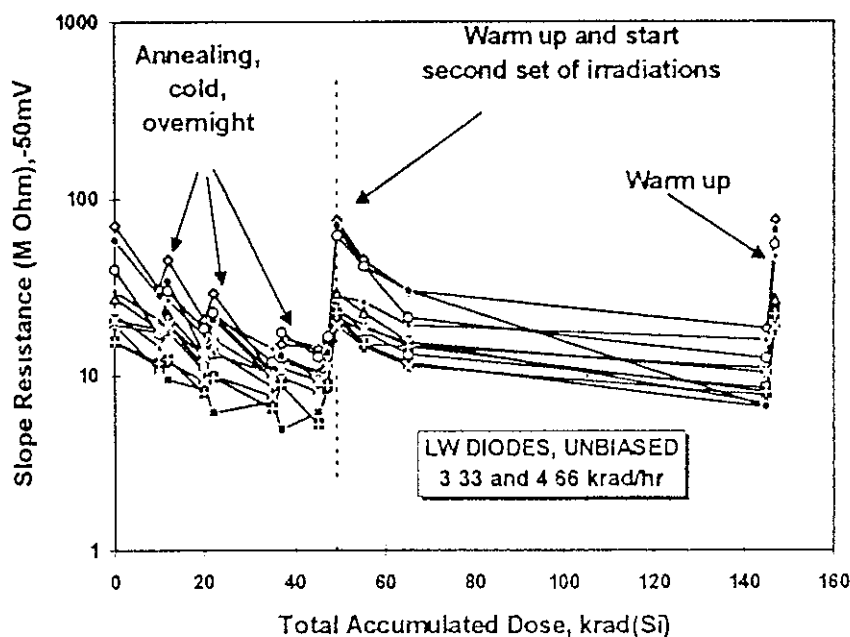


Fig. 5.3-13 Slope resistance data for all diodes in a LWIR 20x1 structure, irradiated unbiased. 25°C blackbody source.

The annealing effects indicate that there will be no major changes in performance for a low dose rate space environment. At higher dose rates, the change in resistance will produce a decrease in injection efficiency, η , since

$$\eta = g_m / (g_m + 1/R) \quad (5-14)$$

where $1/g_m$ is the input impedance of the multiplexer (typically 300k at 100nA) and R is the diode resistance. Even with a decrease in R to 10 M Ohm after 45 krad, η would still be 98%. However this reduction in η may be important for low background applications (since the lower diode current implies that the diode resistance would be lower) or those requiring accurate radiometry - especially as there will be a spread in diode resistance values in a large array and those diodes with a low resistance will be most affected. g_m is given by

$$g_m = \frac{e}{nKT} \left(\eta I_D + \frac{V}{R_D} \right) \quad (5-15)$$

Where n is a factor between 0.4 and 4 depending on the operating condition of the MOSFET. Usually n is taken as 1. I_D is the diode current (dark current plus photocurrent) and V the diode reverse bias. The second term in equation (5-15) is the leakage current through the diode shunt resistance. Solving equation (1) and (2) gives

$$\eta = \left(\frac{1}{2} - \frac{V}{2R_D I_D} - \frac{kT}{2eR_D I_D} \right) + \left[\left(\frac{1}{2} - \frac{V}{2R_D I_D} - \frac{kT}{2eR_D I_D} \right)^2 + \frac{V}{R_D I_D} \right]^{1/2} \quad (5-16)$$

Equation (5-16) implies that the injection efficiency is reduced for low current (I_D) and low values of diode resistance. In the SWIR and MWIR the diode resistance is high enough that η is close to 1. However in the LWIR η can be significantly reduced, especially if viewing a low temperature scene, as noted above.

Figure 5.3-14 shows η for a typical range of photon flux (on each pixel) in the LWIR (taken from the radiometric model for the PRISM LWIR band D).

The figure shows the reduction in η at low signals - which is worse for diodes with a low resistance. However this effect can be calibrated on ground. More important are effects which occur in-orbit, due to detector ageing, changes in bias or temperature and to radiation effects.

Very little is known about the effects of space radiation on IR detector arrays. The most relevant data comes from a recent study on GMIRL detectors [2]. It is to be expected that total ionizing dose will significantly reduce the slope resistance of LWIR diodes (there is only a small effect for MWIR and SWIR). Fortunately, the damage anneals, particularly if the detector is warmed to room temperature. However, the data in the study indicates that the annealing resulted in departures of diode resistance from the pre-irradiation values by around $\pm 10\%$. Hence figure 2 shows the change in injection efficiency for $\pm 10\%$ change in R_D - for nominal values of 300 M and 100 M (which are typical for high performance diodes at $\sim 12.5 \mu\text{m}$ cut off wavelength). It is seen that variations in linearity of $\sim 0.4\%$ can be expected from pixel to pixel and as a change in absolute linearity. Actually it is only the changes in the shape of the curve which are important since other changes can be accommodated by a change in responsivity. However the residual variations are still $\sim 0.1\%$ and are comparable with the PRISM specification limits. Changes of order 0.1% can also be caused by 10% variations in reverse bias voltage and temperature changes 1K (at 50K) as shown in figure 2.

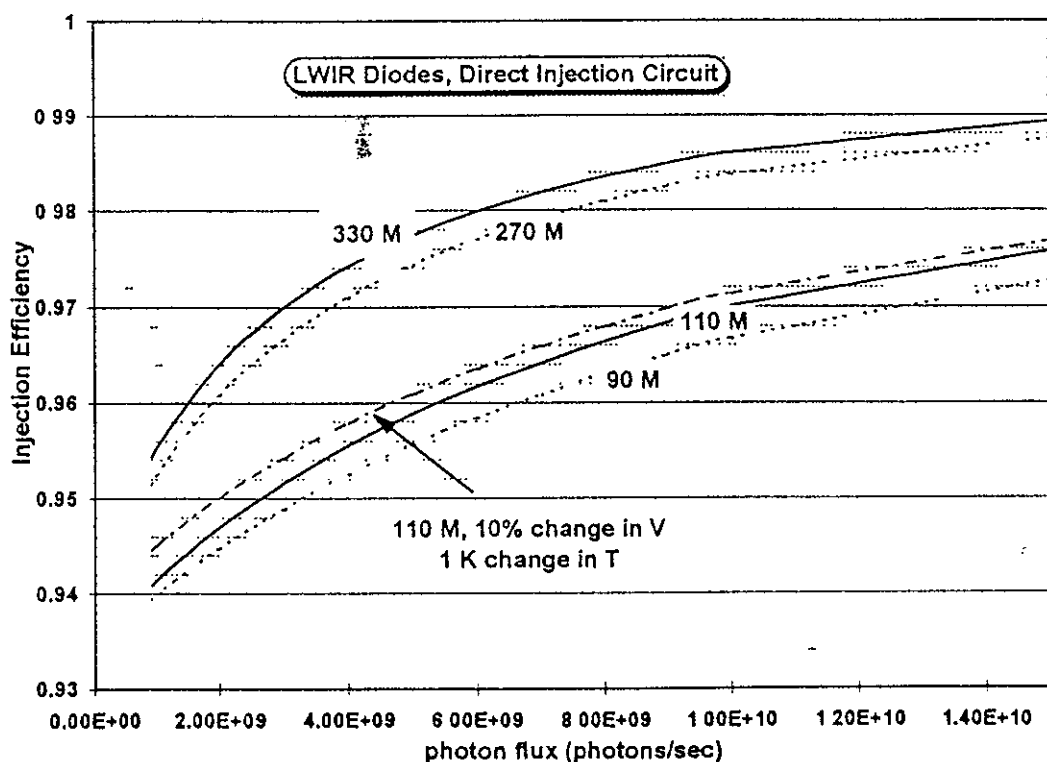


Figure 5.3-14. Injection efficiency for a typical range of photon flux (on each pixel) in the LWIR (taken from the radiometric model for the PRISM LWIR band D).

There are several other effects which should be considered. Firstly there is a dependence of R_D on the photon flux. This is believed to be because, for LWIR diodes in particular, R_D is limited by avalanche multiplication processes [3]. These are sensitive to applied voltage and lead to a resistance term dependent on the flux. However this effect is thought to be less important than the radiation effect discussed above.

Another effect occurs in the SWIR, where diode currents are low (because of the low photon flux). This leads to high values for the input impedance of the multiplexer (equation (2)). This is not a problem for injection efficiency since the diode resistance is also high. But the high resistance, in combination with the diode capacitance, leads to a long RC time constant compared with the stare time.

For a typical minimum current of 1.5×10^6 electrons/pixel/s we have an input impedance of 5.38×10^{10} ohm from equation (2). A typical diode capacitance is expected to be 0.08 pF, giving a time constant of 4.3 ms. Bluzer and Jensen [1] give a frequency dependent $\eta(f)$ as

$$\eta(f) = \frac{gm R_D}{1+gmR_D} \frac{1}{1+RCf} \quad (5-17)$$

where f is the operating frequency ($= 1/2 \times$ stare time). This leads to an injection efficiency ~ 0.75 .

Finally, the linearity of the output amplifier of the multiplexer might be expected to change with operating point (and hence on bias, temperature, total dose). However, it is not expected that the amplifier is especially sensitive and in any case all pixels readout through a given amplifier would be affected, so there will not be pixel-pixel variations in linearity.

To summarise, it is possible that in-flight changes in array performance, due for example to radiation effects, may affect instrument performance at the level specified for instruments such as PRISM. Effects should be most important for LWIR detectors. It is therefore recommended that further investigation into irradiation-induced non-linearities are undertaken. On the other hand the changes in non-linearity may not be large and use of LWIR detectors in high accuracy radiometric instruments would appear to be feasible, especially if specifications can be relaxed somewhat.

5.3.3 Dark Current Mechanisms in MCT MIS Devices

These are the same in principle as for photodiodes but there are differences in detail because of the differences in field geometry (there is no p-n junction but the gate is biased so that the volume beneath it is depleted so as to form a MIS capacitor and potential well). In a MIS device there is a high field at the surface and interface states at the surface can contribute both to g-r and trap-assisted tunneling current. As for photodiodes, the mechanisms for radiation-induced increases in dark current are thought to be mainly surface rather than bulk related (see example papers by Waterman and co-workers at NRL [29], [30], [31]). Basic mechanisms have been discussed by Kinch [32]. Diffusion, depletion and band to band, tunneling currents arise from intrinsic mechanisms and g-r and trap-assisted tunneling currents are due to defects.

5.3.3.1 Diffusion Current

This arises from minority carriers generated within a diffusion length of the depletion region. For high quality n-type material Kinch [30] gives

$$J_{dif} = e n_i (KT \mu_p / 2e \tau_{Ai})^{1/2} \quad (5-18)$$

where μ_p is the hole mobility and τ_{Ai} is the Auger lifetime for intrinsic material. For p-type material the relevant expression is

$$J_{dif} = \frac{e n_i^{3/2}}{p_0^{1/2}} \frac{KT \mu_n}{2e \tau_{Ri}} \quad (5-19)$$

where p_0 is the doping concentration and τ_{Ri} is the radiative lifetime for intrinsic material. Diffusion currents are normally higher in p-type material because of the high value of electron mobility, however this also leads to large diffusion lengths, so that using thin substrates can be of great advantage.

5.3.3.2 g-r Currents

This arises from defect (generation) centres in the depletion region (leading to a depletion current)

$$D_{depl} = e W n_i / \tau_0 \quad (5-20)$$

Where W is the depletion layer depth and τ_0 is the lifetime (assuming a trap level at midgap), and from states at the surface

$$J_s = \frac{1}{2} e n_i S \quad (5-21)$$

where S is the recombination velocity. As in photodiodes, ionizing radiation can lead to increases in surface states which directly give increases in dark current. These will vary with temperature as n_i (ie as $\exp(-E_g/2kT)$). In combination, diffusion and g-r currents will dominate over tunnel currents (pre-irradiation) only at high temperatures (eg above about 50K for TI $x=0.3$ devices [22]).

Baker [33] states that tunnel currents are normally much larger than g-r currents

5.3.3.3 Direct Band to Band Tunneling (DBT) Current

This arises from the same mechanism as in photodiodes (5.3.1.2). Assuming a parabolic barrier and uniform electric field E , the current is given by (Blanks et al [19])

$$J_{\text{DBTBC}} = \frac{e^3 (2m^*)^{1/2} E V}{\pi h^2 E_g^{1/2}} \exp \left[- \pi^2 (m^*/2)^{1/2} E_g^{3/2} / e h E \right] \quad (5-22)$$

but according to those authors, trap assisted tunneling dominates

5.3.3.4 Trap Assisted Tunneling

Again this arises from mechanisms as discussed in 5.3.1.4 for photodiodes, and there is therefore the usual exponential dependence on bandgap and electric field. Figure 5.3-15 shows the transitions that can occur. Yang et al [34] have recently stated that for MIS devices (p-type) the two stage trap assisted process is dominant, rather than the thermally assisted (and one-step tunnel) process. In MIS devices the maximum field is at the surface so there are automatically a large number of states (interface states) to assist in the tunneling process. Yang et al [35] point out that, with anodic oxide and anodic sulphide processes at Texas Instruments, the density of states prior to irradiation varies linearly across the bandgap, with the largest concentration near the valence band. The interface states located in the lower half of the bandgap communicate very efficiently with the valence band (at $T=77\text{K}$ and above) so that electrons can be thermally excited to the interface states and then tunnel through the bandgap into the MCT conduction band (effectively the bandgap for tunneling is narrowed). In contrast for p-type material the electrons have to tunnel across the full bandgap of the bulk material, resulting in a much smaller dark current. Hence p-type devices have a longer storage time and higher breakdown field than n-type devices. This will not necessary be so after irradiation since the distribution of interface states will be different. Moriwaki et al [28] have found that for p-type devices measured using a different technique, both pre- and post-irradiation interface trap concentrations show the usual (ie same as for silicon) 'u' shaped distribution with energy level across the gap.

With monolithic CCDs manufactured from MCT (which are basically arrays of MIS capacitors) tunneling phenomena tend to mandate the use of low clock voltages (~a few volts swing) otherwise the surface fields are too high. This in turn leads to the use of stepped oxide structures if full well capacity is to be maintained (figure 5.3-16) [36]. The resulting changes in insulator thickness lead to uneven shifts in threshold voltage after irradiation and subsequent degradation in the effective full well capacity. For example, Waterman and Killiany [30] found a 15% loss in full well capacity after 10 Krad (ZnS). It has been well known for some time (cf Killiany [37]) that for visible CCDs the overlapping gate technology gives better radiation tolerance than stepped oxides. Note that previous comments (section 5.3.1.4) on dark current uniformity and the need for good process control of doping levels and surface passivation apply to MIS devices also.

5.3.3.5 Radiation-Induced Dark Current Measurements

As with dark currents in photodiode arrays it is sometimes difficult to estimate the relative importance of radiation effects on generation and tunneling currents, especially as most reported measurements are for relatively low temperatures (77K and below) where tunnel currents will naturally dominate (because of their temperature insensitivity). At 77K it does seem that trap-assisted tunneling dominates. Although, as with photodiodes, flatband shifts will alter field distributions and change the tunnel current through the E dependence, studies by the NRL group seem to indicate that dependence on the number of interface traps is dominant (so that dark current increases in proportion to dose). For example figure 5 3-17 [30] shows dark charge versus dose for anodic oxide/ZnS passivated, MCT CCDs and figure 5 3-18 [29] shows the effect of temperature on dark current for 10 μ m cut-off MIS capacitors (the flatness of the curves at low temperatures indicating the dominance of tunneling currents in that regime). Waterman [29] was able to model the g-r part of the curve assuming a radiation induced trap concentration (D_{it}) of 1.6×10^{12} eV-cm² after 1 Mrad(Si). The trap assisted tunneling he modelled assuming

$$J_t = 1.75 \times 10^{-16} D_{it} \quad (5-23)$$

which is the expression given by Kinch [31], (p338) for a uniform D_{it} distribution across the bandgap and a uniform field, E, of 7×10^3 V/cm

Recent work by Moriwaki et al [28] on the determination of D_{it} distributions for MWIR anodic sulfide/ZnS MIS capacitors also show that the dark current is proportional to N_{it} and that trap-assisted tunneling can be important in some cases (figure 5 3-19)

All these measurements seem to indicate that the devices were tolerant to doses in the range 100krad - 1Mrad(Si). However these were simple test structures. It is to be expected that small geometry devices as used in arrays might be more susceptible (eg at the 10 krad level) because of tunneling processes - unless special hardening precautions are taken

5.4 FLATBAND VOLTAGE SHIFTS

As we have seen, charge build up in the passivation/insulator layer and at the interface with the MCT will lead to changes in flatband voltage. In photodiodes this can lead to accumulation or depletion at the surface (depending on the direction of the band bending) and can lead to loss of quantum efficiency (because of inefficient collection of photo-charge) and to increased tunneling currents. In MIS devices the same can occur, and there is also the possibility that the changes in flatband voltage will change the bias point of the capacitor and in monolithic CCDs there can be changes in full well capacity and charge transfer efficiency (due to changes in the 'bias windows' needed for correct operation)

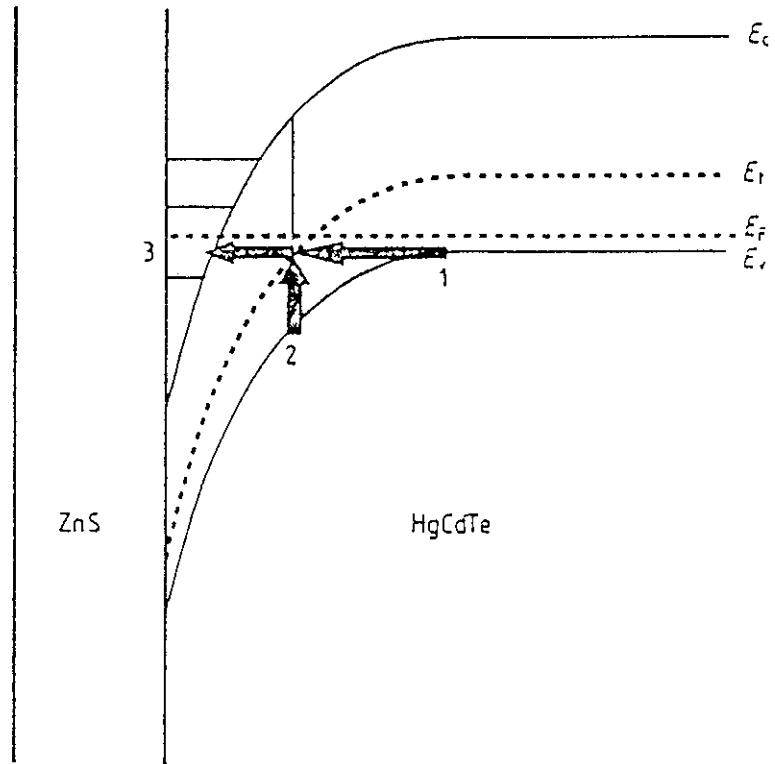


Figure 5.3-15 Schematic energy band diagram for an MIS device in the strong inversion regime [33]

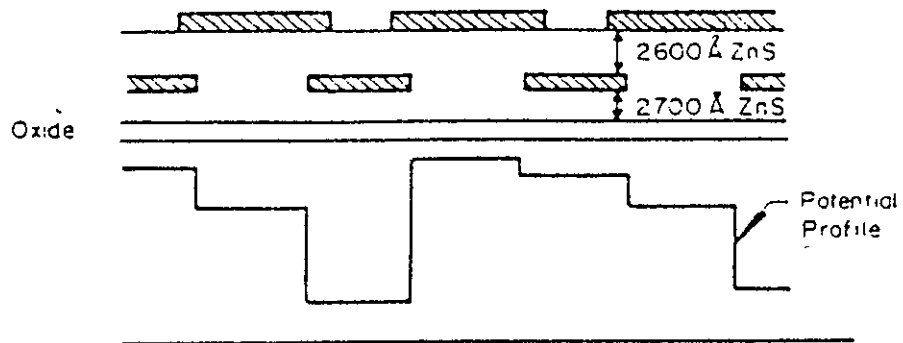


Figure 5.3-16 CCD shift register geometry [35]

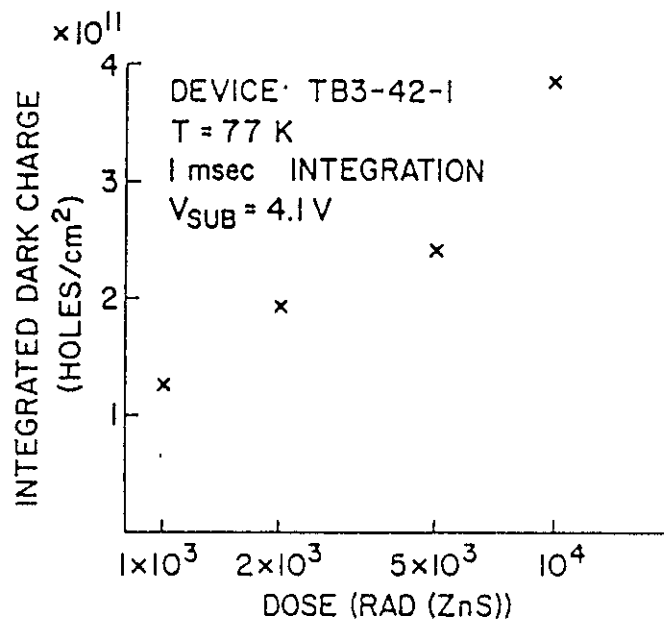
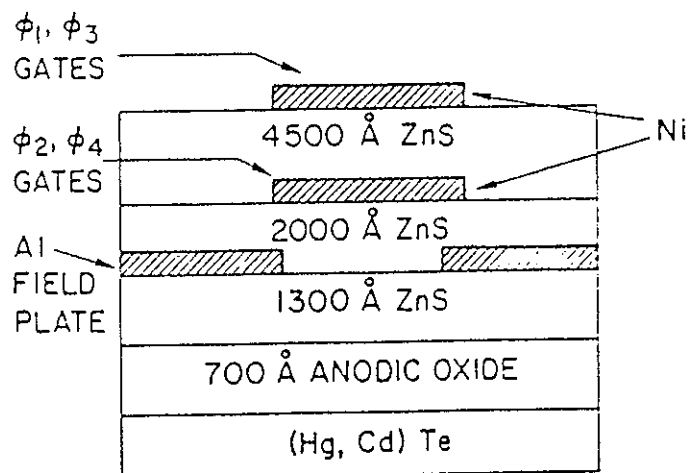


Figure 5.3-17 Dark charge versus dose for the MIS structure shown [30]

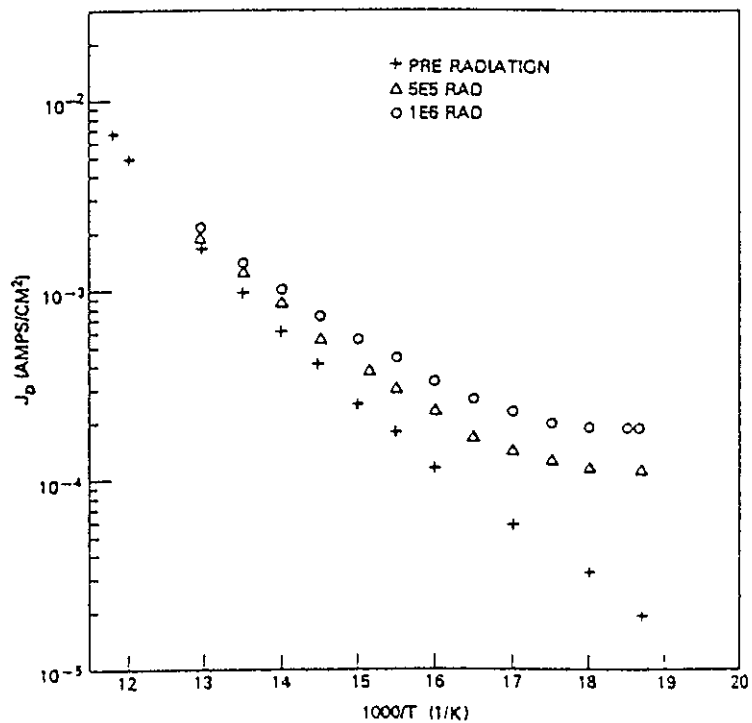
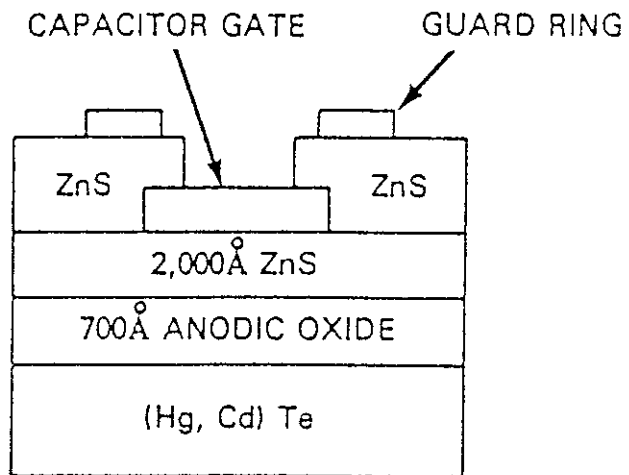


Figure 5.3-18 Dark current versus 1000/T for the structure shown [29]

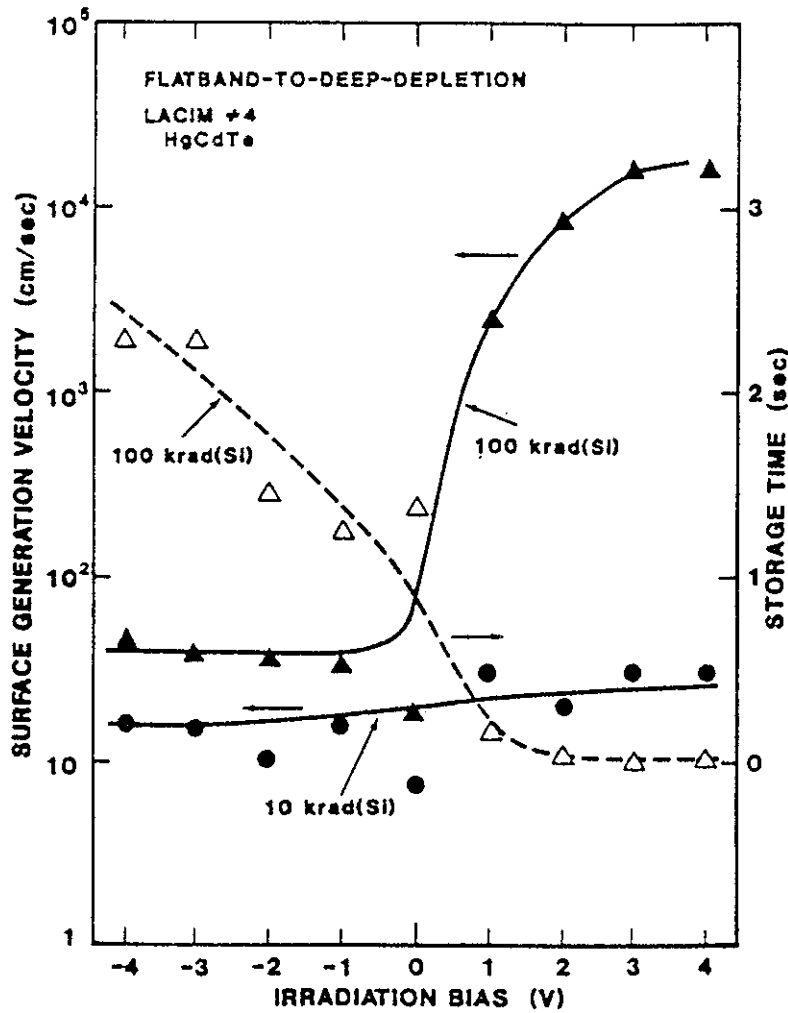
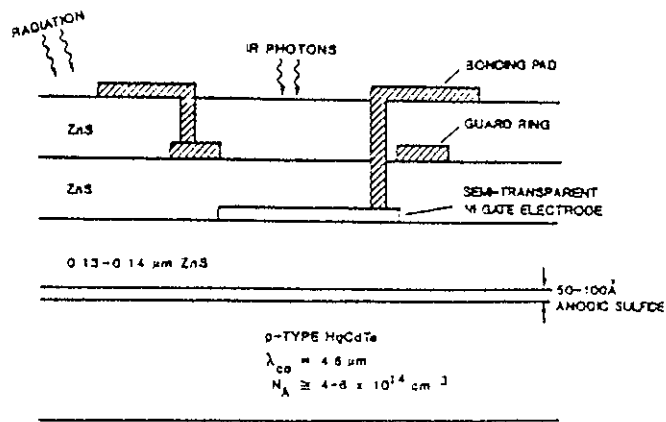


Figure 5.3-19 Surface generation velocity and storage time as a function of irradiation bias for the MIS structure shown [28]

Figures 5 4-1 and 5 4-2 show the values obtained for MIS devices with anodic oxide/ZnS and anodic sulphide/ZnS passivations respectively. Figure 5 4-1 was obtained for a CCD structure and the dependence on insulator thickness can be seen (the $\phi 1$ gates have a thicker insulator than the $\phi 2$ gates in this stepped insulator structure). The dependence on bias during irradiation - with a very small shift for zero field, reflects the dependence of electron-hole yield on electric field (as discussed in section 3 2 1 2). At zero electric field there is enhanced electron-hole recombination. In the figures it can be seen that there is negative flatband shift (net hole trapping) for positive bias and positive shift (net electron trapping) for negative irradiation bias. This results from the fact that both electrons and holes are mobile in ZnS at 77K and either can be trapped at the interface (only electrons would be mobile in SiO₂ at that temperature and they are not trapped in SiO₂).

According to Moriwaki et al [28], though both electrons and holes can be trapped - thus leading to compensation effects (ie both occurring together), in practice this does not happen. They found that trapping of uncombined holes and electrons was not fully efficient for anodic sulphide/ZnS devices but this was explained by recombination of trapped holes (electrons for a negative electric field) with mobile electrons (holes for negative field) injected from the MCT. Net trapping efficiencies of ~30% were reported. For their anodic oxide/ZnS devices, Waterman and Killiany reported net charge losses of ~97% for electric field strengths near 3×10^5 V/cm which confirmed earlier results given by Kalma and Hopkins [38]. The low trapping efficiencies are good news for MCT devices (compared with effects in MOS devices, though the flatband shifts can still be high enough to disrupt device operations after a few tens of krad particularly for a CCD [30] - though in that case in-flight adjustment of biases might be a possibility. Killiany [36] has described a threshold tracker circuit which can automatically measure the threshold voltages for a CCD, though it is somewhat complex and its use has not yet been reported in-flight. Waterman and Schiebel [39] have given results on flatband voltage shift degraded transconductance and decreased subthreshold current gate voltage slopes in MCT MISFETS (as might be used for monolithic on-focal plane processing electronics). Kalma et al [40] have reported very low values for flatband voltage shift in MCT MIS devices with a low temperature photochemically deposited, SiO₂ layer. Figure 5 4-3 compares their results with MOS devices and other passivations. The authors favoured an explanation in terms of equal trapping of holes and electrons (compensation). According to Nemirovsky and Bahir [2], SiO₂ is a useful passivation for MCT and is stable up to 90°C. It is transparent in the 3-5 μ m region, but LWIR devices would need to be back illuminated. At high doses (~200 krad) Moriwaki et al [28] noticed saturation effects, probably due to reductions in the number of traps available.

In general it should be noted that, as for MOS devices, the exact details of the passivation process will have an effect on the magnitude of the threshold voltage shift, so that results will vary with device process and for a given device, from batch-to-batch.

5.5 ANNEALING OF RADIATION DAMAGE

Reductions in charge trapped in the insulator and in interface trap density can be expected if the device is annealed at increased temperature after irradiation. This is possible in flight if an active cooler is used (eg thermoelectric or closed-cycle). Annealing experiments can also give insight into physical mechanisms, especially if measurements are made after short (equal) periods at a variety of temperatures (a technique known as isochronal annealing).

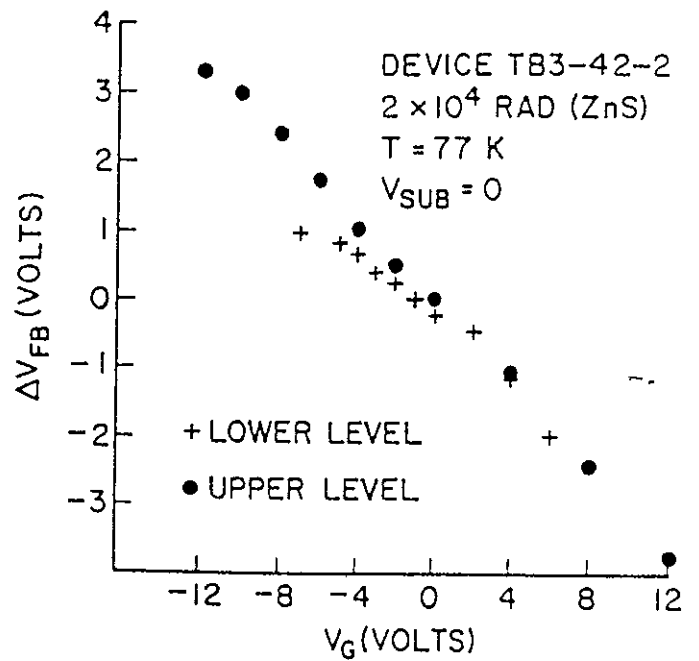
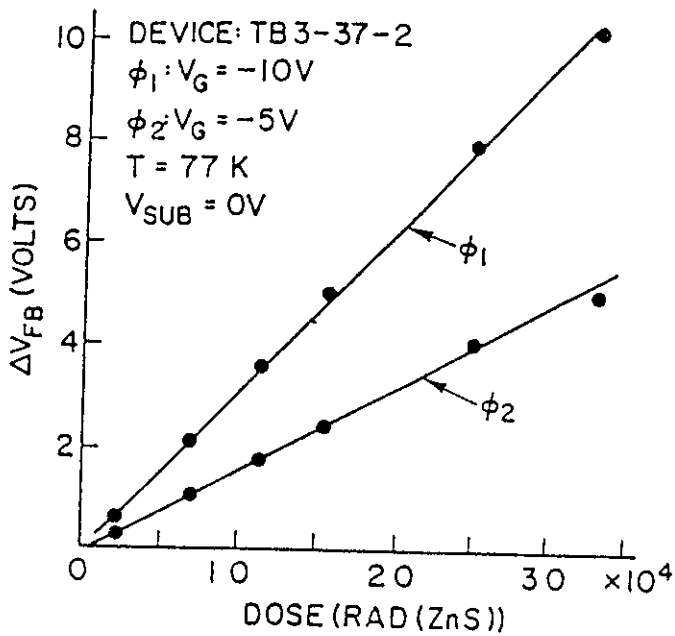
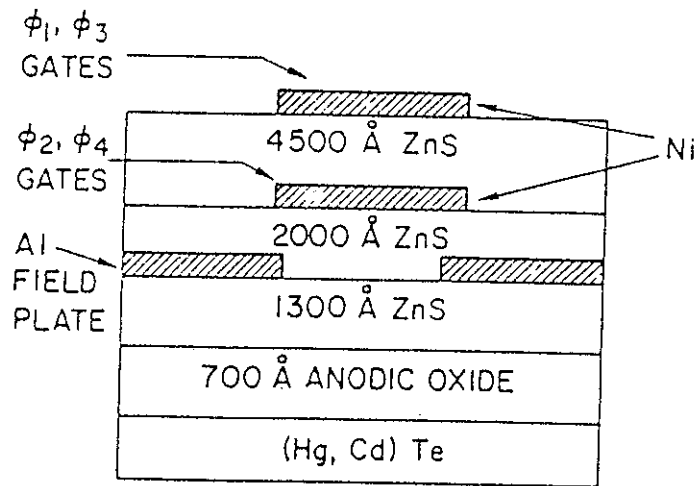


Figure 5.4-1 Flatband voltage shift versus dose and irradiation bias for the structure shown [30]

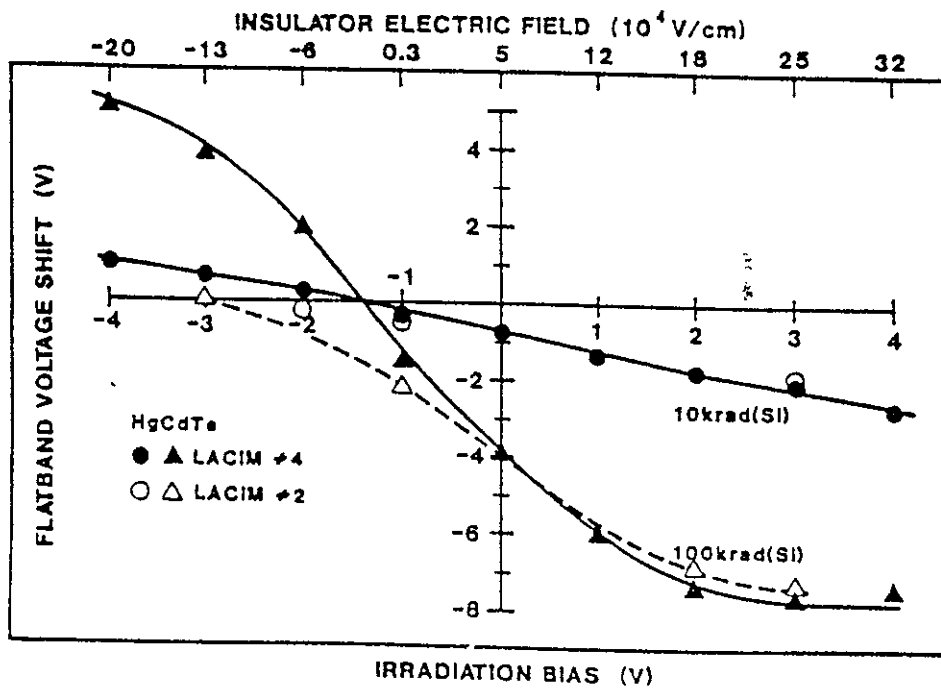
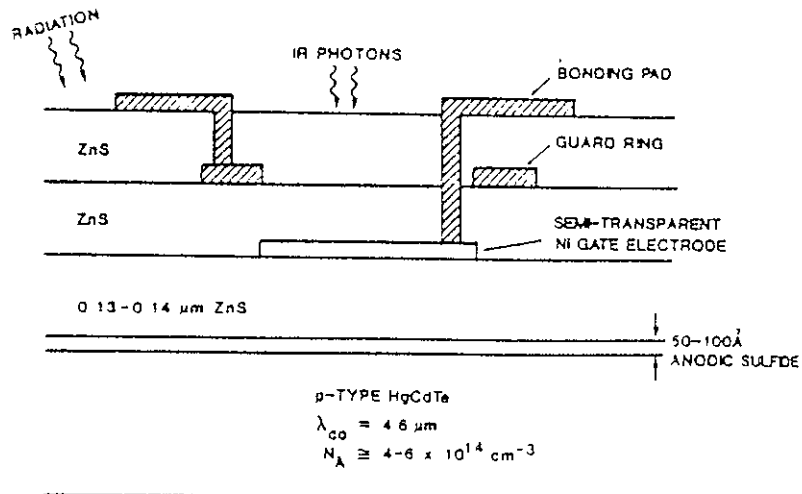


Figure 5.4-2 Flatband voltage shift versus dose and irradiation bias for the structure shown [28]

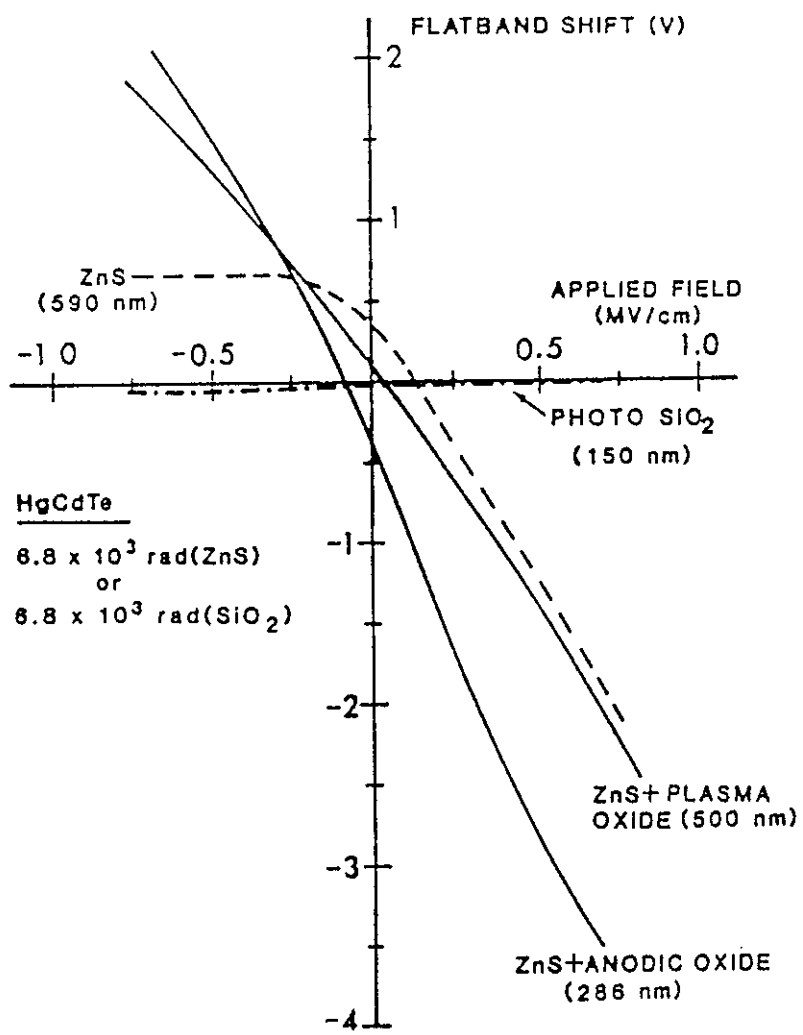


Figure 5.4-3 Flatband shifts for MIS capacitors with a photochemically deposited SiO₂ ('photox') layer [39]

Figures 5 5-1 and 5 5-2 show results from DeWames et al [9] and Domkowski et al [41] on annealing of dark current. Complete recovery is possible after only a short anneal at 300K. It would be useful to know how much annealing can occur for long periods at intermediate temperatures (say ~150K) but there is little information available. Figure 5 5-1 indicates that some annealing might be expected. Williams et al [24] found that partial annealing (in R_{0A} values) occurred for a device irradiated at 40K and annealed at 105K (see table 5 3-1 in section 5 3 1 4).

Figures 5 5-3 and 5 5-4 show results for flatband voltage shift. For the anodic sulphide/ZnS MIS devices (figure 5 5-3, [28]) the unannealed fraction for both irradiation biases and for the various anneal biases decreased monotonically from unity (no annealing) and approached zero (complete annealing) near 275K. These results suggest that, in this case, a significant number of trapped electrons is not present in the insulator, and thus that the flatband shifts for positive applied fields during irradiation are predominantly due to trapped holes. As the insulator electric field during the anneal is reduced, retrapping of thermally-released holes could occur, resulting in a slower annealing rate with increasing anneal temperature. However, no retrapping is evident in this data with the possible exception of measurements made with an anneal bias of -1 V at high temperatures.

In contrast for the photox devices [39] figures 5 5-4 and 5 5-5 indicate complex effects at 275K in that both trapped electrons and holes are present and both anneal at this temperature. However the two types of trapped charge did not anneal simultaneously because the flatband voltage first shifted in a positive direction, indicating a net anneal of trapped holes, and then shifted in a negative direction, indicating a net anneal of trapped electrons. In fact, the initial trapped hole annealing caused the flatband voltage to shift to a more positive value than it had been prior to irradiation. The subsequent trapped electron annealing caused the flatband voltage to shift back to a slightly more negative value than it had been prior to irradiation. This indicated that not all of the trapped holes had been removed during the prior annealing. Additional 300K annealing caused the flatband voltage to return to its preirradiation value, probably because all of the trapped charge became mobile and was removed at this temperature. The slow changes in VFB with temperature indicate a broad range of thermal activation energies.

Figure 5 5-4 also shows results for interface state density for which annealing took place at a single well defined temperature between 200K and 225K. This annealing of interface traps is in contrast to the case in MOS devices where interface state generation is negligible at 80K and occurs when the devices are warmed up.

All these results on dark charge and flatband voltage indicate that operation at temperatures above 77K is advantageous in many cases in that some annealing is likely to occur as the dose builds up (in a long term space application), although dark current would, of course, be higher anyway because of the higher temperature. Alternatively it may be possible to periodically 'boost' the temperature of a device so as to effect annealing. There are disadvantages in this however.

- * thermal cycling can reduce device reliability, particularly for hybrids
- * interface traps will build up in MOS circuits if the devices are warmed. Thus leading to threshold voltage shifts in multiplexer circuits (if on the focal plane)

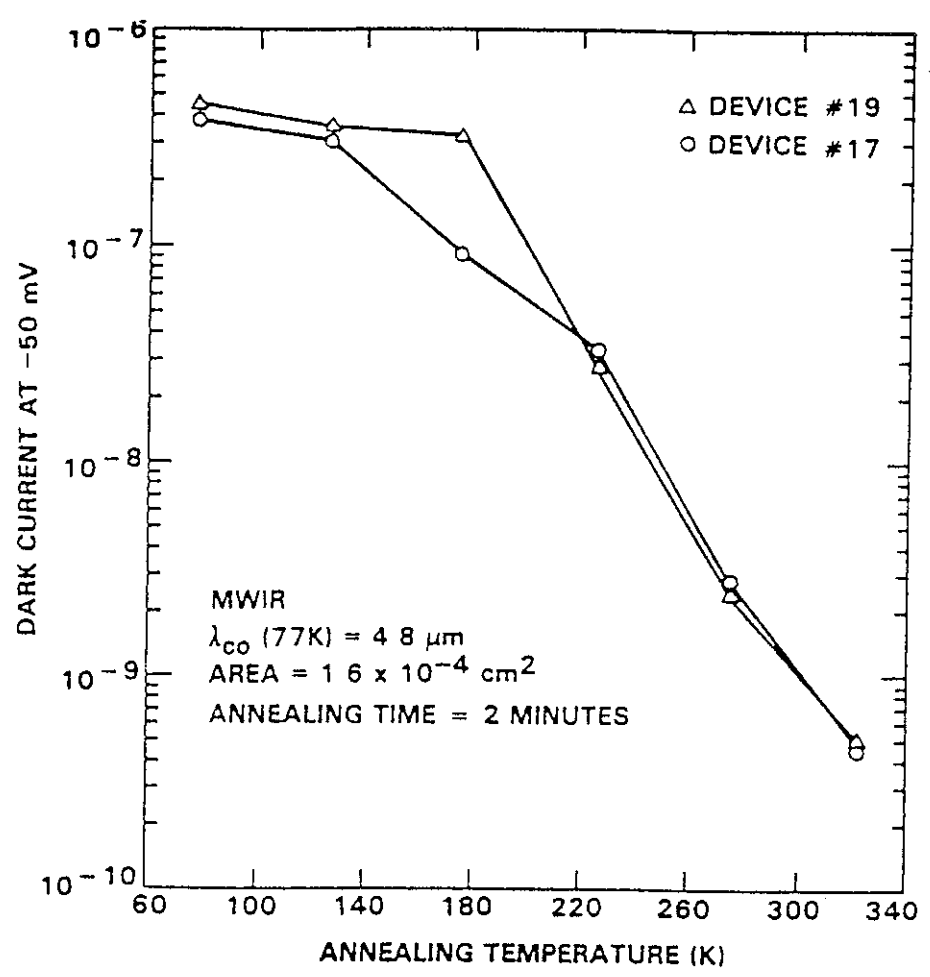


Figure 5.5-1 Isochronal annealing characteristics of MWIR diodes (damage introduced with a nitrogen laser) [9]

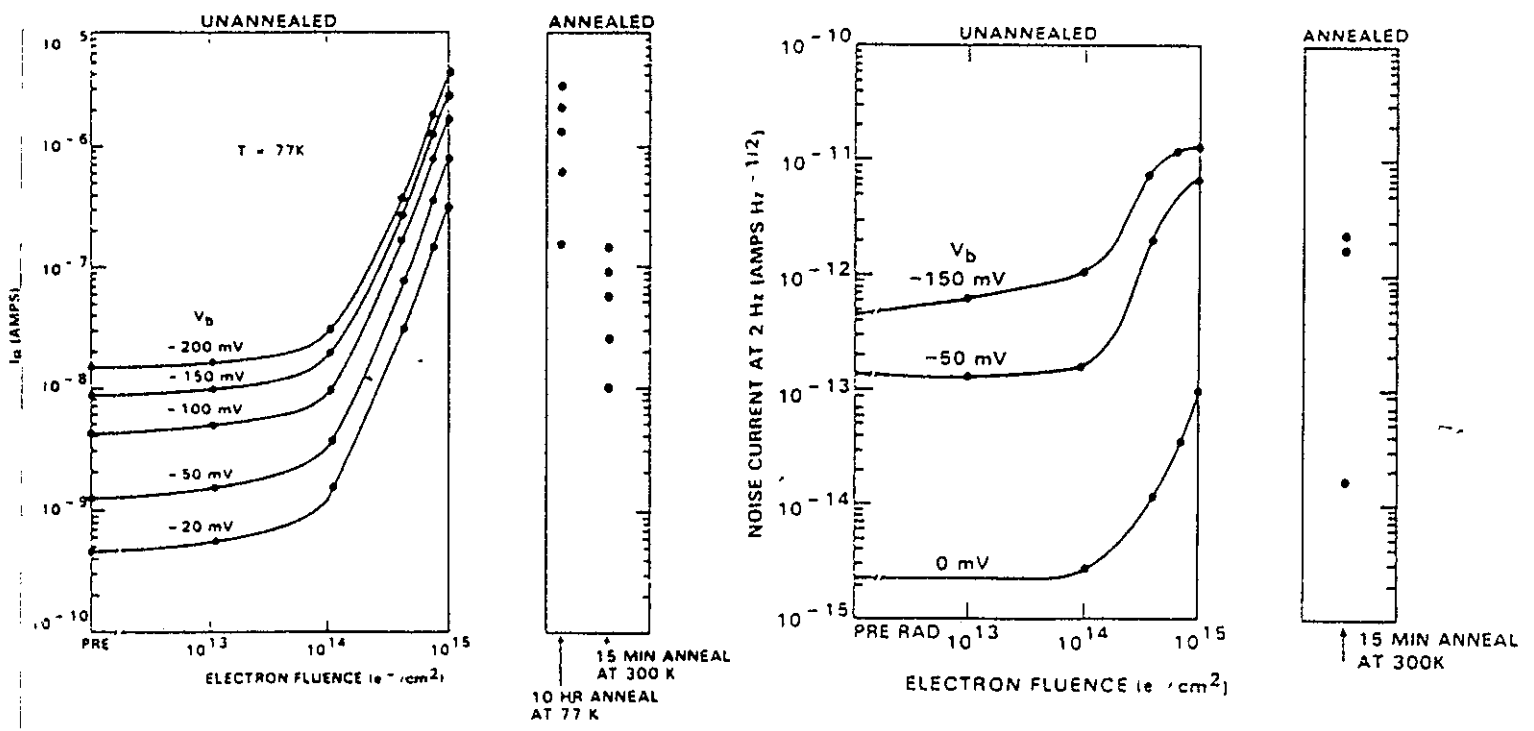


Figure 5.5-2 Leakage current and 2Hz noise current at 77K and after a 15 minute anneal at 300K [40]

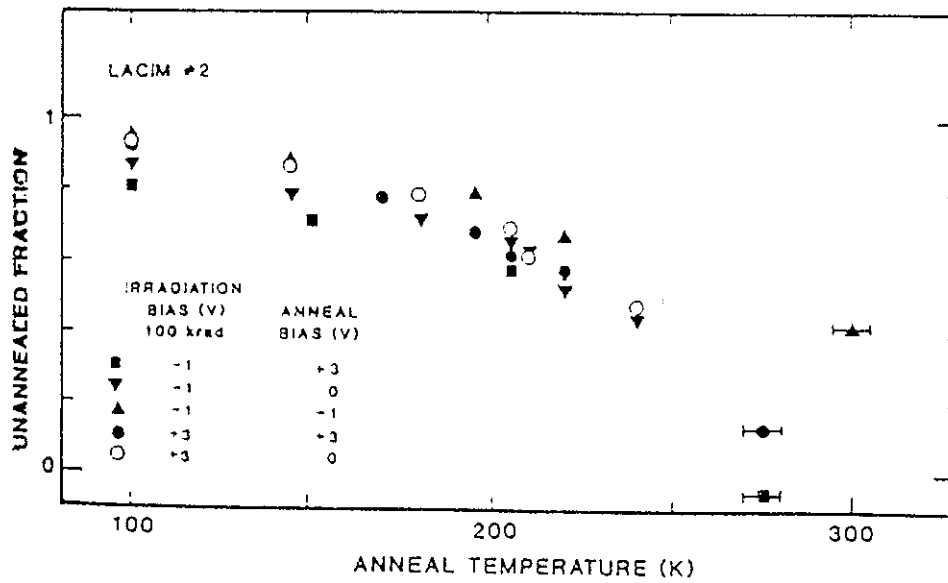


Figure 5.5-3 Unannealed fraction of the flatband voltage shift for a dose of 100 krad(Si) and an anodic sulphide/ZnS passivation [28]

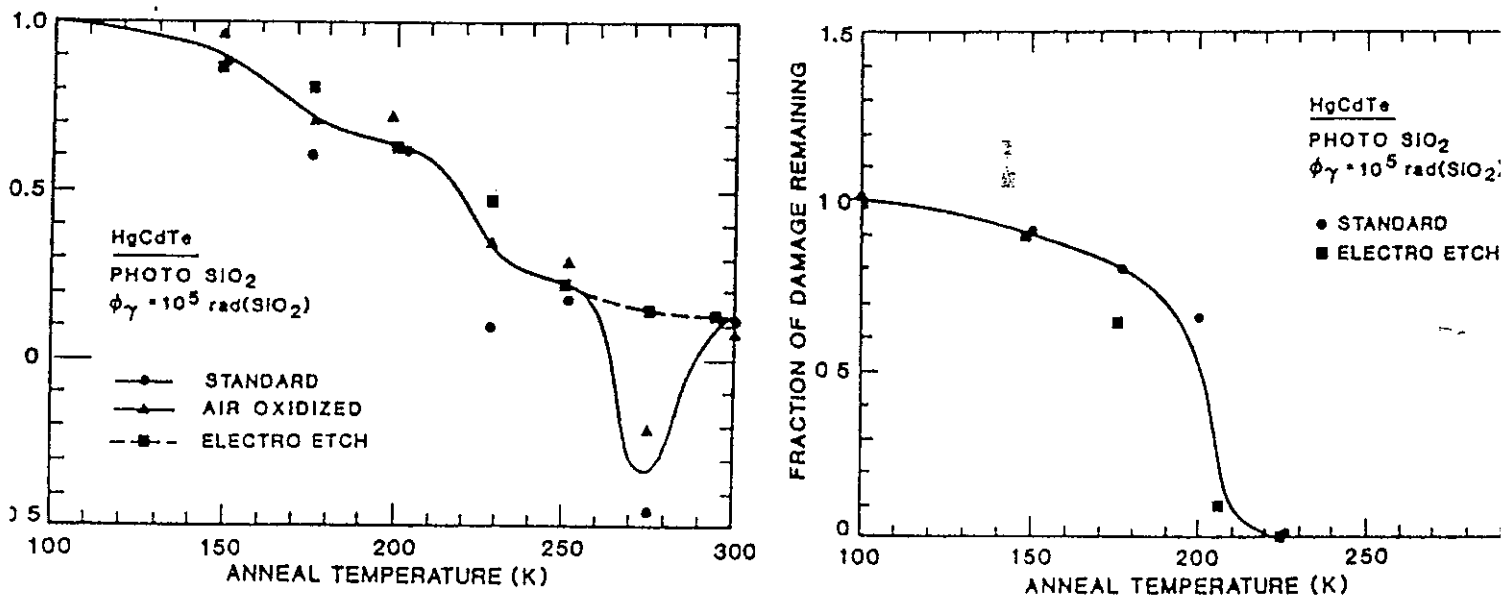


Figure 5.5-4 Annealing of the flatband voltage shift and interface state density for a photochemical SiO₂ passivation [39]

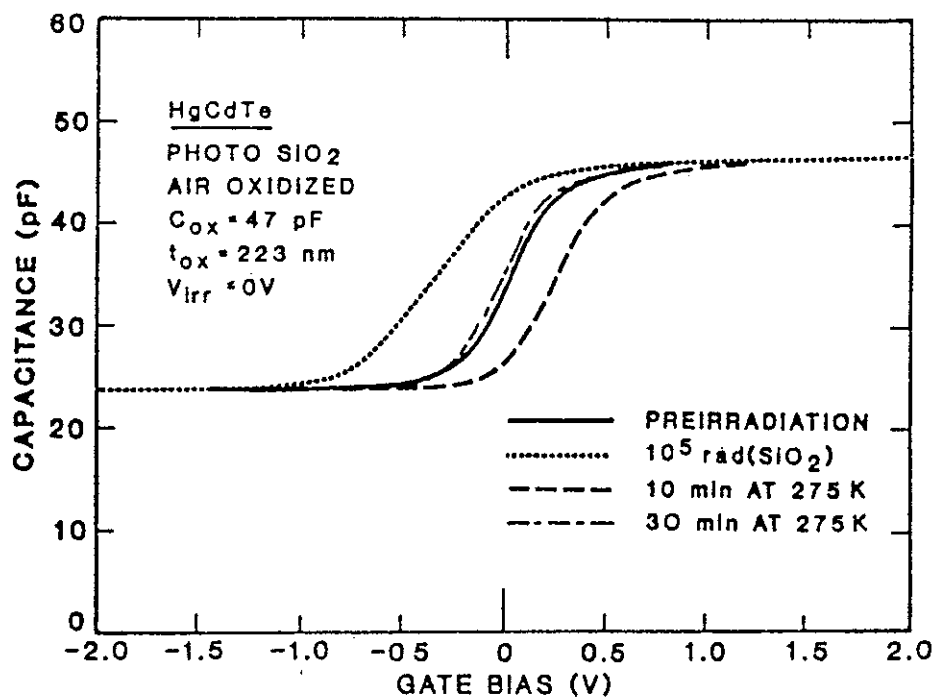


Figure 5.5-5 Isothermal annealing at 275K [39]

-
- [1] A H Kalma, 'Radiation response issues for infrared detectors', Proc NASA/JPL Workshop on innovative long wavelength infrared detectors, Pasadena CA, 24-26 April 1990, 151-157 (1990)
- [2] Y Nemirovsky and G Bahir, 'Passivation of mercury cadmium telluride surfaces', *J Vacuum Science and Technol*, vol A7(2), 450-459 (1989)
- [3] Y Nemirovsky, 'Passivation with II-VI compounds', *J Vacuum Science and Technol*, vol A8(2), 1185-1187 (1990)
- [4] C M Stahle and C R Helms, 'Thermal stability of the anodic oxide/Hg_{1-x}Cd_xTe interface', *J Vacuum Science Technol*, vol B5(4), 1092-1096 (1987)
- [5] E Weiss and N Mainzer, 'The characterisation of anodic fluoride films on Hg_{1-x}Cd_xTe and their interfaces', *J Vacuum Science Technol*, vol A6(4), 2765-2777 (1988)
- [6] E Weiss and C R Helms, 'Composition, growth mechanisms and stability of anodic fluoride films on Hg_{1-x}Cd_xTe', *J Vacuum Science Technol*, vol B9(3), pp 1879-1885 (1991)
- [7] S E Schachman and E Finkman, 'Interface properties of various passivations of HgCdTe', *Optical Engineering*, vol 29(7), pp 795-799 (1990)
- [8] G Sarusi, D Eger, A Zemel, N Mainzer, R Goshen and E Weiss, 'Degradation mechanisms of gamma irradiated LWIR HgCdTe photovoltaic detectors', *IEEE Trans on Nuclear Science*, vol NS-37(6), pp 2042-2049 (1990)
- [9] R DeWames, J Bajaj, E S Yao and G M Williams, 'Laser induced effects in HgCdTe photovoltaic devices', *J. Vacuum Science Technol*, vol A7(2), pp 536-543 (1989)
- [10] M M Moriwaki, J R Srour, L F Lou and J R Waterman, 'Ionizing radiation effects on HgCdTe MIS devices', *IEEE Trans on Nuclear Science*, vol NS-37(6), pp 2034-2041 (1990)
- [11] C L Jones, B E Matthews, D R Purdy and N E Metcalfe 'Fabrication and assessment of optically immersed CdHgTe detector arrays', *Semicond Sci Technol* 6 (1991) C110-C113
- [12] M B Reine, A K Sood and T J Tredwell, 'Photovoltaic Infrared Detectors', in *Semiconductors and Semimetals*, 18, R K Willardson and A C Beer (eds), pp 201-311 (Academic Press, 1981)
- [13] Y Nemirovsky, D Rosenfeld, R Adar and A Kornfeld, 'Tunneling and dark currents in HgCdTe photodiodes', *J Vacuum Science Technol*, vol A7(2), pp 528-535 (1989)
- [14] R E DeWames, J G Pasko, E S Yao, A H B Vanderwyck and G M Williams, 'Dark current generation mechanisms and spectral noise current in long-wavelength infrared photodiodes', *J. Vacuum, Science Technol*, vol A6(4), pp 2655-2663 (1988)

- [15] R E DeWames, G M Williams, J G Pasko and A H B Vanderwyck, 'Current generation mechanisms in small band gap HgCdTe p-n junctions fabricated by ion implantation', *J Crystal Growth*, vol 86, pp 849-858 (1988)
- [16] S E Schacham and E Finkman, 'Surface and implantation effects on p-n junctions', *Semicond Science and Technol*, vol 5, pp S41-S44 (1990)
- [17] R Adar, D Rosenfeld and Y Nemirovsky, 'Tunneling and noise phenomena in HgCdTe photodiodes' in Sixth Meeting in Israel on Optical Engineering, *Proc SPIE*, vol 1038, pp 84-89 (1988)
- [18] P W Norton and A P Erwin, 'Etch pit dislocation formation in $\text{Hg}_{1-x}\text{Cd}_x\text{Te}$ during array hybridization and its effect on device performance', *J Vacuum Science Technol*, vol A7(2), pp 503-508 (1989)
- [19] D K Blanks, J D Beck, M A Kinch and L Colombo, 'Band-to-band tunnel processes in HgCdTe comparison of experimental and theoretical studies', *J Vacuum Science Technol*, vol A6(4), pp 2790-2794 (1988)
- [20] S M Sze, Physics of Semiconductor Devices, 2nd Edn, section 2.3 (Wiley-Interscience, New York, 1981)
- [21] Y Nemirovsky, R Fastow, M Meyassed and A Unikovsky, 'Trapping effects in HgCdTe', *J Vacuum Science Technol*, vol B9(3), pp 1829-1839 (1991)
- [22] D K Blanks, 'Dark current processes in thinned p-type HgCdTe', *J Vacuum Science Technol*, vol B9(3), pp 1764-1769 (1991)
- [23] M E O'Brien and L D Flesner, 'Electron beam testing of LWIR detectors', in Test and Evaluation of Infrared Detectors and Arrays, *Proc SPIE*, vol 1108, pp 23-30 (1989)
- [24] G M Williams, A H B Vanderwyck, E R Blazejewski, R P Ginn, C C Li and S J Nelson, 'Gamma radiation response of MWIR and LWIR HgCdTe photodiodes', *IEEE Trans on Nuclear Science*, vol NS-34(6), pp 1592-1596 (1987)
- [25] H R. Vydyanath, P B Ward, S R Hampton, L Fishman, J Slawinski, J Ellsworth and J B Parkinson, 'High performance (HgCd)Te heterostructure photodiode arrays with improved radiation hardening', in Materials, Devices, Techniques and Applications for Z-plane Focal Plane Array (FPA) Technology, *Proc SPIE*, vol 1097, pp 110-116 (1989)
- [26] Y Yoshida, Y Hisa, T Takiguchi, Y Komine, K Yasamura and K Sato, 'Reduction of surface leakage current in $\text{Cd}_{0.2}\text{Hg}_{0.8}\text{Te}$ photodiode, in Infrared Technology XIV, *Proc SPIE*, vol 972, pp 39-43 (1988)
- [27] R. Triboulet, M Bourdillot, A Durand and T Nguyen Duy, '(Hg,Zn)Te among the other materials for IR detection', in Future Infrared Detector Materials, *Proc SPIE*, vol 1106, pp 40-46 (1989)

- [28] G R Hopkinson, C J Baddiley, D R P Guy and J E Parsons, 'Total Dose and Proton Testing of a Commercial HgCdTe Array' *IEEE Transactions on Nuclear Science*, vol NS-41(6), pp 1966-1973, (1994)
- [29] M M Moriwaki, J R Srour, L F Lou and J R Waterman, 'Ionizing radiation effects on HgCdTe MIS devices', *IEEE Trans on Nuclear Science*, vol NS-37(6), pp 2034-2041 (1990)
- [30] J R Waterman, 'Radiation induced interface trap limited storage times in 10 micron cut off wavelength (Hg,Cd)Te MIS capacitors', *IEEE Trans on Nuclear Science*, vol NS-35(6), pp 1313-1318 (1988)
- [31] J R Waterman and J M Killiany, '2 MeV electron irradiation effects in (Hg, Cd)Te CCDs', *IEEE Trans on Nuclear Science*, vol NS-30(6), pp 4209-4215 (1983)
- [32] M A Kinch, 'Metal-Insulator-Semiconductor infrared detectors' in Semiconductors and Semimetals, 18, R K Willardson and A C Beer (Eds), pp 313-378 (Academic Press, 1981)
- [33] W D Baker, 'Intrinsic focal plane arrays', in Charge-coupled devices, D F Barbe (Ed), pp 25-26 (Springer-Verlag, 1980)
- [34] M J Yang, C H Yang and J D Beck, 'Observation of incoherent tunneling in HgCdTe MIS structure', *Semicond Sci Technol*, vol 5, pp S118-S121 (1990)
- [35] M J Yang, C H Yang and J D Beck, 'Interface properties of HgCdTe metal-insulator-semiconductor capacitors', *Appl Phys Lett*, vol 54(3), pp 265-267 (1989)
- [36] M A Kinch, R A Chapman, A Simmons, D D Buss and S R Borrello, 'HgCdTe Charge-Coupled Device Technology', *Infrared Physics*, vol 20, pp 1-20 (1980)
- [37] J M Killiany, 'Radiation effects in silicon charge-coupled devices', *Topics in Applied Physics*, vol 38, pp 147-176 (1980)
- [38] A H Kalma and M A Hopkins, 'Ionizing radiation effects in (Hg,Cd)Te MIS capacitors', *IEEE Trans on Nuclear Science*, vol NS-28(6), pp 4083-4087 (1981)
- [39] J R Waterman and R A Schiebel, 'Ionizing radiation effects in N-channel (Hg,Cd)Te MISFETS with anodic sulfide passivation', *IEEE Trans on Nuclear Science*, vol NS-34(6), pp 1597-1601 (1987)
- [40] A H Kalma, R A Hartmann and B K Janousek, 'Ionizing radiation effects in HgCdTe MIS capacitors containing a photochemically-deposited SiO₂ layer', *IEEE Trans on Electron Devices*, vol NS-30(6), pp 4146-4150 (1983)
- [41] D W Domkowski, D G Feller, L R Johnson, C I Westmark, C B Norris, C T Fuller and J Bajaj, 'Effects of 6 MeV electron irradiation on the electrical characteristics of LPE Hg_{0.7}Cd_{0.3}Te mesa photodiodes', in *IEEE Trans on Nuclear Science*, vol. NS-33(6), pp 1471-1473 (1986)

6 RADIATION EFFECTS IN INSB AND PTSI ARRAYS

In this chapter we briefly discuss the small amount of published data on IR focal plane arrays using materials other than HgCdTe (which was considered in chapter 5)

6.1 INSB ARRAYS

As discussed in section 1.4.2, InSb detectors are usually fabricated as PV photodiode or MIS arrays with a silicon oxide passivation. Radiation effects to be expected are

- increases in dark current due to increases in interface trap density and to trap-assisted tunneling
- changes in flatband voltage due to oxide charging and build-up of interface traps
- displacement damage induced dark current spikes

Mechanisms for total ionizing dose-induced dark current generation will be similar to those described for MCT arrays in section 5.3. Tunneling currents were seen to be particularly important for narrow bandgap MCT. Measurements on tunneling currents in InSb gate controlled diodes have been described by Adar et al [1]. In InSb the bandgap is wider (0.24 eV at 77K) so tending to lead to smaller tunnel currents. Also, in contrast to MCT, the bandgap in InSb has a negative temperature coefficient. As the temperature decreases the barrier for tunneling electrons becomes larger and the tunneling currents should decrease. In trap-assisted tunneling processes this temperature dependence should be strengthened. Adar et al fitted their data to conventional theories quite well, as described in section 5.3 there is still some controversy over effects in MCT. Tunnel currents have also been studied by Jost [2]. Very little work on radiation-induced effects has been reported, however it is expected that dark current changes are not as serious as with long wavelength MCT.

Chen and Srour [3] have described flatband voltage measurements on unhardened MIS devices. They obtained large shifts of order 0.1V/krad at 77K and 4K (figure 6.1-1) which they attributed to near 100% hole trapping at those temperatures (with no compensation or recombination effects). Presumably lower values could be achieved with improvements in oxide process. Indeed Mueffelmann and Iwasa [4] have reported InSb CID devices tolerant up to 200 krad(Si). Also Hoffmann and Feitt [5] claim that standard SBRC devices have been irradiated to 10 krad(Si) without any degradation in quantum efficiency or leakage current and that improved passivation can give tolerance up to 600 krad(Si).

The charge deposited in transient events is ~ 1740 e/ μm for a minimum ionizing particle. Results given in section 9.2 indicate typical events of 4×10^4 electrons for proton bombardment. Hoffmann and Feitt [5] have modelled the effects for a variety of proton energies and detector geometries as shown in figure 6.1-2.

Effects of proton displacement damage on dark current nonuniformity have been investigated by the SIRTf team and are discussed in chapter 9 (unpublished experimental returns). They also found evidence for charge trapping in the cryogenic CMOS multiplexer, transient events in the multiplexer and for changes in responsivity.

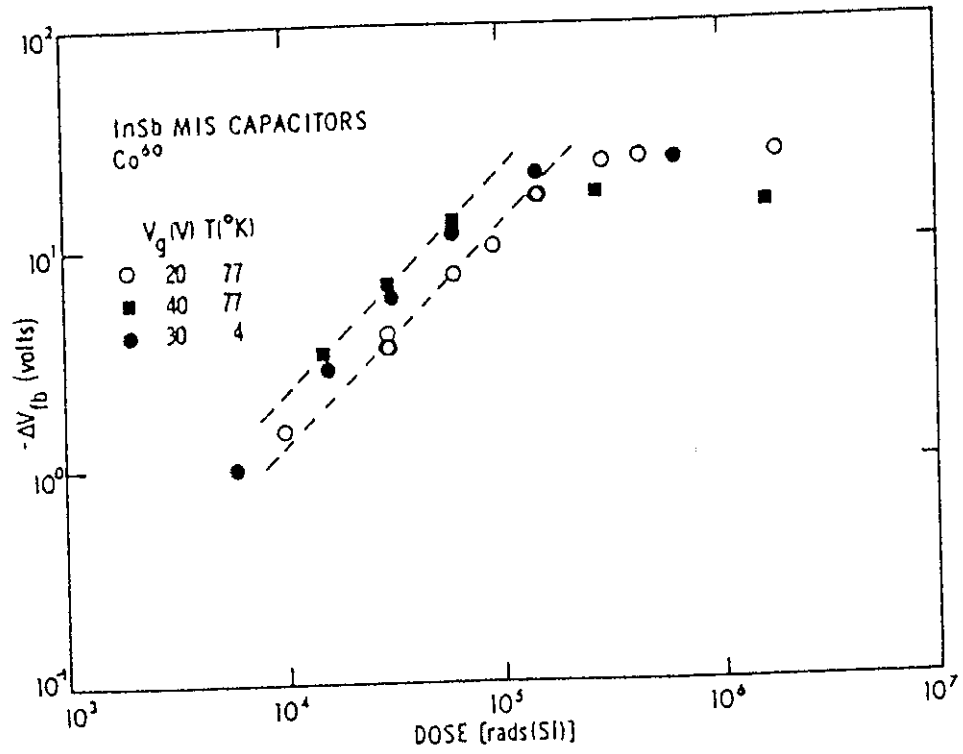
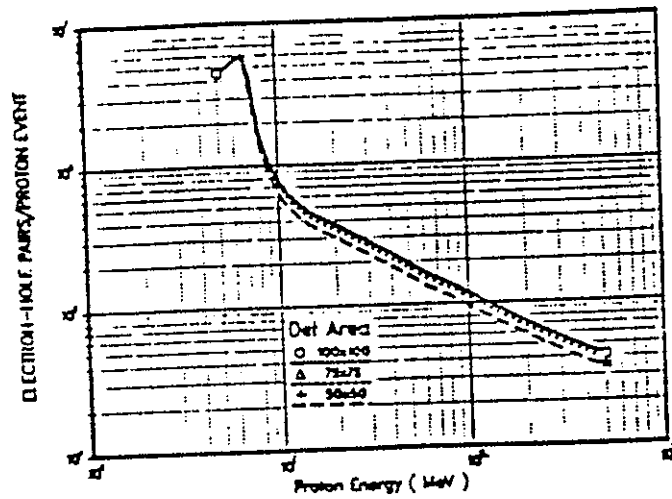
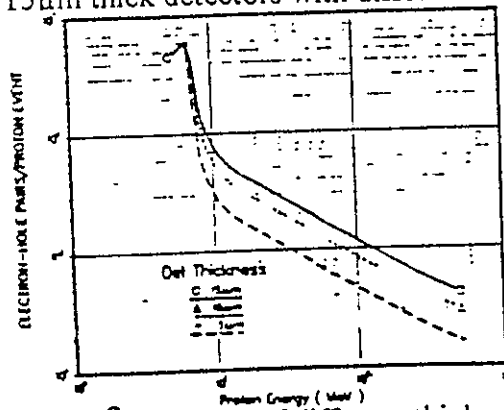


Figure 6 1-1 Flatband voltage shifts versus total ionizing dose for InSb MIS capacitors irradiated at 4 and 77K with several values of applied bias [3]



a) 15μm thick detectors with different areas



b) 100μm² detectors of different thicknesses

Figure 6 1-2 Pulse amplitudes per proton event as a function of proton energy [5]

6.2 PTSI ARRAYS

Very little information is available on PtSi arrays but Ueno et al [6] have looked at effects for the arrays to be used on the Japanese ASTER payload. No significant changes were found after 5 krad of Co60 gamma rays. They measured charge transfer efficiency, quantum efficiency and dark signal.

REFERENCES

- [1] R. Adar, Y. Nemirovsky and I. Kidron, 'Bulk tunneling contribution to the reverse breakdown characteristics of InSb gate controlled diodes', *Solide State Electronics*, vol 30(12), pp 1289-1293 (1987)
- [2] S. R. Jost, 'Dark current phenomena in InSb metal insulator semiconductor (MIS) detectors', *Proc SPIE*, vol pp 409, 62-64 (1982)
- [3] S. C. Chen and J. R. Srour, 'Ionizing radiation effects on indium antimonide MIS devices', *IEEE Trans on Nuclear Science*, vol NS-26(6), pp 4824-4827 (1979)
- [4] W. Mueffelman and S. Iwasa, 'Second-generation technology enhances military imaging', *Laser Focus World*, pp 109-113 (August 1988)
- [5] A. Hoffmann and R. Feitt, 'Study of advanced InSb arrays for SIRTf', Third Infrared Detector Technology Workshop, C. R. McCreight (Ed), NASA-Ames Research Centre, NASA Technical Memorandum 102209, 147-156 (1989)
- [6] M. Ueno, T. Shiraishi, M. Kawai, Y. Yoneda, M. Kimata and M. Nunoshita, "PtSi Schottky barrier infrared focal plane array for ASTER/SWIR", *Proc SPIE*, vol 2553, pp 56-65 (1995)

7 RADIATION EFFECTS ON Si:X DETECTORS

In this section we review the relatively large body of literature on radiation effects on extrinsic Si X detectors used for space based astronomy (IRAS, ISO, WIRE and SIRTf programmes) These detectors are used at long wavelengths and low temperatures in a low background environment

7.1 EXTRINSIC Si:X DETECTORS

Late in the IRAS development programme it was discovered that significant changes in responsivity occurred even at dose levels ~ 1 rad in the detectors following exposure to ^{137}Cs gamma rays and protons Table 7.1-1 [1] below summarizes the results

Table 7.1-1 Radiation test results obtained during the IRAS development programme [1]

Detector Type	Si As	Si SB	Ge Ga	Ge Ga
Band	1	2	3	4
Radiation induced offset (mV)	20	24	125	240
Responsivity ratio during irradiation	1.3	2.4	8	40
Responsivity ratio 30 min after irradiation	1.2	1.9	5	9
Pre-irradiation signal (mV)	6	6	-	0.2
Pre-irradiation noise ($\mu\text{V rms}$)	14	30	-	3
Post-irradiation noise ($\mu\text{V rms}$)	13	110	-	7 spiking

Since significant permanent damage is only expected at high particle fluence levels (as discussed previously) the results were explained in terms of the trapping of ionization-induced electrons and holes which occurs at the very low operating temperature used ($\sim 4\text{K}$) The mechanisms have been discussed in detail by Petroff et al [2] The changes in detector response are due to changes in the carrier lifetime, which increases with dose This is because charge becomes trapped at ionized donors and acceptors Agnès et al [3] have given a good explanation of the effects in their Si Ga array used at low IR backgrounds

'The detector response is proportional to the photoconductive gain G , G itself is proportional to the lifetime of the charge carriers, which is affected by the Si intrinsic ionization By contrast, Ga impurity atoms are ionized by infrared (IR) radiation, the electrons produced in this way are trapped on the remaining phosphorus impurities, causing a decrease of the concentration of P ionized atoms as well as of Ga ionized

atoms (to comply with electric neutrality) The charge carriers' lifetime being proportional to the inverse of the density of Ga ionized atoms, their depletion leads to a responsivity increase Thermal energy is not sufficient at this temperature (4K) to extract the electrons from their P trapping level The detector can nevertheless recover if it is exposed to an IR flux, since the binding energy of the impurity atom P is lower than that of the impurity atom Ga

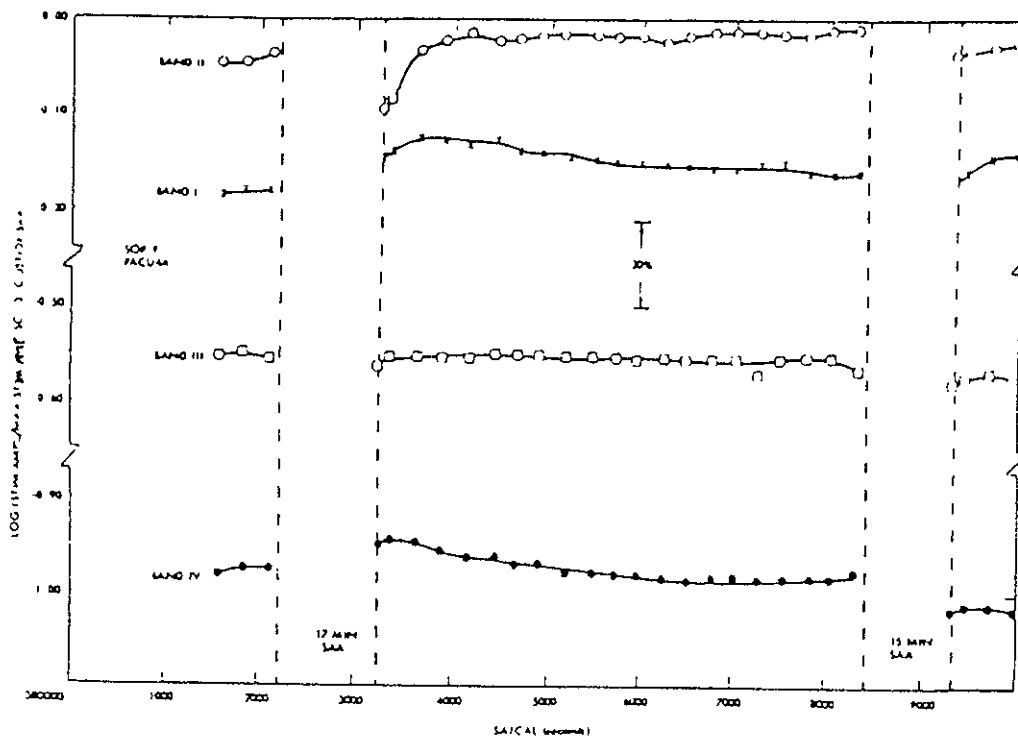
Quantitatively, 1 rad corresponds to an energy deposition per volume unit of Si of $1.5 \cdot 10^{14}$ eV/cm³, ie to the creation of $4.4 \cdot 10^{13}$ electrons/cm³ This can be compared to the concentration of the P sites, where these electrons can be trapped, of the order of 10^{13} /cm³ Therefore, it is not surprising that some radiation effect does take place already at dose levels as low as 1 rad'

Note that response increases after a particle hit and then slowly recovers Because of the low temperatures, recovery is slow (minutes to hours) The differences between detector types are mainly due to differences in concentration of the extrinsic dopant (As, Sb or Ga) Detectors with low dopant concentrations (or compensation due to impurities) suffer most It was also noticed that the radiation effects were strongly dependent on operating conditions such as temperature, bias, IR signal and background level

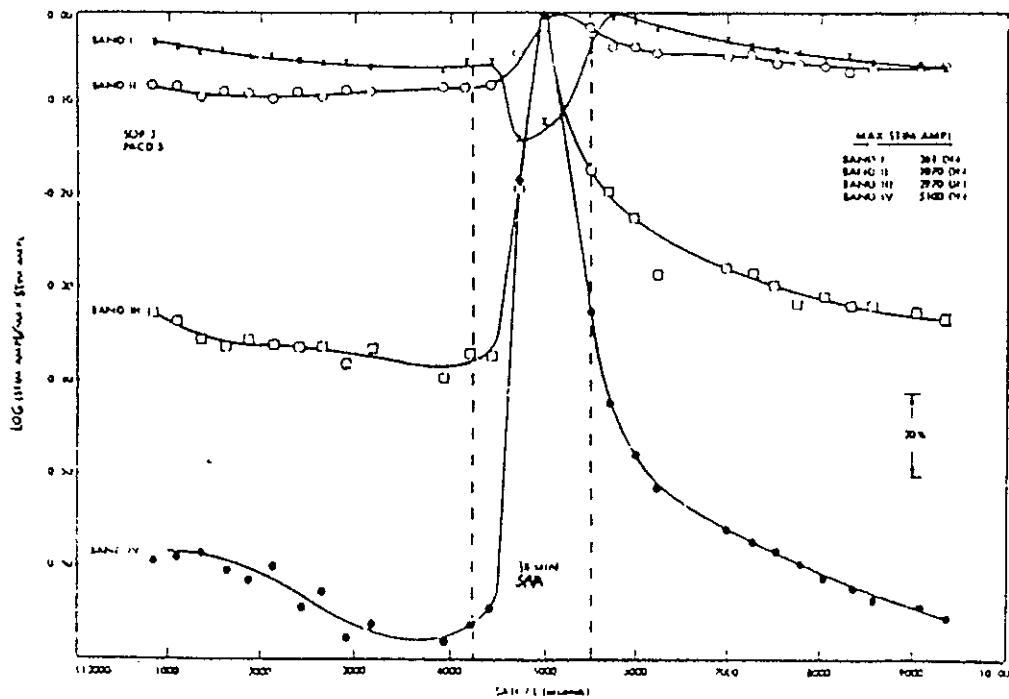
Since the IRAS detectors were discrete elements operated in PC mode, deglitching circuits were invented to remove transient signals (from cosmic rays) [4], [5] and temporary bias boosting was used to recover responsivity after passage through the SAA (a permanent increase in detector bias reduces the detector life due to high field breakdown) The effect of the 'bias boost' is shown in figure 7 1-1 [6]

Because of the IRAS experience, a considerable amount of device testing has been performed for ISO and SIRTf A comprehensive test campaign on the ISOCAM 32x32 Si Ga array has been described by Agnès et al [3] This array is sensitive in the range 4-18µm and was produced in a special development programme by LET1-LIR, a division of the Atomic Energy Commission (CEA-CENG, Grenoble France) and has been described by Sibille et al [7] The array was indium bump bonded to a silicon direct readout (DRO) circuit made with MOS N-channel technology

The source follower MOSFET is permanently biased and its output is sampled to a column bus with a switch Radiation tests were made using γ rays (low and high dose rates), 200 MeV protons and argon ions of 70 MeV/nucleon (to simulate cosmic rays) Agnès et al did not report any permanent damage [3] but changes in responsivity were found as shown in figure 7 1-2 Similar results were found for gamma and proton irradiations (though there were differences in the sizes of transient event glitches due to saturation effects at high ionization densities) Note that response changes were reduced for high IR fluxes Also the effects were worse if the detector was unbiased during irradiation Figure 7 1-3 shows the predicted particle impact rates for the ISO 24 hour orbit There is a high flux of protons during SAA passage followed by bremsstrahlung photons arising from transit through the outer electron belt There is then a 'quiet' time available for observations Recovery after passage through the belts is fairly fast (timescale ~ tens of minutes) However not all pixels are exposed to the same IR flux



SAA effect on detector response with bias boost.



SAA effect on detector response without bias boost.

Figure 7.1-1 Effect of bias boost in IRAS detectors [6]

during irradiation and so the detector gain can drift from one pixel to another - hence frequent pixel-by-pixel gain calibration is planned when in-flight. Note that bias boosting and increases in temperature were not found to improve the response for this array. During the 600 day mission it is expected that the array will be hit by about 30 Fe ions of energy greater than 1 GeV/nucleon and a test was performed with argon ions of the same way. No permanent damage resulted but each particle hit temporarily affects on average 8.4 pixels (taking into account the range of incidence angles encountered in space) recovery of response takes about 1 hr 30 min (figure 7.1-4). In addition to pixels directly affected, neighbouring pixels were also disturbed, the total number being 50-100. Data were also obtained for Ar ions of lower energy (28 MeV/nucleon) and higher LET. No permanent damage resulted.

Software algorithms for removing proton and bremsstrahlung glitches were also studied. The 'half Gauss' method was found to be best. This first rejects data with values above the median then the mean value is calculated on the remaining data. Particle glitches and memory effects after cosmic ray strikes together were calculated to give a dead time, in orbit, of 2% for each pixel.

According to Sibille [7] for the mission dose of 1.5 krad(Si) the accumulated dose did produce drifts in some of the MOSFET threshold voltages in the readout circuit but these were at an acceptable level.

Curing of the ISOPHOT stressed Si-Ge detectors has also been discussed by Wolf [8] and by Patrashin et al [9]. Wolf states that IR flashing can restore the responsivity to better than 2% if combined with a moderate bias boost (or to within 10% if a reduced operating bias is used). Patrashin suggests a method of applying bias pulses which cause a 'non-stationary carrier injection from the contacts and simultaneous impact ionization of impurities'.

The ISOCAM instrument operates at short integration times (~1s). Other arrays (eg on SIRTf) may be required to operate for long exposures. There is then a compromise between signal to noise ratio and contamination by particle hits. This has been considered by Herter [10]. Results for the other ISO arrays (Ge-Ga and Ge-Be used on ISOPHOT) have been given by Blum et al [11].

Results on 58x62 pixel Si-Sb (15-31 μ m) and Si-Ga (4-18 μ m) arrays under development for SIRTf have been given by McKelvey et al [12]. They have used ¹³⁷Cs, ²⁴¹Am and ⁵⁵Fe sources of activities up to 10mCi placed inside the test cryostat. Figure 7.1-5 shows changes in responsivity following ¹³⁷Cs irradiation. As for the ISOCAM array bias boosting was not found to be effective for the Si-Ga array. The Si-Sb array shows even larger changes in responsivity, which McKelvey et al attribute to the higher level of impurity compensation (though the unintended presence of boron) in the n-type Sb material. Figure 7.1-6 shows a γ -ray (660 keV) pulse height distribution for the Si-Sb array. Pulse heights as high as 60,000 carriers were seen (proton interactions would produce much larger pulses).

Finally we note that large changes ($\sim 1000\%$) in responsivity were also noticed for Ge Ga arrays tested for the Diffuse Infrared Background Experiment (DIRBE) [13]. This time a return to close to the pre-irradiation level within 10 minutes was found after an annealing step (T raised from 1.5K to 16.5K for 80 seconds). Co60 γ rays were used for the test (results were also obtained for a particle and 50 MeV protons under higher background, and therefore not worst case, conditions)

7.1.1 Monolithic Si:X Arrays

Virtually no information is available on radiation effects in large Si X arrays. Kalma [14] makes the comment that surface leakage (caused by ionization damage) is particularly important for high impedance devices (eg Si X detectors)

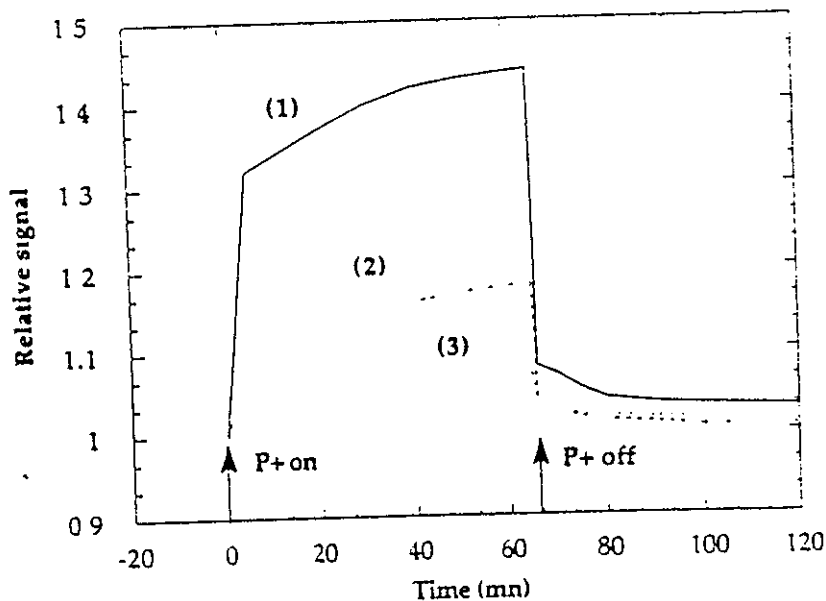


Figure 7.1-2 Influence of the infrared flux on a Si:Ga detector response. The relative variation of the detector signal during and after irradiation with the proton beam has been plotted as a function of time for three levels of infrared flux, namely: curve 1: $1.7 \cdot 10^9$ photons/s/cm², curve 2: $8.5 \cdot 10^9$ photons/s/cm², curve 3: $1.6 \cdot 10^{10}$ photons/s/cm² [3]

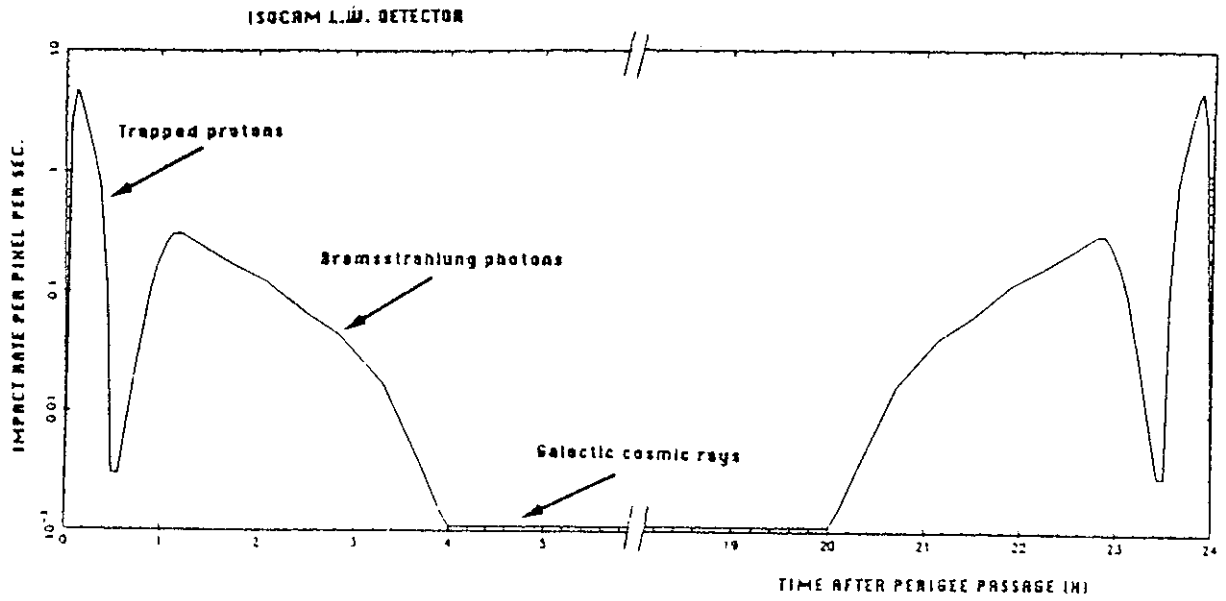


Figure 7.1-3 Glitch rate per pixel per second along the ISO orbit (1000x70000 km, 24 hour) [3]

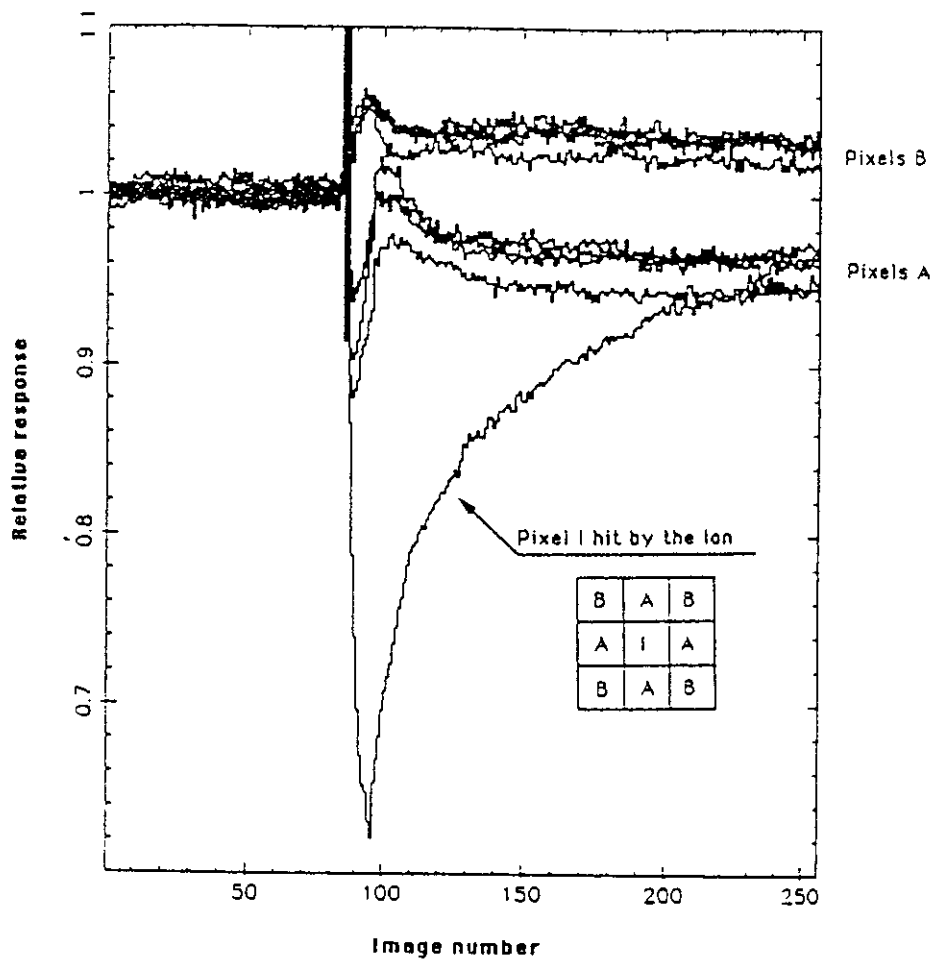


Figure 7.1-4 Relative responses of a Si:Ga pixels hit by an argon ion. Integration time 1s [3]

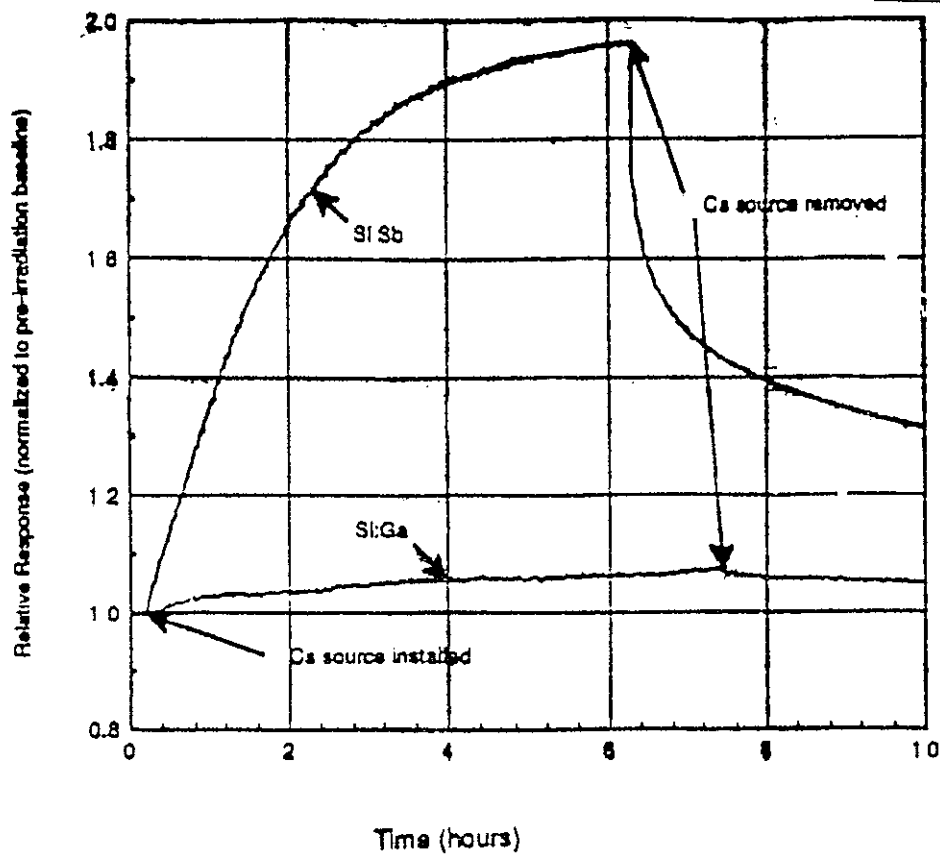


Figure 7 1-5 Si Ga and Si Sb responsivity under γ -irradiation ^{137}Cs (660 keV) source, 0.183 rad(Si)/hr, $T=8\text{K}$, Background $\sim 10^4$ photons/pix/s [10]

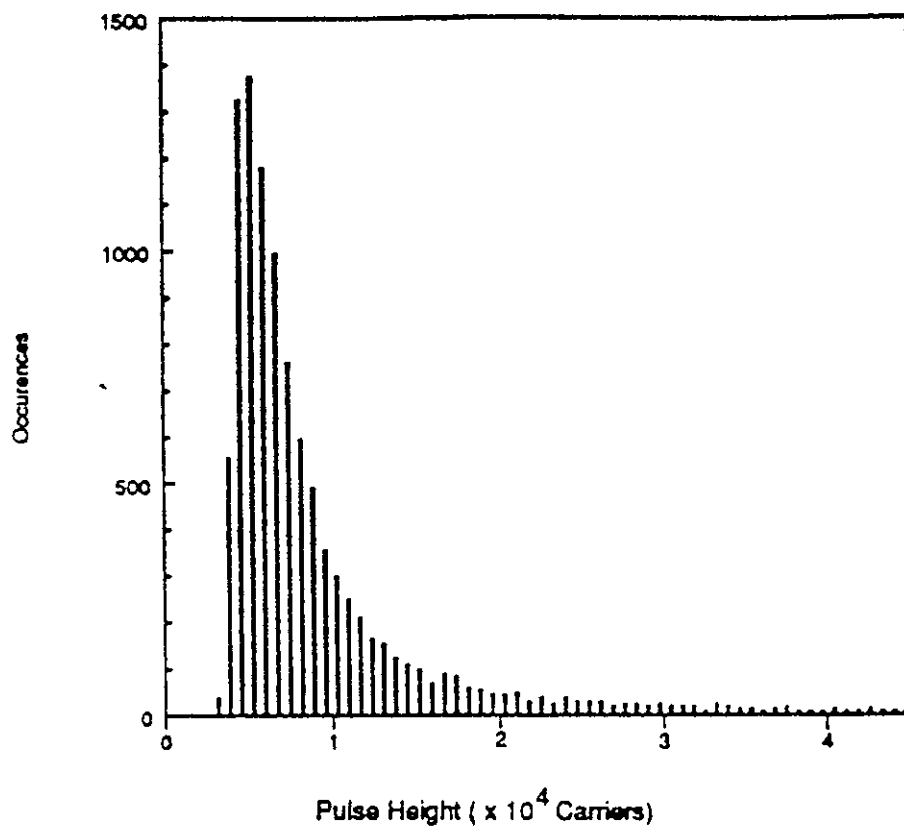


Figure 7 1-6 Si Sb γ -ray pulse height distribution, ^{137}Cs irradiation, $T=8\text{K}$ [10]

7.2 IBC DETECTORS

The structure of IBC detectors was considered in some detail in section 1.4.6.1 and general radiation effects were compared with other detectors in chapter 2. Here we concentrate on the limited amount of specific test results that have been reported.

With IBC detectors many of the drawbacks of bulk extrinsic detectors are ameliorated

- * the detectors are thinner ($\sim 20\mu\text{m}$) making transient signals less (and fewer pixels affected)
- * doping levels are higher - thus compensation effects occur at higher doses
- * device operated in pseudo photovoltaic mode

7.2.1 Ionization Effects

The signals associated with transient particle events have been studied by Montroy et al [15] and the results were reviewed by O'Brien and Flesner [16]. At the time there was some uncertainty regarding whether ionization produced by energetic electrons is exclusively intrinsic (ie electron-hole pairs only) or whether significant numbers of impurity band holes (D^+ carriers) are also excited. If only intrinsic carriers result, in principle it should be possible to discriminate against noise currents due to energetic electron ionization. LWIR excitation produces D^+ carriers rather than intrinsic holes, and it should be possible to separate intrinsic hole from extrinsic impurity band hole currents.

This question was investigated by a series of experiments in which the time responses of Si As IBC detectors to LWIR and to electron-beam excitation were compared [100]. The idea was that because the mobility of D^+ carriers is much lower than intrinsic holes, the contribution of D^+ current resulting from an electron beam excitation should be resolvable. For comparison, D^+ currents were generated using LWIR pulses from a $20\mu\text{m}$ laser diode.

At the temperature used (6K) the response dynamics are dominated by the relative mobilities of the intrinsic and extrinsic carriers and the laser data showed a recovery time of tens of microseconds, which is consistent with D^+ carrier current. The electron beam data were prompt on this timescale. According to O'Brien and Flesner, analysis of these and other data strongly implies that the energetic electrons do not directly excite significant D^+ currents.

Hence transient signals can be predicted on the basis of 1 e-h pair per 3.6 eV of particle energy (as for silicon) - with allowance for recombination effects. Also there is the possibility of intrinsic event discrimination (the IED concept, cf 1.4.6.1).

Recovery from transient events has been studied for the Rockwell 10x50 Si As array by Herter et al [17]. They used a ^{241}Am source giving γ rays of energy 59.54, 17.61 and 13.92 keV with a c ray detected every few seconds. The resulting charge on a detector element was between a few tens of thousands and a few hundred thousand electrons (no detector saturation occurred).

The largest events usually affected three neighbouring pixels those immediately above and below, in the same column (a few $\times 10^4$ electrons) and the immediately preceding pixel in the same row. The recovery in voltage level depended only on the number of detector resets after an event (not on the elapsed time) and was independent of device temperature.

If there was no illumination on the array, roughly 10 resets were required, by which time performance was fully recovered. With an illumination giving a signal of 6500 electrons per pixel between resets (10Hz frame rate) only one reset was needed. Reynolds et al postulated that IR photons anneal the detectors by removing the carriers generated by a γ -hit.

Total dose effects were studied by Moseley et al [11] for the Rockwell Si As array. For the 1.5 krad mission dose for DIRBE they found no significant degradation in performance for alpha particles, 150 MeV proton or Co60 gamma ray irradiation (the background IR signal was $\sim 10^{-14}$ W).

7.2.2 Effects due to Protons, Neutrons and Cosmic rays

As discussed in section 3.3 this has been studied by Clement et al [18] (and also by Clement et al [19]). They found that for cf-252 (fission) neutrons on average two acceptor states were created per unit volume for each incident neutron per unit area. The effect on responsivity is worse for higher quality (higher quantum efficiency and reduced acceptor concentration) detectors. Figure 7.2-1 [16] shows the change in normalized response for a 64x7 Si As array versus time in the neutron beam (beam flux = 1×10^9 neutrons/cm²-sec). Note the responsivity decreases as the square root of the fluence, as expected. A 10% change in signal occurs for a fluence of $\sim 9 \times 10^{11}$ neutrons/cm², presumably the NIEL curve for silicon (figure 3.3-1a) can be used to predict displacement effects for protons.

Recently, Van Cleve et al [20] have discussed the effect of proton damage on Si As arrays for SIRTf and WIRE. A degradation in dark current and dark current noise was seen for specific pixels (8 to 10% of the total at 1.5 V bias and more at higher bias) at a total dose of 140 rad(Si). No details were given of the proton energy and no mechanism was suggested, however Krabach [21] has indicated that the effects may be due to 'punch-through' of the intrinsic blocking layer. This mechanism might also explain the dark current increases seen by Luinge et al at SRON(Groningen) for the 12 x 1 Rockwell Si As arrays flying on the ISO SWS instrument (see section 9.2.2). Certainly it appears that BIB arrays are not as tolerant of the space environment as had been thought.

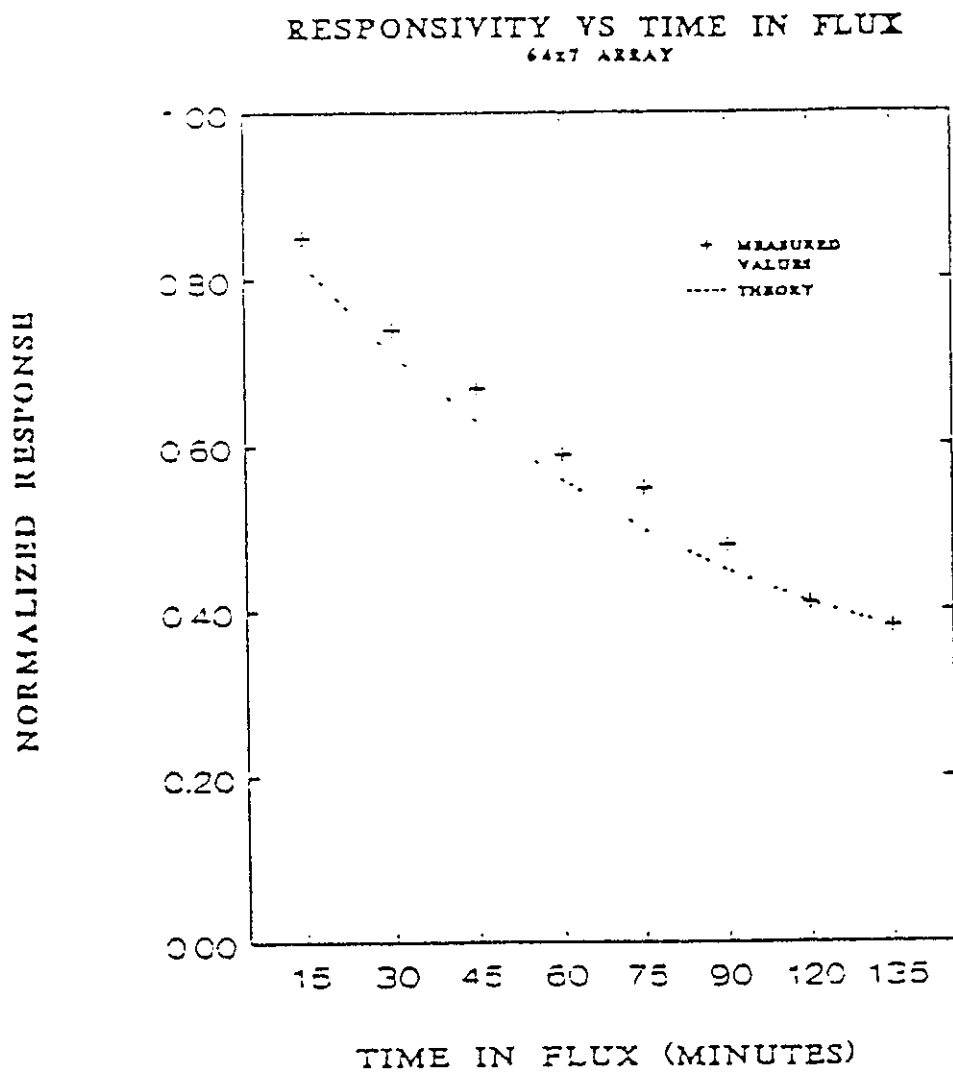


Figure 7 2-1 Effect of fission neutrons on a 64x7 Si As IBC detector responsivity [16] Beam flux = 10^9 neutrons/cm²-sec, maximum fluence = 8×10^{12} n/cm²

REFERENCES

- [1] L Varnell and D E Langford, 'Radiation effects on IRAS extrinsic infrared detectors', *IEEE Trans on Nuclear Science*, vol NS-29(6), pp 1551-1555 (1982)
- [2] M D Petroff, J C Pickel and M P Curry, 'Low level radiation effects in extrinsic infrared detectors', *IEEE Trans on Nuclear Science*, vol NS-26(6), pp 4840-4846 (1979)
- [3] P Agnèse, J J Engelmann and P Mottier, 'Results of radiation tests performed on the ISOCAM infrared detector array', *IEEE Trans on Nuclear Science*, vol NS-38(4), pp 953-963 (1991)
- [4] J G Emming, R F Arentz, C H Downey, E C Long and L G Smeins, 'Pulse circumvention circuit for the infrared astronomical satellite telescope', in Instrumentation in Astronomy V, *Proc SPIE*, vol 445, pp 254-263 (1984)
- [5] E C Long and D Langford, 'Test results and in-orbit operation of the infrared astronomical satellite circumvention circuit', in Instrumentation in Astronomy V, *Proc SPIE*, vol 445, pp 264-271 (1984)
- [6] F J Low, C A Beichman, F C Gillett, J R Honck, G Neugelbauer, D E Langford, R G Walker and R H White, 'Cryogenic telescope on the infrared astronomical satellite (IRAS)', *Proc SPIE*, vol 445, pp 288-296 (1984)
- [7] F Sibille, C Cesarsky, P Agnèse and D Rouan, 'ISO camera array development status', 'Proc Third Infrared Detector Technology Workshop, C R McCreight (ed), NAS-Ames Research Centre, NASA Technical Memorandum 102209, pp 381-386 (October 1989)
- [8] J Wolf, 'Low-background far-infrared detectors and arrays', *Optical Engineering*, vol 33(9), pp 1492-1500 (1994)
- [9] M Patrashin, B Fouks and D Lemke, 'Radiation-induced effects in extrinsic far-infrared detectors', *Proc SPIE*, vol 2475, pp 476-486 (1995)
- [10] T Herter, 'Optimal sampling and sensitivity limits of integrating detector arrays in a space environment', *Infrared Physics*, vol 30(2), pp 97-112 (1990)
- [11] J Blum, Ch Hajduk, D Lemke, A Salama and J Wolf, 'High-energy radiation effects on the ISOPHOT far infrared detectors', *Infrared Physics*, vol 30(1), pp 93-96 (1990)
- [12] M E McKelvey, N N Moss, R E McMurray Jr, J A Estrada, J H Goebel, C R McCreight, M L Savage, F Junga and T Whittemore, 'Laboratory characterisation of direct readout Si Sb and Si Ga infrared detector arrays', Third Infrared detector technology workshop, C R McCreight (Ed), NASA-Ames Research Centre, NASA Technical Memorandum 102209, pp 403-412 (1987)
- [13] S H Moseley, B Lakew and R F Silverberg, 'Effects of ionizing radiation on cryogenic infrared detectors', in Cryogenic Optical Systems and Instruments III, *Proc SPIE*, vol 973, pp 299-307 (1988)

-
- [14] A H Kalma, 'Radiation response issues for infrared detectors', Proc NASA/JPL Workshop on innovative long wavelength infrared detectors, Pasadena CA, pp 24-26 April 1990, 151-157 (1990)
- [15] J T Montroy, R Baron, G C Albright, J Boisvert and L D Flesner, 'Energetic electron-induced impurity ionization in Si As detectors', *IEEE Trans on Nuclear Science*, vol NS-35(6), pp1307-1312 (1988)
- [16] M E O'Brien and L D Flesner, 'Electron beam testing of LWTR detectors', in Test and Evaluation of Infrared Detectors and Arrays, *Proc SPIE*, vol 1108, pp 23-30 (1989)
- [17] T Herter, N Rowlands, S V W Beckwith, G E Gull, D B Reynolds, D H Seib and M G Stapelbrock, 'Improved Si As BIBIB hybrid arrays' Proc 3rd Infrared Detector Technology Workshop, C R McCreight (Ed), NASA-Ames Research Center (October 1989)
- [18] R E Clement, J C Boisvert, R K Bentley and J D Merrian, 'Acceptor state generation in Si As impurity band conduction detectors', Proc IRIS speciality group on infrared detectors vol II, pp 9-19 (1989)
- [19] R E Clement, J C Boisvert and P J Sullivan, 'Characterisation and modeling of neutron induced transient response changes in Si As infrared detectors', *IEEE Trans on Nuclear Science*, vol NS-38(6), pp (1991)
- [20] J Van Cleve, T Herter, R Butturini, G Gull, J R Houk, B Pirger and J Schoenwald, 'Evaluation of Si As and Si Sb blocked impurity band detectors for SIRTf and WIRE', *Proc SPIE*, vol 2553, pp 502-513 (1995)
- [21] T Krabach, JPL, Private Communication , July 1996

8 RADIATION EFFECTS IN SILICON READOUT CIRCUITS

8.1 INTRODUCTION

As discussed in section 1.4.11, silicon readout circuits are usually either CCDs (or similar devices) or CMOS circuits. Several parameters are potentially sensitive to radiation:

- Dark current, but effects should be negligible because of low operating temperatures, large signal levels, and high readout rates
- Charge transfer efficiency is either not applicable (in directly addressed CMOS or FET multiplexers) or will be intrinsically low because surface channel CCDs have been used to maximize signal capacity (in this case CTE will be affected by total ionizing dose, but will only be significantly degraded further at high dose levels)
- Oxide trapped charge and interface traps will cause shifts in the effective bias and clock voltages applied to the device. In CMOS circuits the shifts produced in thick field oxides, even at low total doses, can be enough to turn on parasitic leakage paths and dramatically increase power consumption and even prevent device operation
- for CMOS circuits, changes in threshold voltage can also affect fixed pattern noise, detector biasing, readout noise and charge sensitivity, depending on the circuit used
- single event latch-up is potentially a problem for CMOS circuits
- it will be seen in section 9.2 that radiation-induced charge can become trapped for long periods (hours) in CMOS circuits operated at cryogenic temperatures. Also transient noise pulses can be produced in the multiplexer as well as the detector itself

8.2 SILICON CCD READOUTS

As noted above, dark signal and charge transfer efficiency are not likely to be significantly affected in space environments. However threshold voltage shifts are potentially important.

CCDs, like any other MOS circuit, are susceptible to threshold voltage shifts after being subjected to ionizing radiation. CCDs with a planar geometry and even gate oxide thickness are preferred in order to maintain an unchanged potential profile across the pixels (ie avoid stepped oxide structures). As always, oxide processing is important and for radiation tolerant oxides it is usually recommended to strip and regrow oxides after ion implantation (used to create buried channels and channel stops).

Use of thin oxides is of course an advantage (providing the dielectric strength is good enough to ensure device reliability). Even with radiation tolerant gate and inter electrode insulation it is important to make sure that thick field oxides used for isolation between MOSFETS (and for channel stops) do not lead to parasitic effects (this is a general rule for VLSI circuits). Flatband

voltage shifts in reset transistors and output amplifiers can lead to shifts in the 'operating windows' needed for correct biasing. In these cases radiation tolerance can be improved by adjusting biases in flight.

As far back as 1979, Saks et al [1] described a radiation hard low temperature p-channel CCD with a dual oxide/nitride dielectric. At 80K a flatband voltage shift of only -0.8 V/Mrad was measured. In 1981 Bluzer et al [2] described a similar MNOS CCD but operating surface channel and in 1983 Saks and Modolo [3] described N-surface and N-buried channel CCDs (again with an MNOS structure: 10nm oxide and 50-100nm nitride) which were operational following 1 Mrad(Si) at 80K. Note both types of CCD (surface channel, SC, or buried channel, BC) has its own advantages and disadvantages. For example, the SC-CCD has a higher signal charge capacity (useful in hybrid IR focal plane array technology), while the BC-CCD has a much better transfer efficiency. Considering radiation-hardening, there are two significant differences between SC and BC devices. (1) Threshold voltage shifts in the MOS insulators depend on the electric field in the insulators during irradiation, and the electric field is a function of the device type. For typical operating conditions, the (N-channel) SC-CCD should be more radiation tolerant than the (N-channel) BC-CCD. (2) The SC-CCD is much more sensitive to the creation of interface states by ionizing radiation because the signal charge in the SC-CCD is in intimate contact with the interface, whereas signal charge in the BC-CCD resides several hundred nanometers away from the interface. However, measurements have shown that the formation of interface states by ionizing radiation is either substantially reduced or completely suppressed when cooled to 80K. However on warming the interface traps can be expected to and then are permanent - thus severely degrading the performance of SC-CCDs. Figure 8 2-1 shows the D_{it} formation on warming, in this case for a BC-CCD (Saks and Modolo [3]) most of the increase occurred between 100 and 200K. This puts a limit on the maximum temperature that can be used for a hybrid detector employing a surface channel CCD and on the amount of annealing that can be achieved in the IR detector. Unhardened commercial CCDs would be expected to give shifts in the range 0.01 to 0.1 V/krad at room temperature, making them marginally suitable for doses above ~ 30 krad. Little information is available for unhardened CCDs used at low temperatures, although commercial CCDs are often employed by space astronomers at temperatures $\sim 100^\circ\text{C}$. Recently, thin dielectric (i.e. hardened) buried channel CCDs have become commercially available for use near room temperature.

Cluzel et al [4], have described total dose, dose rate and neutron measurements on CCD devices manufactured by LETI/LIR and Thomson/TMS. Though threshold voltage shifts were observed, the overall effects on device performance were stated to be small. The $1.5 \mu\text{m}$ process CCD multiplexers tested (biased) at 77K showed flatband shifts of 10 mV/krad and 30 mV/krad for the parallel input stages and the reset level of the output stage respectively. The damage was fully annealed after 1 week at 300K. They also reported measurements on a $3 \mu\text{m}$ process. However these were for the CCD unbiased and at 300K.

8.3 GAAS CCDS AND MOSFETS

These were described in section 1.4.11, where their particular advantages of high speed operation, good charge handling capacity and compatibility with GaAs/AlGaAs QW detectors were discussed. GaAs is an inherently radiation hard technology and total dose tolerance well in excess of Mrad is to be expected.

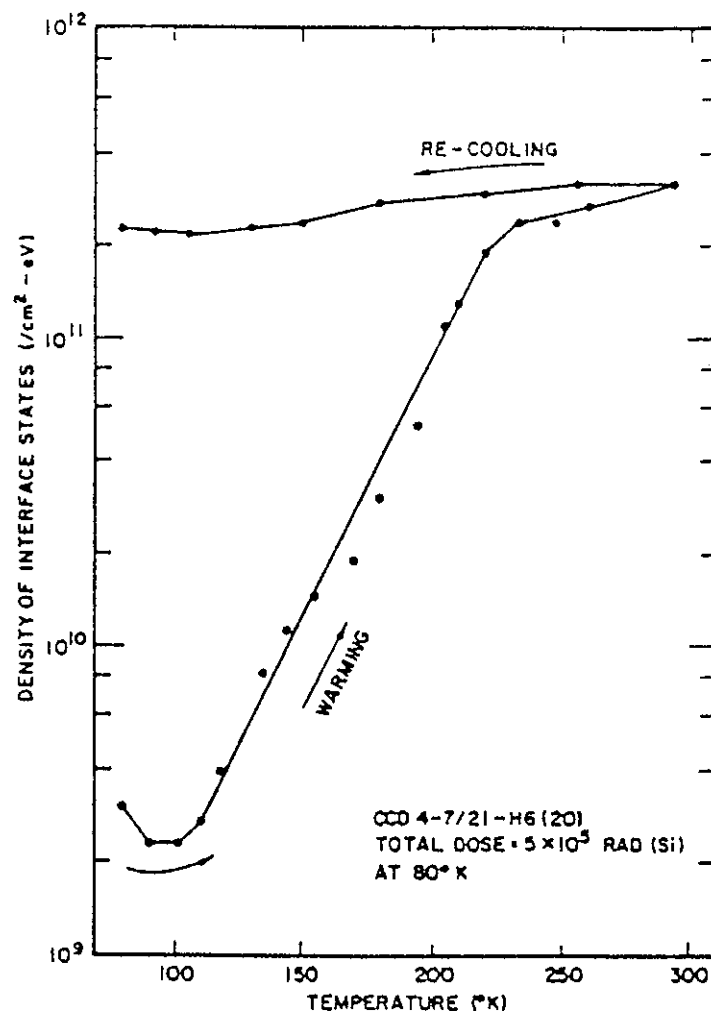


Figure 8.2-1 D_{it} in a BC-CCD after 500 krad as a function of anneal temperature and after re-cooling [3]

8.4 EFFECTS IN CMOS CIRCUITS

Trapped charge and interface trap build-up in low temperature MOS components was considered in chapter 2. As discussed, there are several possibilities for producing radiation tolerant low temperature oxides, eg use of thin oxides or high electric fields, dual dielectric insulators or reoxydised nitrided oxides (RNO). Silicon-on-insulator technologies (eg SIMOX or bond and etch back BESOI) can also be useful. Hughes for example have used a BESOI technology for their cryogenic radiation hard devices. With the technical feasibility of achieving radiation tolerant devices at 77K the issues resolve around producibility, compatibility and availability of tolerant MOS circuits in association with a particular IR detector array. Most US IR detector array manufacturers (e.g. Hughes and Rockwell) claim to have a radiation hardened cryogenic CMOS process.

In Europe the two main manufacturers of candidate devices for space use (Sofradir, France and GMIRL, UK) tend to use a variety of CMOS foundries, depending on their needs for device process and production need. Mietec Alcatel is currently favoured as a European radiation tolerant CMOS process.

As stated above, the effects of oxide trapped charge and interface traps will depend on the type of readout circuit. The radiation environment itself will deposit ionization charge fairly uniformly across the device area, but nonuniformities in flatband voltage shift can arise from variations in processing (in dielectric thickness, for example). Devices with an intrinsically high spatial nonuniformity due to threshold voltage or current gain variations (for example the source follower per detector, SFD, or gate modulation input, GMI, circuits discussed in section 1.4.11) may be suspect. The basic direct injection circuit will be seen below and in chapter 11 to be sensitive to changes in the direct injection voltage. This causes changes in the appearance of defect pixels and on responsivity.

The effect of radiation on field oxides has been discussed by several authors (for example Pickel [5] (c.f. figure 8.4-1)). It is possible to harden transistor isolations, for example by using guard rings [6].

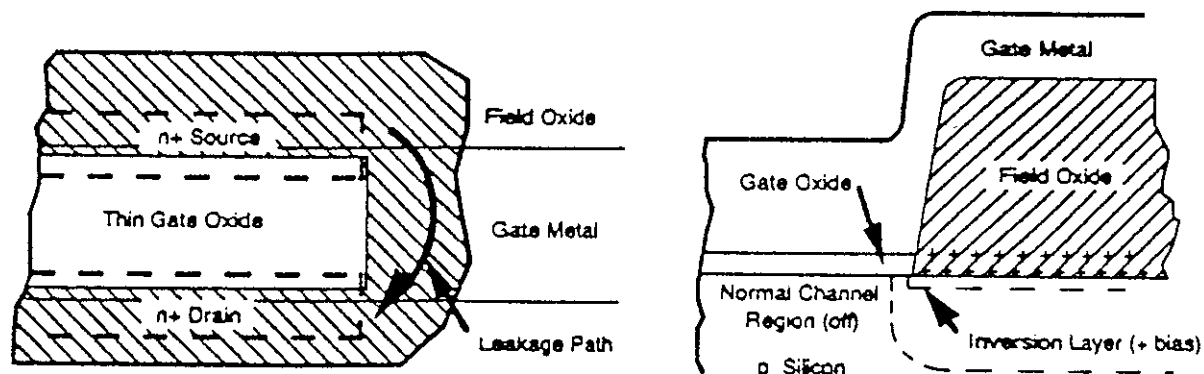


Figure 8.4-1 Effect of radiation on field oxides

Single particle induced latch-up [7] is potentially a problem for unhardened CMOS circuits. However the susceptibility is generally regarded to decrease with temperature. Hence at the temperatures used for IR arrays we should not expect to see latch-up. However there are no reports of this in the open literature.

8.4.1 Previous Sira results on GMIRL CMOS Multiplexers

Recent work by Sira [8] is relevant to CMOS readout circuits. This study examined total dose effects on GMIRL direct injection circuits - exactly the same multiplexers as used for the 256x4 array tests described in chapter 11. The test objects were taken from standard production batches fabricated by ES2 on 12 μ m epitaxial silicon using their ECPD15 double layer metal, single layer polysilicon process. There were no modifications for low temperature operation (other than increased design margins on threshold voltage).

Figure 8 4-2 shows the change in the effective voltage on the direct injection gate (VDIG) with total dose. The shift was ~ 3 mV/krad for all devices, irrespective of bias or temperature during irradiation. There was no significant change in VDIG with storage after irradiation (even at 80 $^{\circ}$ C). Similar results (shifts in the range 2-5 mV/krad) were observed for the threshold shifts for the other clock and bias lines. The relevant cobalt60 results are consistent with the gate oxide threshold shifts being due to hole trapping, and with interface trap generation not being significant in terms of device performance (otherwise we would expect more pronounced effects as devices are warmed up after 85K irradiation). The gate oxide thicknesses (t_{ox}) were ~ 25 nm and we can use the following simple formula as a first approximation

$$\Delta V_{ot} = -3.8 \times 10^{-2} t_{ox}^2 F \text{ mV/krad} = 24F \text{ mV/krad} \quad (8-1)$$

where F is the product of the hole trapping factor and the initial yield of electron hole pairs. A shift of 3 mV/krad gives F as 0.13, indicative of a fairly soft oxide (both at 85 and 293K). However the field oxide thickness is ~ 700 nm and it is likely that threshold shifts are much larger so that parasitic leakage paths are being turned on at doses (under bias) of ~ 15 krad, thus causing excessive device currents.

Figure 8 4-3 shows the currents in the 5V supply to buffer circuits in the multiplexer (VDD Buffer). The other 5V supplies - to analog and digital circuits showed similar behavior. The current remained essentially constant for unbiased devices, but when irradiated whilst dynamically biased to a dose of greater than about 10-15 krad(Si), the currents increased exponentially, the devices ceased to clock properly and the Test Enable switch did not function correctly (it could not be turned OFF properly). Hence the multiplexers can be regarded as having failed. This sudden onset of leakage currents and loss of functionality suggests that a parasitic transistor is being turned on. The most likely cause is a flatband voltage shift in the field oxide which isolates the various gates in the readout circuit. The turn-on point for the leakage was 25 krad(Si) for the hybrid array irradiated with 10 MeV protons, probably because of increased recombination in the field oxide. It appears that these field oxide shifts can anneal out because after 3 months storage at room temperature the biased devices were again functional (but only when cooled). This is illustrated in figure 8 4-3. Figure 8 4-4 shows that a 168 hour anneal at 80 $^{\circ}$ C is equally effective and that on re-irradiation a further 10 krad was

needed before the currents increased again, indicating that the annealing did not leave any significant memory of the original irradiation

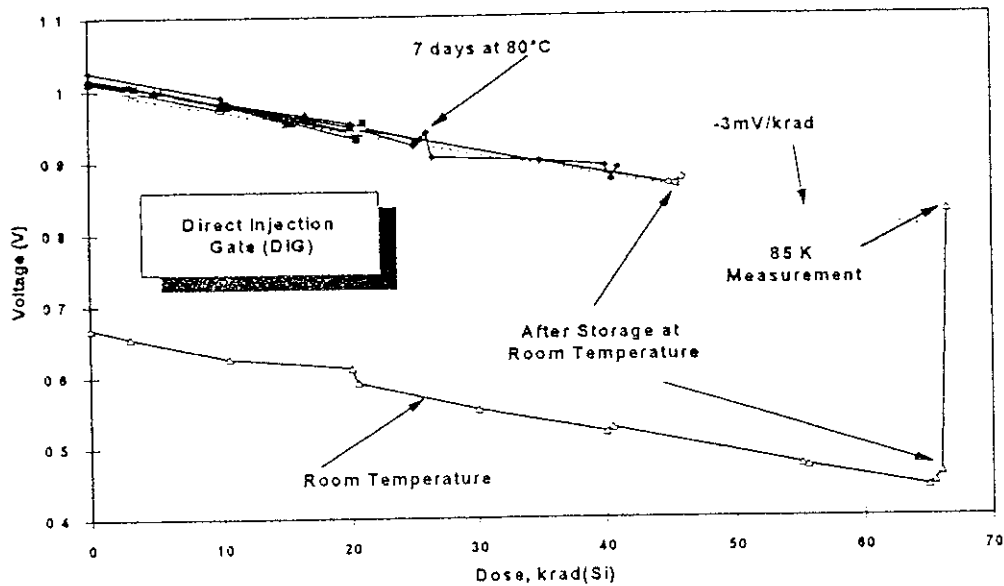


Fig 8 4-2 variation of VDIG with dose Devices biased during irradiation are shown with filled symbols and those irradiated unbiased (pins shorted) with open symbols Annealing measurements are shown slightly displaced horizontally One device was irradiated at 293K, with a final measurement (after 65 krad) made at 85K for comparison with the other devices Measurements for the hybrid array are also shown (•) One of the biased multiplexers (♦) was baked at 80°C after 25krad, with no significant change in VDIG

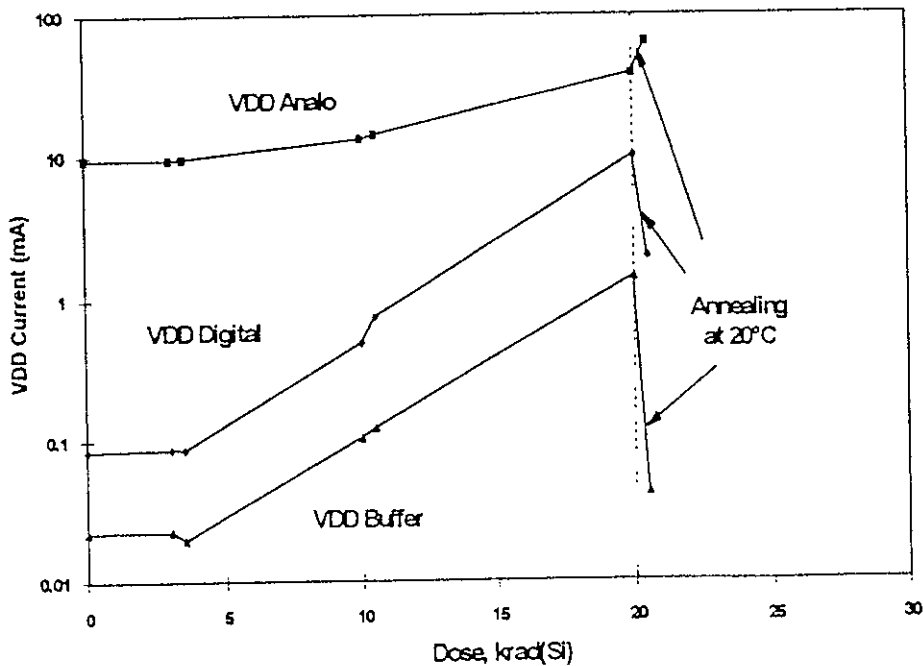


Figure 8 4-3 Power supply currents for a multiplexer biased during irradiation and annealed for 3 months at 20°C

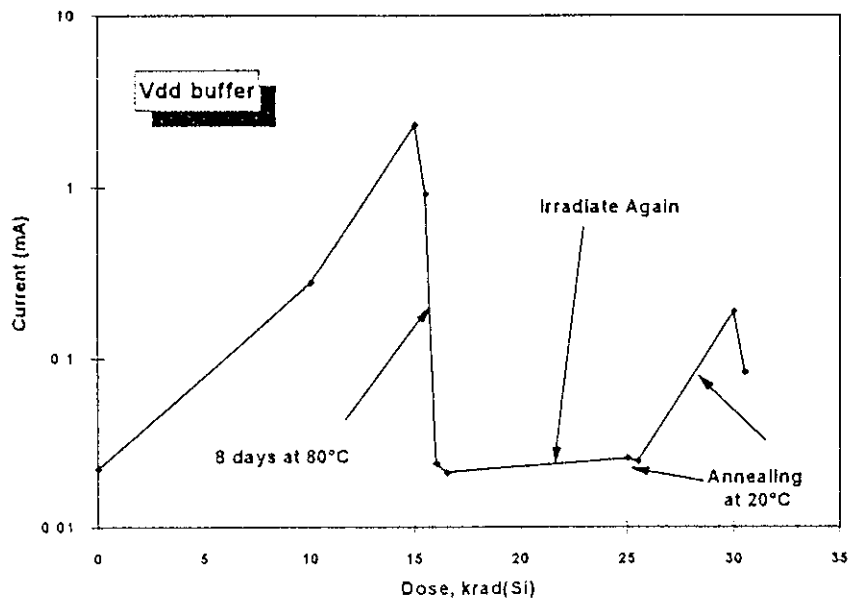


Fig 8 4-4 VDD Buffer current for a multiplexer biased during irradiation, annealed for 168 hours at 80°C and re-irradiated

The transition temperature at which annealed devices started to function depended on the dose received and on the annealing time. This is to be expected since the effect of a change in operating temperature is itself to cause a threshold voltage shift, which at some point will be large enough to overcome that induced by the radiation damage in the field oxide and to switch off the parasitic leakage path. The transition temperature was also influenced by the choice of VDD Digital, and Clock High voltages.

The recovery of functionality after storage for a few months at 20°C (or hours at 50°C) indicates that the holes trapped in the field oxide can anneal - and that if a device is stored at these temperatures then tolerance to the low dose rate space environment can be much improved. It is advantageous to power the device only when necessary since unbiased irradiations do not show leakage current increases.

REFERENCES

- [1] N S Saks, J M Killiany, P R Reid and W D Baker, 'A radiation hard MNOS CCD for low temperature applications', *IEEE Trans on Nuclear Science*, vol NS-26(6), pp 5074-5078 (1979)
- [2] N Bluzer, D Affinito and F C Blaha, 'Generation of SiO₂ interface states at low temperature with ionizing radiation', *IEEE Trans on Nuclear Science*, vol NS-28(6), pp 4074-4079 (1981)
- [3] N S Saks and J M Modolo, 'Radiation effects in N-channel MNOS CCDs at low temperature', *IEEE Trans on Nuclear Science*, vol NS-30(6), pp 4197-4204 (1983)

-
- [4] J Cluzel, A Guiga, R Tronel and M Vilain, 'Radiation Effects on CCD' RADECS 91, *IEEE Proceedings*, pp 3 27-3 32 (1992)
 - [5] J C Pickel, 'Novel devices and sensors', *Short Course Notes*, IEEE Nuclear and Space Radiation Effects Conference, Snowbird, Utah, July 19, 1993
 - [6] D R Alexander and D G Mavis, 'Design issues for radiation tolerant microcircuits in space', *Short Course Notes*, pp V-1 to V-54, IEEE Nuclear and Space Radiation Effects Conference, Indian Wells, CA, July 15, 1996
 - [7] G Bruguier and J-M Palan, 'Single particle-induced latchup', *IEEE Trans Nuclear Science*, Vol 43 (2), pp 522-532 (1996)
 - [8] G R Hopkinson, C J Baddiley, D R P Guy and J E Parsons, "Total Dose and Proton Testing of a Commercial HgCdTe Array" *IEEE Trans on Nuclear Science*, vol NS-41(6), pp 1966-1973 (1994)

9 EXPERIMENTAL RETURNS

In this chapter we present unpublished results from organisations that have performed IR array testing. Section 9.1 discusses data collected by MMS and 9.2 data collected by Sira.

9.1 MMS SURVEY

In this section we present information gathered by MMS. This was given in document 447/OSP/NI/96-256 and is included here with only minor changes to the text.

Table 9-1 List of IR focal planes investigated by MMS

Name of experiment	Name of mission	Year of launch	Type of orbit	Type of FPA	Manufacturer	Prime
IKS	Vega 1/2	1985	Cometary Rendez-vous	CMT monodetector		Meudon Observatory
ISM	Phobos 1/2	1989	Mars orbiter	PbS linear arrays	SAT	Meudon Observatory
OMEGA	Mars 96	1996	Mars orbiter	InSb linear array	SAT	Institute d'astrophysique Spatiale
ISOCAM	ISO	1995	Earth elliptic	InSb CID - Si Ga 2-D arrays	SAT LIR	CEA-SAp
DISR	Huygens	1997	Inter-planetary	InGaAs linear array	TCS	Meudon Observatory
CIRS	Cassini	1997	Inter-planetary	CMT diodes	LIR	CEA-SAp
MIR	Spot IV	1997-98	LEO	InGaAs linear array	TCS	MMS
MOP	Meteosat	1970-1990	GEO	CMT monodetector	GMIRL	MMS
Severi	MSG	1990-2000	GEO	CMT monodetectors InGaAs monodetector	GMIRL TCS	MMS

9.1.1 IKS, Phobos, MOP

No information was available for IKS, Phobos and MOP, mainly because

- People were less acquainted with radiation problems on IR FPAs,
- Traceability of radiation experiments were not the major problem for the instrument developers

In addition, due to its DC restore internal operation, the dark current of the MOP CMT monodetectors could not be measured, hence precluding a detection of its possible variation

9.1.2 The DISR Experiment

The DISR FPA is a linear array made of 2×150 pixels ($200 \times 35 \mu\text{m}$ pixel size) of InGaAs diodes grown on InP substrate and hybridised to a CCD multiplexer. The tests were made at ambient temperature (during its decent in the Titan atmosphere, the detector will work between $+20^\circ\text{C}$ and -100°C)

9.1.2.1 Tests for Total Dose

The qualification of DISR for total dose effects was considered as covered by the tests made in the frame of the MIR program (see section 9.1.5). The materials and the multiplexers are nearly the same as the ones from MIR (only the pixel size and arrangement are different)

9.1.2.2 Proton Test

These tests were made at the University of Orleans facility. The specification of the Cassini-Huygens missions looks severe, as it considers the case of large solar flares occurring when the probe will be located near Venus

Tests were made with protons of 30 MeV energy (taking into account the effect of the window of the FPA if any). The proton beam was diffused by a gold screen and the dosimetry takes into account the angular gradient for the energy. The typical procedure was

- fluence equal to $0.4 \cdot 10^{10}$ protons/cm²,
⇒ intermediate characterization of the detector
- fluence equal to $1 \cdot 10^{10}$ protons/cm²,
⇒ intermediate characterization of the detector
- fluence equal to $2.5 \cdot 10^{10}$ protons/cm²,
⇒ final characterization of the detector

The total duration of the irradiation was nearly 3 hours. In addition to the complete characterization made after the irradiation, I(V) characteristics were plotted a few minutes after the irradiation (9-50 mV of inverse polarization)

The main conclusions were

1 the results showed that there was a problem with InGaAs/InP material, for instance

- very large increase of dark current as high as $\times 100$ were measured (see figure 9-1)
- small increase of power consumption (approx 30%)
- small decrease of quantum efficiency (approx 10%)

The same tests were made on equivalent diodes in InP (therefore using the same technology, metallization,) without any problems. The problem should therefore be located in the InGaAs active layer or at the InP/InGaAs interface. The thickness of the different layers were then modified and tests on corresponding samples were made to confirm a less sensitive detector structure (which is today implemented at the level of the flight model of DISR)

2 tests were made at different dose rates, showing that

- the dose rate has no important effects
- the integrated dose is the dominating parameter

3 the effects of dark current increase have no relation with the dark current distribution before the irradiation. One should therefore conclude that their origins could be different (surface and bulk contributions)

4 no annealing effects were detected

9.1.3 The Isocam Experiment

9.1.3.1 The SW Channel

The FPA consists of a monolithic InSb CID, 32x32 pixels (100 μm for the square pixels). The thickness of the active layer is in the 10-15 μm range. Tests were made at 4 K.

9.1.3.1.1 *Total Dose Effects*

The specification was 2 krads and tests using γ rays were made up to 5 krads. No change was detected.

NB. A problem of this detector is its large level of readout noise (1500 e⁻ for 1 10⁶e⁻ of charge handling capacity). It was therefore difficult to detect small radiation effects.

9.1.3.1.2 *Heavy Ion Effects*

The tests were made at GANIL, using an Argon beam of 95 MeV energy (the energy was approximately 60 MeV at the level of the FPA). The array was scanned to avoid too many events per pixel. Pronounced events were detected, but without impact on the long term performance of the array.

9 1 3 1 3 *In-flight Behaviour*

Typical statistics show one impact every 10 seconds. Each impact only influences one pixel at a time. With SW, observations can be made during the full 24 hours of the orbit.

9 1 3 2 The LW Channel

LW modelling and behaviour was presented in the paper from Engelman and Agnese. This FPA is a 32x32 pixel array (100 μm for the square pixels) of Si Ga hybridized to a Si DVR multiplexer (using indium bumps). The working temperature is in the 2-4 K range.

After a few months in orbit, the main conclusions were:

- 1 the particle rate is approximately two times higher than what was modelled (both for the proportion of affected pixels and for the temporal event rate),
- 2 there are two types of events
 - impacts which disappear after 2-3-4 readouts (90% of the total number),
 - impacts which remain after 100-1000 readouts (10% of the total number)
- 3 in the histogram representing the number of events versus the number of affected pixels, there is a peak equal to 32 (when a full line or column is contaminated),
- 4 glitches can present various signatures (rectilinear, curvilinear, several particles leaving for one particle entering),
- 5 with LW, it looks to be better to stop the observations one hour before the perigee, after the electron belt, but before the proton belt
- 6 the hit rate is highly variable with time and location

9.1.4 The CIRS Experiment

The FPA is made of 10 CMT diodes (without readout circuit) – 140 μm square pixels, with a wavelength cut-off equal to 9.15 μm at 77 K. The diodes are front-side illuminated (the irradiation will also be front-side applied). Diodes are integrated in a cryostat (liquid nitrogen), and the reverse polarization was -20 mV, see figure 9-2.

See section 9.1.2 for the Cassini-Huygen specifications. It should be noticed that the passive cooler will be deployed after Jupiter. Therefore, the FPA will be nearly at ambient temperature near Venus.

9 1 4 1 Total Dose

The specification is 20 krads. The tests were made with a 30 krads dose, at LMRI/Saclay (Co^{60} , with 1.17 MeV and 1.33 MeV for energy). The electrical bandpass was 50 Hz (to be compared with the 1/f knee frequency, in the 10-30 Hz range). See figure 9-3 for a description.

of the test set-up. The photon noise was reduced (using a thin metallic foil), and therefore low when compared to the Johnson noise from the diodes.

Measurements were made after the irradiation using a spectrum analyser. The noise was chosen for the measurements as

- it should present high sensitivity to degradation,
- it is the most important system parameter

A few I(V) characteristics were also plotted (in the $-100 - + 20$ mV range), mainly to check that avalanche (nearly -300 mV) stays far away from the operating conditions.

No change was detected (see figure 9-4)

9.1.4.2 Tests with Protons

This test was made using the Tandem facility in Saclay. See figure 9-5 for the test set-up. The energy was 10 MeV, and the beam was diffused at 15° by a thick block of gold. The cryostat was modified to adapt its interface with the test chamber (replacing one window). The beam was therefore always in vacuum. The fluence was few 10^{11} protons/cm² and the rate corresponds to few 100 events/s/pixel. Real time visualization was possible by using an oscilloscope. The level of the impacts was low. At the end of the tests, a spectrum was acquired. No permanent degradation was detected (one can see a small increase of noise on figure 9-6).

9.1.4.3 Tests with Heavy Ions

The Tandem booster was used (Saclay), with a O₁₆ beam. The energy was 128 MeV. This figure was calculated to allow an energy deposition in the 2 μ m active layer thickness which corresponds to the energy of representative Fe cosmic ray ions.

Large peaks were detected. The typical flux was approximately 1 event/sec. No upset was detected. The nominal performance was recovered in very little time after the impact. At the end, no permanent degradation was detected. See figures 9-7 and 9-8 for traces of typical particle hits.

9.1.5 The MIR Experiment for Spot 4

The MIR FPA is formed by butting ten elementary modules. For each module, the number of InGaAs/InP pixels is 600 (staggered arrangements), hybridized by wire bonding to a linear readout circuit (Si CCD technology). During the tests, the temperature of the FPA was -10° C and the circuit was powered off.

The total dose was 3.6 krad, with a rate equal to 150 rad/hour. Tests were performed at DERTS (Departement d'Etude et de Recherche en Technologie Spatiale).

After the tests

- no variation of noise in darkness were detected,
- a small decrease of dark current was detected

9.1.6 The Omega Experiment

No results were available

9.1.7 The Sevirii Experiment

No results were available

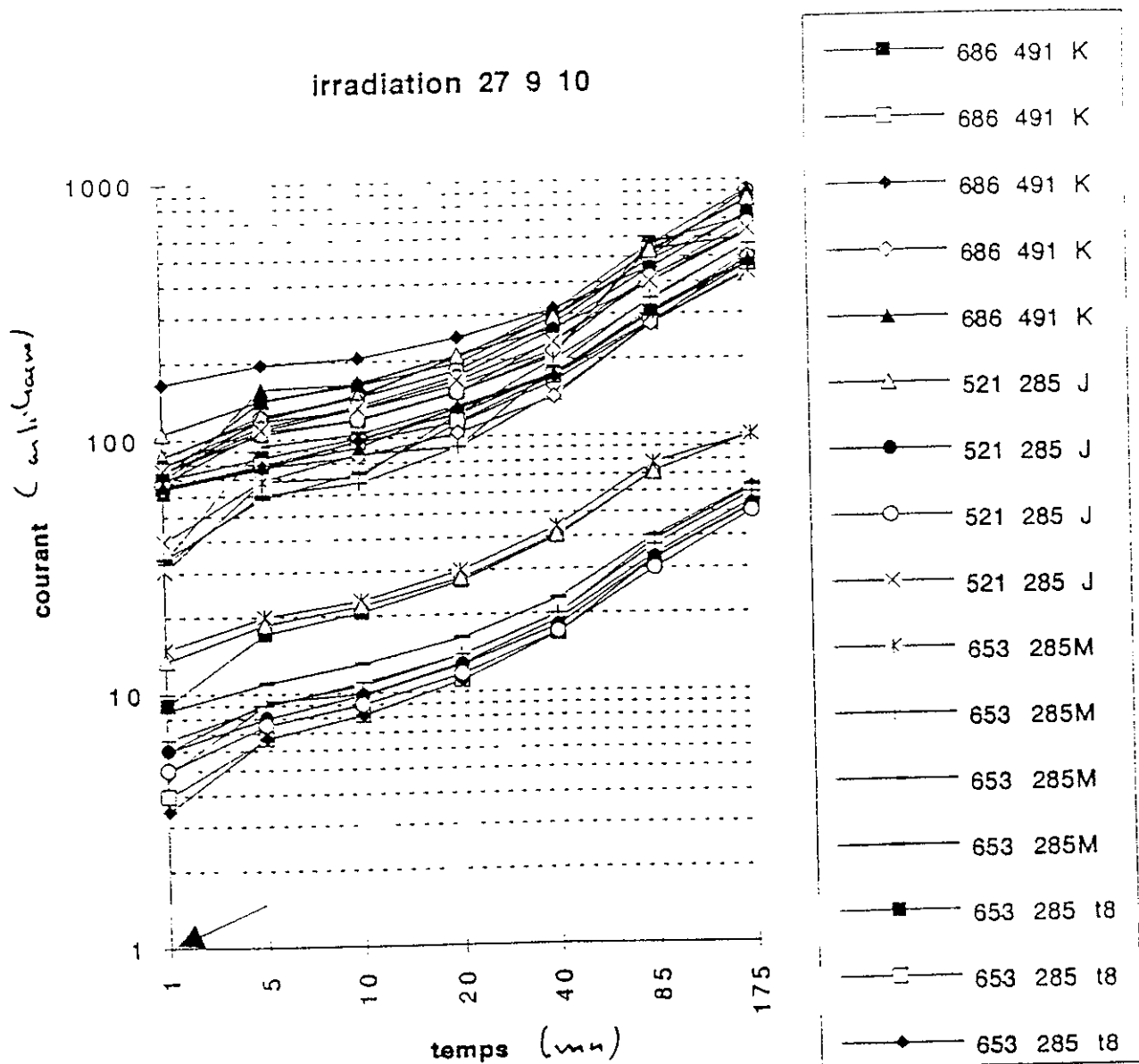
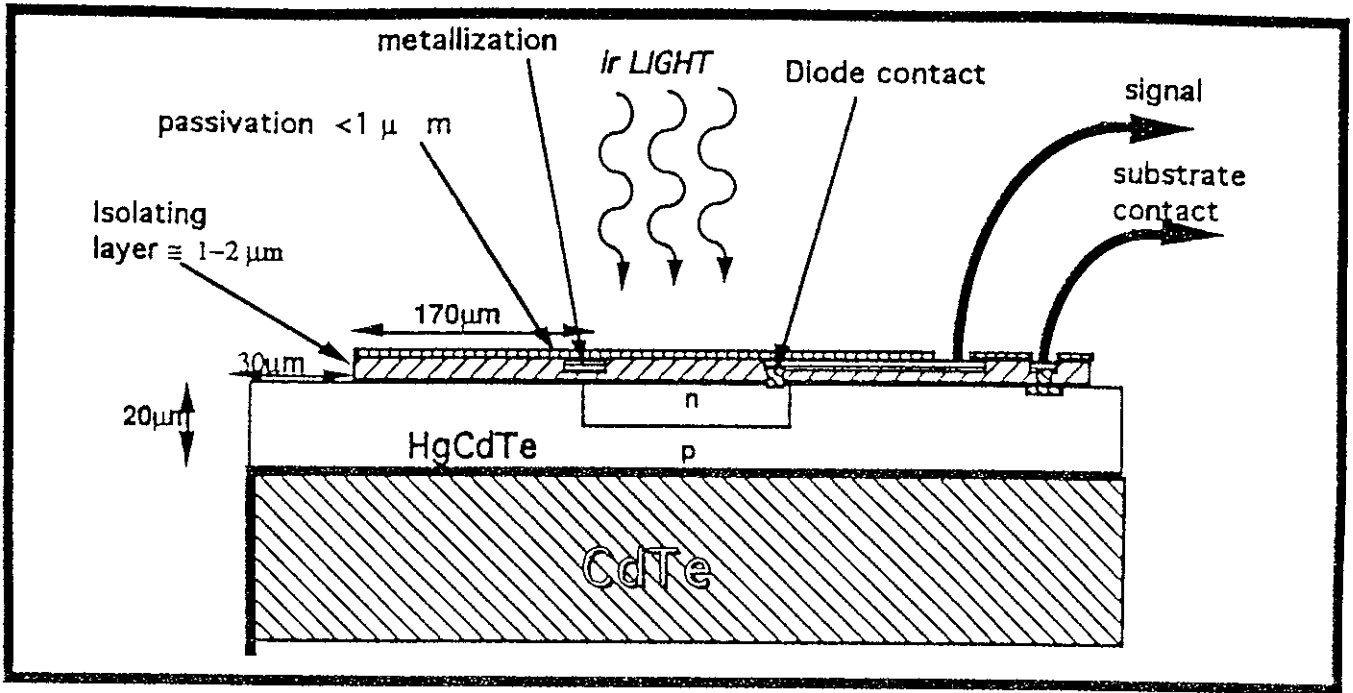
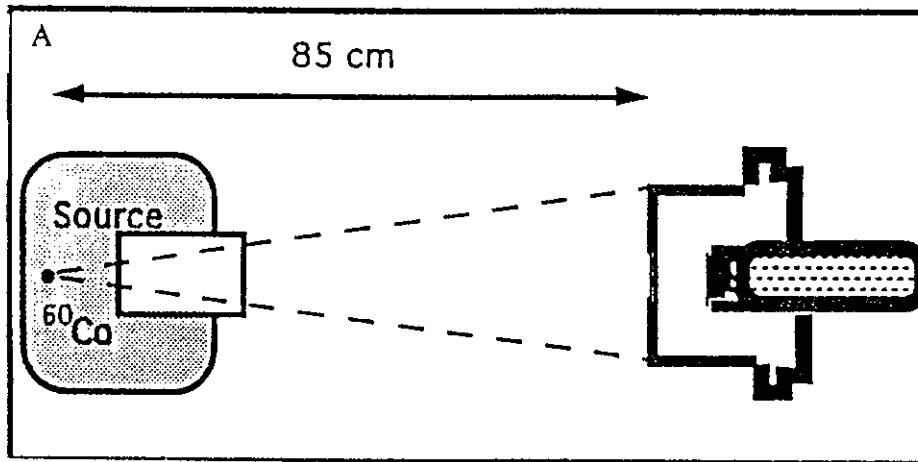


Figure 9-1 Increases in dark current for first version InGaAs/InP diodes for DISR, flight detectors gave improved performance

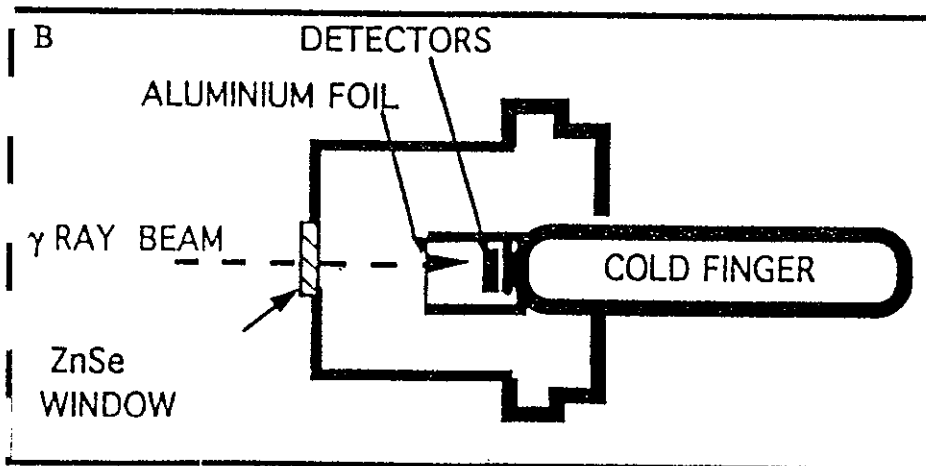


CIRS MEETING -----washington -----SEPTEMBER 92

Figure 9-2 Structure of MCT diodes for CIRS The isolating layer is optically matched for a given wavelength, but there is a thin passivation layer



γ ray source

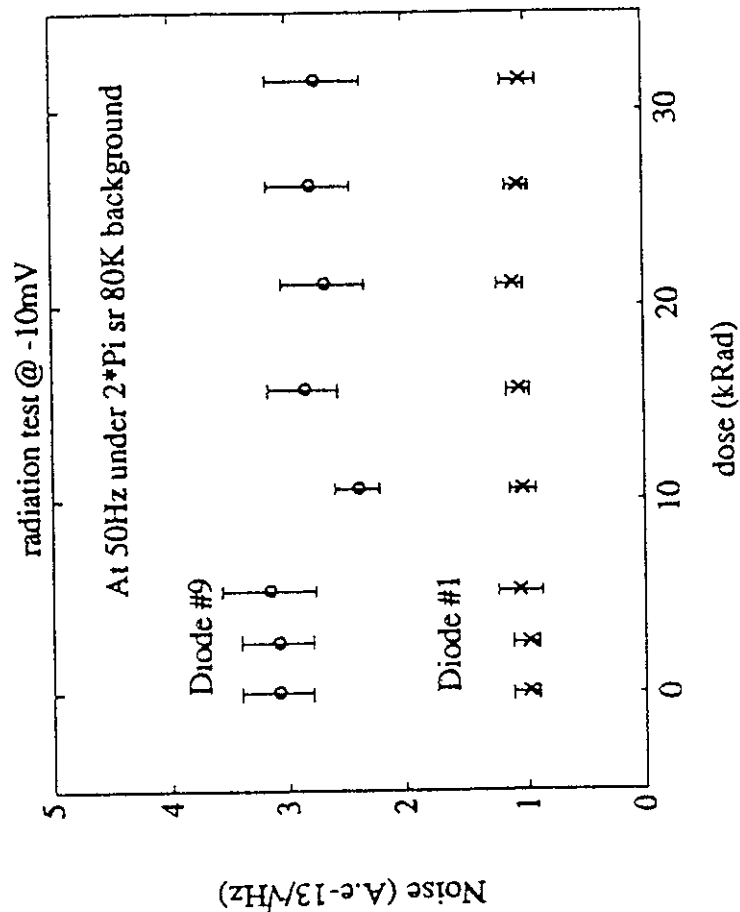


test cryostat

Figure 9-3 Test set-up for CIRS Co60 irradiations

"on line" noise tests for two diodes (#1 & #9) and
 "off line" measurement of diodes characteristics

NOISE TEST



I(V) CHARACTERISTIC

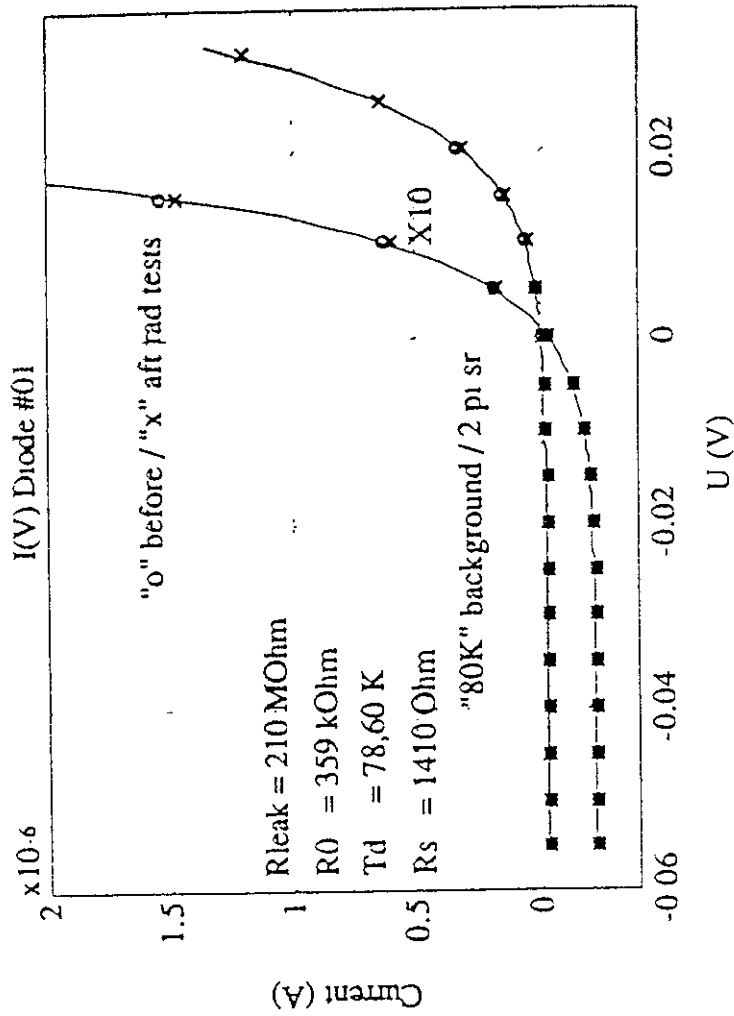


Figure 9-4 Test results for CIRS Co60 irradiations - no significant changes seen



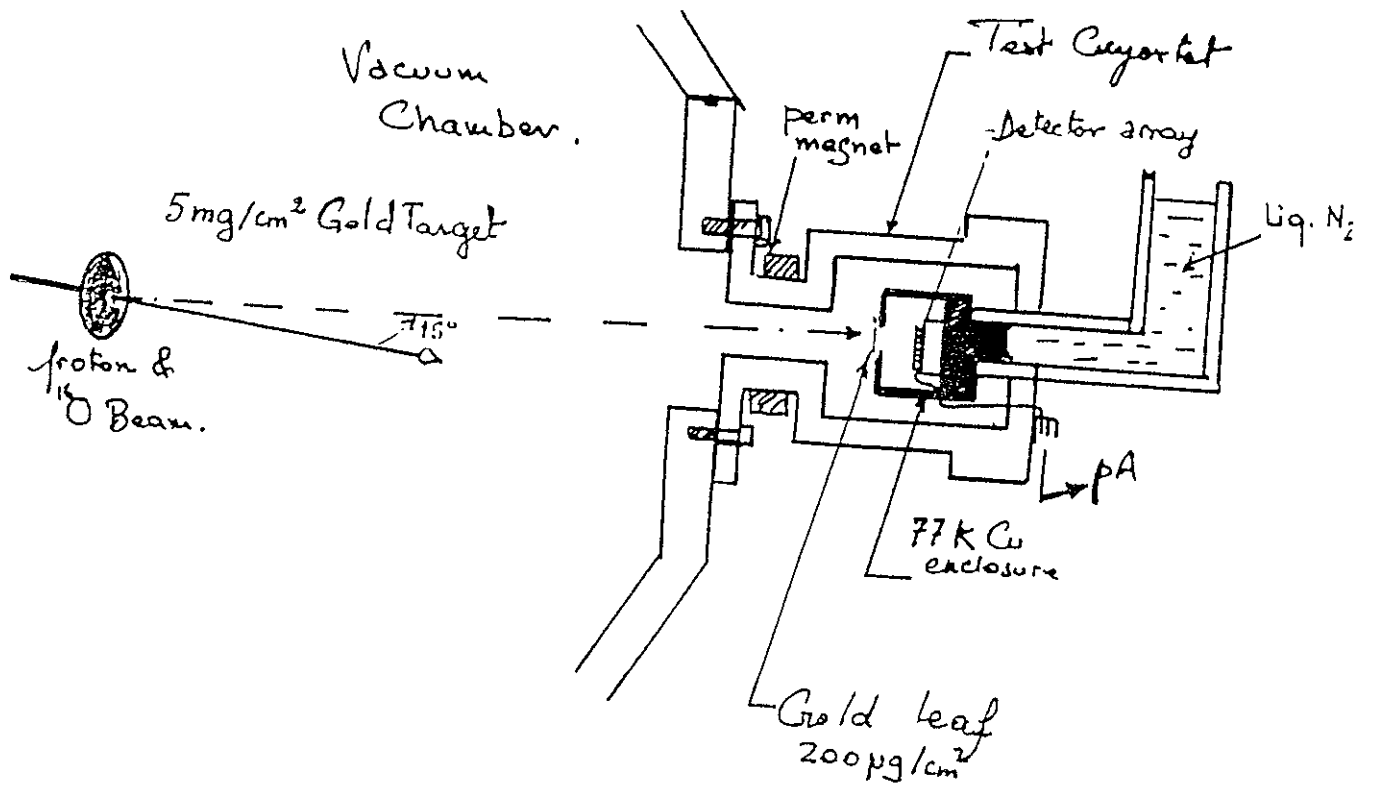


Figure 9-5 Test set-up for CIRS proton irradiations

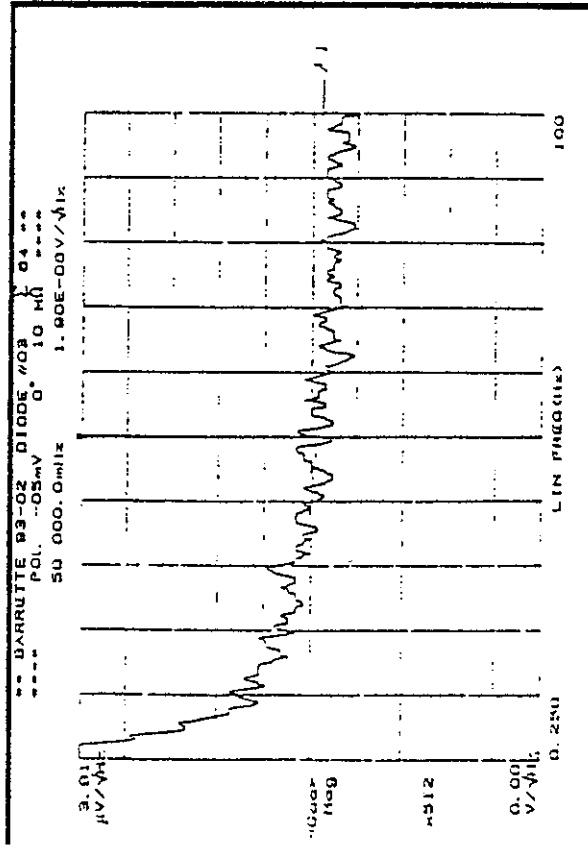
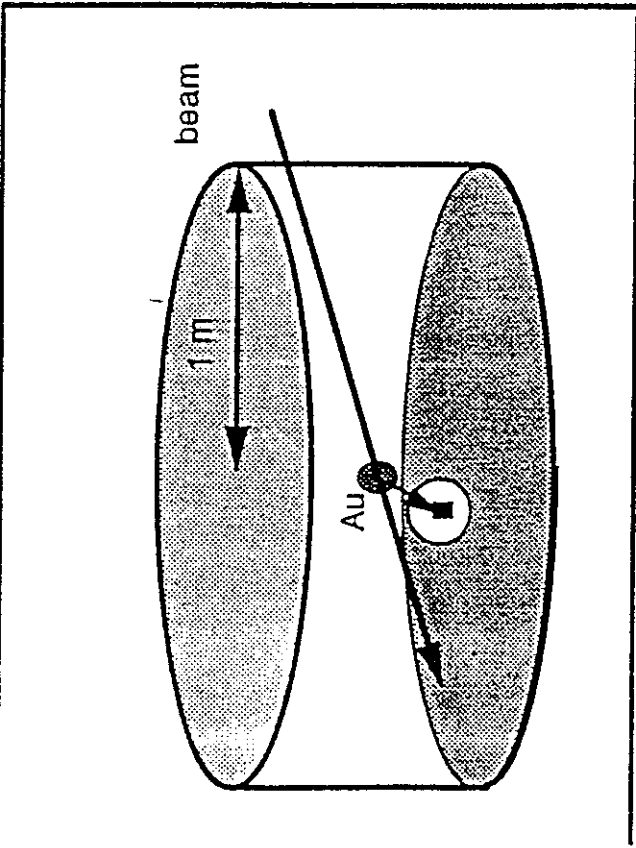
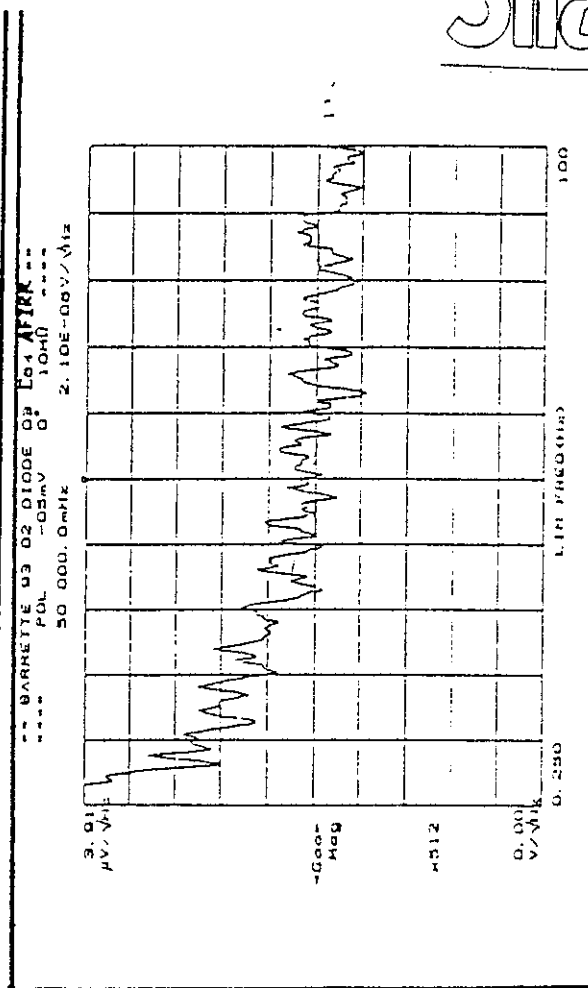
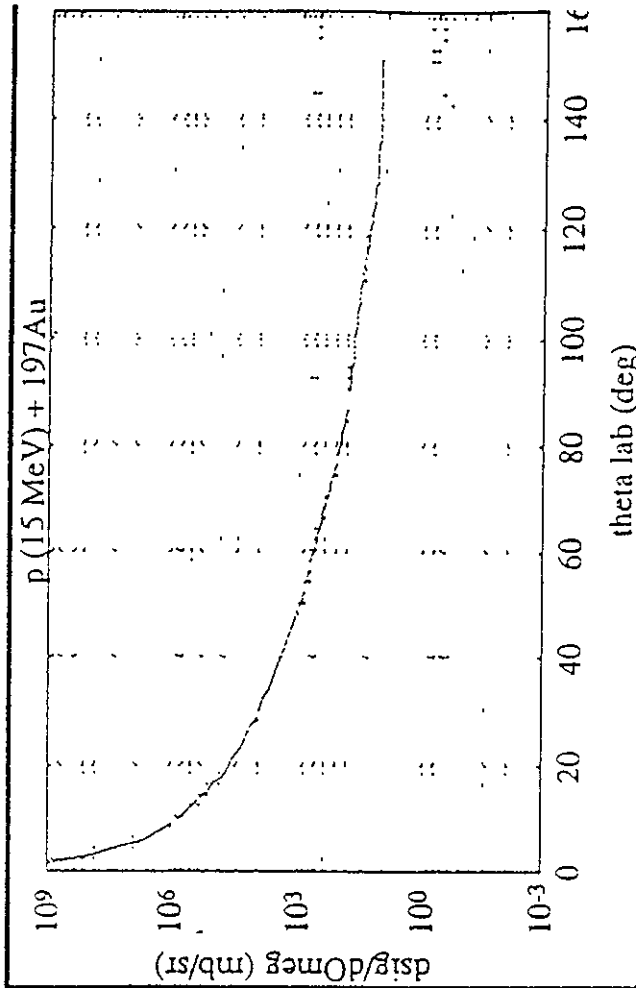
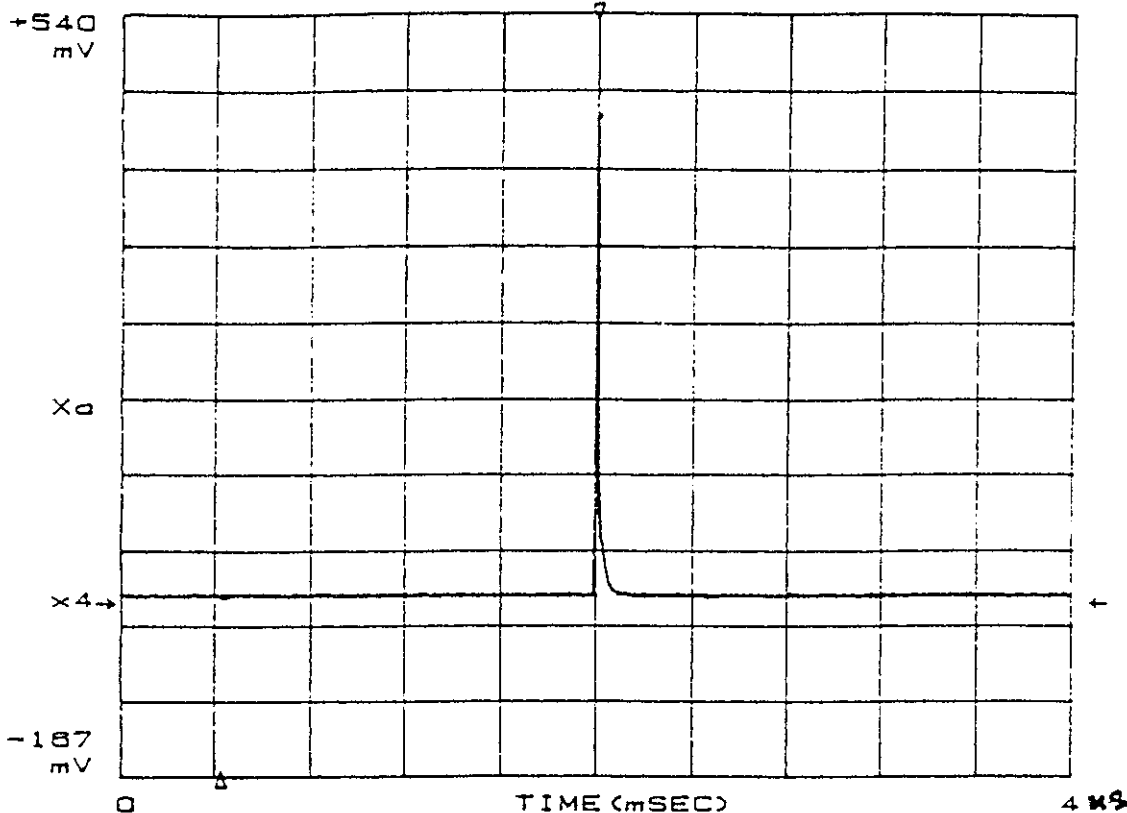


Figure 9-6 Test results for CIRS proton irradiations - no significant changes seen, though small increase in noise

** DIODE 03 018 128 MeV

DELTA 1 570.31 μ SEC

4.45E-01V p-p



** BARRETTE 93-02 DIODE 03 180 128MeV*

couplage AC

*** POL 0mV 5/08/93

DELTA 1 824.22 μ SEC

3.27E-01V p-p

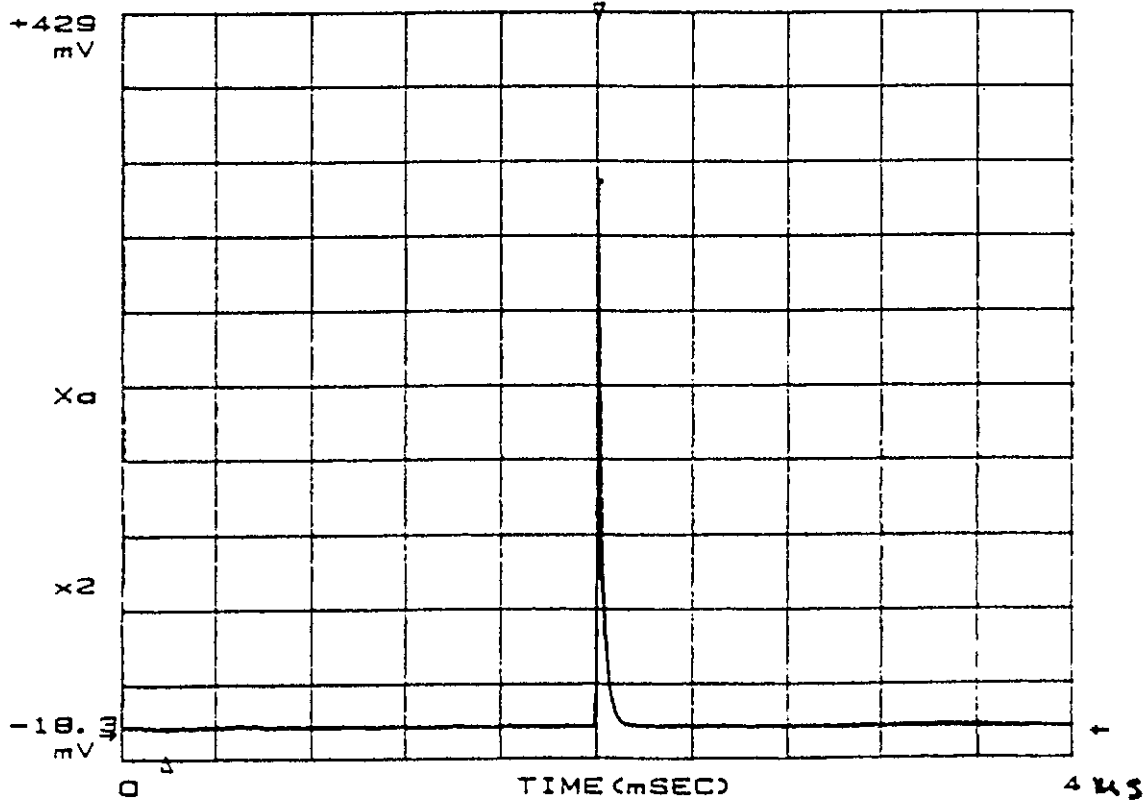
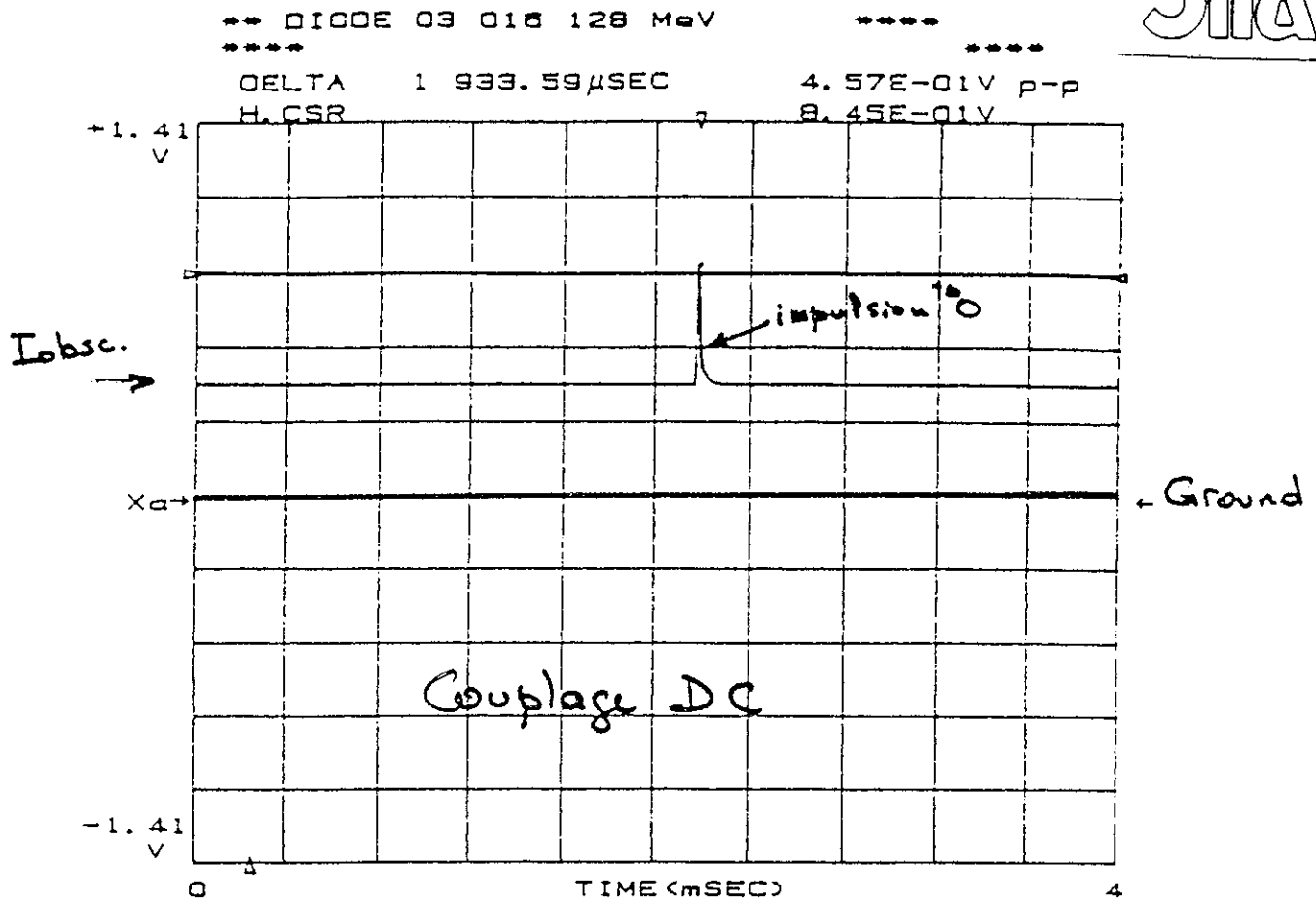


Figure 9-7 Typical traces for O₁₆ hit on CIRS MCT diode



Couplage AC

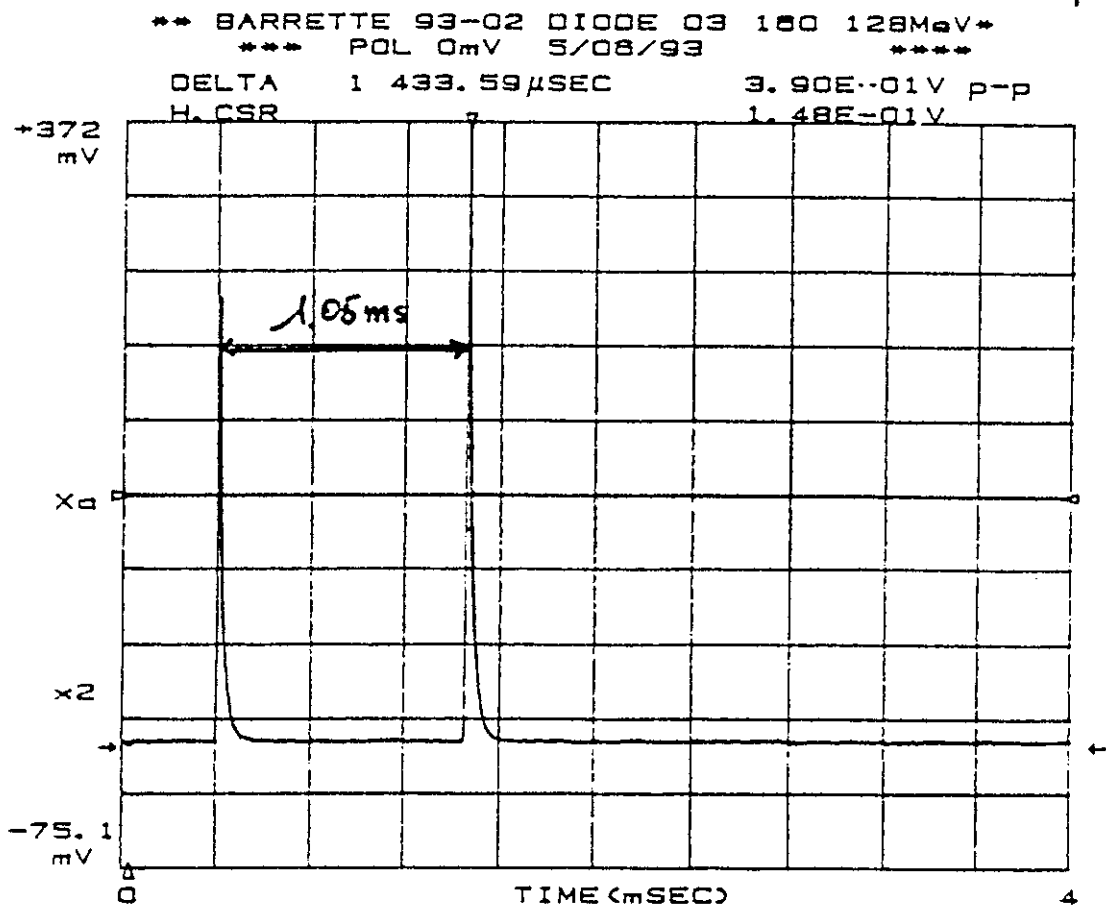


Figure 9-8 Typical traces for O₁₆ hit on CIRS MCT diode

9.2 SIRA FINDINGS

9.2.1 InSb Arrays for SIRTf

W Forrest of the University of Rochester has provided unpublished information on the testing of 58 x 62 and 256 x 256 InSb arrays using X-rays gamma rays and protons

9 2 1 1 X-ray radiation tests of a 58 x 62 InSb Array

- results given in Technical Memo, August 1989
- Gd-153 X-rays (mainly 41 keV), total dose ~ 5 krads (InSb)
- transient events observed, consistent with expected hit rate and assumption of 1 e-h pair per 1 eV deposited (and 30% conversion efficiency of X-ray energy)
- X-rays produce trapped charge in the multiplexer which slowly leaks away after irradiation (on timescale of ~ 100 s) - this shows itself as an increase in dark signal (can be factor 100 increase)
- no significant change in readout noise
- isolated pixels with large dark current (dark current spikes) were observed These could be largely annealed by cycling the gate voltage Spikes possibly due to the sensitivity of the mux used (FPA-72) to changes in gate voltage
- upper limit of 2% responsivity change

9 2 1 2 Gamma and Proton Tests of a 58 x 62 InSb Array

- results given in Technical Memo, December 1990
- different multiplexer used (RH4, SBRC)

Gd-153 Test

- no evidence for the dark current spikes found previously and reduced overall dark current increase
- persistent responsivity change which was non-uniform across the array (+1.3% in the thickest region, +3.0% in the thinnest region)

Proton Test

- 20 and 80 MeV protons incident on the array, total dose up to 130 rads (InSb)
- transient events typically 4×10^4 electrons, with immediate recovery
- proton events seen in the multiplexer - giving negative signals
- dark signal increase seen (as before) This decayed after irradiation over timescales of minutes - presumably again due to charge trapping in the multiplexer
- persistent dark current spikes seen - about 200 in all 50% were removed by cycling the gate voltage and 35 were left after warming from 10 K to 35 K and back
- no change in noise performance
- no change in responsivity seen

9 2 1 3 Gamma Irradiation of 256 x 256 Array

- results given in Technical Memo, January 1994
- FPA131 used with SBRC CRC463 multiplexer
- Cs-137 used, 662 keV gammas
- transient events seen, size up to 4×10^4 electrons

9 2 1 4 Gamma and Proton Tests of 256 x 256 InSb Array

- results given in Technical Memo, September 1995
- CRC744 multiplexer used

Gamma irradiation

- Cs-137 used, 662 keV gammas
- transient events seen
- hot pixels seen, which were partly removed by cycling the gate voltage and almost completely removed after a thermal anneal
- no changes in quantum efficiency

Proton irradiations

- 20 and 80 MeV protons incident on the array at 23° angle through the dewar wall
- dark signal increases, which decayed in minutes, again observed
- dark current spikes again observed 39% of pixels were initially affected, decaying to <1% after 30 minutes, 38 left after several weeks
- no changes in quantum efficiency
- no changes in linearity

9.2.2 Results from SRON (Groningen) on the ISO SWS Experiment

- most recent data from test report by W Lunge and W Haringa, February 1997
- 12 x 1 Si As blocked impurity band (BIB) arrays from Rockwell showed increases in dark current in-flight (figure 9-9) - effects not seen in bulk extrinsic or InSb channels
- 100 MeV protons used in a ground test at PSI, Zurich
- 50 rad gave a considerable increase in dark current, which decayed after irradiation - particularly at low (1.8 V) - so low bias is the best operating condition
- various curing methods (e.g. bias, thermal boost) were tried, but did not significantly reduce the dark signal after it had decayed during an 11 hour waiting period

9.2.3 ATSR

Some information was obtained from John Delderfield at DRAL (UK)

ATSR has single element detectors, mostly 1.5 mm kovar shielding

- PC CMT (G-MIRL)
- PV InSb (SAT)
- Si diodes (Centronics)

No changes in performance have been seen so far and no increased noise during passage through through the south atlantic anomaly (SAA)

As it was an AO instrument, there was no specific ground testing of detectors, but 3 year lifetime guarantees were asked for from the manufacturers

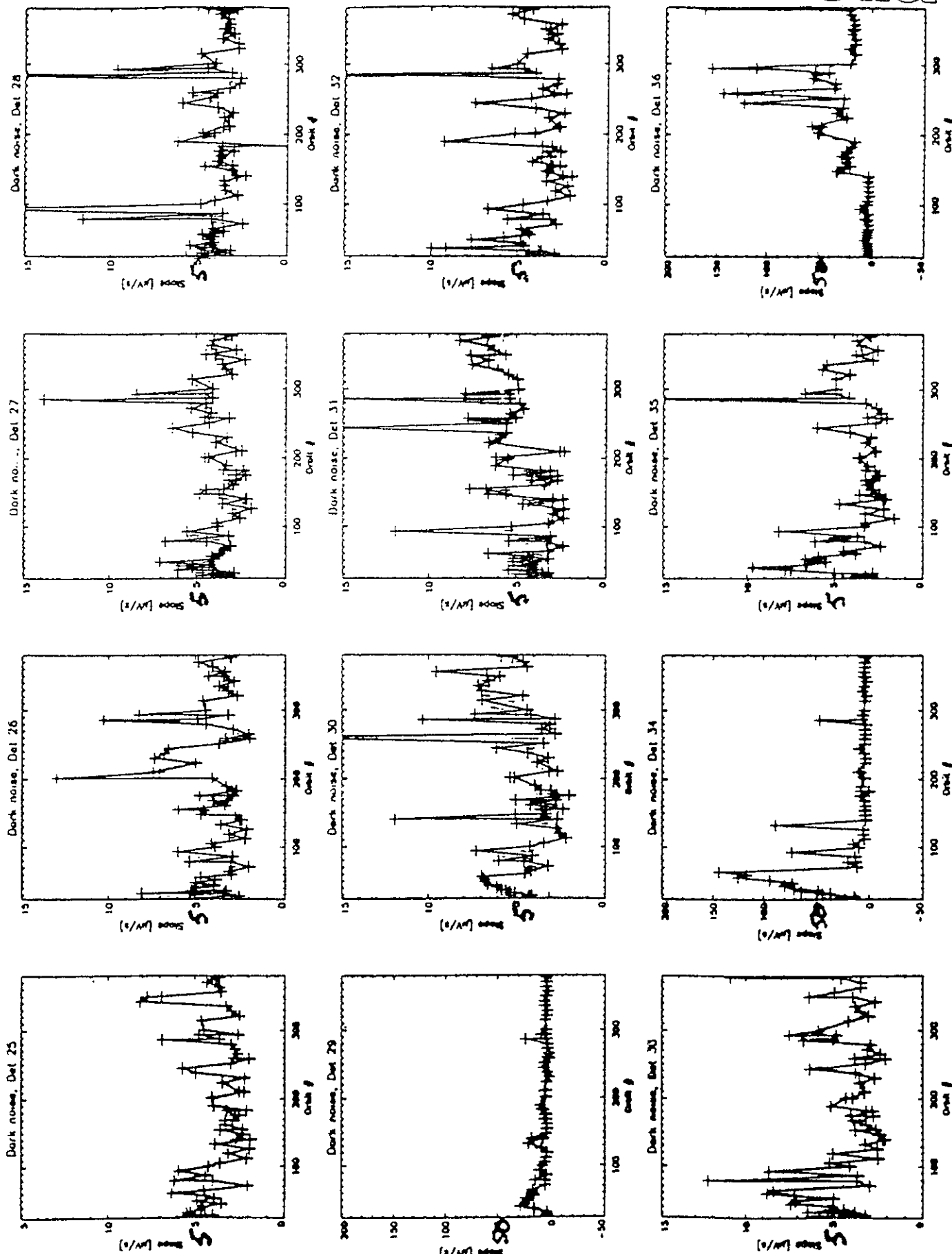


Figure 9-9 In-orbit results for dark current in the ISO SWS Si As BIB detectors, Luinge and Haringa, 1997

10. EXPERIMENTAL DETAILS OF RADIATION AND TEST SET-UP

In this section we give details of the arrays to be tested, the test set up used and the irradiations performed. Chapter 11 gives the results obtained.

Before testing was carried out a test plan (document A/9920/00/C102/GRH/001) was issued and approved by MMS and ESA. The test programme conformed with this plan apart from relatively minor deviations in the tests performed.

10.1 TEST OBJECTS

The present work is concerned with the investigations of radiation effects in 2-D IR sensor arrays. In the ESA statement of work, arrays of InSb and MCT (Mercury Cadmium Telluride) were cited as being of special importance.

Several US manufacturers (Cincinnati Electronics, Hughes, Amber Engineering, Rockwell) were contacted and either did not reply or offered devices well above the target price.

The main interest is in any case in European arrays (since these are most likely to be used on ESA instruments). The principle manufacturers in Europe are

AEG, AIM (Germany)
Sofradir (France)
G-MIRL (UK)

These manufacturers only produce MCT devices. AEG did not offer prices within the target budget. Sofradir suggested the loan of arrays mounted inside a liquid nitrogen dewar, but the presence of a permanent magnet would allow only Cobalt-60 testing. G-MIRL could provide either 256x4 (essentially a staggered linear array) or 128x128 arrays which are bare devices and could be subjected to alpha particles or proton testing. Therefore it was decided that the G-MIRL MCT arrays should be used for this project. The decision was also based on the availability at Sira of drive electronics for the 256 x 4 G-MIRL array. With some modifications, this was also useable for the 128 x 128 array.

It was considered to be advantageous to test both a LWIR and a MWIR array so that effects in the two MCT alloys could be compared. An LWIR array was only available in the 128 x 128 format and a MWIR array only in the 256 x 4 format. Hence one of each type was purchased.

The devices consist of an array of MCT loophole diodes mounted on CMOS multiplexers. The package is designed for bulk nitrogen cooling as shown in figure 10.1-1. The inner part is a sapphire substrate on which the CMOS multiplexer is mounted, the outer part is made of glass reinforced plastic and attaches via four thin 'legs', which act as thermal breaks and allows the electrical connectors to be at room temperature.

Figure 10.1-2 shows a cross section through a loophole diode. Note that the only material on the top surface of the diode is about 1.4 μm of ZnS, which acts as a passivation and anti-reflection

coating The current from the photodiodes passes to an integration capacitor via a direct injection gate and then to sample and hold and buffer amplifier circuits

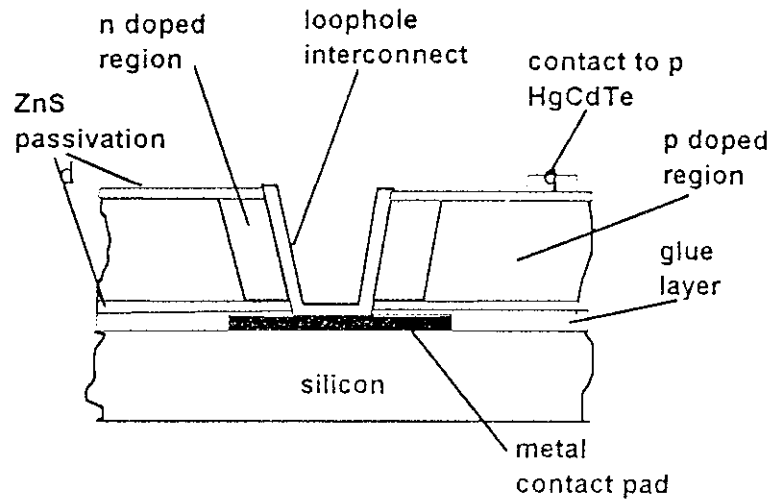


Figure 10 1-2 Schematic diagram of a G-MIRL 'loop-hole' diode

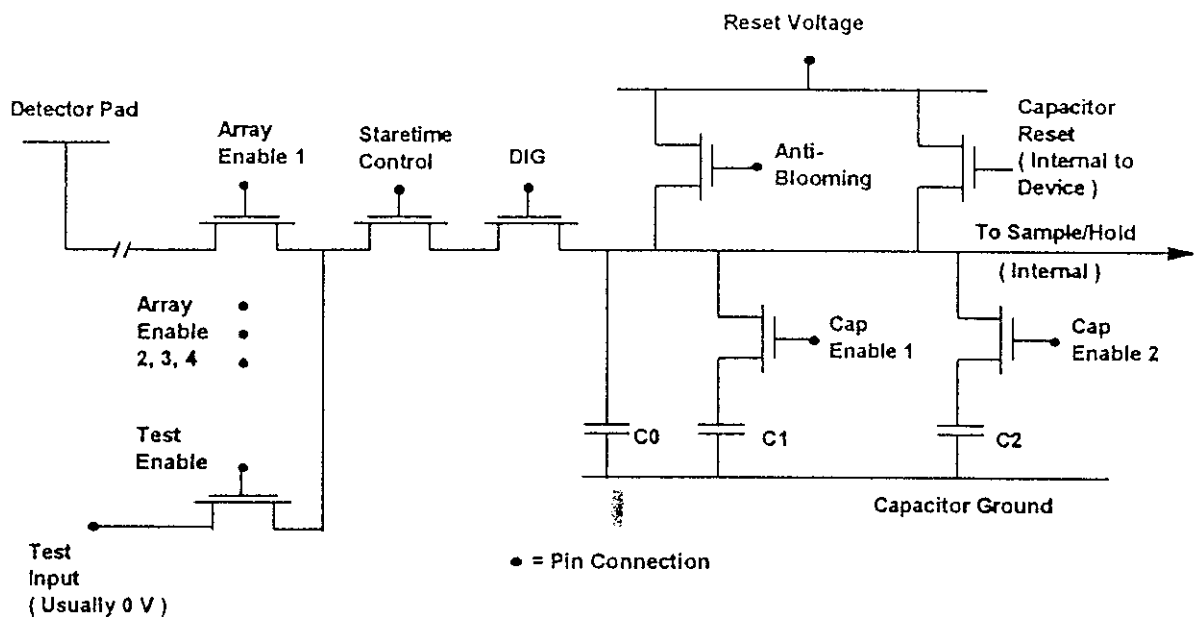


Figure 10 1-3 Multiplexer architecture for the 256 x 4 array The 128 x 128 array does not have an array enable gate and has three rather than two switchable integration capacitors

Both types of array read the pixels into four outputs (the 128 x 128 array is organised as four 64 x 64 pixel quadrants and the 256 x 4 is a staggered linear array) The circuit functions include stare time, control, selectable integration capacitors, an on-chip analogue store and anti-blooming control The basic architecture is shown in figure 1 1-3 The readout circuit uses 5 V clocks Also included on the sapphire substrate are temperature sensing diodes These operate at constant current (either 10 mA or 100 μ A) and the voltage across the diode is monitored (approximately 1 V at 80 K)

Note that since the devices were of 'engineering grade' they contained an appreciable number of defective diodes. The commonest fault is that the diodes show a 'soft' IV characteristic. This makes them sensitive to the choice of direct injection gate voltage (VDIG) as explained below. Small changes in VDIG (either due to temperature or total ionizing dose) can make the defective pixels change from white to dark spots.

According to GMIRL experience, the best injection efficiency is normally achieved with a diode reverse bias voltage of between 20 and 50 mV. The correct bias can be achieved by examination of the video waveform on an oscilloscope. At zero volts VDIG the array outputs will all be at reference level and the diodes will be in forward bias. As VDIG is increased, output pedestals will appear for each pixel and the diode bias point will move through zero bias into reverse bias. The magnitude of the output pedestal is proportional to the current flowing through the corresponding diode at the operating point. The diodes are at near zero bias when VDIG is adjusted to give the minimum spread in output pedestals (i.e. minimum nonuniformity in the image). This is shown in figure 10 1-4.

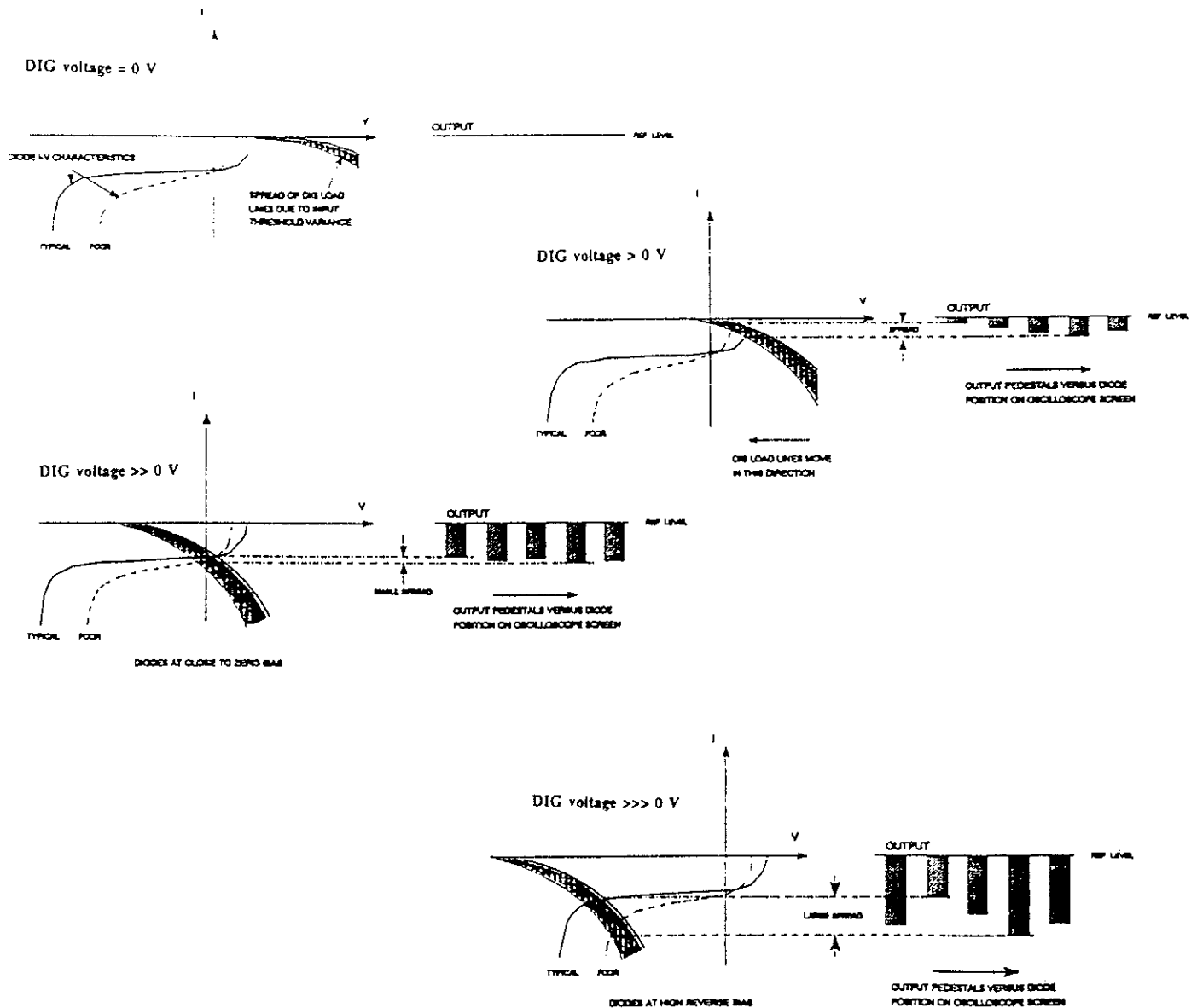


Figure 10 1-4 Effect of changes in VDIG on the diode bias point and array output

10.1.1 256 x 4 Array

The array used was of type E3253 and is described in GMIRL report number 10410/U. The device serial number was 96G-007. The array actually consists of two arrays of 256 x 4 diodes and two of 512 x 2. The arrangement is shown in figure 10 1-5 and figure 10 1-6 is a photograph of the silicon multiplexer die. The diode pitch is 40 μm . The average cut-off wavelength was 6.4 μm (corresponding to a bandgap of 0.19 eV).

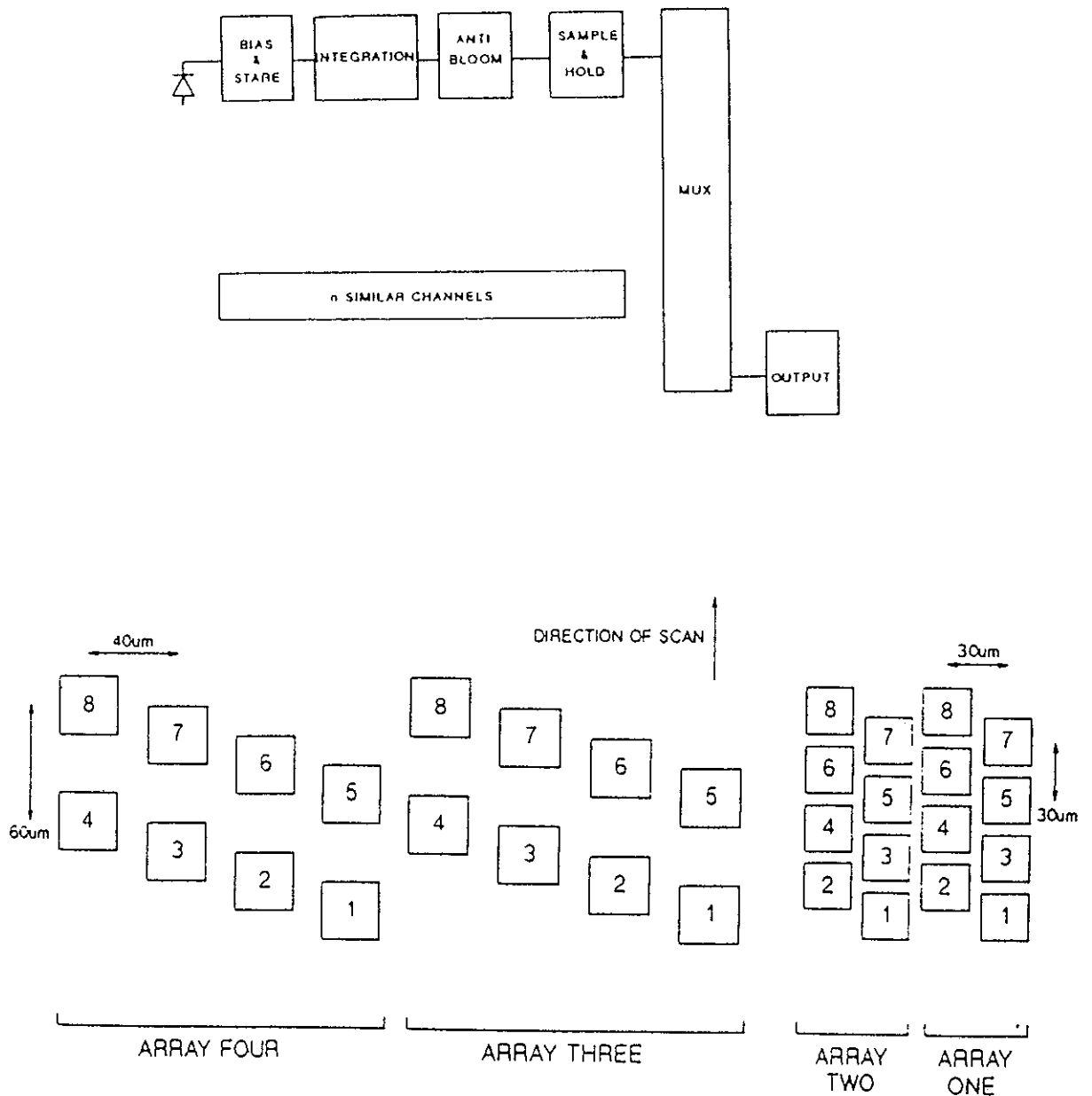


Figure 10 1-5 Arrangement of the diodes in the staggered linear array

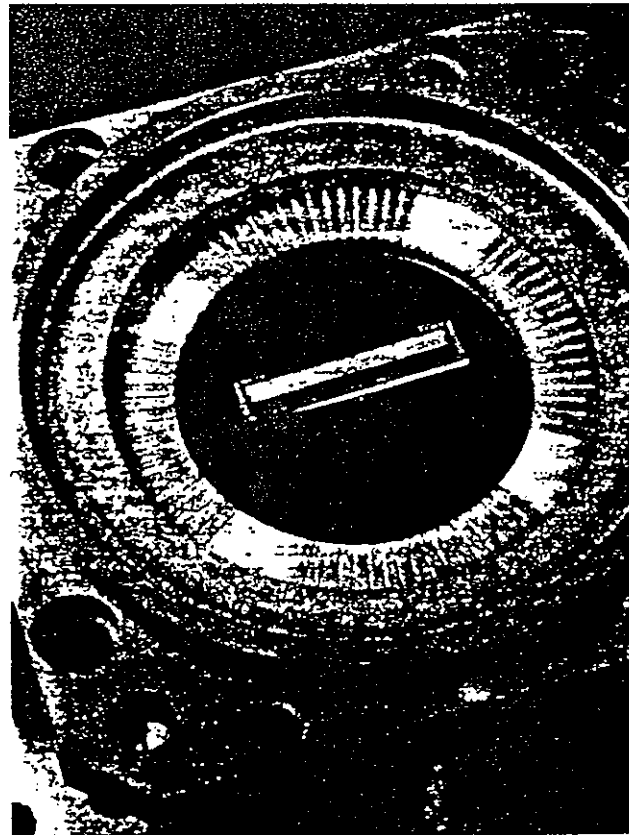
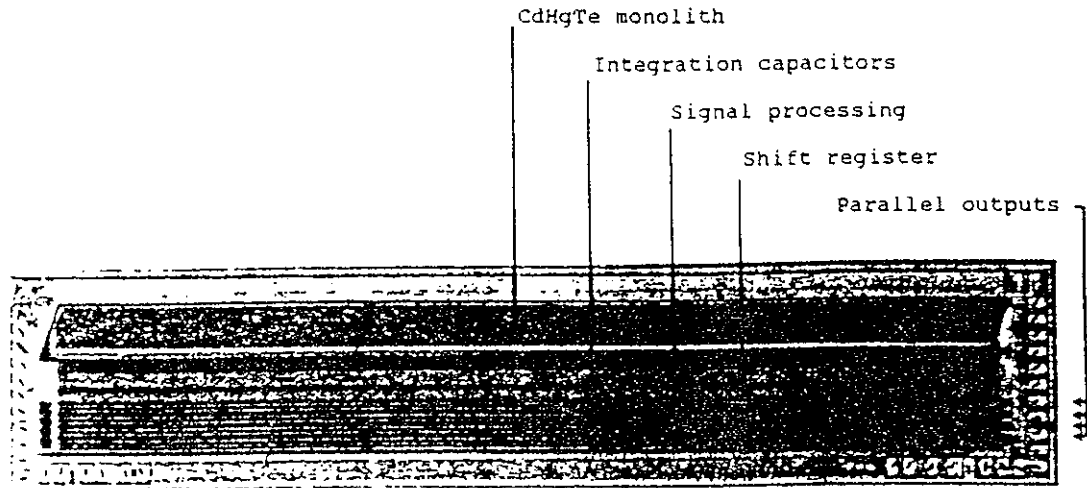


Figure 10 1-6 Photomicrograph of the multiplexer die for the GMIRL staggered linear array

10.2 TEST CIRCUITS AND EQUIPMENT

A block diagram of the test system is shown in figure 10 2-1. The shaded boxes show those items which are needed to bias a device whilst in an irradiation. A brief description of the various system components is given below. Figure 10 2-2 is a photograph of one of the liquid nitrogen dewars, the blackbody source and the test electronics.

10.2.1 Cooling Arrangements

The devices under test were operated in an Oxford Instruments MN15 INV liquid nitrogen cryostat. Interchange of devices is straightforward on removal of the cryostat front plate. Re-evacuation is performed using a Balzers TSH060 turbo pump station. The cryostat is evacuated to $\sim 2 \times 10^{-4}$ torr and there is margin to allow for several days storage between pump downs. Without the devices under test (and its associated wiring harness) the liquid nitrogen boils off in 30 hours, when in an upright position and in roughly 15 hours when in a horizontal position. With an array in place (and unbiased) these times are reduced to approximately 24 hours and 12 hours respectively. This is more than adequate for cooled storage overnight. Figures 10 2-3 and 10 2-4 show the arrays mounted in their dewars.

The array is coupled to the cold bottom plate of the cryostat with a conical plug of high conductivity copper. The operating temperature of the multiplexer within the cryostat is approximately 80 K. Powering the array increases its temperature by a few K, and there can also be variations (again of a few K) in operating temperature depending on the thermal contact between array, plug and cryostat baseplate on assembly and on the vacuum inside the cryostat. The array temperature can be accurately monitored using four temperature sensitive diodes which are mounted onto the sapphire substrate of the device. It was found that there were day to day differences in the operating temperature of ± 1 K (probably due to changes in ambient temperature and the vacuum inside the cryostat).

The temperature sensing diodes are provided with a constant current and the voltage across each diode is measured. The camera unit supplies two of the temperature diodes with a constant current of 1 mA. The other two are fed directly from a Keithley 236 source measure unit, which can give any desired constant current and simultaneously measure the diode voltage. Normally a current of either 1 mA or 100 μ A is used. The camera unit provides 1 mA because a) this was specified in early versions of the documentation from GEC Marconi Infrared and because a 1 mA source is much easier to construct. GEC Marconi Infrared have supplied calibration curves at both 1 mA and 100 μ A (the difference is not very large).

10.2.2 Camera Unit

This supplies bias and clock signals to the device under test (DUT), switches the four video outputs into a single preamplifier and relays the temperature sensing lines to either a voltmeter or source measure unit.

The bias and clock voltages are controlled via digital to analogue converters (DACs), 12 bit and 8 bit respectively. Separate control is available on clock high and low levels. The DACs are loaded, via a Dallas Microcontroller, from an AT computer along an RS232 link.

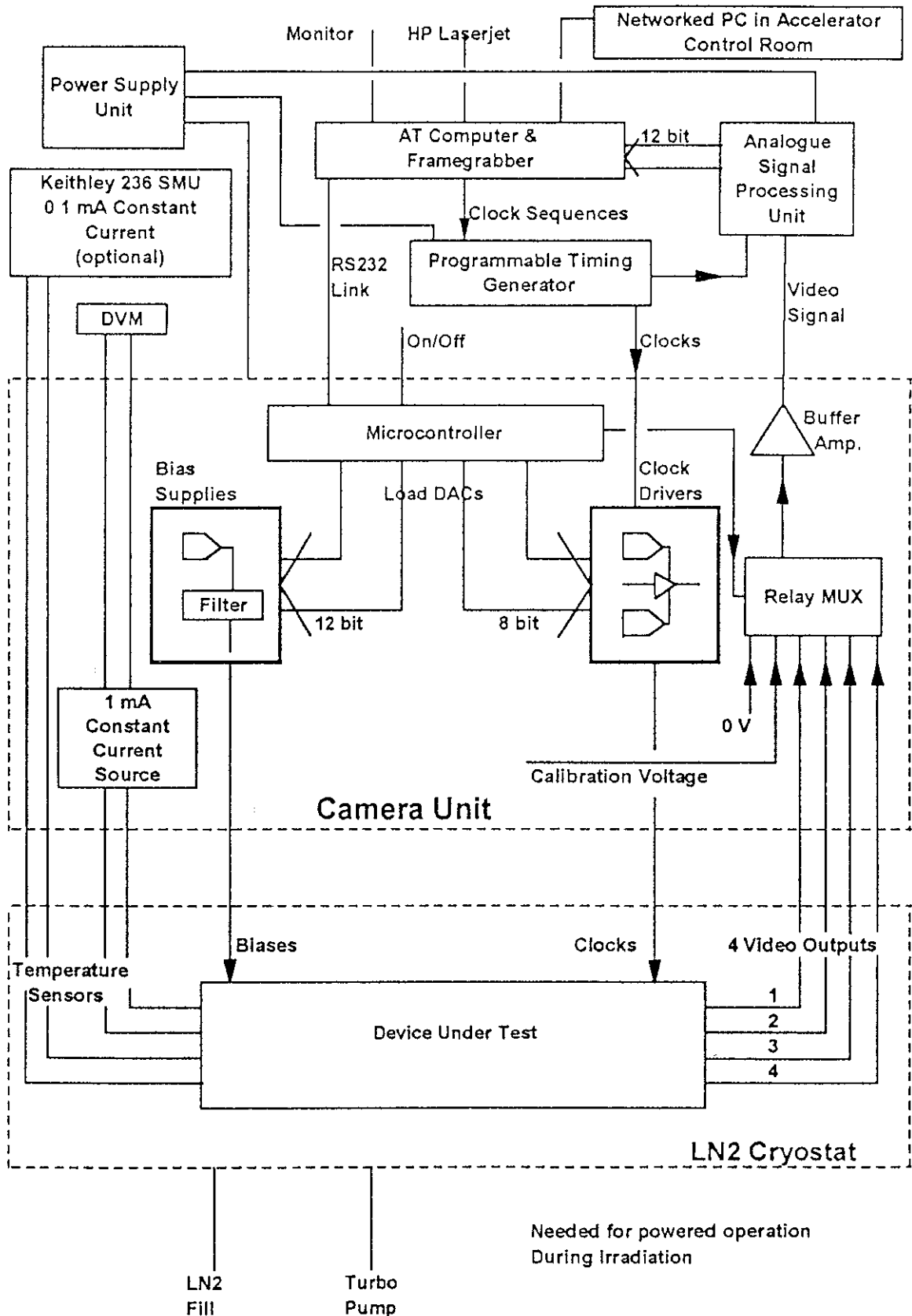
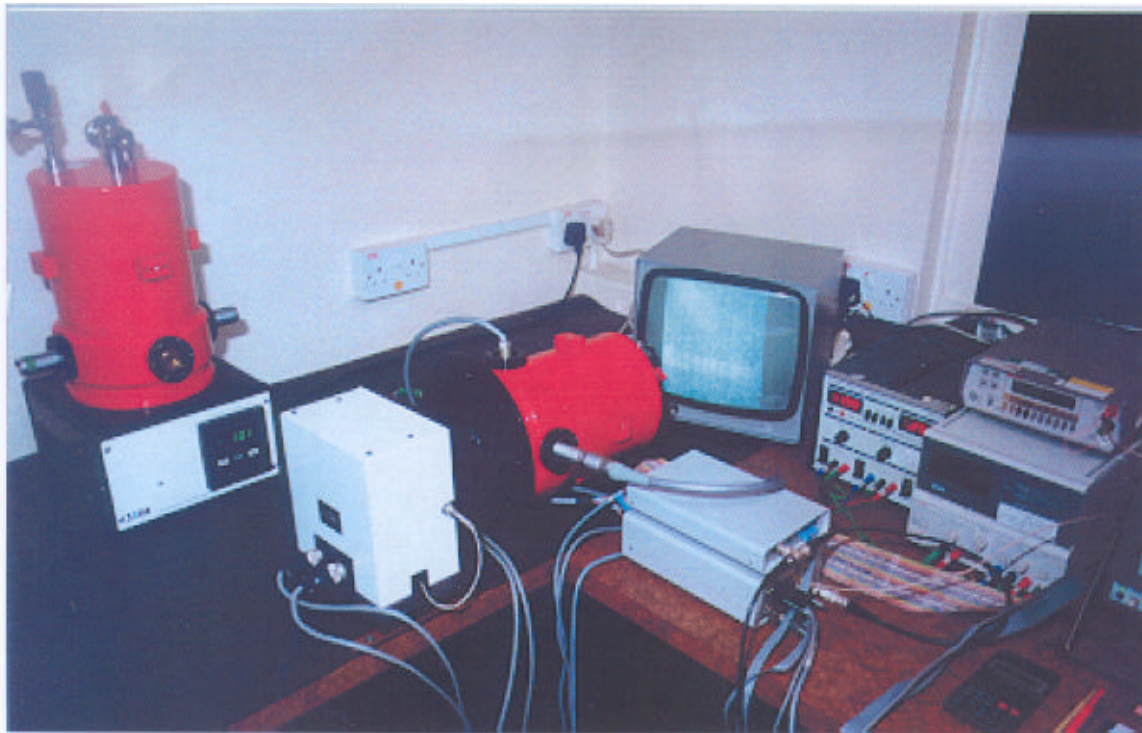
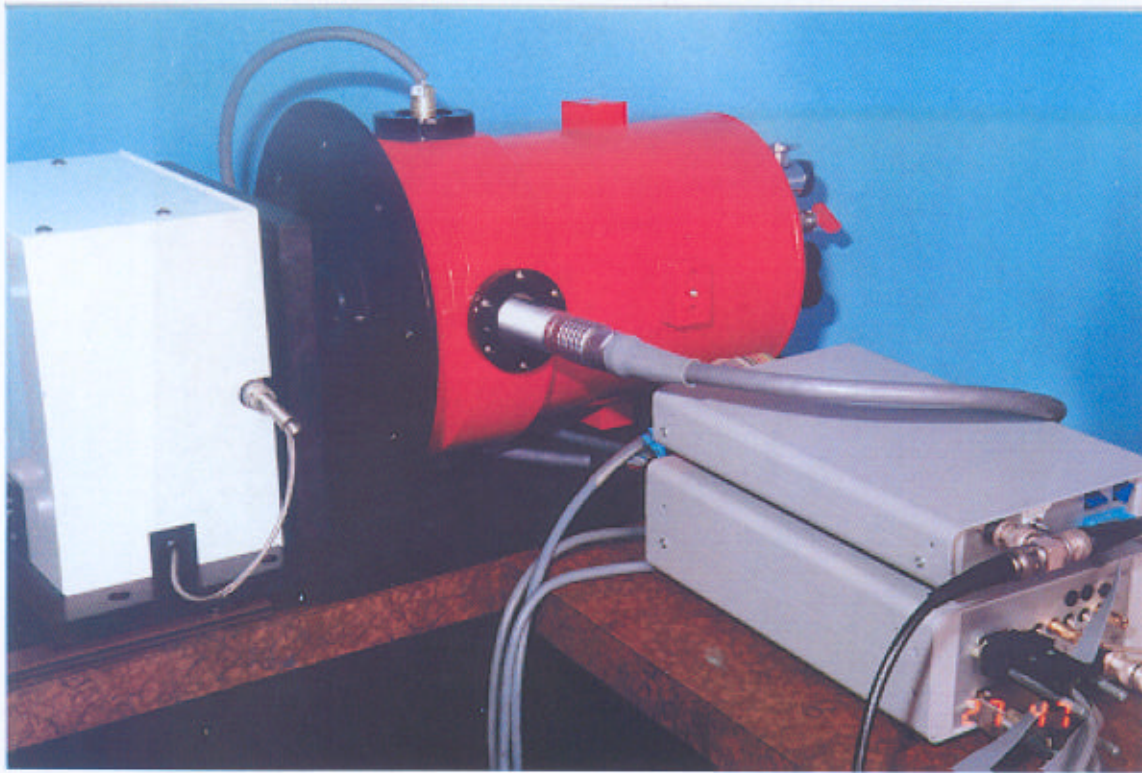
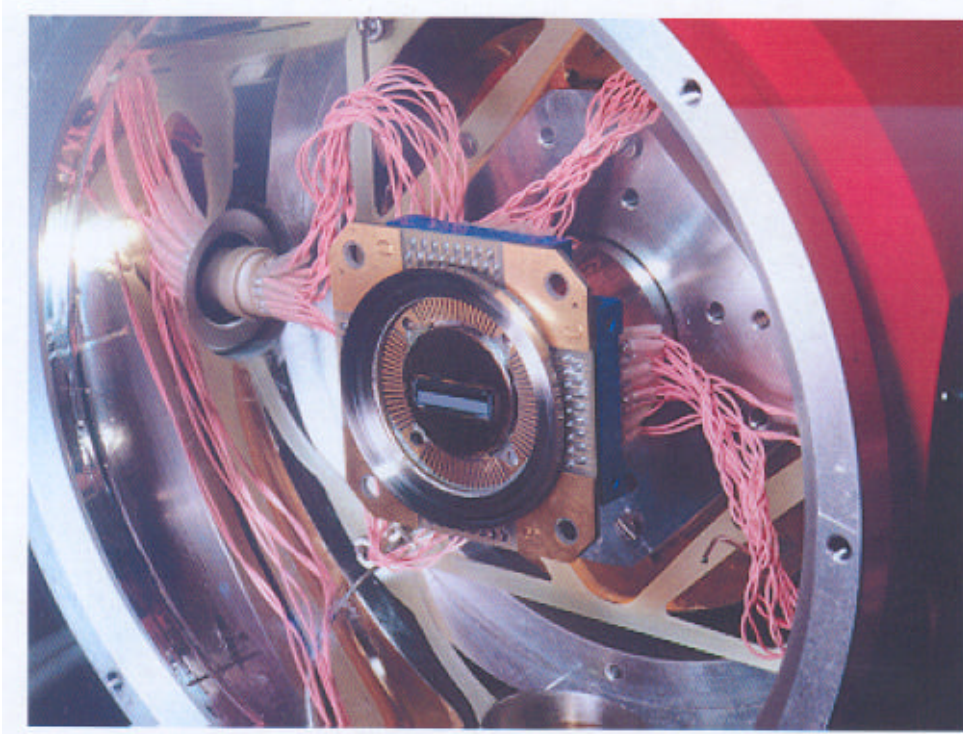


Figure 10.2-1 Block diagram of test system



Figures 10.2-2 Photographs of test dewar, blackbody source and test electronics.



Figures 10.2-3 The 256 x 4 GMIRL MWIR array mounted in its dewar

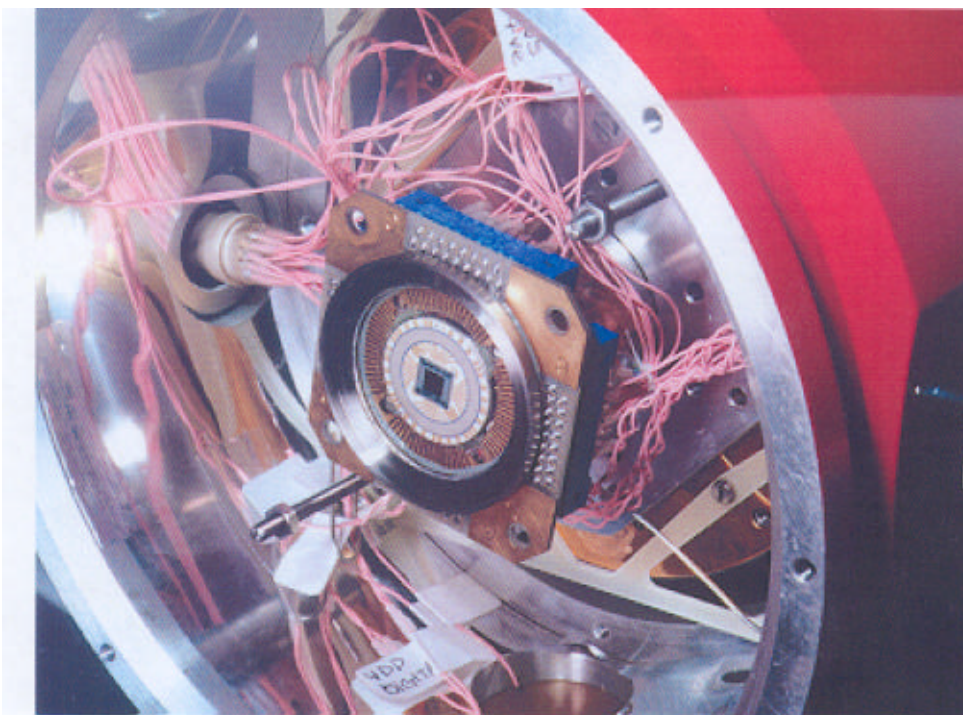


Figure 10.2-4 The 128 x 128 GMIRL LWIR array mounted in its dewar

Special features are

- * After each load the microcontroller is put in 'sleep' mode, whereby its internal clock is stopped - thus ensuring that there is no pick-up onto the DUT supplies
- * On/off control of DUT operation (all DACs at 0V) either manually or under software control
- * Microcontroller ensures safe power up/down sequence for biases and clocks
- * In-built battery-backed memory of the microcontroller 'remembers' DAC voltage settings during power off. Hence the computer is not needed when operating (at constant bias and clock voltages) in an irradiation cell
- * Multiplexing of the four video outputs by software control
- * 0V or a test input voltage can be switched into the video line for calibration of gain and offset
- * Operation of the DUT at up to 8 MHz pixel rate
- * Interpreter for microcontroller commands enables easy control of voltages from data acquisition software

10.2.3 Programmable Timing Generator

The Timing Generator produces TTL level clock waveforms for the camera unit. It consists of a series of RAM-controlled sequencers. The number and frequency of pulses in a train and the grouping together of different trains to form the overall pulse sequence for the multiplexer are variable. Sequences are generated by typing user-friendly high level statements on the host computer to generate a file containing the sequence information. This file is then down-loaded to the RAM in the Timing Generator via the parallel printer port.

Because the pulse trains are variable, it is simple to generate the sequences necessary for driving a variety of arrays and for variation of stare time etc.

The Timing Generator operates at clock rates of up to 64 MHz. There are 23 separate output lines, thus allowing for control of external circuitry such as clamps, sample and holds and ADCs, as well as clocking the test objects.

In general it is possible to store several different complete sequences in the timing generator at any one time, though the number depends on their complexity. Hence the operator can switch sequences without reloading from the host computer. This is particularly useful for example when changing integration times.

The normal operating frequency for the multiplexers is 5 MHz/pixel. This is achieved with a 40 MHz master oscillator. Operation at 8 MHz (64 MHz master clock oscillator) has been verified.

10.2.4 Power Distribution Unit

This is a set of bench power supplies for providing bias to the programmable timing generator and camera head, and analogue signal processing unit

10.2.5 Analogue Signal Processing Unit

This contains a switchable gain amplifier, DAC controlled offset stage and 12 bit ADC (which can convert at rates up to 10 MHz/pixel) ADC timing is under control from the programmable timing generator

10.2.6 AT Computer and Framegrabber

This was a Pentium 75 MHz computer with 32 Mbyte RAM and 750 Mbyte hard disk

Slotted into the ISA-bus was a VS100 framegrabber/image memory card manufactured by Imaging Technology Inc. This is capable of capturing normal CCIR video signals or non-CCIR variable scan rate pictures up to a pixel rate of 10 MHz. The image memory is 1024 x 1024 x 12 bits deep. A 512 x 512 window of this memory can be output to the display at any one time. The variable scan rate pictures can be input either as digital data up to 12 bits deep (as in this case), or as an analogue signal to be digitised with an internal ADC. The internal ADC digitises to 8 bits.

For operation at the proton facility at Harwell the Pentium computer was networked to a 486 PC in the control room of the accelerator. This allowed remote operation of the array electronics, display of images and acquisition of data. This was necessary for the observation of transient pulses from particle hits.

10.2.7 Test Software

Sira has written system-level software which acts as an interpreter for the VS100 image memory board functions and allows these functions to be selected in a user-friendly manner and assembled together to form sequences for automated testing or data analysis. Examples of functions available with simple commands are

- * image acquisition (either continuously or as single frames)
- * pan and zoom
- * image scaling and off-setting
- * display of a cursor on the image display and readout of a 5x5 matrix of pixel values on the computer console
- * cursor movement from keyboard or mouse

- * selection of points, lines, columns or areas of interest by keyed commands or by mouse
- * calculation of mean and standard deviation of areas of interest and display of histograms Also dumping of this data to a file
- * recording of intensity profiles across slices through images
- * detection of pixels above or below a set threshold (eg for analysis of image non-uniformity)
- * adding or averaging successive images to reduce random noise
- * addition, subtraction, division or multiplication by previously stored images
- * statistical analysis of values from one pixel (or a group of pixels) from successive frames for noise analysis
- * saving of image data, either in VS100 or standard TIF (tagged image file) format
- * operations on input and output look-up tables (LUTs)
- * control of Unidex mirror drives
- * control of Bentham Instruments monochromator
- * loading of bias and clock supply voltages into the microcontroller memory in the camera head

Examples of operations are

- * definition of sequences or regions of interest and recording of mean, standard deviation etc
- * measurement of output signal as a function of bias or clock voltages
- * interaction with the programmable timing generator so as to form linearity plots by successive changes in integration time and recording of image values from a specified region of interest

Data files (such as histograms) can be analysed and plotted using standard spreadsheet or graphics packages This is made easy since it is possible to flip in and out of the command program without reloading any parameters or losing the screen display

Built into the command program are safeguards to ensure that files cannot be overwritten by giving two files the same name The database is organised by giving each device a unique directory All files relating to a device are stored in its directory To keep track of the current directory the directory name appears as the prompt from the command program

10.2.8 Modifications made for the present contract

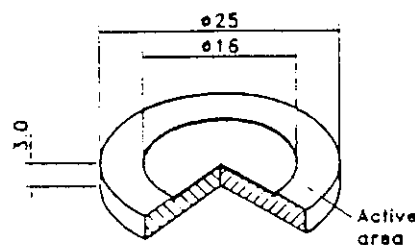
Below is a list of the modifications to the test equipment and software that were needed in order to perform the present contract. The previously existing items were designed for operating the 256 x 4 array only.

- fitting of an existing germanium window to one dewar front plate
- fitting of a rotating arm (for mounting alpha source) to one dewar front plate
- rewiring of harness in one dewar so as to provide the correct biases and clocks for the 128 x 128 array
- fitting of cold shield to both dewars
- modification of signal digitization circuit to allow for higher gain
- writing timing of generator data acquisition and analysis software for the 128 x 128 array
- manufacturing of new dewar front plate to allow mounting on the proton beam line, also modification of dewar fill tube
- manufacturing of apertures to allow linearity measurements

10.3. IRRADIATIONS

10.3.1 Alpha Particle Irradiations

A 2.58 k Bq Am²⁴¹ Beta Planchet source (Amersham International, type VZ-1366) was mounted on a rotating arm attached to the front plate of the cryostat and was used for measurements in the laboratory at Sira. A diagram of the source is given in figure 10.3-1.



VZ-1366

Figure 10.3.-1 Am²⁴¹ source

The source was recently purchased and has a DKD certificate (DKD-K-06501, July 1996) It produces 5 484 MeV alpha particles at a rate of 1190 /s Note that since the source is thin, there is negligible loss in energy of the alpha particles as they are emitted

Assuming an energy loss rate of 0 585 MeV/(Mg/cm²) this implies a maximum ionising dose rate of 19 9 rad (Si)/hr or 0 48 krad/day This was low enough that excessive total dose could not be accumulated inadvertently Previous experience has shown that TID effects are significant after a few krad, with functional failure (annealable) at 15 krad(Si) for powered devices Further details of count and dose rates are given in chapter 11

It was originally planned to use the alpha particle source for the observation of transient events, then to perform unbiased irradiations to examine displacement damage effects Proton irradiations were planned if interesting effects were seen which needed further study In practise (c f chapter 11), it proved to be difficult to convincingly demonstrate transient effects due to the low event rate with the alpha source (though some events were seen with the 256 x 4 MWIR array) No displacement damage effects were seen for exposures of several days duration It was therefore decided to perform proton irradiations in order to obtain some kind of results The proton exposures did show transient events but with a lower event amplitude and occurrence rate than expected No evidence was found for displacement damage - but there were significant total dose effects With an improved knowledge of the transient event size and rate, more alpha particle tests were performed at Sira and transient events were then seen, but again with event rates and amplitudes lower than originally predicted Unfortunately the 256 x 4 array was accidentally damaged just prior to the Harwell proton tests and so the later alpha particle tests could only be performed on the 128 x 128 array Limited beam time at Harwell in any case limited the proton tests to one device

Irradiations of the 128 x 128 and 256 x 4 arrays were performed at Sira during the period 5th to 27th March 1997, with a subsequent short (half day) test for alpha particle transient events on 30 April 1997

The 128 x 128 LWIR array irradiations were as follows

date	duration	operating conditions
5/3/97 to 7/3/97	47 0 hrs	80 K, biased
7/3/97 to 10/3/97	60 0 hrs	Room temperature, unbiased
11/3/97 to 12/3/97	18 0 hrs	80 K, biased
12/3/97 to 13/3/97	31 0 hrs	Room temperature, unbiased
13/3/97	1 0 hrs	80 K, biased
25/3/97 to 27/3/97	48 0 hrs	80 K, biased
30/4/97 to 1/5/97	16 0 hrs	80 K, biased

Images were recorded after each irradiation

The 256 x 4 MWIR array irradiations were as follows

date	duration	operating conditions
19/3/97 to 20/3/97	24 0 hrs	80 K, biased

10.3.2 Proton Irradiations of the 128 x 128 Array

These used the 10 MeV Tandem Van de Graaff accelerator at Harwell, UK. The irradiations were performed on 17 April 1997.

An important outcome of the test programme was the development of a method of proton irradiating an IR array whilst operating at 80 K and biased and of operating the array drive electronics remotely from the control room of the accelerator.

One of the 1815 INV dewars was mounted directly on the beamline (in a horizontal configuration) as shown in figure 10 3-2. A new dewar front plate was manufactured at Sira to allow mounting onto a flange attached to the Harwell sample chamber at the position normally used for the Faraday cup. The usual sample mounting plate inside the chamber was moved into a sideways position so that the proton beam could pass it, on the way to the dewar. A vacuum valve was mounted in between the dewar and the sample chamber and this was found to be useful in allowing the sample chamber to be kept evacuated whilst mounting and de-mounting the dewar. The dewar was evacuated separately with the Sira turbo pump system before opening the valve.

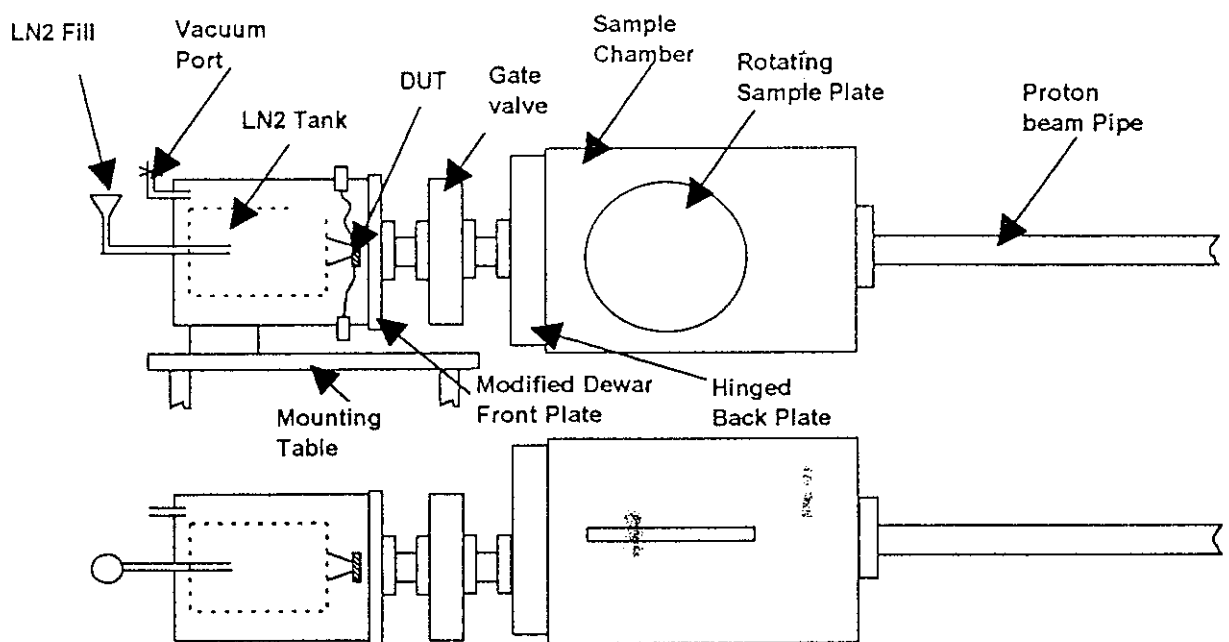


Figure 10 3-2 Mounting of the LN2 dewar on the proton beam line at Harwell

Some experimentation in the liquid nitrogen filling procedure was needed as the dewar is only designed for filling in the vertical position. However after trying several fill tubes of varying lengths and bore diameters, a satisfactory arrangement was achieved and it was found that a constant device temperature of 80 K was maintained throughout the tests on the beam line.

The tests started with low flux observations of transient events with the 128 x 128 LWIR array biased. The collection of data could be performed remotely (in the control room) by networking a second PC to the camera control computer which was situated in the beam room.

For the transient event measurements the proton flux was 1.8×10^6 p/cm²/s and the irradiations lasted for 100 s each. Thereafter the flux was increased, keeping the irradiation time constant at 100 s for each fluence step. Dosimetry is believed to be accurate to $\pm 5\%$. The irradiations were

fluence step	fluence ($\times 10^9$ p/cm ²)	accumulated total dose, krad(Si)	irradiation duration (seconds)	bias condition
1	0.18	0.1	100	biased
2	0.18	0.2	100	biased
3	0.18	0.3	100	biased
4	0.18	0.4	100	biased
5	3.6	2.4	100	biased
6	9.0	7.4	100	unbiased
7	9.0	12.4	100	unbiased
8	18.0	22.4	100	unbiased

Images were recorded after each step and measurements of threshold voltage shift were made immediately before irradiation and after steps 5,6,7 and 8.

Measurements of image data and threshold voltage shifts were also made on return to Sira to establish annealing behaviour. These were made on 21/4/97, 4 days after irradiation.

It should be noted that there are several drawbacks to using proton irradiations, in this way

- 1) the total beam time is limited by cost constraints to 1-2 days
- 2) the proton flux must be kept low so as not to accumulate total dose too quickly (irradiations were performed with the array unbiased unless looking for transient effects so as to reduce TID effects)
- 3) the dewar has to be dismounted from the beam line before making optical tests - hence the array has to be warmed to room temperature (resulting in some annealing)

However the increased particle fluence compared with the alpha source made transient events easier to observe and also allowed a convincing demonstration of the absence of displacement damage. An alternative method would be to use a higher energy proton beam (e.g. at PSI, Zurich) and to irradiate in air through the germanium window of the dewar. However, for logistical reasons this test could not be performed within the timescale of this programme, in any case the main objectives of the programme were achieved with the 10 MeV irradiations at Harwell.

10.4 TEST MEASUREMENTS

This section gives a brief description of the measurements performed

10.4.1 Functionality

Overall functionality was checked by examination of each of the four output waveforms with an oscilloscope. After adjustment (and recording) of the DIG voltage each video waveform should show reset and saturation levels, with pixel voltages in between. No adjustment of any of the other bias or clock voltages was needed during the course of the tests.

10.4.2 Measurements of Image Data

For the 256 x 4 array, the pixel values for 256 consecutive frames (ie lines) were accumulated in the framegrabber memory for each of the four video outputs, the average of 16 of these 'frames' was then recorded and saved on disk. For the 128 x 128 array the same procedure was followed for each image (recorded images were the average of 16 frames). The readout noise on single images was due mainly to external pickup (approximately 80 ADC units, rms) and was not considered to be an important parameter for test measurements.

10.4.3 Threshold Voltages

These measurements were made on the 128 x 128 array, detailed measurements on the 256 x 4 array having been made in a previous Sira study.

The average value of a large number of pixels was found and subtracted from the reset level to give an effective 'signal' value which can be measured as a function of bias or clock voltage to determine threshold voltages. These are the voltages above (or below) which either the multiplexer ceases to operate (giving pixel values of 0 or full scale) or at which switching in behaviour occurs (as for the cap enable pulses). Typical traces are given in figure 10.4.3-1. It can be seen that there are sharp transitions for clock, line sync, test and integration capacitor enable voltages. Also the output is very sensitive to the DIG voltage.

10.4.4 Pixel Uniformity Versus dig Voltage

Images for the 128 x 128 array were normally recorded for several values of VDIG since this voltage has an important effect on pixel nonuniformity as explained in section 10.2.

10.4.6 Temperature Measurement

When the dewar contains liquid nitrogen the on-chip temperature gave a constant reading (corresponding to a temperature ~80 K). The temperature sensors were found to be insensitive to radiation dose (in agreement with a previous Sira study).

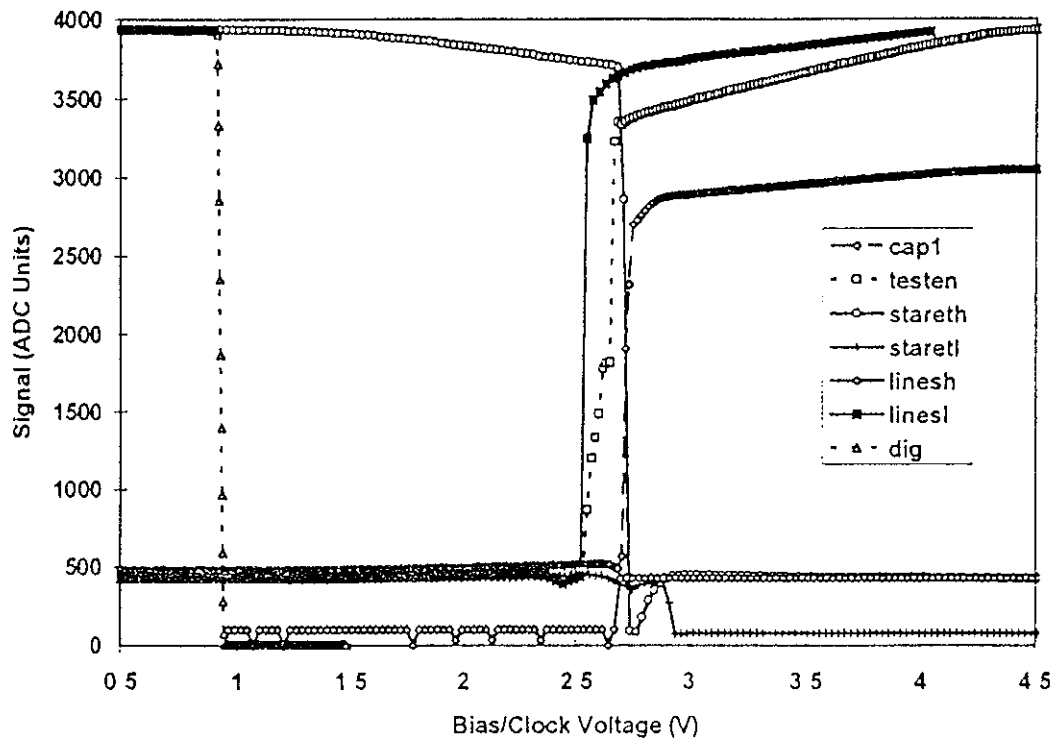


Figure 10 4 3-1 Variation of signal level with bias/clock voltage for the 128 x 128 array

10.4.7 Power Consumption

Because of modifications to the test electronics required to operate the 128 x 128 array, power consumption could not be monitored. However this parameter should only be sensitive to total dose and was investigated for the 256 x 4 array in a previous Sira study.

10.4.8 Pixel Response Uniformity

This was measured while viewing a black body source at various temperatures (in the range from ambient to +60°C). The detector was placed close to the black body but in a defined geometrical arrangement (so that measurements can be repeated). The measurements were made at the start and end of the irradiation programme.

10.4.9 Linearity

Measurements of signal for the 128 x 128 array were made at the start and end of the irradiation programme at various temperatures (as discussed above) and with various apertures placed in front of the germanium window of the dewar. Measurements of linearity were also made by changing the stare time of the array.

10.4.10 Transient Signals

These were be measured with the array viewing the alpha particle source against a uniform background at ambient temperature and also on the proton beam line. Because the event was found to be low, a variety of data collection techniques were tried

- 1 visual examination of images in near real time (with a reference background image subtracted) - with a time delay of a few seconds between each image displayed
- 2 recording of sequences of images (with a reference image subtracted)
- 3 automatic analysis of a large number of images by first subtracting a reference background image and then recording pixels above a defined threshold

Method 3 was found to be particularly effective, although small changes in array operating conditions sometimes lead to changes in the fixed pattern noise and false triggering of the threshold level - particularly for runs lasting 10 minutes or more. Also careful choice of threshold level was needed

11 RESULTS OF THE EXPERIMENTAL TEST PROGRAMME

11.1 Signal Calibration

Measurement of the array output voltage on an oscilloscope and the corresponding ADC counts recorded by the digitising electronics gave a voltage calibration, for the three switchable digitizer gains, of

low gain	medium gain	high gain
510 $\mu\text{V}/\text{ADU}$	163 $\mu\text{V}/\text{ADU}$	52.6 $\mu\text{V}/\text{ADU}$

For both arrays the lowest value of integration capacitance was always used so as to obtain the highest sensitivity. The data sheet values being 0.6 pF for the 128 x 128 array and 1.1 pF for the 256 x 4 array. We then have the following ADU to electron conversions

	low gain	medium gain	high gain
128 x 128	1360 e/ADU	435.2 e/ADU	140.4 e/ADU
256 x 4	2490 e/ADU	800 e/ADU	257 e/ADU

11.2 Transient Events

Transient events due to particle hits were measured in the two HgCdTe arrays during irradiation with 5.48 MeV alpha particles and 10 MeV protons. Calculations using the TRIM code [1] show that the energy loss in LWIR and MWIR HgCdTe is,

200 keV/ μm	for 5.48 MeV alpha particles
15 keV/ μm	for 10 MeV protons

Information from the manufacturer indicates a thickness for the HgCdTe slice of 9 μm . For the alpha particles particularly, there will be some slowing down in the MCT and it is estimated that the energy loss is roughly 2 MeV in 9 μm . Taking the energy lost in creating an electron hole pair as 1.1 and 1.3 eV for LWIR and MWIR MCT, respectively, we get expected signals of

	MWIR HgCdTe (bandgap 0.19 eV)	LWIR HgCdTe (bandgap 0.12 eV)
alpha particle event size	1.5 x 10 ⁶ electrons	1.8 x 10 ⁶ electrons
proton event size	1.1 x 10 ⁵ electrons	1.2 x 10 ⁵ electrons

Information from a previous study [2] showed that proton events in LWIR diodes are not larger than 2×10^5 electrons

In fact, even after increasing the gain and dynamic range of the off-chip electronics, it proved difficult to observe events. This was partly because the event sizes were low (see below), but also because the stare times available with HgCdTe arrays are low and so a large number of images need to be examined. The stare time requirements are set by the need not to saturate the detectors with signal from the thermal background. On the other hand this background cannot be too low since a low diode current will result in a high input impedance for the direct injection circuit and poor injection efficiency. It was found practicable during these tests to operate the linear MWIR array at a pixel rate of 0.5 MHz with a stare time of 540 μ s and the 128 x 128 LWIR array at a pixel rate of 2 MHz with a stare time of 32.5 μ s. Note that since the 2-D array operates in a line readout (rather than a fully staring) mode, the effective number of pixels is a factor of 4 less than for the linear array (for each video output the line length is 64 pixels rather than 256) so that the area array is less efficient at detecting events. In addition the particle flux cannot be allowed to be high enough to cause total dose effects in the readout circuit.

During the proton tests of the 128 x 128 array, a flux of 10^6 protons/cm²/s was used. Irradiations of 100 seconds duration were performed which each gave a total ionizing dose of 0.1 krad. It will be seen below that these irradiations were enough to cause significant changes in the direct injection gate voltage and changes in the fixed pattern noise and a few 10s of seconds is an upper limit on the useful irradiation time at this flux. During the experiment the main effect as viewed on a TV monitor was the gradual appearance of white pixels due to the shift in VDIG. No transient events could be seen by eye. Two sequences of 12 images were also recorded and these, at first glance, also did not show transient events. Hence the test was abandoned and higher fluence irradiations were performed to look for displacement damage and total dose effects (incidentally the next irradiation, at twenty times the flux, was also performed with the array operational and no events were seen by eye).

On closer examination of the 24 recorded images at Sira it was found that some of the signals did not correspond to known white spot defects (induced by VDIG changes) and must have been due to transients. With hindsight it would have been desirable to have recorded more images during the transient tests, but there would have been a limit on the practical number (but maybe this could have been increased by a factor 10).

Seven events were identified, with signal sizes as follows

- 8.9 x 10⁴ electrons
- 5.7 x 10⁴ electrons
- 9.4 x 10⁴ electrons
- 12.8 x 10⁴ electrons
- 6.8 x 10⁴ electrons
- 8.2 x 10⁴ electrons
- 10.3 x 10⁴ electrons

Some of these events are likely to be the result of tracks which are shared between more than one pixel. If this occurs in the column direction then the signal charge is not seen (staring for different lines occurs at different times). This probably explains the lower values. As a rough approximation we take the event size as

$$\text{event size for 10 MeV protons} = 1 \times 10^5 \text{ electrons}$$

This is in good agreement with the prediction and is consistent with the lack of observation in the previous test [2]

If data is collected from an image with N pixels, each with a stare time T , then if the measured event rate is E events/image then this must correspond to an incident flux, S , on the detector (in particles/cm²/s) given by

$$S = E / (A N T) \quad (11-1)$$

where A is the area of a diode

With a stare time of 32.5 μ s the event rate corresponds to an event rate of 3.1×10^5 events/cm²/s compared with the particle fluence of 1.8×10^6 protons/cm²/s - assuming a pixel diameter of 30 μ m. That is the event rate was a factor 6 down on expectations. A possible explanation is that the effective diameter of a pixel is less than the pixel pitch, perhaps because the electric field at the edge of the depletion region is not large enough to prevent recombination (bear in mind that for a loop-hole diode the depletion region takes the form of a vertical cylinder with a central hole for the via contact).

Alpha particle tests on the 128 x 128 array were repeated on return to Sira but with an observation sequence which automatically searched for events above a threshold 150 ADU at medium gain (corresponding to 6.53×10^4 electrons). This was found to be a good compromise for reliably finding transient events and yet reducing the number of false events due to readout noise, fixed pattern noise drifts and residual signals from transient events split between pixels. Note that the larger signals from the alpha particles helps in the event discrimination. Figures 11.2-1 and 11.2-2 show the individual event sizes for two experimental runs, both for the charge in individual pixels and the summed charge when events were split between pixels in the line direction. As noted above, charge split in the column direction is lost. A third experimental run, carried out towards the end of the project gave similar results. Figure 11.2-3 shows the histogram for the event amplitudes for the combination of all three runs and summing of charge in adjacent horizontal pixels.

Events can clearly be seen at an amplitude of

$$\text{event size for 5.48 MeV alphas} = 5 \times 10^5 \text{ electrons}$$

The fact that the alpha particle event size is a factor 3 below predictions, whereas the proton results were in good agreement may be because of recombination effects. The charge density within the alpha particle tracks will be an order of magnitude greater than with 10 MeV protons.

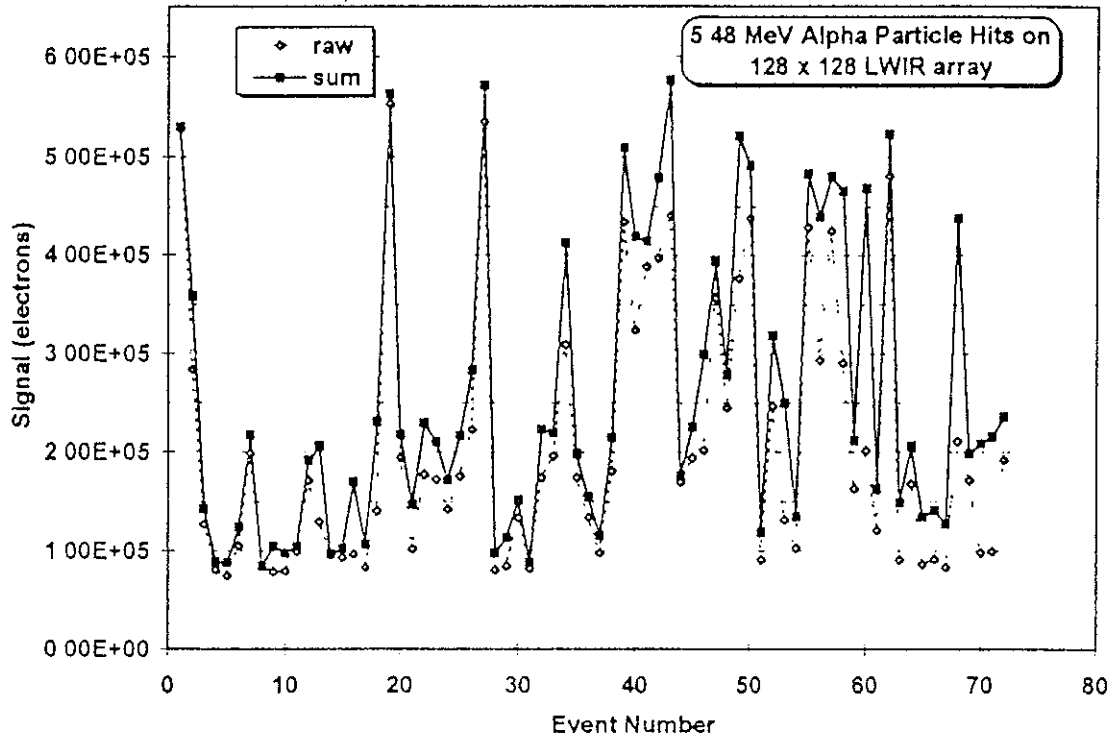


Figure 11 2-1 Transient event amplitudes for alpha particle hits on the 128 x 128 LWIR GMIRL array (run # 1, from thresholding of 29,908 images)

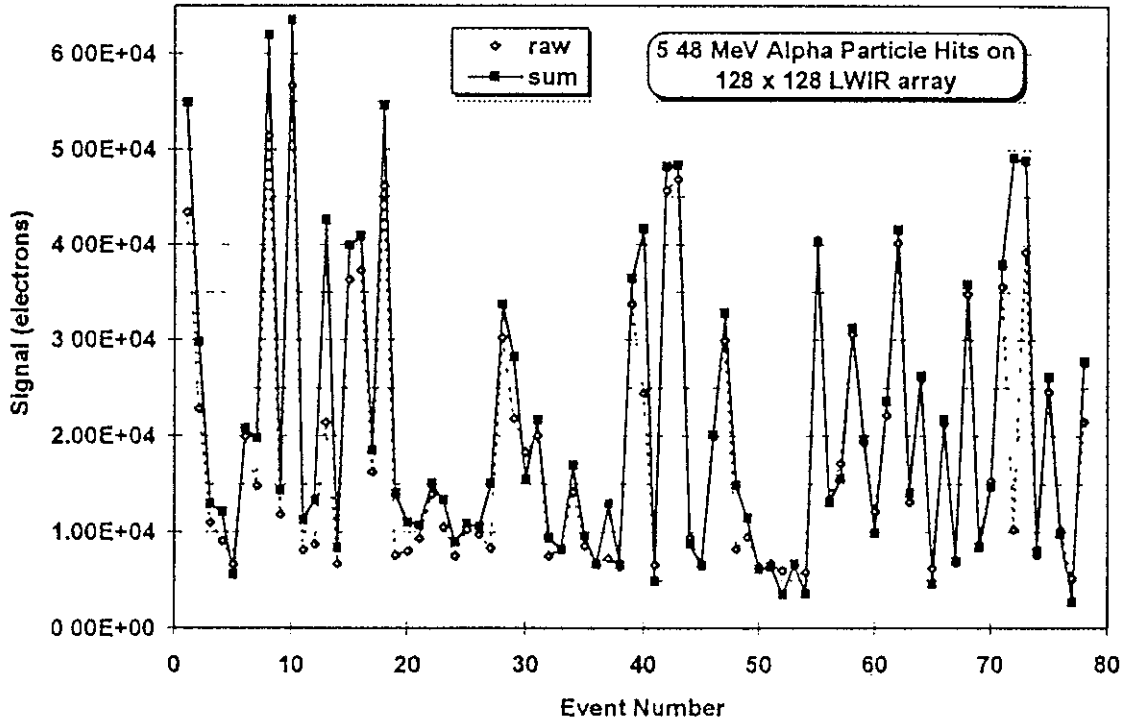


Figure 11 2-2 Transient event amplitudes for alpha particle hits on the 128 x 128 LWIR GMIRL array (run # 2, from thresholding of 30,000 images)

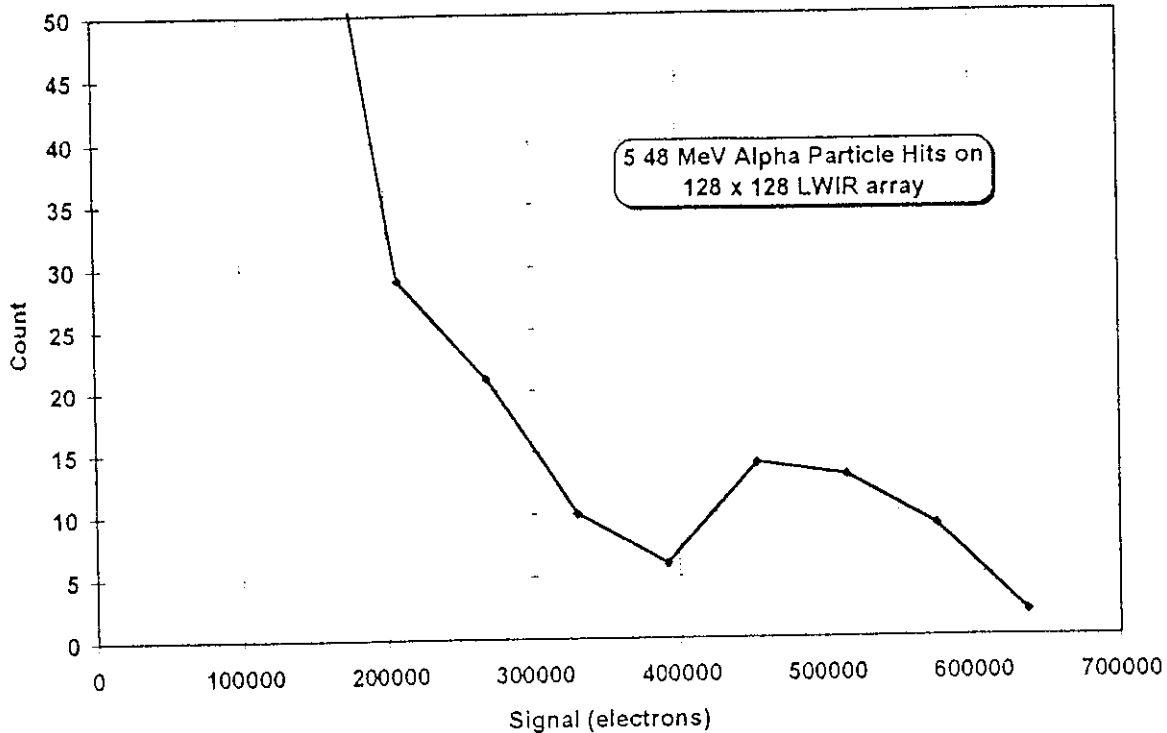


Figure 11 2-2 Histogram of summed events from all three experimental runs

Three control runs performed with the alpha particle source rotated away from the array gave only a small number of noise events near the threshold (less than 10^5 electrons). Also the existence of split events in the horizontal, but not the vertical direction, is consistent with the array architecture and supports the contention that genuine particle events have been observed.

The plots above suggest an event rate of roughly 10 large sized events in 30,000 64×64 pixel images. This indicates an event rate of approximately $350 \text{ hits/cm}^2/\text{s}$ which compares well with the activity of the source and the effective area = 0.8 cm^2 , since the source was mounted close to the 1 cm diameter aperture of the cold shield, again assuming a pixel diameter of 30 mm . Since the alpha particles will be incident on the array at a range of angles, it is possible that the particle detection efficiency is high even if there are dead spaces between pixels (which is the possible explanation for the low count rate observed with normally incident protons).

Alpha particle events were also observed with the 256×4 MWIR array. The event size was

$$\text{event size for 5.48 MeV alphas} = 1.1 \times 10^5 \text{ electrons}$$

The event rate was roughly 14 large hits in 10980 frames of 256 line images. With a pixel diameter of $30 \text{ }\mu\text{m}$ and a stare time of 540 ms we get an incident flux rate of $5.1 \text{ hits/cm}^2/\text{s}$. The reasons for this low hit rate are unknown at present, but may be associated with the different pixel geometry of the 256×4 array. From figure 10 1-5 of the previous chapter we see that for array 4 (the one used) there is a pixel pitch of $60 \text{ }\mu\text{m}$ in the vertical direction (and only one line of diodes is readout through a single video output). This is twice the pitch of the 128×128 array and so the 'fill factor' will be smaller. The fact that the event size is less than for the

LWIR array may be because the difference in array architecture leads to many more 'split' events and that the full event size has not been observed

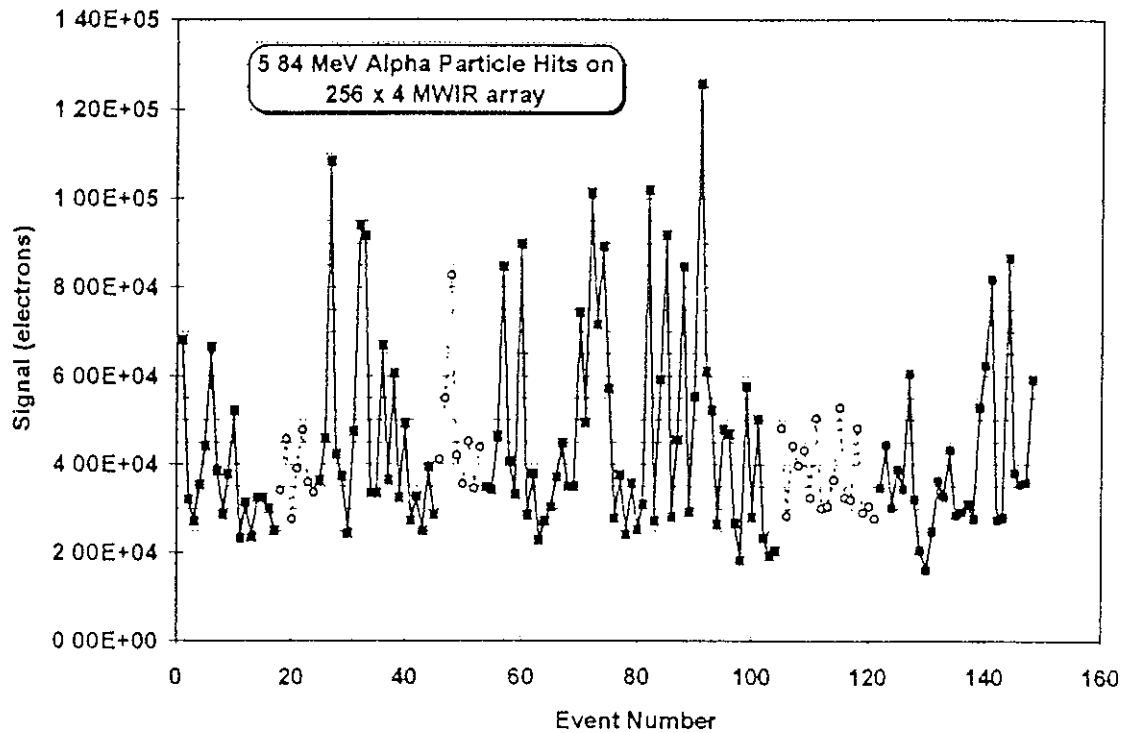


Figure 11 2-4 Transient event amplitudes for alpha particle hits on the 256 x 4 MWIR GMIRL array (7 runs, giving a thresholding of 10,980 frames in total, each containing 256 line images)

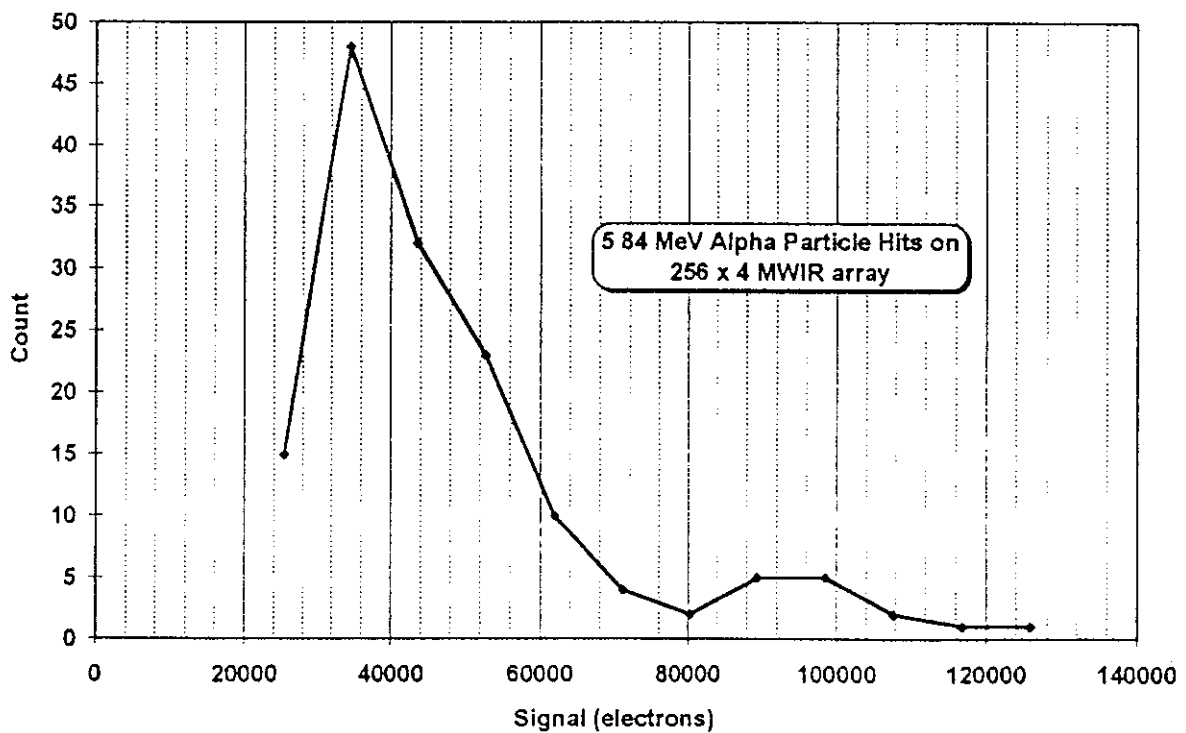
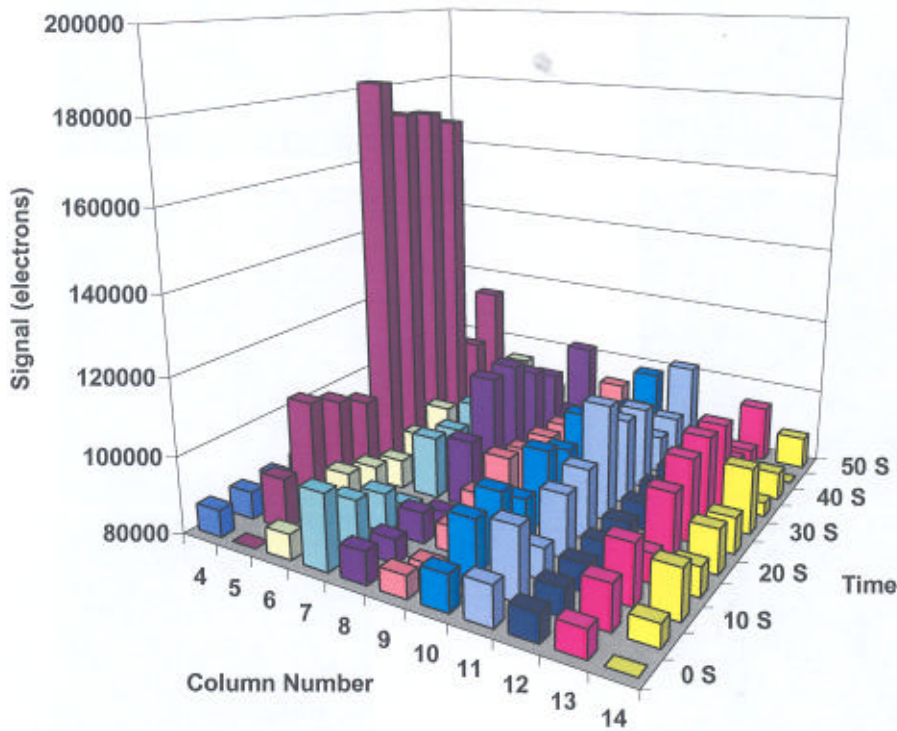


Figure 11 2-5 Histogram of summed events from the data of figure 11 2-4

11.2.1 Quasi Transient Proton Event

During the proton test, it was noticed that 4 consecutive images of the 24 that were saved, showed a bright pixel. This cannot be a transient event in the normal sense since it was present for more than on e image (in fact it lasted for 20s before disappearing). It is possible that this was a displacement damage event which rapidly annealed. Figure 11.2-6 shows the time evolution of the event. This type of event was not noticed in any of the other tests.

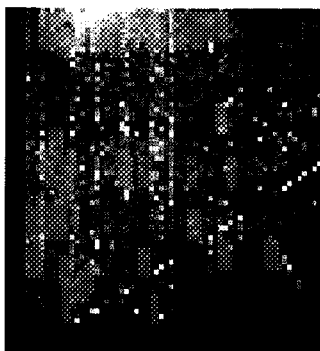
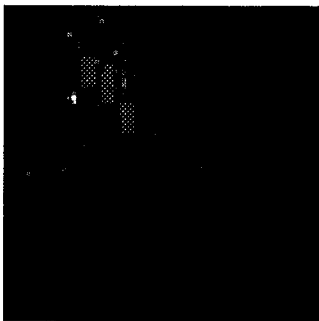
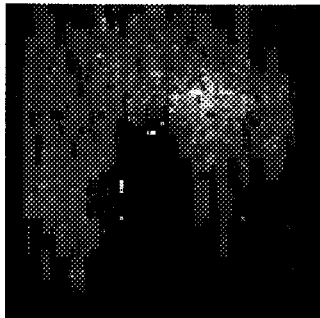
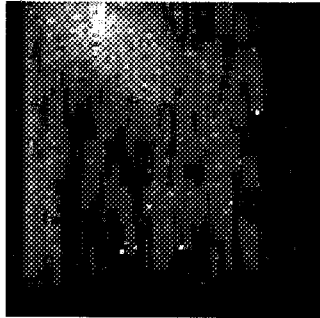
Figure 11.2-6 shows the time evolution of an event which occurred during proton testing. A bright pixel in column 5 appeared and lasted for approximately 20 s.



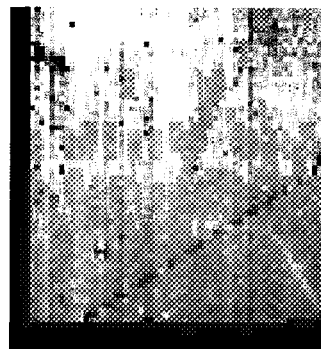
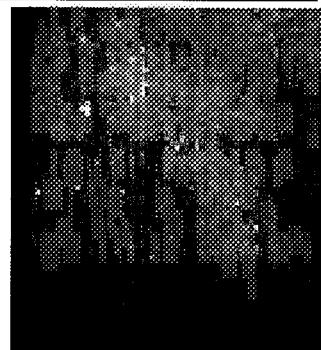
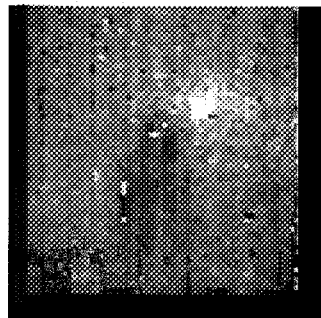
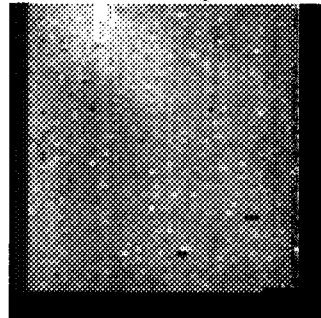
11.3 Displacement Damage

Images before and after alpha and proton irradiation were examined for changes which might indicate increases in diode current due to displacement damage. No significant changes were seen after the preliminary alpha tests or with the proton irradiations. The images were compared in several ways: by subtracting images, by alternate display on the monitor (blinking mode) and by examination of line or column traces. Below are images obtained before and after the proton irradiation (one image for each 64 x 64 quadrant of the 128 x 128 array).

Before proton irradiation



After 4×10^{10} p/cm²



It is somewhat difficult to detect changes in the above images due to the shifts in average level (and in the appearance of pre-existing defect pixels) which are caused by total ionizing dose-induced shifts in the effective DIG voltage (see below). Alternate display of images on the monitor, coupled with examination of the way pixel values change with VD1G was found to be the most effective method. Where differences between images were seen, it was found that the pixels concerned were always pre-existing defects which were sensitive to VD1G.

As a further example, figures 11.3-1 and 11.3-2 show plots of individual pixel values before and after proton irradiation. There were no new defects due to the irradiation. Figure 11.3-3 shows line traces across an image after each irradiation step.

Figure 11.3-1 plot of individual pixel values before proton irradiation (video output 1).

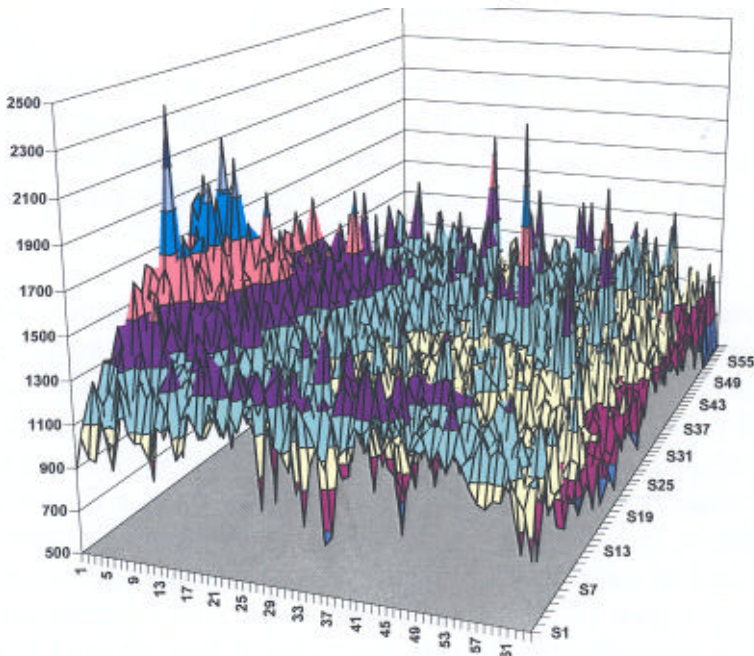
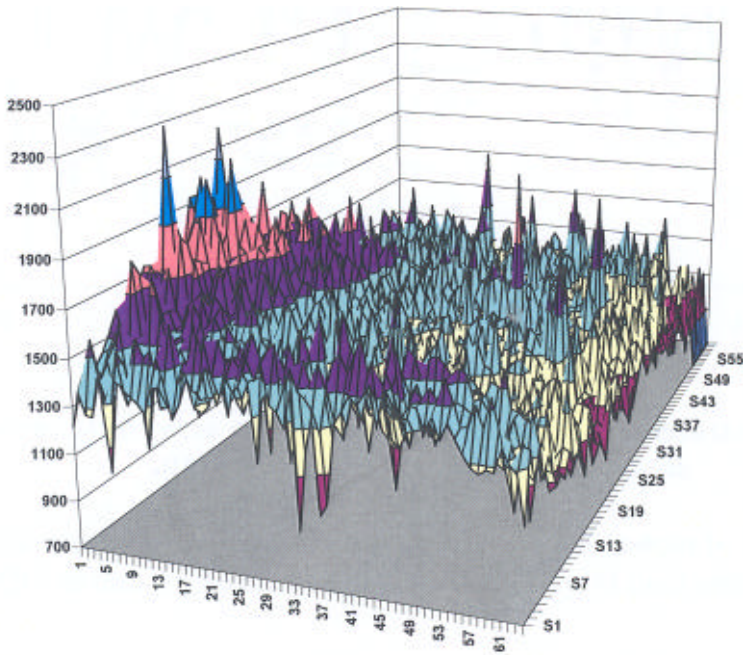


Figure 11.3-2 Plot of individual pixel values after proton irradiation (video output 1).

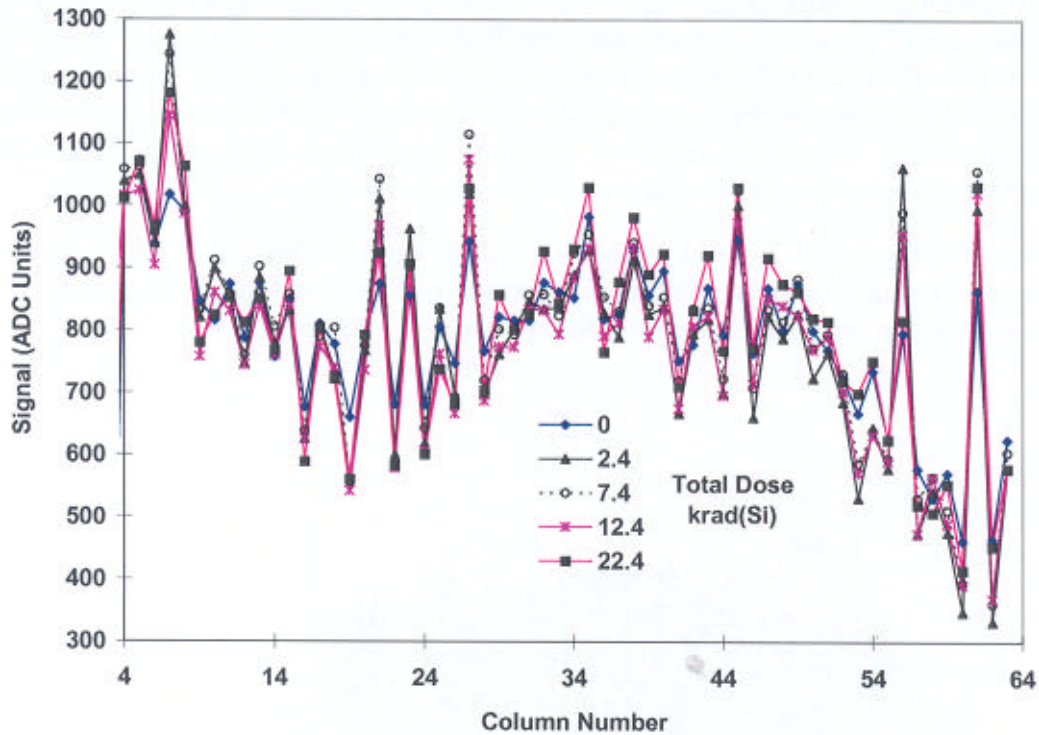


Figure 11.3-3 Line traces across an image from the area array after each irradiation step; total dose is indicated in krad(Si).

The limit on detection of proton induced defects was roughly 1×10^5 electrons (with a typical stare time of 32.5 us) this limit is appreciably less than the changes due to TID-induced shifts in VD1G.

The result is important in that if good quality (low defect count) arrays are procured for flight use, they are likely to remain free of defect pixels.

Although proton tests were not performed on the linear array, results before and after alpha particle testing are available. The total fluence of alpha particles received was roughly 0.2 krad(Si). No new defects were found. Typical plots of output data before and after alpha irradiation are given below (in all there are four arrays, each with 4 outputs, making 16 plots in all).

An exception to the general finding that no changes in the fixed pattern noise were seen is that for the last set of post irradiation measurements on the 128 x 128 array (made 19 days after the proton irradiation) a cluster of three dark defects with a white defect nearby appeared near the centre of one of the 64 x 64 quadrants (output 1). This had been an intermediate exposure to alpha particles (for 16 hrs, giving a fluence of about 3×10^7 /CM²/S). It is not known whether this was due to the irradiation or to a latent 'intrinsic' defect. After a final exposure for 696 hours to room temperature, unbiased alpha irradiation the defect pixels were normal again. However one pixel on each of three out of the four 64x64 pixel arrays showed a small increase in signal. Out of interest, two of these pixels (and the 8 pixels surrounding them) were observed for a period of approximately 30 minutes to see if they showed random telegraph signal behaviour (as has been observed in silicon CCDs). No effects were seen however.

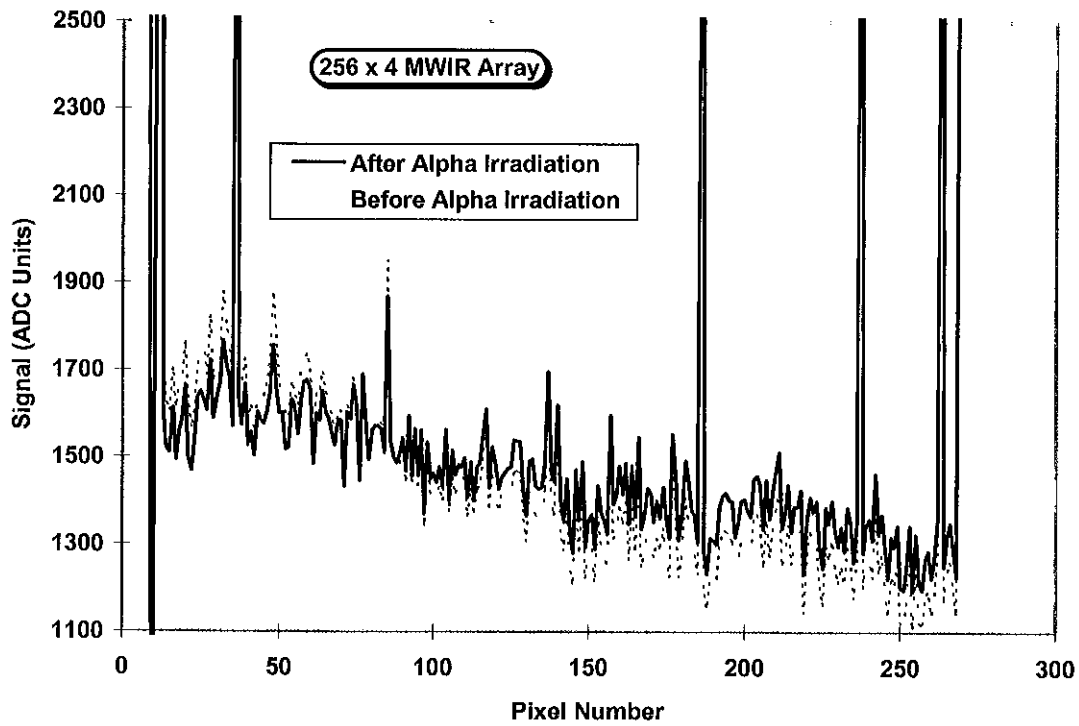


Figure 11.3-4 Plot of individual pixel values before and after proton irradiation (array 3 video output 1).

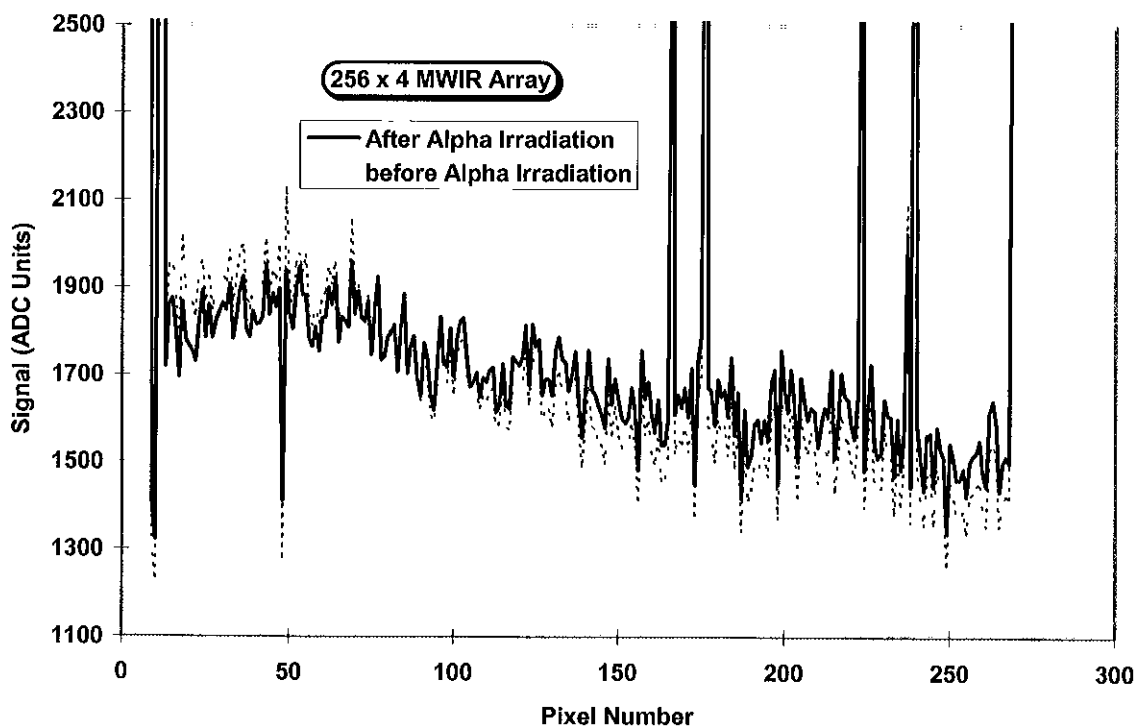


Figure 11 3-5 Plot of individual pixel values before and after proton irradiation (array 3 video output 1).

11.4 Total Ionizing Dose Effects (TIDE) on the 128 x 128 LWIR Array

11.4.1 Threshold Voltage Shifts

The main effect of the proton irradiations was the change in the appearance of defect pixels due to shifts in the effective direct injection gate voltage (VDIG). These changes were noticed during the 0.1 krad irradiations to search for transient events. During the 100 s irradiations, the defect pixels increased in brightness as shown in figure 11.4-1

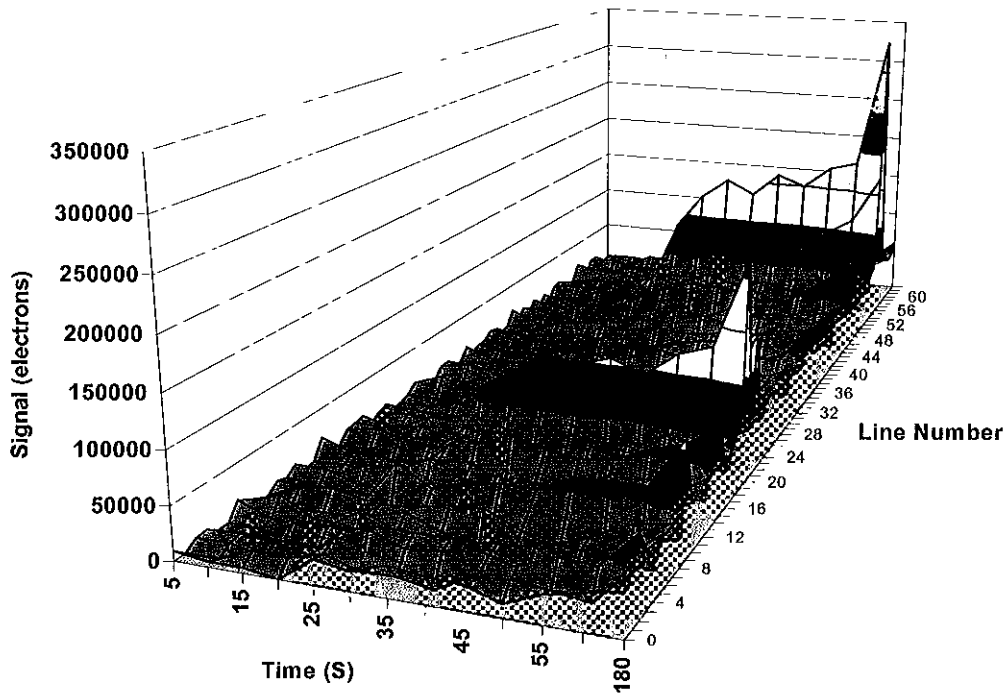


Figure 11.4-1 Plots of pixel values for one column of a 64 x 64 quadrant as a function of irradiation time. The points at 180 s were obtained after the irradiation had finished (the irradiation duration was 100 s and gave 0.1 krad total dose)

Changes in the image can be seen after only 30 s (0.03 krad or 5.4×10^7 p/cm²). Measurements were also made during the higher dose proton irradiations, both of the optimum DIG voltage (which gives best nonuniformity) and of the average signal (for a whole 64 x 64 quadrant) versus VDIG. From figure 11.4-2 it can be seen that the optimised VDIG data gives a good linear relation with total dose, indicating a shift:

$$\text{change in direct injection voltage} = -2.6 \text{ mV/krad(Si)},$$

the VDIG v. signal data is also in good agreement. This shift is similar to the value of -3.2 mV/krad found previously [2] for 256 x 4 GMIRL arrays. This should not be surprising since both types of array are manufactured using the same process (Atmel-ES2 ECPD15). Figure 11.4-3 shows the signal v. VDIG data. The optimized image data lie within the voltage band shown. There was only a slight annealing (~ 2 mV) of the shift after irradiation with storage for 19 days at room temperature (unbiased). Note that a shift in VDIG of less than 50 mV will cause a full scale (reset to baseline level) change in signal. It is likely that changes in diode

reverse bias voltage will also cause changes in 1/f noise. That fact that the data point at 2.4 krad lies on the fitted line indicates that the shift is not sensitive to bias (as found previously) - the first 2.4 krad was biased and the remainder not

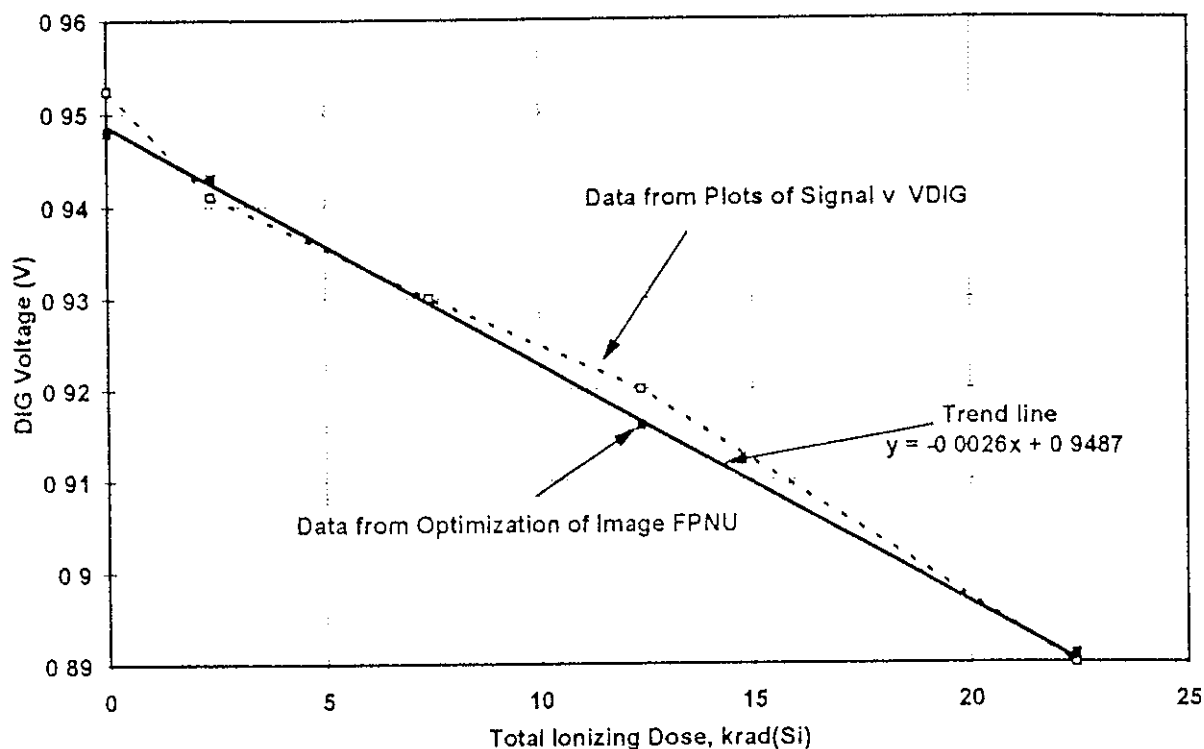


Figure 11 4-2 VDIG versus total ionizing dose (10 MeV proton irradiation)

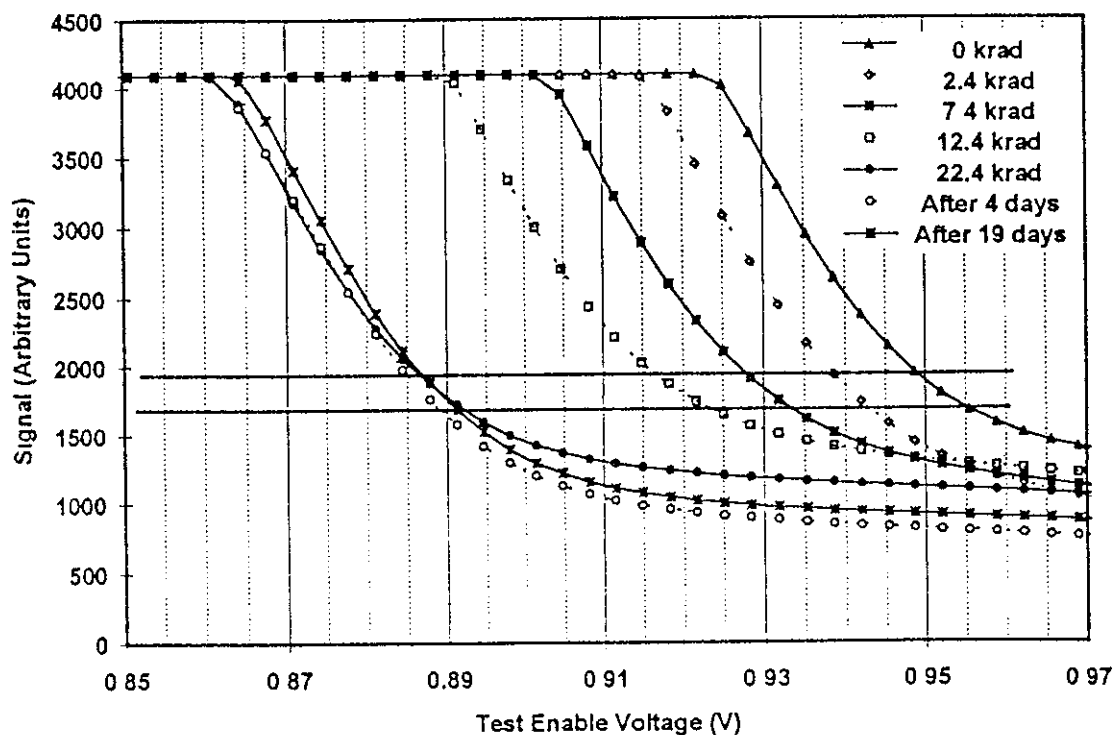


Figure 11 4-3 Signal versus VDIG for several values of TID

Threshold shifts for other bias and clock voltages are shown below

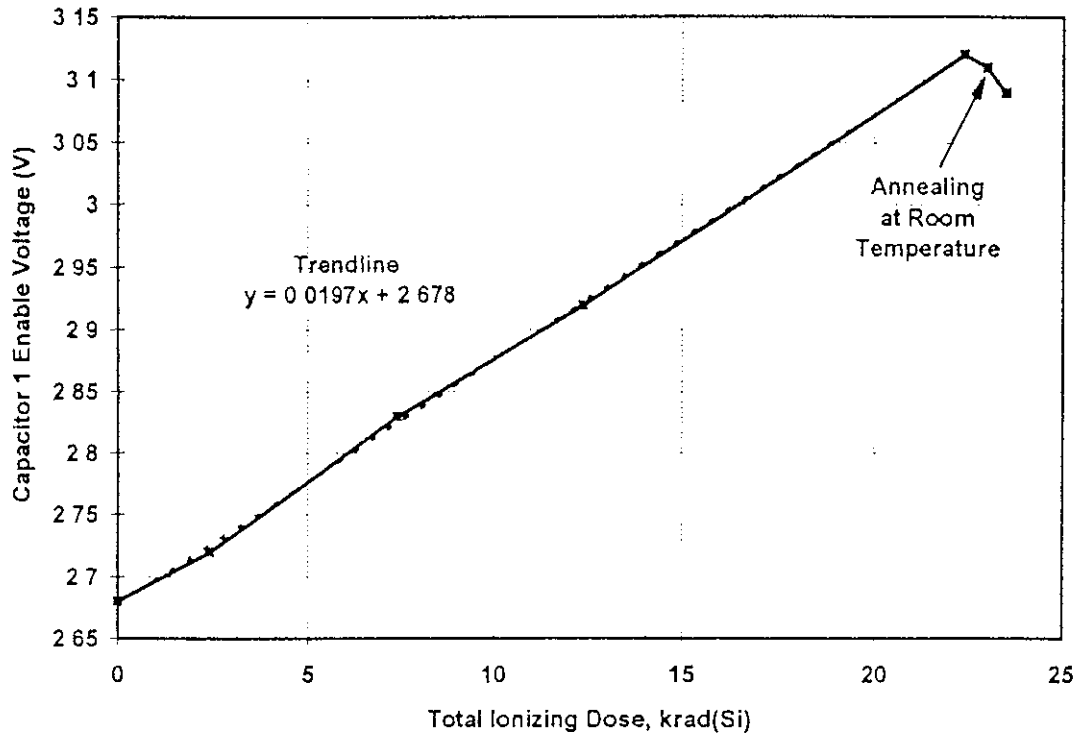


Figure 11 4-4 Cap1 enable voltage versus total ionizing dose (10 MeV proton irradiation)

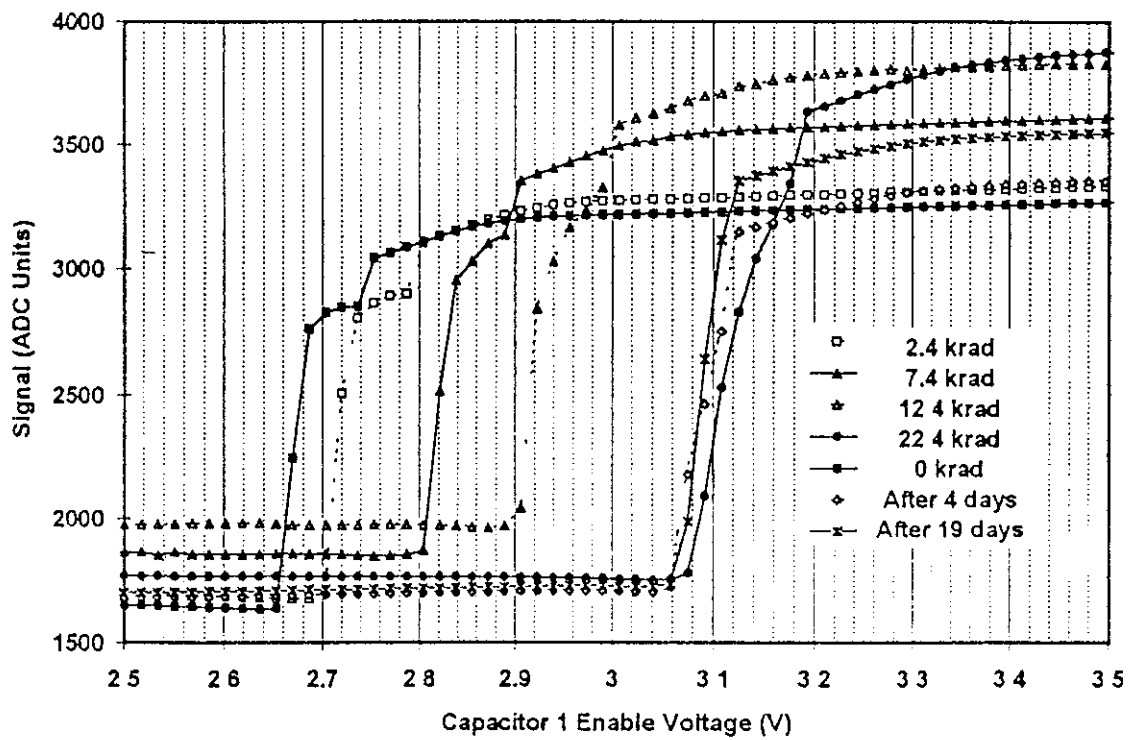


Figure 11 4-5 Signal versus cap1 enable voltage for several values of TID

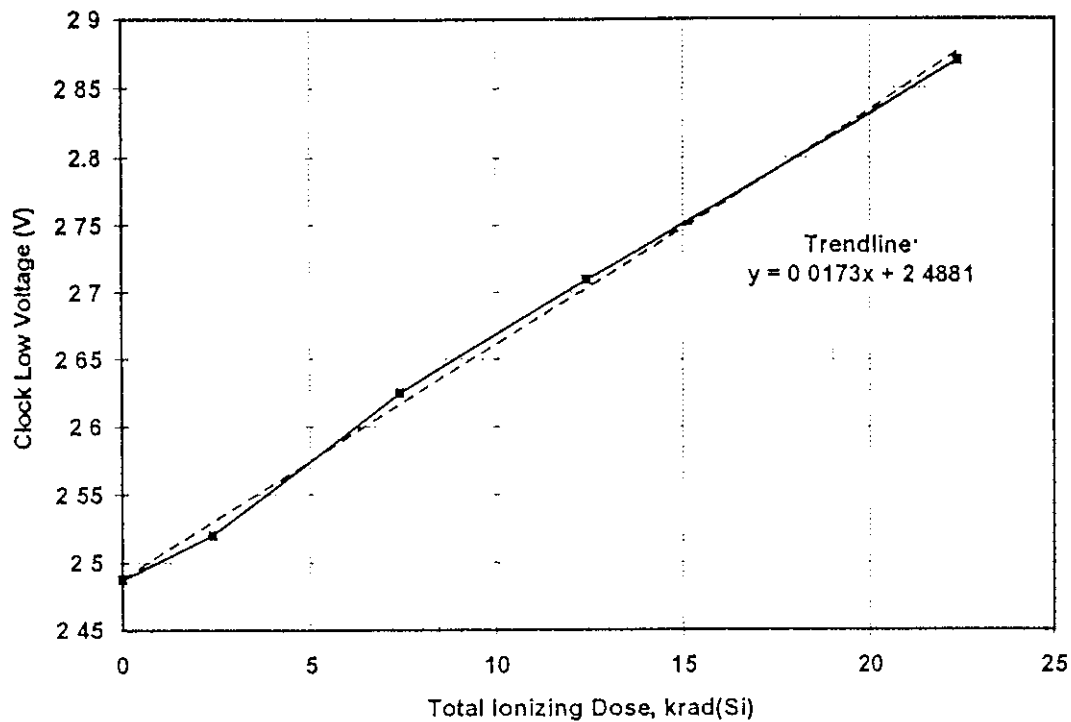


Figure 11 4-6 Clock Low voltage versus total ionizing dose (10 MeV proton irradiation)

The results on voltage shifts are summarized in the table below

Voltage	Shift (mV / krad)	Annealing mV shift in 19 days at RT
DIG	-2.6	YES, 50 mV
Cap1 Enable	20	YES, 30 mV
Clock High	18	YES, 50 mV
Clock Low	17	NO
Line Sync High	14*	NO*
Line Sync Low	13*	not measured
Stare Time High	13*	NO*
Stare Time Low	22*	not measured

* = no measurements made at Harwell, shifts estimated from measurements at Sira before and after irradiation

The shift for the bias voltages, excluding VDIG, is quite large at ~ 18 mV/krad and all in the positive direction. This contrasts with the previous results on the 256 x 4 array [2] where the shifts were in the range 2.5 to 8 mV/krad and all negative apart from the Line Sync High voltage. The differences may be explainable by differences in the CMOS circuitry, but information from the manufacturer indicates that the same process (Atmel-ES2 ECPD15) is used for both.

At the end of the project the array was subjected to 29 days unbiased alpha particle irradiation, giving approximately 6 krad total ionising dose. The observed voltage shifts were small (~ 20 mV) and probably due to a combination of alpha irradiation-induced shifts, annealing (which tends to compensate for these) and measurement errors.

11.4.2 Linearity and Responsivity of the 128 x 128 array

A black body source was used to illuminate the array. There are several ways to measure the linearity:

- 1 plot signal as a function of stare time (at fixed blackbody temperature)
- 2 plot signal against black body temperature
- 3 use a fixed temperature (say 60°C) and measure signal for various diameters of entrance aperture

Figure 11 4-1 shows average signal for a 64 x 64 quadrant versus stare time. The data were obtained before irradiation at the lowest electronics gain and using coaxial attenuators (factor 2.91) so that whole voltage range of the detector could be digitized by the ADC. It is seen that the response is non-linear for high and low signals. At low signals this will be due to poor injection efficiency and at high signals to the output amplifier response. The voltage range of 4.4 V corresponds to 1.65×10^7 electrons. A similar response was found in the previous study [2] for the 256 x 4 array, but the premature accidental damage to the sample used for these tests prevented linearity measurements in this case. For most measurements with the 128 x 128 array, a higher electronics gain was used and no attenuators. Hence only the central, linear, part of the curve was used. Figure 11 4-2 shows plots using this restricted range, before and after irradiation. There were no significant changes after irradiation.

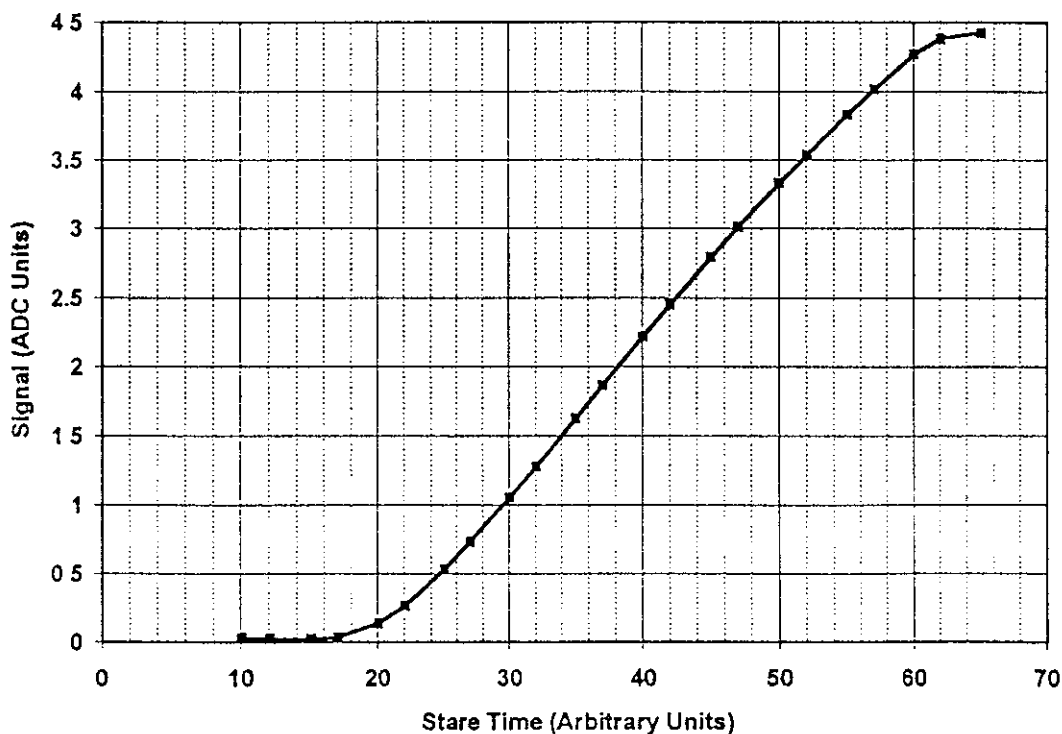


Figure 11 4-1 Average signal for a 64 x 64 quadrant versus stare time (low gain) - full voltage range of the array digitised

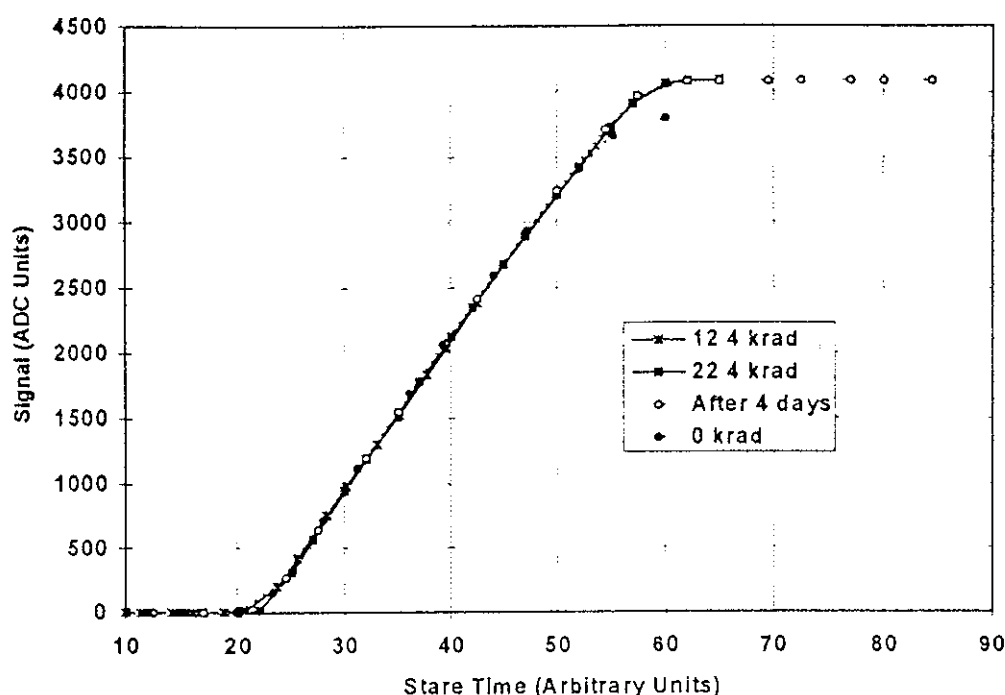


Figure 11 4-2 Average signal for a 64 x 64 quadrant versus stare time (mid gain) - restricted voltage range of the array digitised

Linearity measurements obtained with a black body temperature of 60°C and various entrance apertures are shown in figure 11 4-3 (average signal over a 64 x 64 quadrant). There is good agreement with a linear response.

Figure 11 4-4 shows results obtained by varying the black body temperature. The plots are histograms of pixel values for a 64 x 64 quadrant with the fixed pattern noise obtained at a blackbody temperature of 30°C subtracted. It is seen that the widths of the gaussian peaks increase with signal - as would be expected if the nonuniformity is due to changes in responsivity. These variations give an rms uniformity of ~ 5%. Figure 11 4-5 shows the linear relation between average signal and blackbody temperature. Plots were also made of the signals from 64 individual pixels (from a 'good' column of the array). These were used to determine the pixel responsivities before and after irradiation.

Figure 11 4-6 shows plots of pixel response before and after the 22.4 krad 10 MeV proton irradiation. There is a considerable scatter on the points, indicating that the responsivities have changed by an rms amount similar to the original dispersion - i.e. about 5%. A check was made that the effect was not caused by a change in the direct injection voltage - similar plots were obtained regardless of the VDIG value used when data was acquired. Figure 11 4-7 shows a good linear correlation of pixel responsivities with changes in VDIG. However it also shows that the average responsivity changes with VDIG - either because the diode response changes with bias voltage or because the injection efficiency changes (because of changes in the diode slope resistance). Figure 11 4-8 shows that the change in average (absolute) responsivity is

1.66%/mV shift in VDIG Using the change in VDIG with total dose found above (2.6 mV/krad) we get

$$\text{change in absolute diode responsivity} = 4.3\% / \text{krad(Si)}$$

assuming that VDIG is not changed to compensate for the radiation induced shift

Figure 11 4-9 plots the diode responsivities obtained 4 and 19 days after irradiation. There is a good correlation, indicating that the responsivities do not vary much from day to day and that the variations found after irradiation are real.

Figure 11 4-10 shows responsivities before and after the final 29 day unbiased alpha irradiation at room temperature. These values were obtained by taking a succession of images at varying stare times (figure 11 4-2 showed that the response is linear). It is seen that there was little change in responsivity for the estimated total dose of ~ 6 krad(Si), the scatter in the responsivities being about 1%. This result should be representative for low dose environments where the detector is periodically warmed to room temperature or otherwise experiences annealing of damage in the MCT diodes.

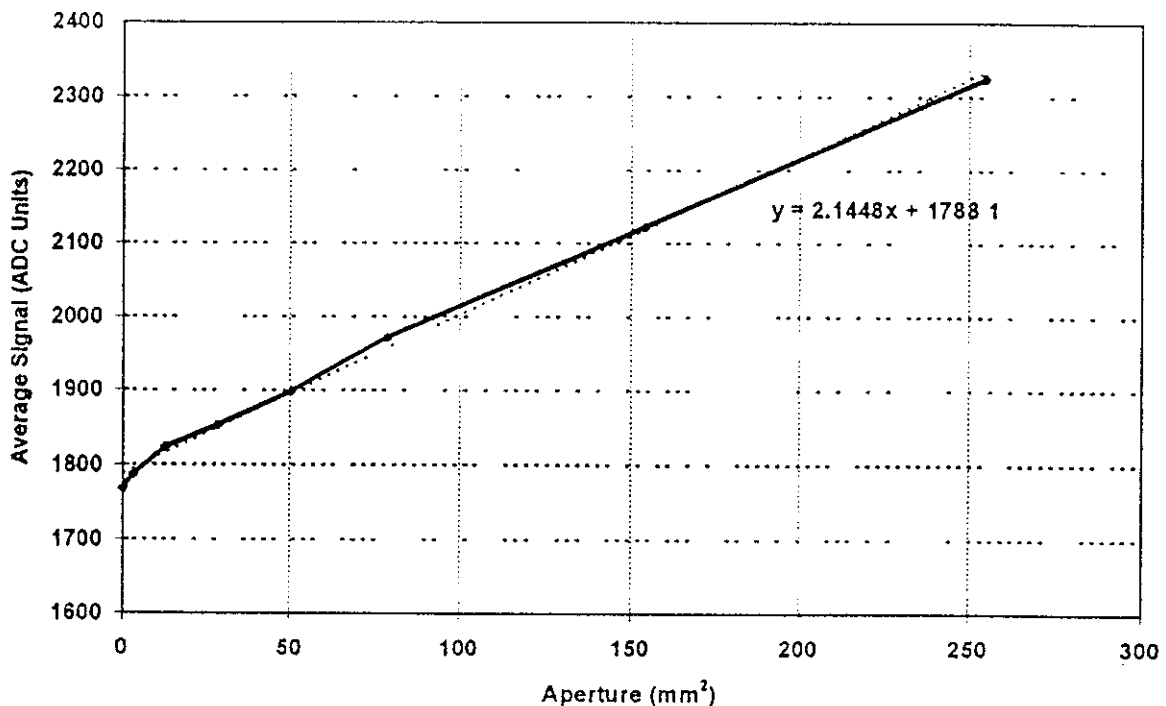


Figure 11 4-3 Average signal for a 64 x 64 quadrant versus aperture (low gain) - restricted voltage range of the array digitised

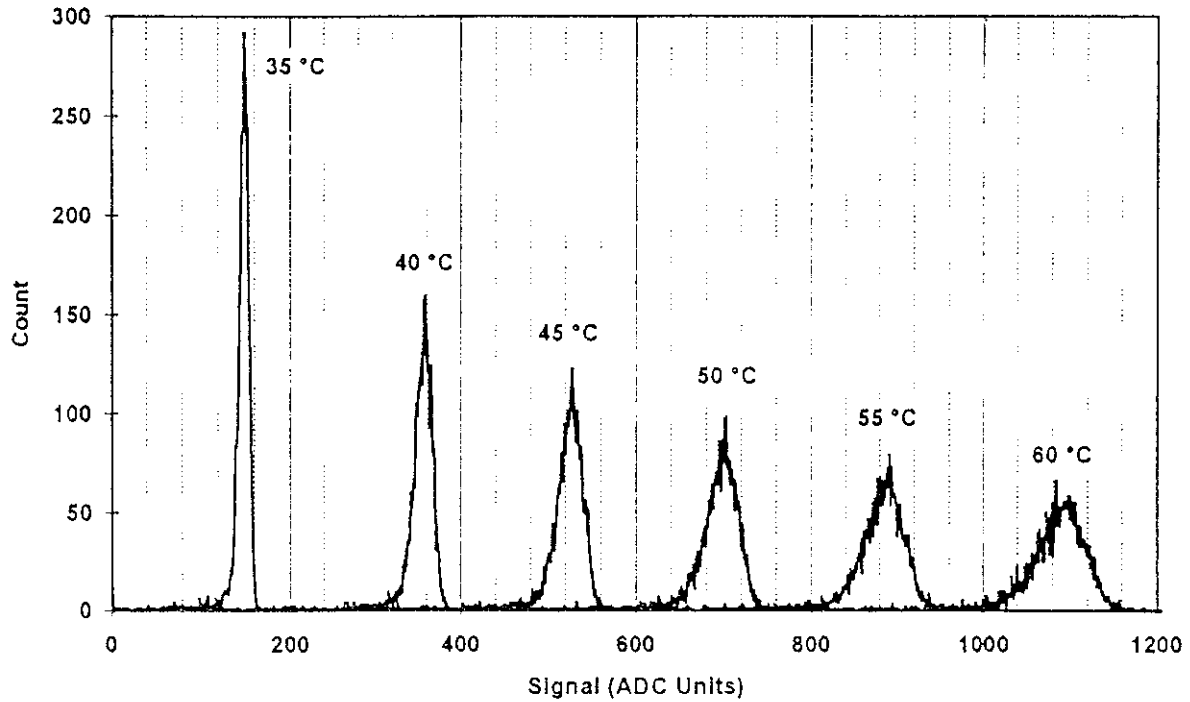


Figure 11 4-4 Histograms of pixel values for a 64 x 64 quadrant (low gain) for several blackbody temperatures. The fixed pattern noise obtained at a blackbody temperature of 30°C is subtracted.

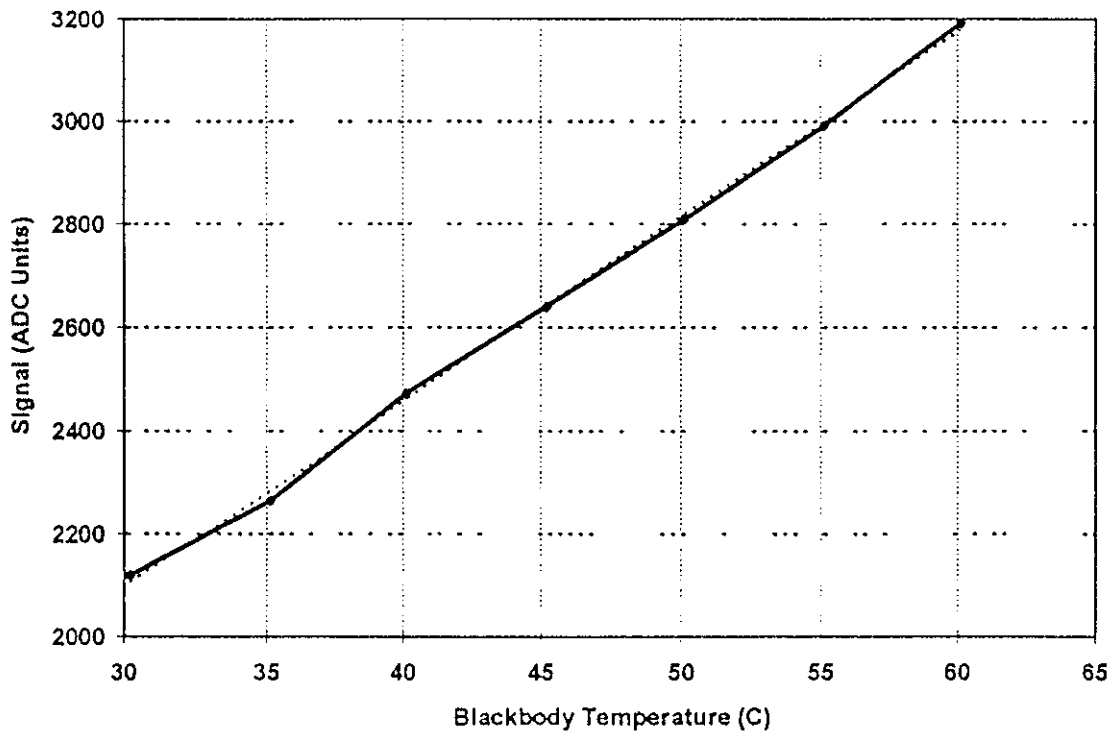


Figure 11 4-5 Plot of average signal against blackbody temperature for a 64 x 64 quadrant of the LWIR array.

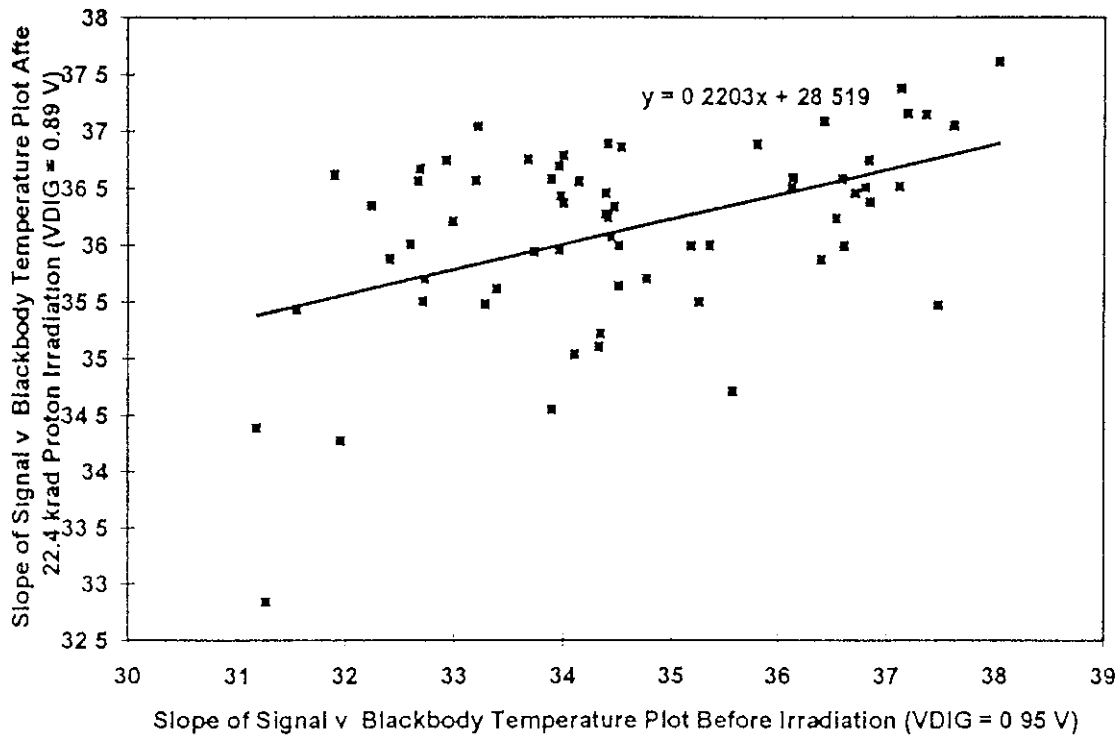


Figure 11 4-6 Plots of pixel response before and after the 22.4 krad 10 MeV proton irradiation

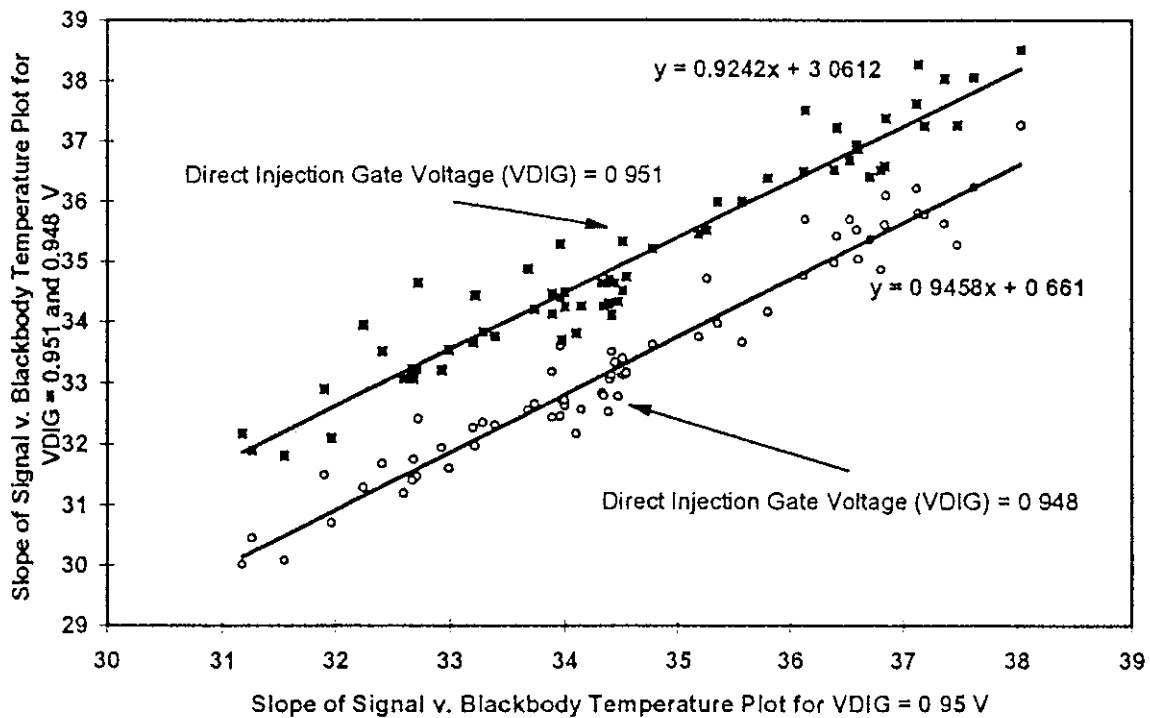


Figure 11 4-7 Plot of Pixel responsivities at VDIG = 0.95V, compared with values at VDIG = 0.951 and 0.948 V

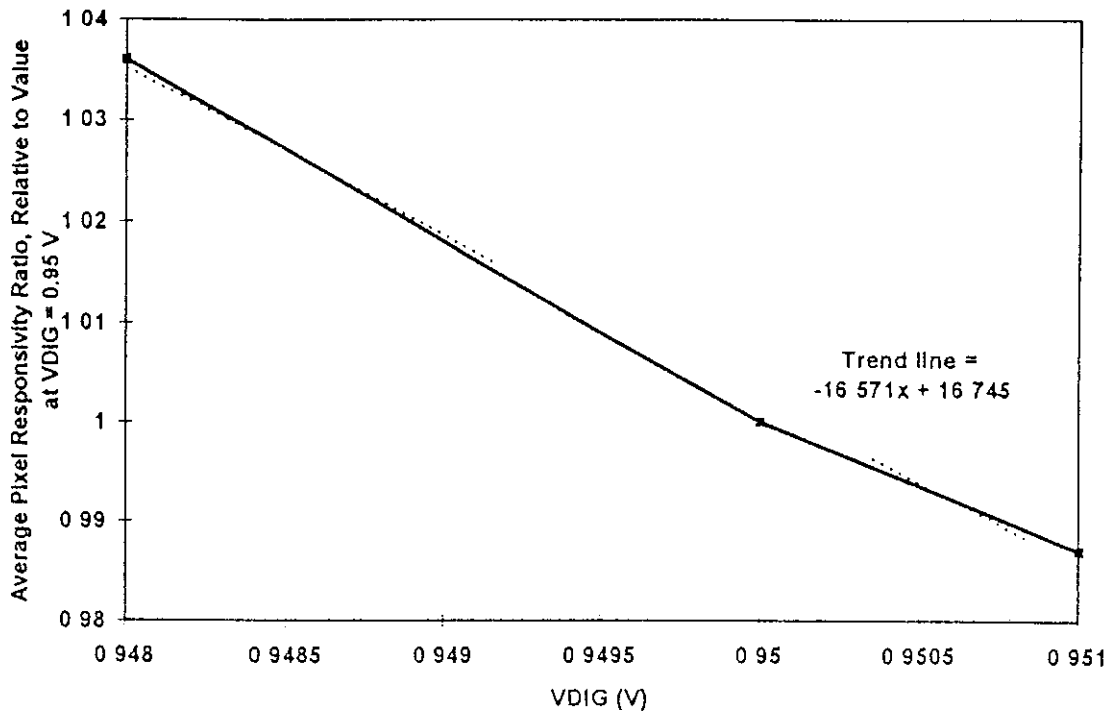


Figure 11 4-8 Change in average (absolute) responsivity with VDIG

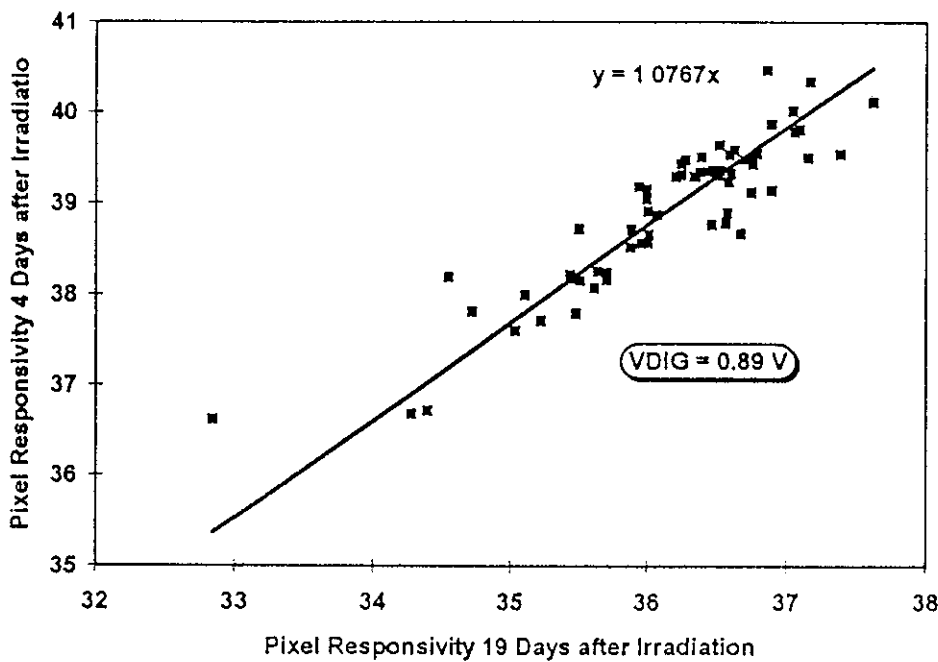


Figure 11 4-9 Diode responsivities measured 4 and 19 days after proton irradiation

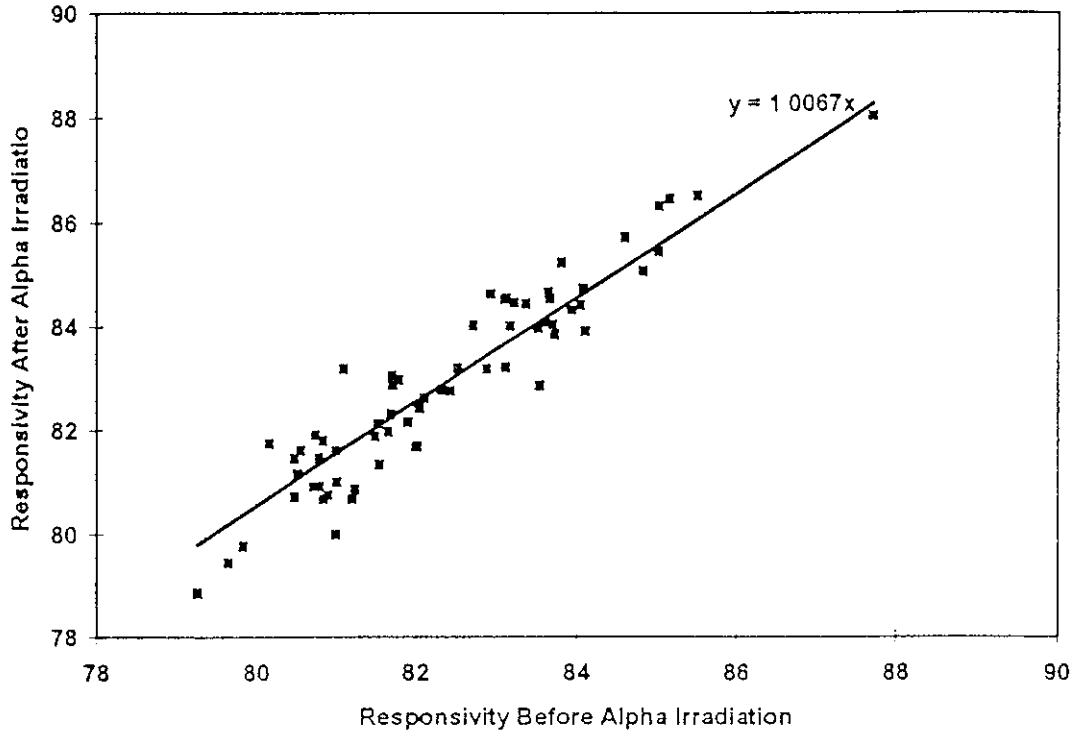


Figure 11 4-10 Responsivities for pixels in column 27 of a 64 x 64 quadrant of the LWIR MCT array before and after 29 days alpha particle irradiation at room temperature to ~ 6 krad(Si)

References

- [1] J F Ziegler, J P Biersack and U Littmark, 'The Stopping and Range of Ions in Solids', (Pergamon Press, Oxford, 1985), PC version developed by J P Biersack and J F Ziegler, IBM Research, York-Town, NY, U S A
- [2] G R Hopkinson, C J Baddiley, D R P Guy and J E Parsons, "Total Dose and Proton Testing of a Commercial HgCdTe Array" *IEEE Trans on Nuclear Science*, vol NS-41(6), pp 1966-1973 (1994)

12 DISCUSSION AND IMPACT ANALYSIS

In this chapter we discuss the main findings of the study and the impact for future space missions (as far as this can be judged from our existing knowledge) The implications for future detector test programmes and for hardness assurance are also considered Finally, we present some suggestions for further work

12.1 PERMANENT EFFECTS IN DETECTOR MATERIALS

12.1.1 MCT

Total ionizing dose will lead to charge trapping and interface trap generation in the passivation layer and can cause changes in leakage currents and diode slope resistance – particularly with narrow bandgap LWIR arrays

The implications of the decrease in resistance will depend on the type of readout circuit For the commonly used direct injection readout there will be a loss in injection efficiency and hence pixel responsivity However available evidence suggests that this will show significant annealing in the low dose rate space environment – particularly if the array is periodically warmed to room temperature The results of chapter 11 indicate that changes in the responsivity of individual pixels will be limited to a few percent This effect could be important for radiometric instruments but is comparable to (in fact, probably smaller than) the changes due to temperature variations and total dose effects in the multiplexer (it was found that detector responsivity can change by as much as 4%/krad if the voltage on the direct injection gate is not adjusted in-flight) These changes mean that radiometric instruments would almost certainly contain blackbody sources for periodic calibration during a mission (see also Sira document CAL-SIR-FR-001, final report on ESTEC contract number 11584/95/NL/CN, 'Strategies for Calibration of Imaging Spectrometer Data', June 1997)

With the engineering grade detectors studied in this work it was found that proton and alpha particle-induced displacement damage effects were not important compared with the total dose effects described above However this finding should be re-examined in the course of instrument development, when better quality detectors are available

The above comments refer principally to the use of MWIR (3-5 μm) and LWIR (7-10 μm) diodes with direct injection circuits operated at 80 K Extrapolation to shorter wavelength (SWIR) or longer wavelength (e.g. 12-13 μm cut-off) diodes or to use of other readout circuits is somewhat uncertain However we make the following tentative comments

Tentative comments on extrapolations of available MCT data

- SWIR detectors

These have a very high resistance and so total dose effects (in both the diode and the readout circuit) are expected to be less important The operating temperature will be

higher (say 150 K) and the array uniformity may be better than for longer wavelength detectors – hence it is possible that displacement damage-induced dark current variations may be detectable

- LWIR detectors

For detectors with longer wavelength cut-off than considered in this study (for example 12-13 μm) the diodes have a low resistance and are harder to couple to readout circuits. Hence total dose effects can be expected to be more important. The diodes will be operated at a lower temperature (~ 50 K) and so dark current will tend to be dominated by tunnelling effects. Proton-induced trap assisted tunnelling may then become important. However, given the lack of major effects at 10 μm cut-off and the fact that on-orbit calibration will probably be performed, there seems to be no immediate cause for concern for missions observing bright targets (e.g. Earth remote sensing missions). For low background observations (e.g. space astronomy), radiation effects may be more important, but such missions tend to use longer wavelengths, for which MCT would not be the material of choice.

GaAs/AlGaAs quantum well photodetector (QWIP) arrays are a good alternative to MCT for the LWIR, though tending to need lower operational temperatures. The available evidence suggests that detector performance would not be affected in the space environment (but the detector array will need to be coupled to an appropriate readout circuit). QWIP arrays have the advantage of good producibility and uniformity. They have a high impedance and so are easy to interface to CMOS readout circuits.

- Other readout circuits

As discussed in section 14.11, the source follower per detector (SFD), the gate modulation input (GMI) and the cascade amplifier per detector (CAD) circuits are susceptible to threshold voltage and gain non-uniformities and so may be more sensitive to TID effects than the direct injection circuit studied here - though effects will, of course, depend on the oxide technology used.

12.1.2 InSb

The SIRTf results discussed in section 9.2.1 suggest a susceptibility to proton-induced dark current spikes (rather as for a Si CCD). No major problems for total dose effects in the passivation layer have been reported in the literature for the devices studied so far.

12.1.3 GaAs/InGaAs QWIP Detectors

These were compared with MCT detectors in section 12.1.1 above. They appear to show good tolerance to all types of radiation.

12.1.4 Extrinsic Silicon

The effects of quasi permanent charge trapping on the responsivity of extrinsic silicon detectors has been well known since IRAS. Use of blocked impurity band (BIB) detectors is a way of overcoming this sensitivity. However recent results (discussed in section 9.2.2) show that proton-induced increases in dark current can be produced in individual detector elements. A conclusive identification of the mechanisms involved has not been published, but the effect is believed to be due to punch-through of the intrinsic silicon blocking layer.

12.1.5 Other Detector Materials

There are a number of infrared detector materials, for example, InGaAs, lead chalcogenides (e.g. PbSe, PbTe), PtSi, Si/SiGe for which very little information is available.

12.2 PERMANENT EFFECTS IN SI READOUT CIRCUITS

Both surface channel CCD and CMOS circuits are used to readout signals from IR detector arrays. The most common being CMOS. There would appear to be no major concerns with using Si S-CCD circuits in a space application. Dark current will be low because of the low operating temperature, though CTE may be degraded (but it is usually in any case low at liquid nitrogen temperatures). For CMOS circuits the trend to thin gate oxides improves radiation tolerance but there are the usual concerns about parasitic leakage paths being turned on in field isolations, and also for latch-up. In principle, CMOS circuits can be hardened for total dose effects, so the issues involved become ones of foundry selection and hardness assurance. These will be discussed further in section 12.5.

12.3 TRANSIENT EFFECTS

In any semiconductor material, transient noise events are produced by charged particle hits and bremsstrahlung photons. In a space environment, the effects will occur during passage over the poles and through the South Atlantic Anomaly (SAA). The size of the events depends on the track length (angle of incidence and detector thickness), the energy loss per unit length (dE/dx) of the material and the energy lost (ϵ) in producing an electron hole pair. For the materials of interest for the IR, ϵ is in the range 1-4 eV. In silicon CCDs ϵ is 3.6 eV, full well capacities are $\sim 5 \times 10^5$ electrons and detector thicknesses are $\sim 20 \mu\text{m}$, so a typical event is $\sim 1/250^{\text{th}}$ full well. For a LWIR MCT detector, 10 microns thick a typical proton event is $\sim 10^5$ electrons and the full well $\sim 10^7$ electrons – so relative to the full well capacity, the events are similar in size to those expected for a Si CCD.

Very rarely, a charged particle will produce a nuclear reaction with a target nucleus, with emission from the nucleus of a proton, neutron or alpha particle. This spallation product will generate its own transient charge which will typically be of order 10^5 electrons assuming ~ 0.1 MeV deposited. However the probability of such events occurring is very small. An approximate calculation can be made as follows.

$$\text{event rate} = \sigma \rho V N_A \Phi t_{\text{int}}/A \quad (12-1)$$

where σ is the cross section for inelastic nuclear reactions for a given proton energy and target material
 ρ is the density
 V is the active volume of a pixel
 N_A is Avagadro's number = 6.02×10^{23}
 Φ is the particle flux
 t_{int} is the integration time and
 A is the atomic weight of the target material

Inelastic nuclear cross sections have been given in several publications. Petersen [1] gives plots of cross sections of various reactions in In, Ge and Si as a function of proton energy. Janni [2] has tabulated total cross sections for protons of energies 0.9 to 10000 MeV on H, He, C, O, Al, Cu, Ag and Pb and Letaw et al [3] give an empirical formula for estimating total cross sections down to 10 MeV. The cross section does not change much with proton energy and is typically 0.7 barns (1 barn = 10^{-28} m²) for Si, rising to about 2 barns for dense materials such as HgCdTe.

Assuming an HgCdTe detector (density 7.6 g/cm³), pixels of 30 μ m diameter and 9 μ m thickness and an integration time of 10 ms we get an event rate of

$$5 \times 10^{-8} \text{ events/pixel/frame}$$

for a proton flux of 1.5×10^4 p/cm²/s which is typical for a 2000 km equatorial intermediate orbit [4]

12.4 RADIATION TESTING OF IR DETECTOR ARRAYS

Testing for total dose effects is normally carried out using Cobalt60 gamma rays since this has been shown to be a good simulator both for bremsstrahlung photons and for the protons (of energy several hundred MeV) in the space environment – especially if a low dose rate is used.

Although total dose effects can be seen with protons, it is much preferred to test at the lower dose rates and lower charge densities available with Cobalt60 gamma rays. Certainly low energy (e.g. 10 MeV) proton testing cannot be expected to give good quantitative data on field oxide damage (for which recombination effects are more important, compared with gate oxides, because of the increased oxide thickness and lower electric field).

Testing for displacement damage can be carried out using a proton accelerator. 10 MeV is often used but higher energies are possible. Higher energy protons are more capable of causing nuclear (spallation) reactions in target nuclei, however in silicon it is commonly accepted that the damage created does not depend on the details of the interaction process but simply scales with the non-ionising energy loss (NIEL). This proportionality with NIEL has not been studied for MCT or InSb and so cannot be regarded as established in these materials. Hence the lack of observation of displacement effects at 10 MeV with the GMIRL array does not necessarily

imply that no effects will be seen at higher energies. However, many materials (e.g. InGaAs, GaAs, Ge) do seem to show a good correlation between damage and NIEL so that we would expect any non-scaling of the damage in MCT to affect only a detailed quantitative calculation. The fact that no significant displacement damage was seen for 10 MeV protons (or for the alpha particle test) suggests that no damage would be seen for high proton energies either. At some stage this will need to be confirmed, (e.g. when more flight representative detectors are available) but it is suggested that this has a low priority at this stage.

Before the experimental programme was performed, it was hoped that alpha particle testing in the laboratory would be useful for measuring displacement damage and transient events. In fact it turned out that the displacement effects were small and the size of the transient events was smaller than expected, probably because of electron-hole recombination along the alpha particle track. It was also found that proton testing of cooled IR arrays could be performed relatively easily – at least at 10 MeV. It is therefore recommended that proton, rather than alpha particle, testing is performed in future. Note that the situation with displacement damage in silicon imagers (CCDs, CIDs, APSs etc.) is different because this damage is much easier to observe and alpha particle testing may still have a place.

Next we consider the types of detector to be tested and characterisation methods. The high cost of IR devices and associated test equipment probably means that evaluation testing of arrays prior to selection for flight instrumentation is not likely to be possible in many cases. Rather, it is expected that radiation testing will need to occur on prototype or engineering model detectors, procured for specific instrument development for flight projects. However it is suggested that the teams involved in detector development may not have the necessary radiation effects expertise to carry out an in-depth radiation evaluation. The Agency may therefore wish to consider how radiation effects and instrument development engineers can be brought together.

Finally, we summarise the conclusions of this section as follows

- use Cobalt60 for total dose testing
- use protons for displacement damage testing (dependence on NIEL to be investigated when good quality arrays are available)
- consider use of prototype or EM detectors for evaluation testing (plus associated test equipment)

12.5 HARDNESS ASSURANCE

In this section we consider the steps needed to ensure that devices tested give results representative for devices used in-flight. It is expected that in many cases the detector arrays will not be produced as part of a radiation hardening programme and that process controls will not be used by the vendor to monitor and control radiation tolerance. It will therefore be necessary to perform radiation lot acceptance on devices from the flight batch. Because of the cost of devices it will not be possible to test in large quantities. However it should normally be possible to procure bare readout circuits (un-hybridised to the detector array) for total dose testing and, in some cases, small arrays of detectors used for process control. In this way it may

be possible to gain information on device-to-device variations and to investigate dependencies on bias, dose rate, irradiation temperature and annealing

In the case of the GMIRL arrays studied here and in a previous Sira study, it was established that room temperature testing produced the same total dose effects as irradiation at 80 K. However this may not always be the case and would need to be verified, for each type of readout circuit. It was also found that device-to-device variations in the commercial samples tested were small – giving some confidence that testing small numbers of devices (~10) can give meaningful results. In addition, it was found that annealing effects can take place over timescales of the order of 1 month. So this has to be borne in mind when designing test programmes

A difficulty which may be encountered when considering the choice of commercially available devices is that an early evaluation of candidate detectors may not give representative results because the manufacturer may change his CMOS foundry or detector process. The possibility of this has to be carefully considered and assurances of process stability obtained from the manufacturer whenever possible

12.6 SUGGESTIONS FOR FURTHER WORK

In this section we present a brief list of topics for further work

- further investigation of transient events
 - it would be useful to develop techniques to study proton-induced transient events with better statistics
- further investigation of response nonuniformity changes with total dose
 - having established in this study that linearity can be measured by a variety of techniques and that changes in individual pixel responsivity do seem to be caused by irradiation, it would be useful to perform further studies to obtain a more extensive dataset
- testing of other array types
 - there are several detector technologies for which little radiation effects data exists, for example InGaAs and InSb. Also detailed characterisation will be needed of both detector and multiplexer arrays to be used on all future flight projects (whatever the detector type)
- testing of latch-up in CMOS circuits at low temperatures
 - this would be a very useful study and would determine if latch-up can occur in IR multiplexers at operational temperatures

REFERENCES

- [1] E L Petersen, "Nuclear reactions in semiconductors", *IEEE Trans on Nuclear Science*, vol NS-27(6), pp 1494-1499 (1980)
- [2] J F Janni, "Proton range-energy tables" *Atomic Energy and Nuclear Data Tables*, vol 27, pp 147-529 (1982)
- [3] J R Letaw, R Silberberg and C H Tsao, "Proton-nucleus total inelastic cross-sections an empirical formula for $E > 10$ MeV", *Astrophys J Suppl Series*, vol 51, pp 271-276 (1983)
- [4] MMS fax of 14 Aug 1997 from T Carriere